Knudsen Pumps and Their Potential Application to Artificial Pneumatic Micro-Muscles Actuation

Dingdong Zhang

Université Fédérale
Toulouse Midi-Pyrénées

THÈSE

En vue de l'obtention du
DOCTORAT DE L'UNIVERSITÉ DE TOULOUSE

Délivré par l'Institut National des Sciences Appliquées de Toulouse

---

Présentée et soutenue par

Dingdong ZHANG

Le 9 octobre 2023

Pompes de Knudsen et Leur Application Potentielle à l'Actionnement de Micro-Muscles Pneumatiques Artificiels

---

Ecole doctorale : **MEGEP - Mécanique, Energétique, Génie civil, Procédés**

Spécialité : **Dynamique des fluides**

Unité de recherche :
ICA - Institut Clément Ader

Thèse dirigée par
Stéphane COLIN, Bertrand TONDU et Marcos ROJAS CARDENAS

Jury

M. Gian Luca MORINI, Rapporteur
Mme Irina GRAUR, Rapporteure
M. Gwenn ULLIAC, Examinateur
M. Stéphane COLIN, Directeur de thèse
M. Bertrand TONDU, Co-directeur de thèse
M. Marcos ROJAS-CARDENAS, Co-encadrant de thèse

UNIVERSITÉ DE TOULOUSE

Institut National des Sciences Appliquées de Toulouse

Toulouse, France

Knudsen Pumps and Their Potential Application to Artificial Pneumatic Micro-Muscles Actuation

Pompes de Knudsen et Leur Application Potentielle à l'Actionnement de Micro-Muscles Pneumatiques Artificiels

by

Dingdong ZHANG

张定东

A Dissertation for the Partial Fulfillment of the

Requirements for the Degree of

Doctor of Philosophy

October 2023

Certified by the members of the Dissertation Committee:

1st member	Prof. Stéphane COLIN
(Supervisor)	Institut National des Sciences Appliquées de Toulouse
2nd member	Prof. Bertrand TONDU
(Co-supervisor)	Institut National des Sciences Appliquées de Toulouse
3rd member	Asst. Prof. Marcos ROJAS-CARDENAS
(Co-supervisor)	Institut National des Sciences Appliquées de Toulouse
4th member	Prof. Gian Luca MORINI
(Reporter)	Università di Bologna
5th member	Prof. Irina GRAUR
(Reporter, President of jury)	Université d'Aix-Marseille
6th member	Gwenn ULLIAC
(Examiner)	FEMTO-ST, CNRS

书山有路勤为径，学海无涯苦作舟

In the world of books, a diligent path leads up the mountain;
in the sea of learning, hard work is the boat.

Dans le monde des livres, un chemin diligent mène à la montagne;
dans la mer de l'apprentissage, le travail acharné est le bateau.

Acknowledgements

First and foremost, I would like to express my deep and sincere gratitude to my supervisors, Stéphane Colin, Bertrand Tondu and Marcos Rojas-Cardenas, for their guidance and support during the whole project and their understanding and endless patience during the most difficult times. They are not just outstanding researchers, but also remarkable individuals with great values. I sincerely think that I could not have found better mentors for these three years.

I also want to thank to the whole microfluidics team at the Institut Clément Ader for their valuable help through the project. I am very grateful to Lucien, Christine, Pascale and Ahmad not only for the scientific discussions and precious technical advice with my project, but also for showing me the work environment I would like to find in my future. I would also like to specially thank Nicolas Laurien and Stéphane Orieux for all the technical support and help in the laboratory. Additionally, to all my fellow colleagues in Toulouse (former and new), an international and endless list composed by people from France, China, Germany, Italy, India, Lebanon, Thailand; thanks for all those necessary coffee breaks over both scientific and not-so scientific discussions.

I also want to express my gratitude to Prof. Klaus Bade, Mr. Stefan Hengsbach and Mr. Samuel Bergdolt at KNMFi of KIT in Germany for providing me the samples during part of this project and showing me some important issues on microfabrication. Additionally, for part of the technical support and training at Laboratoire de Physique et Chimie des Nano-Objets (LPCNO) in Toulouse regarding the microfabrication efforts, I am deeply grateful to Etienne Palleau, Simon Raffy and Matthieu Raison for teaching me everything I have learnt about working in a clean room.

I would like to thank the defense committee: Prof. Gian Luca Morini, Prof. Irina Graur, and Mr. Gwenn Ulliac for their encouragement, insightful comments, and interesting questions.

I would like to give my special thanks to Guillermo López Quesada, Slaven Bajic, Franz Schweizer and Phassawat Leelaburanathanakul for their helping with the experiments, numerical simulations, and interesting talks on science and nature in those coffee breaks. Besides, I would also like to thank a group of students who completed their internship in the microfluidic group with their greatly help for modeling on artificial mini-muscles. They are Elek Bogaers, Lea Decroix, Pablo Mir, Lucia Vicente-Martinez, and Thomas Villemez.

I would also like to thank the members of Institut Clément Ader and Ecole Doctorale MEGeP. I enjoyed my research experiences at Institut Clément Ader with those outstanding

researchers. Additionally, I am very grateful for the friendship with other PhD students from China, especially Gang Huang, Shuli Wang, Taiwei Xu, Huikangyue Bao, Zhenhang Wu, Lei Ren, Wenbo Li and Chong Wang.

I acknowledge the scholarship of China Scholarship Council (CSC) which awarded a scholarship for my studies in France.

Finally, I am grateful to everyone that I have met in every step of the way. Every single experience and moment has taken me to this point after living in Toulouse. Not forgetting to thank the ones always waiting for my return, growing in number little by little, because wherever they are I know I will be welcome. Most importantly, I would like to thank my parents and family. Their love, support and encouragement provide me endless power and energy to pursue my scientific dream.

Abstract

Knudsen micropumps represent a category of miniaturized pumps that operate without any moving parts. They function by applying a temperature gradient that generates gas flow based on the principle of thermal transpiration. Their versatility makes them suitable for various applications, including vacuum generation, gas separation, and gas chromatography.

The main objective of this thesis is to design a Knudsen micropump tailored for actuating artificial pneumatic micro-muscles controlled by varying levels of vacuum.

Pneumatic artificial muscles can perform more or less complex movements by applying a pressure difference between their internal volume and the external environment. Given the efficient vacuum generation capability of Knudsen micropumps, they have the potential to effectively control artificial pneumatic micro-muscles for diverse applications such as micro swimmers, micro-robots, micro-grippers, or more complex micro-actuators.

In this thesis, a multistage Knudsen micropump is designed numerically. It requires the use of numerous microchannels. Various types of microchannels are then designed, manufactured, and experimentally analyzed. Concurrently, pneumatic muscles are simulated, manufactured, and tested on a miniaturized scale. A preliminary analysis of the dynamic performance of a combination of Knudsen micropump and artificial pneumatic micro-muscle concludes this work.

Keywords: microfluidics, Knudsen pumps, rarefied gas flows, two-photon polymerization, artificial micro-muscles

Résumé

Les micropompes de Knudsen représentent une catégorie de pompes miniaturisées qui opèrent sans aucune pièce mobile. Elles fonctionnent grâce à l'application d'un gradient de température qui génère l'écoulement de gaz selon le principe de la transpiration thermique. Leur polyvalence les rend adaptées à diverses applications, parmi lesquelles la génération de vide, la séparation de gaz et la chromatographie en phase gazeuse.

L'objectif principal de cette thèse est de concevoir une micropompe de Knudsen adaptée à l'actionnement de micro-muscles pneumatiques artificiels, contrôlés par des niveaux variables de vide.

Les muscles artificiels pneumatiques peuvent effectuer des mouvements plus ou moins complexes par l'application d'une différence de pression entre leur volume interne et l'extérieur. Étant donné la capacité des micropompes de Knudsen à générer efficacement du vide, elles sont potentiellement capables de contrôler efficacement des micro-muscles artificiels pneumatiques, en vue d'applications potentielles variées (micro-nageurs, micro-robots, micro-pinces ou micro-actionneurs plus complexes).

Dans cette thèse, une micropompe de Knudsen à plusieurs étages est dimensionnée numériquement. Elle nécessite l'utilisation de nombreux microcanaux. Divers types de microcanaux sont alors conçus, fabriqués et analysés expérimentalement. Parallèlement, des muscles pneumatiques sont simulés, fabriqués et testés dans une version à mini-échelle. Une analyse préliminaire de la performance dynamique d'une combinaison de micropompe de Knudsen et d'un micro-muscle pneumatique artificiel vient conclure ce travail.

Mots-clés : microfluidique, pompes Knudsen, flux de gaz raréfiés, polymérisation à deux photons, micro-muscles artificiels

Contents

List of Figures

List of Tables

Nomenclature and Acronyms

Acronyms

3D-DLW	3D direct laser writing
AAO	Anodic aluminium oxide
BGK	Bhatnagar–Gross–Krook
BTE	Boltzmann transport equation
CDG	Capacitance diaphragm gauge
CFD	Computational fluid dynamics
DF	Dry film
DMD	Digital micromirror device
DSMC	Direct simulation Monte Carlo
DVM	Discrete velocity method
FEA	Fluidic elastomer actuator
HGF	Helmholtz Gemeinschaft
HS	Hard sphere
IPL	Inverse power law
KNMFi	Karlsruhe Nano Micro Facility
KP	Knudsen pump
KμP	Knudsen micropump
LP-VPAM	low-profile vacuum-powered artificial muscle
MCE	Mixed cellulose ester
MEMS	Micro-Electro-Mechanical-System
ONO	Oxide–nitride–oxide
PAM	Pneumatic artificial muscle
PC	Personal computer
PGMEA	Propylene glycol methyl ether acetate
PM	Porous medium
PMMA	Poly (methyl methacrylate)
PAμM	Pneumatic artificial micro-muscle
RIE	Reactive ion etching
TPD	Thermomolecular pressure difference
TPP	Two-photon-polymerization

UH-PAM	Ultralight hybrid pneumatic artificial muscle
UV	Ultraviolet
VAMP	Vacuum-actuated muscle-inspired pneumatic structure
VHS	Variable hard sphere
VSS	Variable soft sphere

Latin Symbols

A_S	Cross-sectional area (m^2)
C_{10}	Material constant (Pa)
D_h	Hydraulic diameter (m)
D_S	Mean molecular spacing (m)
D_1	Incompressibility parameter (Pa^{-1})
d	Microtube diameter (m)
d_{mol}	Mean molecular diameter (m)
F	Force amplitude (kg m s^{-2})
$\mathbf{F}$	External force vector per unit mass (m s^{-2})
f	Velocity distribution function after collision (m^{-6} s^3)
f'	Velocity distribution functions before collision (m^{-6} s^3)
G_P	Dimensionless mass flowrate due to a pressure gradient
g_r	Relative molecular velocity magnitude (m s^{-1})
h	Microchannel height (m)
$\bar{I}_1$	First deviatoric strain
J	Total volume ratio
J^{el}	Elastic volume ratio
Kn	Knudsen number
K_0	Bulk modulus (Pa)
k	Boltzmann constant (1.381×10^{-23} J K^{-1})
k_2	Coefficient for calculating the mean free path for various IPL models
L	Microchannel length (m)
L_C	Characteristic length of the flow domain (m)
L_{sv}	Characteristic length of a sampling volume (m)

lk	Leak rate (Pa s^{-1})
m	Mass of a molecule (kg)
$\dot{m}$	Mass flowrate (kg s^{-1})
N	Number of stages of a KP
N_t	tensile strength (Pa)
n	Unit vector normal to the wall and directed toward the fluid domain
n	Number of molecules
n_d	Number density (m^{-3})
n_c	Number of parallel microchannels in a KP stage
P	Pressure (Pa)
Pr	Prandtl number
Q	Heat flux vector (W m^{-2})
Q	Collision integral
$\dot{Q}$	Consumed power (W)
R_g	Specific gas constant (J kg^{-1} K^{-1})
r	Position vector (m)
r	Microchannel radius (m)
r_{i-j}	Distance between two molecules' centres (m)
s	Unit vector tangent to the wall
S	Surface area (m^2)
T	Temperature (K)
t	Time (s)
U	Strain energy per unit volume (J m^{-3})
u	Macroscopic velocity vector (m s^{-1})
V	Tank volume (m^3)
V_0	Initial internal volume of the deformable portion of a PAμM (m^3)
V_s	Dead volume of a PAμM connected to a KμP (m^3)
V_{total}	Initial total volume of an uncontracted PAμM (m^3)
v	Most probable molecular velocity (m s^{-1})
W_D	Diffuse scattering kernel
W_{DS}	Maxwell scattering kernel
W_S	Specular scattering kernel

(x, y, z)	Cartesian coordinates (m)

Greek Symbols

α	VSS coefficient
β	Tangential momentum accommodation coefficient (TMAC)
δ	Rarefaction parameter
δ_m	Mean rarefaction parameter
δ_{Dirac}	Dirac delta distribution
ε	Slope of the curve linear fitting (Pa^{-1})
λ	Mean free path (m)
λ_i	Principal stretch
$\overline{\lambda_i} = J^{-1/3}\lambda_i$	Deviatoric stretch
λ_T	Wavelength of the laser beam (nm)
μ	Dynamic viscosity (Pa s)
μ_0	Initial shear modulus (Pa)
η	Efficiency
υ	Mean collision rate (s^{-1})
ζ	Index relating pressure and temperature ratios
$\boldsymbol{\xi}$	Molecular velocity vector after collision (m s^{-1})
$\boldsymbol{\xi}'$	Molecular velocity vector before collision (m s^{-1})
ξ	Thermal velocity amplitude (m s^{-1})
$\overline{\xi}$	Mean thermal velocity amplitude (m s^{-1})
ρ	Density (kg m^{-3})
σ_s	Limit shear strain
τ_s	Shear stress (Pa)
θ	Angle of incidence (rad)
θ'	Angle of reflection (rad)
Π	Mechanical power (W)
ω	Index relating temperature and dynamic viscosity
κ	Constant in IPL model

ψ	Constant in IPL model
Ω	Solid angle (sr)

Subscripts

0	At initial time
c	Cold
h	Hot
i	Inlet
in	Inner, internal
m	Mean
max	Maximum
min	Minimum
n	Direction normal to the wall towards the fluid domain
o	Outlet
out	Outer
0	Reference condition
s	Direction tangent to the wall
slip	Slip at the wall
w	Wall
*	Refers to a molecule that interacts with another molecule

Introduction

Knudsen micropumps, also known as thermal transpiration micropumps or Knudsen compressors, are a type of micropump that operate without any moving parts. These micropumps utilize a temperature gradient applied along the solid walls of the pump to generate gas flow, eliminating the need for a traditional pressure gradient. They are not only capable of creating pressure differences but can also generate a vacuum. Knudsen micropumps find applications in various fields, including vacuum generation, gas separation, gas chromatography, gas sampling, and heat dissipation. As a result, they have garnered significant attention from researchers over the past few decades, leading to the development of various designs aimed at optimizing their performance in terms of pressure difference and mass flowrate.

The objective of this work is to design and lay the groundwork for the manufacturing of a specialized Knudsen micropump. This micropump is intended to actuate artificial pneumatic micromuscles, which can be controlled by varying levels of vacuum. The research provides the initial stages of development for a multistage Knudsen pump, with the ultimate goal of optimizing it to offer a specific response time tailored to its intended application.

Artificial muscles, often referred to as muscle-like actuators, are designed to respond to external stimuli, resulting in various types of deformations. One specific type of artificial muscle is known as the pneumatic artificial muscle (PAM), which operates based on a pressure difference created between its inner volume and the surrounding environment. In recent years, a novel variation of PAM has emerged, controlled not by inflation but rather by adjusting the level of vacuum within it.

Knudsen pumps (KPs), due to their capability to generate vacuum efficiently and their compact size, have the potential to serve as valuable tools for controlling micro-sized PAMs. The integration of KPs with pneumatic artificial micro-muscles represents an innovative and promising research area, offering intriguing scientific and technical challenges. This coupling could find applications in areas such as micro-scale swimmers, robots, grippers, and more, by enabling energy generation, conversion, and storage in microsystems.

In this study, a novel multistage KP design is introduced and thoroughly examined using numerical analysis. The objective is to optimize this design to meet specific performance requirements for controlling pneumatic muscles. Each individual stage of the Knudsen pump comprises multiple parallel microchannels connected to small reservoirs. Diverse microchannel configurations have been devised, successfully produced, and experimentally tested using rarefied gas flows driven by isothermal pressure. These experiments confirm the feasibility of

the fabrication process for creating the complete KP. Furthermore, the research includes the development of 3D-printed mini and micro-muscles, followed by a comprehensive investigation of their behavior using both numerical simulations and practical experiments.

The structure of the thesis manuscript is divided into two main parts, comprising five chapters in total, with an additional sixth chapter that establishes an initial connection between these two parts. Here's a brief summary of the content covered in each chapter:

Part I: Knudsen Pump

- **Thermal Transpiration Micropumps (Chapter 1)**: This chapter introduces the principles and technologies involved in designing Knudsen pumps. It provides an overview of the thermal transpiration flow phenomenon and presents the state of the art in Knudsen pump research, along with various applications.
- **Microscale Gas Behavior (Chapter 2)**: Chapter 2 delves into the theoretical foundations of gas behavior at the microscale, particularly focusing on rarefied gases and the Knudsen number. It discusses different flow regimes related to rarefaction levels and presents key models for simulating gas flows in Knudsen pumps.
- **Manufacturing and Characterization (Chapter 3)**: This chapter details the manufacturing processes and experimental measurements of Knudsen pump elements, including single straight microchannels. It describes the fabrication techniques, experimental measurements, and numerical simulations, providing insights into the behavior of Knudsen pumps.

Part II: Artificial Micro-Muscles

- **Artificial Micro-Muscles (Chapter 4)**: Chapter 4 reviews artificial pneumatic micro- and mini-muscles, with a specific focus on those actuated by negative pressure differences. It categorizes these muscles based on their designs and architectures, highlighting various deformations they can generate.
- **Characterization of PAMs (Chapter 5)**: Chapter 5 goes into detail about the numerical simulations and experimental tests conducted on artificial mini-muscles subjected to negative pressure conditions. It explains the simulation methods and presents the results of experiments, providing insights into the behavior of these muscles.

Integration of Knudsen Pumps and Micro-Muscles

- **Knudsen Pumps and Micro-Muscles Integration (Chapter 6)**: Chapter 6 serves as a bridge between the two parts of the project, exploring the combination of Knudsen pumps and artificial muscles. It introduces an initial concept and offers preliminary calculations regarding the dynamic performance of this combined system.

The thesis concludes with a "**Conclusions**" section summarizing the research undertaken and outlines potential directions for future work in the field.

Chapter 1 - Thermal transpiration micropumps

Summary

In this chapter, we propose a detailed bibliographic review devoted to thermal transpiration micropumps, also called Knudsen micropumps.

Thermally-driven pumps have been extensively investigated for several decades both from theoretical and experimental points of views. With the development of improved micromanufacturing techniques, different micropumps based on porous materials or micromachined channels have been designed. However, fabrication techniques for manufacturing micromachined channels were still complex to implement. Recently, emerging microfabrication techniques have allowed improving the geometry and performance of thermally-driven micropumps.

Due to the miniaturization of micro-devices, which led to the development of microfluidics, gas micropumps are necessary for a number of applications in various fields, as for example the analysis of gas pollutants in the atmosphere. One kind of appealing gas micropump is the so-called Knudsen pump (KP), the principle of which was first described by Martin Knudsen [1], a Danish physicist. KPs are operating by thermal transpiration effect and require rarefied gas conditions. The main features of KPs are their high miniaturization, a robust structure without any moving part, and an operating mode that requires only a temperature gradient along the wall. Therefore, they could provide reliable and precise control of gas microflows for different applications. As expected, since the seminal work from Knudsen, thermally-driven micropumps have attracted interest of numerous scholars, and systematic developments have already been conducted.

The first section of this chapter (Section 1.1) is an introduction to KPs. The physical mechanism exploited to actuate KPs, namely, the thermal transpiration phenomenon, is described in Section 1.2. The different designs of KPs proposed in the literature and their classification, as well as the various applications are illustrated in Sections 1.3 and 1.4, respectively.

1.1 Introduction to Knudsen pumps

Micro-Electro-Mechanical-Systems (MEMS) were firstly introduced in the 1990s [2], and their development has rapidly grown in the past decades. Microfabrication techniques have thus been widely used to develop a variety of fluidic micro-devices, such as micro fuel cells, lab-on-chip systems, fluidic microsystems for chemical preconcentration, micro-gas chro-

matographs and mass spectrometers, catalytic fuel reformers [3] and microdrones [4]. A key research area in the field of MEMS concerns micro-pumps [5], usually classified as mechanical (requiring moving parts) and non-mechanical (without any moving part) micropumps. The energy source used for driving fluid flows in these two types of micropumps can be different. Due to the presence of moving parts, the life span and reliability of mechanical micropumps are limited. Thus, non-mechanical micropumps are now extensively studied and start to be used taking advantage of the absence of fragile moving parts, simple concept and facility to generate thermal energy. One of the most developed current researches on non-mechanical micropumps concerns KPs, which have been numerically and experimentally investigated for a few decades.

A KP is a kind of micropump designed for gases, also referred to as "thermal transpiration pump" or "Knudsen compressor". Its principle is based on the thermal transpiration phenomenon [6,7], which occurs in rarefied gas flows in the presence of temperature gradient and makes gas molecules creep from a cold region towards a hot region. This kind of thermally driven flow can, for example, be generated in a micromachined channel or a porous medium with no initial pressure difference when the boundary walls are submitted to a temperature gradient. Since its first description by Knudsen [1], thermal transpiration has been attracting a strong interest in the scientific community in the domain of gaseous microfluidics.

Due to their simple structure without any moving part, Knudsen micropumps (KμPs) can provide reliable and precise control of gas microflows. A lot of studies have demonstrated that KPs have a wide potential range of applications for handling gas at the microscale, which has favored more research and development than for mechanical gas micropumps [5]. This trend has benefited from the development of new microfabrication techniques, and computational models, as well as specific experimental setups. At present, a variety of configurations, with different materials have been used for the design of KPs. Their applications include vacuum generation [8–17], gas separation or concentration [18–31], power generation [32–36], power scavenging and heat pumping [37–39], gas chromatography [40–44], among others. However, considerable work is still required to optimize the performance of KPs for more practical and potential applications.

1.2 Thermal transpiration-physical mechanisms

Thermal transpiration can be observed in the presence of temperature gradients when a gaseous flow is rarefied, *i.e.* when the mean free path λ of the gas molecules is not negligible compared with the characteristic dimensions of the flow, typically the hydraulic diameter D_h

in the case of internal microflows. In that case, the Knudsen number *Kn*:

$$Kn = \frac{\lambda}{D_h} \tag{1.1}$$

can become high enough so that the interaction of the gas molecules with the walls plays a predominant role and specific phenomena such as velocity slip, temperature jump and thermal creep become significant.

The thermal creep phenomenon is also known as thermal transpiration phenomenon. Imposing a tangential temperature gradient along a wall leads to a local gas flow, according to a quite simple physical mechanism illustrated in Fig. 1.1.

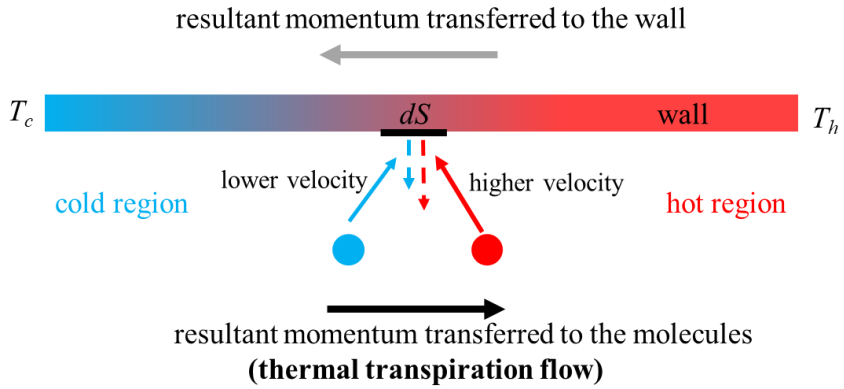

Figure 1.1 – Physical mechanism of thermal creep flow, in the case of a diffuse reflection of the molecules at the wall.

Due to the temperature gradient along the wall ($T_h > T_c$), gas molecules in the hot region have a higher thermal energy, *i.e.* a higher kinetic energy, than that of gas molecules in the cold region. Consequently, the momentum of the gas molecules close to the wall is higher in the hot (right side of Fig. 1.1) than in the cold (left side of Fig. 1.1) region. Hence, when molecules coming from the hot side and cold side are colliding the same small wall area *dS*, this area will statistically gain a resultant momentum oriented in the left direction, assuming that the frequency of collision of molecules with this small area does not depend on their origin (from hot or cold sides) [45]. According to Newton's third law of motion, the molecules will be in average subjected to a reaction force in the opposite direction. Thus, the molecules close to the wall will move from the cold region towards the hot region, resulting in a gas flow along the wall in the direction of the temperature gradient. The concerned molecules are located in a thin region called the Knudsen layer, the thickness of which is of the order of the mean free path. When this thickness is not too small compared with the hydraulic diameter of

a microchannel or a pore, the thermal creep at the wall can generate a flow in the whole microchannel or pore section. This now well-known thermal transpiration (or creep) flow phenomenon was firstly analyzed by Reynolds [6] with an apparatus composed of two chambers with different temperatures connected to a plate of porous medium. He observed a gas flow through the porous medium from the cold chamber towards the hot chamber. As a consequence, this gas flow was able to generate a pressure increase in the hot chamber and a pressure decrease in the cold chamber. From his experimental and theoretical analysis, Reynolds could conclude several laws:

1. The gas flows through the porous plate from cold to hot region when the same pressure is applied on both sides of the plate. The mass flowrate depends on the absolute temperature and on the temperature difference between both sides, as well as on the chemical nature of the gas, on the relation between the density of the gas and the size of the pores, and on the thickness of the plate.
2. A pressure difference must be imposed between the two sides of the plate (with a higher pressure on the hot side) in order to prevent a net gas flow through the plate. When the net flow is zero, this pressure difference depends on the temperature difference, on the chemical nature of the gas and on the mean pressure, but not on the thickness of the plate.
3. The pressure difference obtained in the previous law also depends on the rarefaction level of the gas, and it can reach its maximum value between free molecular (when intermolecular collisions can be neglected) and hydrodynamic (when the fluid can be considered as a continuum, at least out of the Knudsen layer) regimes, *i.e.* mainly in the transition flow regime (for which neither the gas intermolecular collisions nor the gas-wall collisions can be neglected) and possibly in the slip flow regime, for which rarefaction has effects located close to the walls.

Thus, the role of rarefaction pointed out by Reynolds plays a key role in the thermal transpiration phenomenon. The important notion of rarefaction, that increases with the ratio of the mean free path of the molecules over the characteristic length of the flow (typically the hydraulic diameter), will be detailed in Chapter 2.

The thermal transpiration flow is one typical temperature-driven flow, which has been extensively studied since its initial observation (see Chapter 2). Therefore, optimizing the geometrical and operating configurations is of great interest for the design of different kinds of KμPs associated to sensors or actuators that require specific response times.

Moreover, some other thermally-induced flows have been described and analyzed theoreti-

cally, numerically, and experimentally in the literature. These various thermally-driven gas flows can be classified in several types as follows: thermal transpiration (or creep) flows [5,45,46], inverted thermal transpiration (or creep) flows [47,48], thermal-stress slip flows [49], nonlinear-thermal-stress flows [50–52], thermal edge flows [53] and radiometric flows [54,55]. These flows are illustrated in Fig. 1.2. The physical mechanisms involved in each case are explained in detail in a review written by Wang et al. [5].

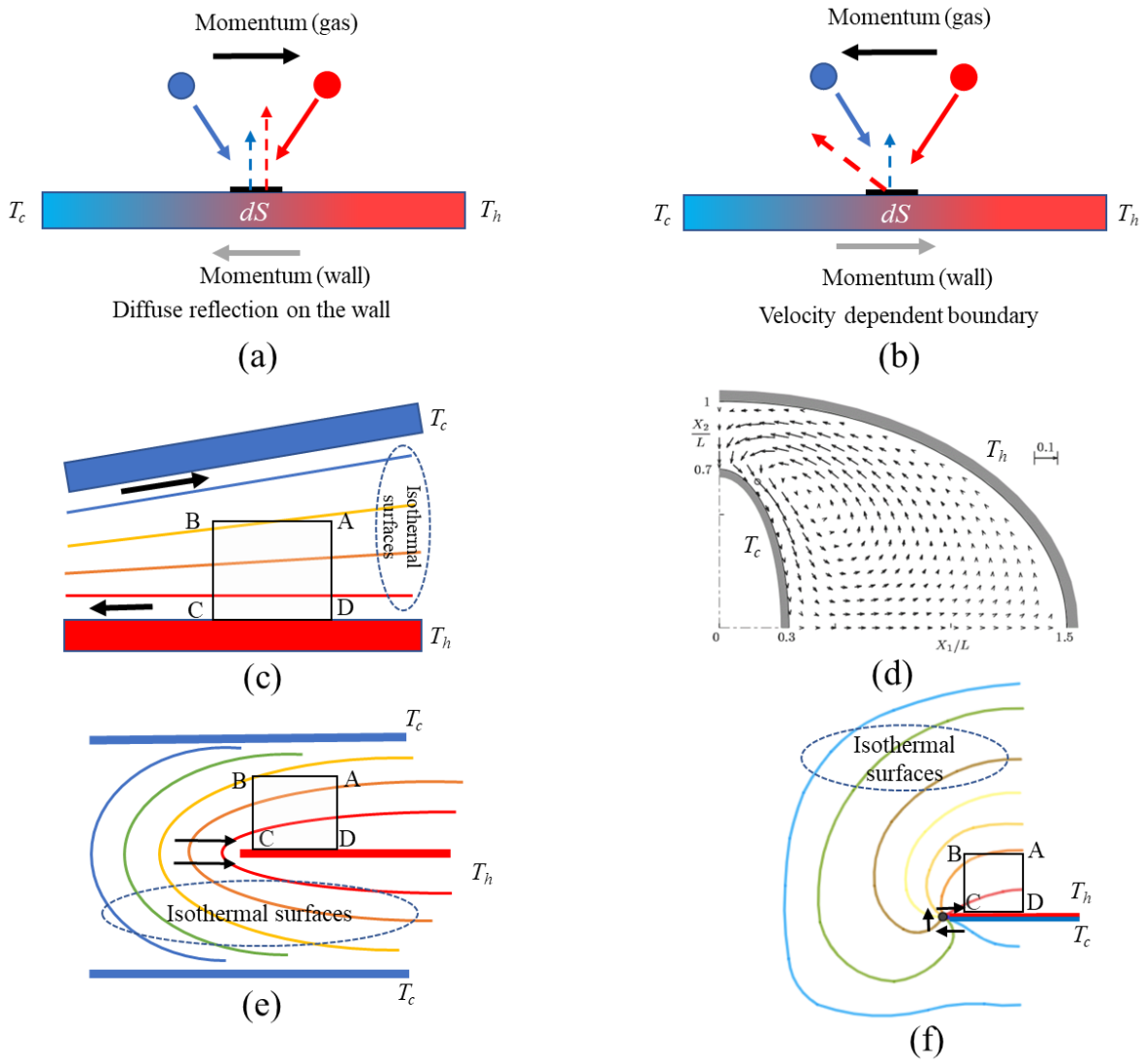

Figure 1.2 – Classifications of thermally-driven flows. a) Thermal creep flow on a flat surface as is the case in a constant-section microchannel; b) inverted thermal creep flow; c) thermal-stress slip flow; d) nonlinear-thermal-stress flow simulation [45] for $T_h = 5T_c$; e) thermal edge flow; and f) radiometric flow.

As previously explained, the **thermal creep flow** (Fig. 1.2a) is induced by a momentum transfer between the gas molecules and the wall subjected to a temperature gradient. This momentum transfer requires a non-specular wall surface and it is more efficient with a fully

diffuse wall boundary.

On the other hand, if the wall has specific properties with velocity-dependent accommodation coefficients, *i.e.* such that the collision of the gas molecules depends of their velocity, an **inverted thermal creep flow** could be produced in the opposite direction (Fig. 1.2b). Theoretically, this situation could occur if gas molecules with higher velocities experience more specular collisions with the wall than gas molecules with lower velocities. This case has only been investigated from a theoretical point of view [48] by Direct Simulation Monte Carlo (DSMC), but it has not been experimentally observed yet.

A thermally driven flow can also be generated with isothermal walls, when these walls are not parallel, which results in non-parallel isothermal surfaces within the gas. A thermal stress is then generated on any surface within the gas [45]. Considering a control volume ABCD within the gas, it can be demonstrated that the resulting net stress on this volume is zero, but it is no longer the case when this volume shares one of its sides with the wall. In that case, the balance on this side is modified and it results in a net stress on the control volume, that generates a slip flow at the wall, as illustrated in Fig. 1.2c. This is the so-called **thermal-stress slip flow**, which is oriented toward the converging direction along the hot wall and toward the diverging direction along the cold wall. A detailed explanation of this phenomenon requires an analysis from an asymptotic approach based on the Boltzmann equation, as developed in the Book of Sone [45].

In case of large temperature gradients, additional nonlinear terms should be considered and lead to an additional flow contribution, known as **nonlinear-thermal-stress flow**. Contrarily to the case of thermal creep flow and of thermal-stress slip flow, the walls do not play a direct role to this flow: they are only at the origin of a temperature field with non-parallel isothermal surfaces. An example of simulation of this flow contribution is illustrated in Fig. 1.2d that shows the flow velocities between two coaxial elliptic cylinders with uniform and different temperatures.

The above described thermally-driven flows can be derived from an asymptotic theory, which shows that thermal creep and the nonlinear-thermal-stress flows are obtained at the first order of the Knudsen number *Kn* and that thermal-stress slip flow is at the second order of *Kn*. In addition, this asymptotic theory assumes that the local Knudsen number based on the radius of curvature of the wall is small. In case of sharp edges, this assumption is no longer valid, but a thermally driven flow can be observed and has been numerically simulated by Aoki et al. and experimentally confirmed by Sone and Yoshimoto [53]. This so-called **thermal-edge flow** appears when a thin plate is heated and has a uniform hot temperature T_h in a colder en-

vironment, as shown in Fig. 1.2e where the plate is placed in a microchannel with cold walls at temperature T_c. The resulting curvature of the isothermal surfaces leads to a configuration similar to that of the thermal-stress flow (Fig. 1.2c) in the region close to the edge, both in the gas region close to the wall edge upper and lower sides. The consequence is a thermal-edge (slip) flow in the direction of the black arrow on both sides of the edge. Farther from the edge this effect disappears as the isothermal surfaces become parallel. A more complex situation can be observed if the plate has one side heated and one side cooled, as is the case of the Crookes radiometer [56,57]. The generated flow, sometimes called **radiometric-flow** is shown in Fig. 1.2e. The gas flows around the plate, passing by the edge from the cold side to the hot side. This effect is used in certain Knudsen pumps and allows separation of gas species as the effect strength is linked to the molecular mass of the species [30].

All the above described phenomena allow a thermally-driven gas flow that can lead to more or less complex configurations of KPs able to pump a rarefied gas without any mechanical moving elements.

1.3 Transpiration-flow based Knudsen pumps concept and developments

Since the KP (or Knudsen compressor) concept initially introduced by Knudsen, it has been attracting a lot of scholars' research interests on its performances due to its appealing advantages, such as its operation without moving parts, a quite simple structure, and a wide range of applications. Indeed, these researched have demonstrated that KPs can be used in many fields such as vacuum generation, gas separation, heat pumping [38,39] and power generation. A very basic one-stage KP is composed of one straight microchannel, with a hydraulic diameter D_h and a length L, and connected to two reservoirs maintained at two uniform but different temperatures T_h and T_c, as shown in Fig. 1.3. A temperature gradient is then generated along the microchannel wall.

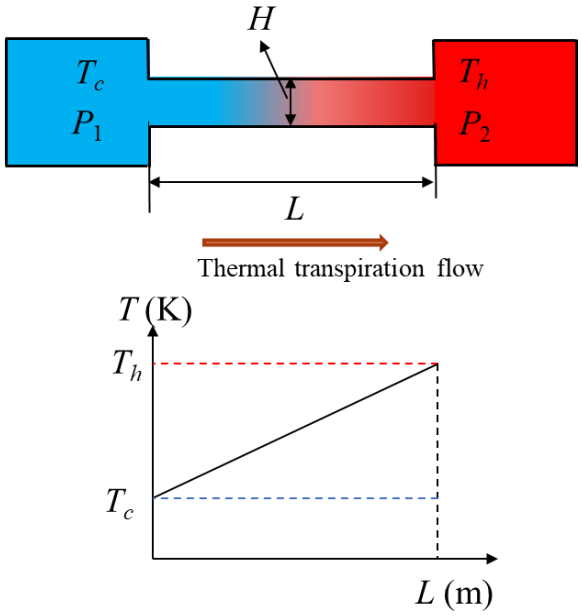

Figure 1.3 – Classic schematic of a single-stage KP based on thermal transpiration.

The working principle of this simple KP is the following. At the initial time $t = 0$, $P_1 = P_2$, and $T_h > T_c$. Due to the temperature gradient along the walls, a thermal transpiration flow starts through the microchannel from the cold reservoir toward the hot reservoir. As a result, P_2 increases as P_1 decreases with time, and the pressure difference $\Delta P = P_2 - P_1$ increases. This pressure difference induces an inverted pressure-driven (or Poiseuille) flow, from the hot side toward the cold side, which increases with time. Finally, the temperature-driven and the pressure-driven flows will balance each other, leading to a net mass flowrate $\dot{m} = 0$ and a final pressure difference $\Delta P > 0$ between the two reservoirs.

Furthermore, as explained in Chapter 2, in the final equilibrium state, the maximum value of the pressure ratio that can be achieved is limited by the temperature ratio:

$$\left(\frac{P_2}{P_1}\right)_{t\to\infty} \leq \sqrt{\frac{T_h}{T_c}} \tag{1.2}$$

This limit can theoretical be approached when the level of rarefaction is optimal, *i.e.* when the mean Knudsen number has a specific value, generally of the order of unity. More generally, the equilibrium state for a given configuration leads to a pressure ratio function of the temperature ratio as in Eq. (1.2), but with an index $\zeta < 0.5$ that depends on the operating conditions:

$$\left(\frac{P_2}{P_1}\right)_{t\to\infty} = \left(\frac{T_h}{T_c}\right)^{\zeta} \tag{1.3}$$

Based on the above unit architecture, a typical multistage KP made of a series of micro and

macrochannels can be designed for increasing the final pressure ratio generated by the pump (see Fig. 1.4). The left side of the macrochannels, that replace the previous reservoirs of the single-stage pump, are locally heated by an element, whereas the right side is cold, due to heat exchanges with the surrounding. As a consequence, in this configuration, both micro and macrochannels are subjected to a temperature gradient, but in opposite directions. Thus, each stage of this multistage pump includes a pumping sub-stage (a microchannel) and a counter-flow sub-stage (a macrochannel). Microchannels hydraulic diameters are chosen in such a way that the Knudsen number is close to its optimal value, resulting in a significant thermal transpiration flow. On the other hand, the Knudsen number in the macrochannels is much lower, due to a much higher hydraulic diameter and the thermal transpiration flow is consequently low compared to that in the microchannels. Therefore, for the whole system, in the initial configuration where $P_i = P_o$, the gas flows from the left side to the right side, resulting in a net thermally-driven flow with a mass flowrate $\dot{m}$. If for example the left extremity of the assembly is closed, the pressure will decrease up to a final configuration where the resulting pressure-driven flow from right to left will counter-balance the thermal-driven net flow from left to right. The net global flowrate will then be zero, and they will be a pressure decrease in each stage of the pump, that finally can lead to a low pressure at the left extremity of the pump. Increasing the number of stages will decrease the value of this final pressure. As it is the case for a classic pump, between these two extreme characteristic points ($\Delta P = P_o - P_i = 0$ and $\dot{m} = \dot{m}_{\max}$ reaches its maximal value, or $\dot{m} = 0$ and $\Delta P = \Delta P_{\max}$, also known as blocking pressure, is maximal) there is a series of working points that describe the characteristic steady behavior of the pump $\Delta P = fct\,(\dot{m})$ able to deliver a certain mass flowrate $\dot{m}$ while generating a certain pressure difference ΔP.

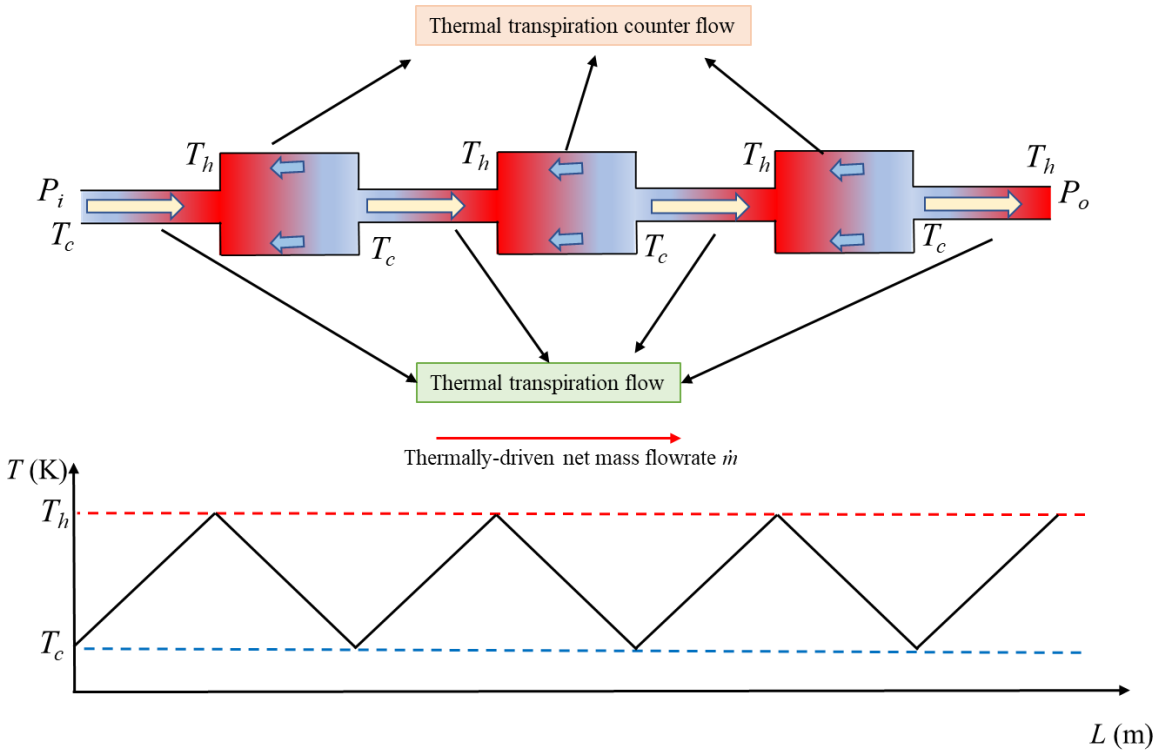

Figure 1.4 – Classic schematic of a multistage KP.
The arrows show the thermally-driven flow in each sub-stage.

Several numerical studies have been performed to investigate the performance of multi-stage KPs such as the one showed in the above figure. Lopez-Quesada [1] clarified that the maximum pressure difference $\Delta P_{\max}$ is increased while the maximum mass flowrate $\dot{m}_{\max}$ keep the same value when the number of stages is increased, if the stages are all geometrically identical and the pressure is the same in the open configuration for which $\Delta P = 0$. On the other hand, it is possible to increase the mass flow rate by linking the macrochannels with several parallel microchannels. In short, increasing the number of stages will improve the possible pressure difference generated by the pump and increasing for each stage the number of parallel macrochannels will increase the possible flow rate provided by the pump.

The classical structures mentioned above involve straight cylindrical channels with uniform circular or rectangular cross sections. It is however possible to design KPs with different channels, even with non-uniform cross sections, for a purpose of optimization. With this kind of motivation, in recent years, scholars proposed alternative configurations of KPs. The main configurations can be classified into two different groups, according to the structure of the pumping sub-stages: micromachined channels (microchannels) or porous media. Both have been numerically and experimentally studied for several decades.

1.3.1 Knudsen pumps based on microchannels

The behavior of micromachined channels has been extensively studied not only for single stage, but also for multi-stage KPs. Two main groups, in the USA, have succeeded in fabricating KμPs with first results in the beginning of the century: the group of Eric Phillip Muntz from the Southern California University and the group of Yogesh Gianchandani from the University of Michigan.

A first single-stage KμP was fabricated in 2003 by the group of Yogesh Gianchandani at the University of Michigan. It was micro-machined on a single-chip with a glass substrate and a silicon wafer by using a six-mask process, and integrated two pressure sensors [17]. With a single channel between two cavities, it could perform under atmospheric pressure and was only the second prototype of KP able to do that, the main difficulty being to control the fabrication of microchannels with hydraulic diameters small enough in order to reach rarefied regimes at atmospheric pressure, which are required for the generation of thermal creep. In this case, the microchannels was 100 nm in depth, and the whole prototype had a small footprint of 1.5 × 2 mm^2. For an achieved temperature difference of 9 K between the hot and the cold chamber, the input power was 80 mW, and the pressure could be decreased from 101 to 47 kPa, corresponding to a compression ratio of 2.15.

A few years later, in 2012, the same group developed a 48-stage KμP (Fig. 1.5a and b) composed of silicon microchannels which were designed for vacuum applications. A 5-mask single-wafer microfabrication process was implemented for making this pump with macrochannels 0.15 μm in depth. By cascading the stages in series, the pumping of air from a cavity and the outlet at atmospheric pressure (*i.e.* 101 kPa) resulted in a high pressure drop of 95 kPa, with an input power of 1350 mW and a temperature difference of 55 K between hot and cold points [8]. A compression ratio of 15 was then obtained. When actuated at a lower outlet pressure of 33 kPa, the compression ratio reached a value of 50. Further, in 2014, a 162-stage KP was designed and fabricated by the same group [9]; this micropump comprised a high-pressure part which 54 stages designed for decreasing the pressure from 101 to 7 kPa, and a 108-stage low-pressure part used to reach a final pressure of 120 Pa (Fig. 1.5c). The dimensions of the microchannels and connecting reservoirs were different in the two parts (with higher dimensions in the low-pressure part), in order to adapt the Knudsen number for better performances. Therefore, the microchannels were 0.1 et 0.8 μm in depth for the high and low-pressure parts, respectively. However, the stages of the same part of the pump were identical. The results showed that this multistage KP can achieve a greater pressure drop than the previous one, with a very high compressor ratio (about 844), for an input power is 0.39 W and a

temperature difference of 56 K between hot and cold points. The footprint of the two above-described KPs were 10.35 × 11.45 mm^2 for the 48-stages pump and 12 × 15 mm^2 for the 162-stage pump, respectively.

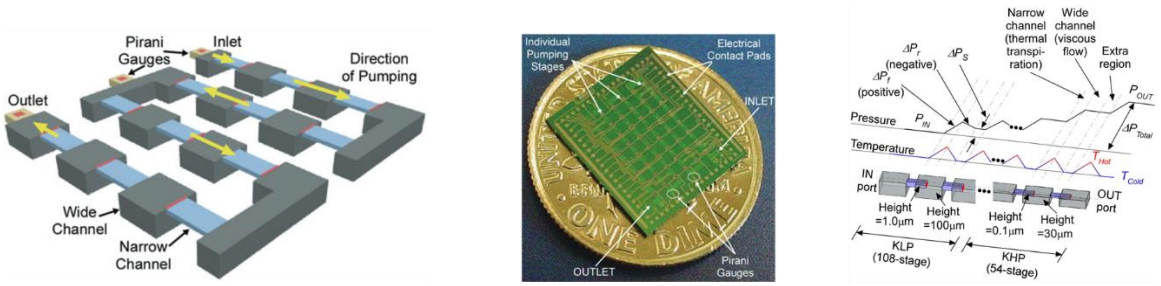

(a) (b) (c)

Figure 1.5 – Multistage KPs. a) schematic of a 48-stage KP cascading in series; b) fabricated sample of this 48-stage pump; and c) schematic of a 162-stage KP including a high pressure part (KHP) and a low pressure part (KLP) [8,9].

Configurations involving several parallel microchannels connected to two macrochannels were also numerically investigated [14,21,22,58,59] since 1996. For example, the thermal transpiration and pressure-driven flow in a microchannel were both considered by Vargo et al. [14] for the numerical design of multistage KPs with parallel microchannels in each stage. Using a cascade analysis, they demonstrated that a microscale pump could be designed for supplying a micro-mass spectrometer with a molecule flow rate of 5 × 10^{14} molecules/s. If the pump should work with an inlet pressure of 0.13 Pa, its global volume would be of 13.9 ml and the required input power of 2400 mW, and for an inlet pressure is 1.3 Pa, the pump volume would be of 0.16 ml and the input power of 28.5 mW. In this estimation, the energy consumption was assumed to be dominated by thermal losses through the material of the microchannel substages.

Microchannels arrays micromachined in aerogel membranes have also been tested experimentally and numerically by Han et al. [73] and the same configuration was further simulated by direct simulation Monte Carlo (DSMC) by Heo and Hwang [74]. In the experimental single-stage compressor prototype developed by Han et al., 99 circular macrochannels, 210 μm in diameter, have been drilled in the membrane, one side of which was heated thanks to an aluminum thermal guard with a series holes of 500 μm in diameter facing each microchannel [60], as shown in Fig. 1.6. This single-stage Knudsen compressor was able to generate a pressure difference of 3.4 Pa with an initial pressure of 136 Pa, but there is no information in the paper on the temperature gradient generated by radiative heating of the thermal guard. For

another prototype, the aerogel membrane was drilled with six rectangular channels, each 500 μm in height and 5 mm in width.

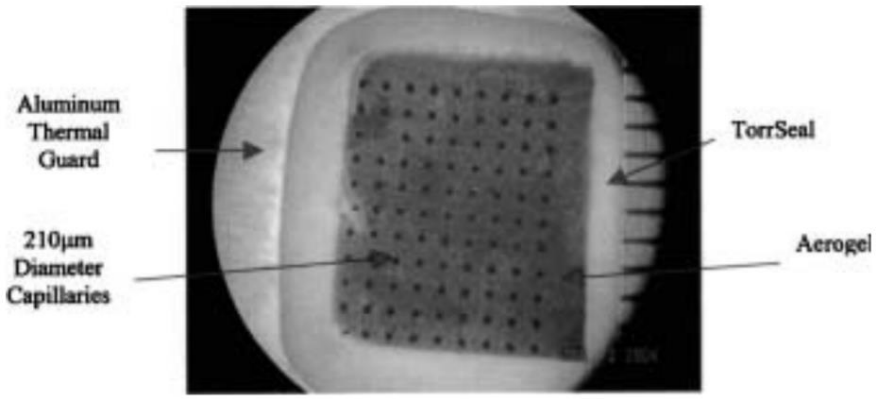

Figure 1.6 – A KP composed of an aerogel membrane with capillaries and an aluminum plate with a bigger orifice in the center [60].

An interesting application of KPs concerns gas separation, as the thermal creep strength is a function of the molecular species. Gas separation by mean of a Knudsen compressor was numerically investigated by Takata et al. [22] with models based on the kinetic theory of gases, by testing various molecular models (hard spheres, Maxwell molecules, inverse power-law potentials, Lennard-Jones model) implemented in the McCormack model equation. The capability of gas separation was demonstrated, although the Bhatnagar–Gross–Krook (BGK)type model equation based on Maxwell molecules was not able to capture the phenomenon. Nevertheless, this research was limited to the simplest case of a mixture composed of only two species of monatomic gases (helium, neon and argon). Later, the same group analyzed more in detail the performances of this configuration, notably in terms of time efficiency focusing on a mixture of helium and argon [21]. It was demonstrated that the increase of the number of parallel micro-channels and the number of the stages (Fig. 1.7) can improve the separation and compression performances, but at the price of an increase in time. Thus, a compromise among degree of separation, compression, and time consumption could be explored for more effective structures.

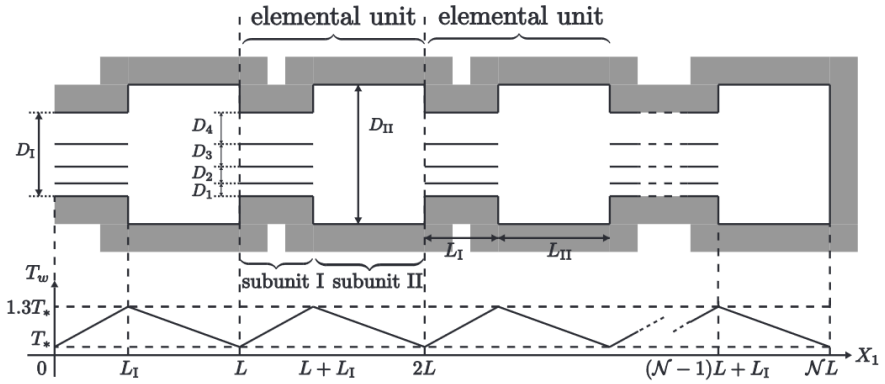

Figure 1.7 – Schematic of a cascading KP used for gas separation and compression [21].

Lopez Quesada *et al.* [62] confirmed with an increase of the number of identical stages, the maximum pressure difference could be increased, but the maximum mass flowrate is the same as in the case of only a single-stage KP, meaning that the number of stages has no influence on the mass flowrate, providing that each stage has the same geometry. Han [63] analyzed with the DSMC method the performances of a low-pressure Knudsen compressor stage, and shown the impact of the reverse thermal creep and the complex behavior of the flow with the presence of vortices in the chambers connected to the microchannel extremities. They also pointed out the impact of the Knudsen number in these chambers on the temperature decrease between the hot and the cold regions of the chamber: when the Knudsen number is too high, this temperature decrease is reduced for the geometrical configuration considered. The consequence is that for a multi-stage layout, the operational temperature difference of the next stages is decreased and the thermal creep in the microchannels is reduced.

Recently, the flow performance of gas mixtures KPs with rectangular microchannels was explored by Zhang et al. [64] with the DSMC method. Considering a diatomic gas mixture of N_2-O_2, they confirmed that the thermal transpiration strength is correlated to the molecular mass of the species: the thermal transpiration phenomenon is more significant for N_2 than for O_2 due to its lighter mass, even in this case were the molecular mass ratio between oxygen and nitrogen is quite low (1.14). Du et al. [65] further studied the flow characteristics in a KP for a H_2-N_2 mixture, still with the DSMC method and comparing variable hard spheres (VHS) and variable soft spheres (VSS) collision models. They investigated various concentrations and pressure values and observed a non-negligible influence of the collision model. It was confirmed that the lighter species, H_2, has a larger velocity than N_2, and that increasing the concentration of H_2 in the gas mixtures, causes an increase in the velocity of H_2 while contributing to an increase in the velocity of N_2.

Shao, Ye and their co-authors [66,67] simulated the behavior of a hydrogen Knudsen com-

pressor, assuming a slip-regime modelled by the Navier-Stokes equations associated to velocity slip and temperature jump boundary conditions. First, they analyzed the effects of obstacles (with rectangle and triangle shapes) in a plane microchannel connecting a cold and a hot reservoir by varying the lengths and heights of these obstacles [66]. The results demonstrated that the presence of the obstacles can increase the compression ratio with a beneficial effect by increasing their lengths in a certain range and by decreasing their height. In their second paper [67], the authors considered a multi-stage Knudsen compressor and concluded that the global pressure increase was proportional to the number of stages. They focused on the impact of the height of the connection channels subjected to a thermal creep counter-flow between two stages and observed that a higher connecting channel improves the global pressure increase, more by reducing the pressure drop in the connecting channels, which experience symmetrical vortexes, than by modifying the pressure increase in the microchannels.

Most of the papers in the literature focus on KPs with rectangular (or sometimes circular) straight microchannels, but a few works illustrate the performances of KPs with other shapes of microchannels. A KP configuration with two-dimensional curved straight microchannels composed of straight and semicircular segments (Fig. 1.8a) has been proposed by Aoki et al. [68–70]. The interest of such a layout is that there is no presence of both micro and microchannels, the whole structure being a long serpentine microchannel made of a succession of the patterns represented in Fig. 1.8a. The numerical approach based on the kinetic theory of gases showed that the thermal creep effect is more pronounced in the curved parts of the channel than in the straight part, although the temperature difference is the same. As a consequence a net flow is observed from the cold to the hot section in the curved part and in the hot to the cold section in the straight part, leading to a global pumping from section A to section C. Leontidis et al. [71,72] confirmed this result from numerical simulations using the commercial computational fluid dynamics (CFD) code Fluent®, by running the Navier-Stokes equations with user defined functions taking into account velocity slip and temperature jump boundary conditions, *i.e.* assuming a slip flow regime. An attempt to fabricate such a KP was unsuccessful due to the weakness of the pumping effect compared to outgassing and leakages due to the non-optimal fabrication process.

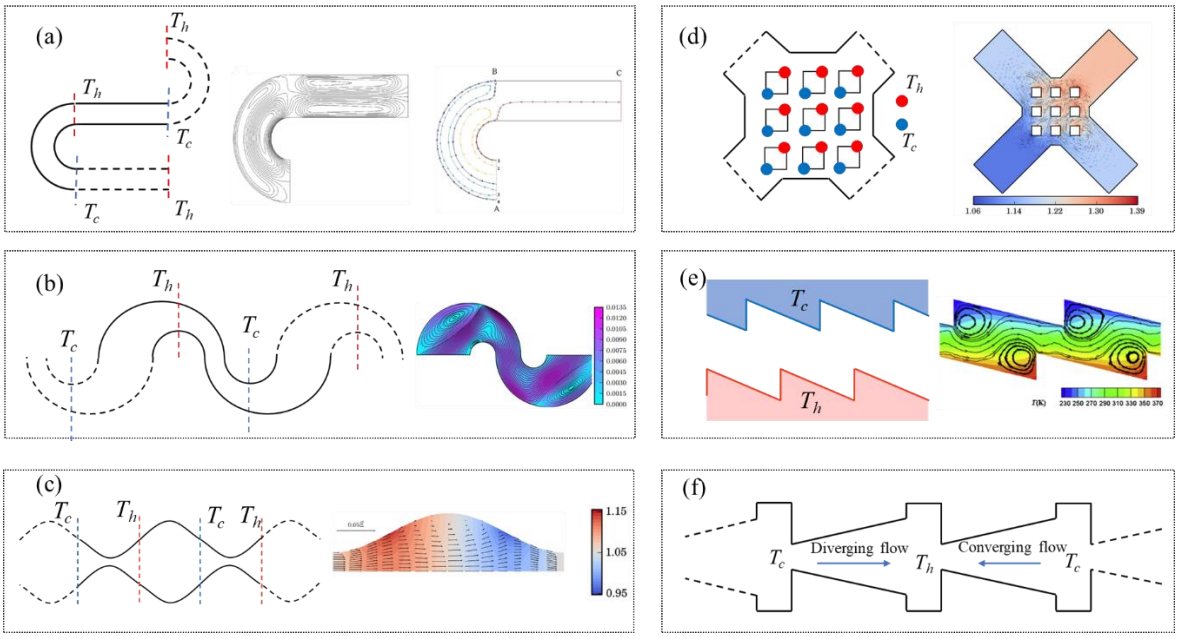

Figure 1.8 – Different KP structures. (a) curved channel [68–72]: middle: velocity streamlines [72] and right: path lines of the fluid particles released from section A [72]; (b) curved channel with different radius [73]: right: dimensionless velocity of nitrogen with streamlines for Kn = 0.1 [73]; (c) sinusoidal channel [74]: right: dimensionless pressure contours and flow velocity vectors [74]; (d) matrix channel [74]: right: dimensionless pressure contours and flow velocity vectors [74]; (e) ratchet channel [75,76]: temperature contours and streamlines [76]; (f) tapered channel [62,77,78]. The hot and cold temperatures at specific points or sections are denoted by T_h and T_c, respectively.

To achieve a better performance, a curved channel with non-uniform cross section (Fig. 1.8b) was proposed later by Bond et al. [73]. This kind of KPs can generate over twice the mass flowrate of the previous configuration. Subsequently, the same team proposed two new geometries (sinusoidal microchannel (Fig. 1.8c) and matrix microchannel Fig. 1.8d)) to evaluate their performance [74] to make a comparison via a kinetic approach with the curved channel design, as well as with the classical KP design. The matrix configuration connects 4 channels with a square area in which solid plots with square sections are dispatched, each plot having a cold edge and diametrically opposed hot edge. This layout results in a net thermally driven flow from the bottom left channel to the top right channel. By changing the location of hot and cold points, different directions of flows (for a chosen inlet channel to a chosen outlet channel) can be generated. Finally, it was found that the matrix pump design allows the greatest pressure difference, and the classical design offers the greatest mass flowrate. To verify these conclusions, experimental works should be performed.

In the case of ratchet channels (Fig. 1.8e), the pumping element consists of two facing isothermal walls at different temperatures, with at least one of them with a saw-tooth surface.

This configuration presents the interesting feature that it is easier to control the temperature of an isothermal surface rather than local hot and cold points. It was numerically investigated by Chen et al. both by DSMC and with Navier-Stokes equations associated to appropriate slip velocity and temperature jump boundary conditions [75,76]. The analysis revealed the mechanism of this pump: a temperature gradient appears in the gas along the vertical walls of the ratchet and generates a vertical transpiration flow from the top to the bottom. This initial flow induces vortices able to drive by viscosity a net flow from left to right, *i.e*. in a direction parallel to the walls. Nonetheless, the study was limited to 2D simulations without considering the influence of lateral wall in the third dimension, Thus, it would be necessary to consider 3D simulations and to perform experimental investigations.

Scholars also made some numerical investigations to optimize the performance of KPs using tapered microchannels [62,77,78]. The numerical simulations showed that the performances strongly depend on the channel convergence or divergence angle. In the layout shown in Fig. 1.8f studied by Tatsios et al. [71], the small chambers connecting the tapered channels are maintained at uniform hot or cold temperatures, but a net mass flowrate is observed from left to right, because the tapered channels exhibit a diode effect: the diverging channel provides a higher mass flowrate than the converging channel, for the same temperature gradient and same geometrical parameters.

It can be seen that various geometries of microchannels have been investigated by scholars. Most of the above presented configurations have been studied numerically, but for most of them there is clearly a lack of experimental data. However, these studies can provide some useful guidance for future investigations in order to design and optimize KPs.

1.3.2 Knudsen pumps based on porous materials

For thermal transpiration pumps, as an alternative to the various geometries of microchannels mentioned above, several kinds of porous materials can be used. Their use was easier when microfabrication capabilities were still limited. The small dimensions of capillaries or pores is suitable for reaching the good level of rarefaction to generate thermal transpiration flows [5]. So far, a few porous materials, either natural or artificially synthesized, have been used for that purpose. Several numerical simulations and experimental investigations have been conducted for exploring the performances and optimize Knudsen pumping with porous media.

Taguchi numerically analyzed a gas flow in the so-called Kayashima's device, which consists of a long porous channel with a periodic structure alternating gaps and porous medium. The porous medium was made of a square array of circular cylinders [79] with uniform sur-

faces temperatures that increase along the porous channel. The same pattern and same temperature distribution were reproduced along each porous medium area framed by two gaps. The analysis was done with a kinetic model based on the BGK equation and diffuse reflection boundary conditions. It provided properties of the flow for a number of stages between 5 and 100, and for various pressure and temperature ratios in both steady and unsteady conditions.

In 2017, a novel method for predicting the performance of a multistage KP using a porous material was carried out [80]. In this two-step method, the performance of a single-stage KP is first experimentally analyzed, and leads to a 1D model that can be applied to a multistage KP (Fig. 1.9). Finally, the proposed method works properly to predict the performance of the KP with an experimental validation with devices having 1 to 4 stages.

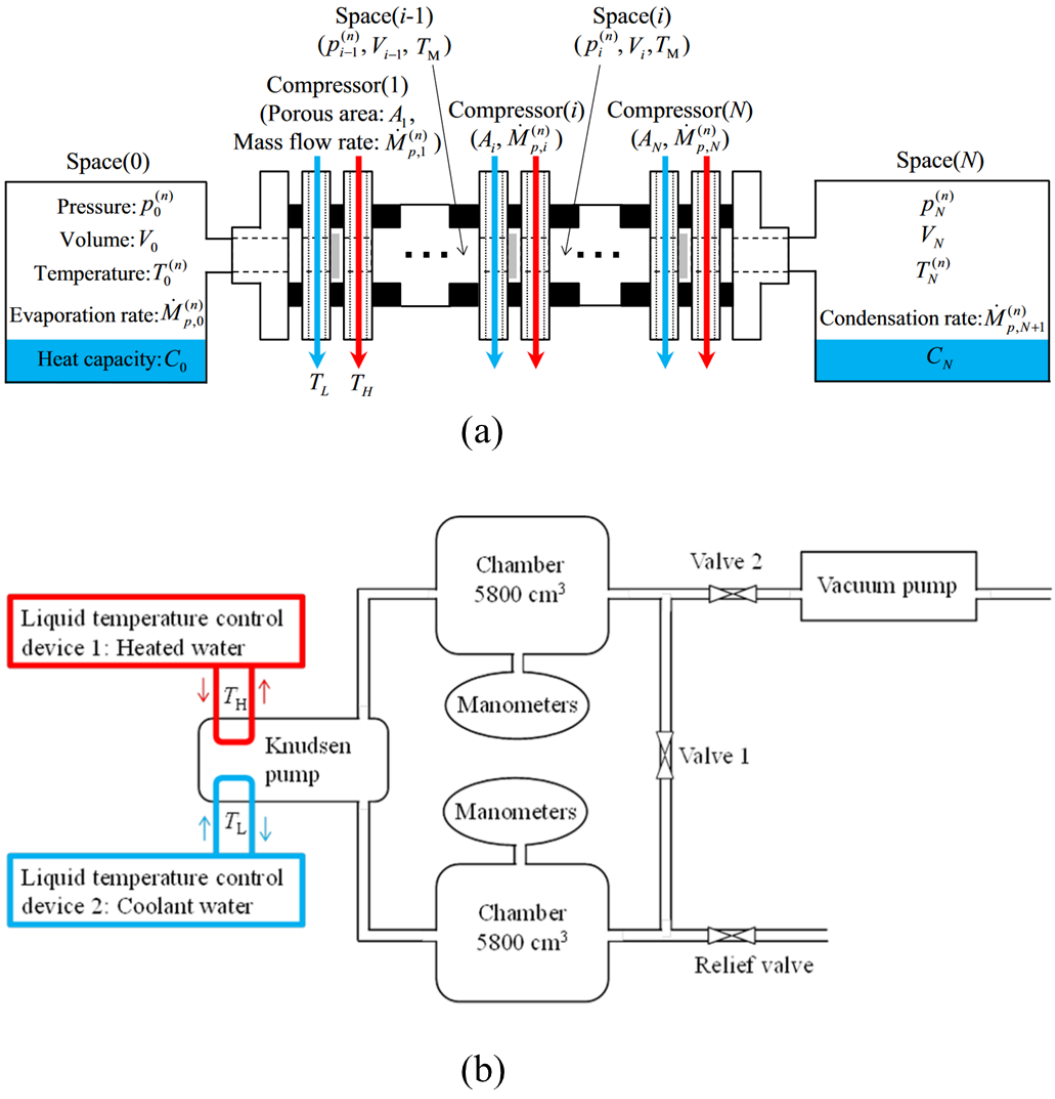

Figure 1.9 – a) schematic for the performance prediction model of multistage KP [38]; b) diagram of experimental setup [80].

Another kind of thermally induced system [20] designed for gas separation is composed of two KPs equipped with mixed cellulose ester (MCE) microporous membranes able to generate transpiration flows with a maximum temperature difference of 100 K (Fig. 1.10). The system was successfully used for the partial separation of gas species in a mixture of helium and neon.

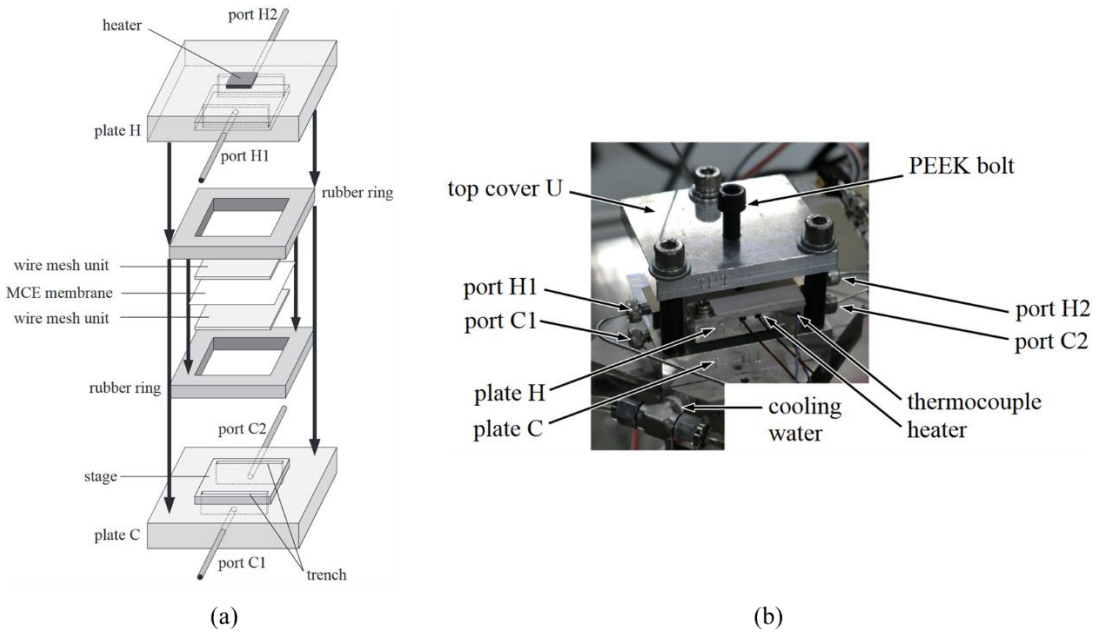

Figure 1.10 – a) Exploded view of a KP using a MCE membrane; b) Overview of the real KP implemented in the gas separator [20].

Another KP using natural zeolites was reported in [81]; it included two circular zeolite disks with a flexible heater sandwiched between them (Fig. 1.11). The gas flow was thermally generated through nanopores under atmospheric pressure. The authors claimed a high reliability of this gas micropump.

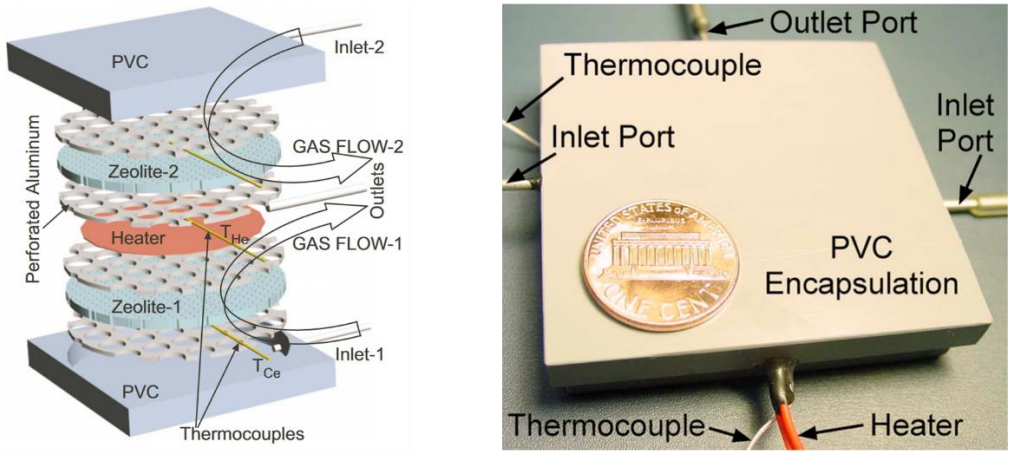

(a) (b)

Figure 1.11 – a) Exploded view of a zeolite-based KP; b) Real manufactured gas micropump with polyvinyl chloride PVC encapsulation assuring thermal insulation [81].

A bidirectional KP actuated by a thermoelectric modulus and using nanoporous material was designed and fabricated by Pharas and McNamara [82]. The direction of gas pumping was simply changed by inversing the electrical current direction. Two different designs shown in Fig. 1.12 were proposed: a so-called lateral design and a radial design. The second design was able to generate a flow rate 50 times higher than the lateral design, thanks to a higher temperature gradient and a more uniform temperature distribution. With a typical pore size of 0.1 µm, a maximum volume flow rate of 0.012 ml/s and a maximum pressure difference of 1.69 kPa could be measured at atmospheric pressure conditions.

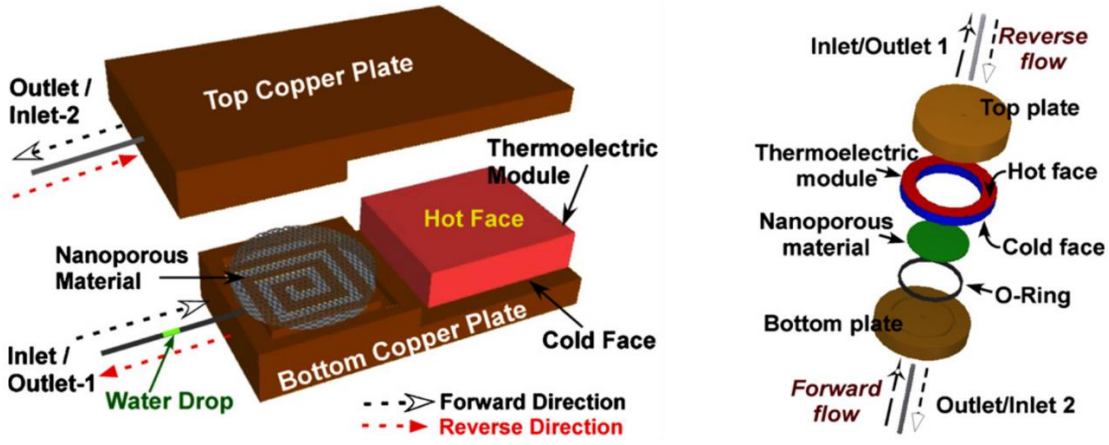

(a) (b)

Figure 1.12 – Illustration of two different designs of KPs with nanoporous materials actuated by thermoelectric modules. a) Lateral design; b) Radial design [82].

The above presented KPs using nanoporous materials have the advantage of simplicity, as

they generally do not require the implementation of complex microfabrication techniques, compared to the microchannel-based KPs. In addition, porous media can have a low thermal conductivity, which is useful to control high temperature gradients. However, rather few experimental investigations were performed to explore the performance of the porous material-based KPs. Numerical simulation and theoretical design are also harder than for microchannel-based transpiration pumps, for which the internal dimensions can be controlled with high precision. In addition, actual microfabrication techniques offer more flexibility to individually design each stage of a multi-stage pump, for which the hydraulic diameter of the microchannels should vary from one stage to another to keep in each stage an optimal pumping efficiency, based on an optimum value of the local Knudsen number.

1.4 Applications of Knudsen pumps

The appealing features of KμPs (high miniaturization and motionless internal structures) facilitate the developments of specific MEMS in various applicative domains. The main applications of KPs are briefly described in this section.

1.4.1 Knudsen pumps used for gas separation

Due to the different molecular masses of each gas species in a gas mixture, transpiration flow will have more or less effect on each species, with a higher effect on the lightest species. Species separation in a binary mixture two monatomic gases was experimentally evidenced in 2014 using thermal transpiration through nanopores [18]. This first experiment results in a mole percentage variation of up 15%, after transpiration through mixed cellulose/ester porous membrane, 30×30 mm^2 in area, applying a temperature difference of 45 K and a pressure difference of 2 kPa. The experimental results had a good agreement with previous numerical results and gave a solid foundation to explore gas separation by means of KPs, *i.e.* by applying only a temperature gradient. Subsequently, a series of works demonstrated that a large variation of mole fraction could be achieved between the two ends of KPs [20,24,25,27,29].

Recently, a specific KP inspired by the Crookes radiometer was proposed for gas separation. In a numerical analysis conducted by DSMC, Baier and Hardt [30] demonstrated that a KP consisting of a channel with vanes having one specular wall and one diffusive wall could be used to separate helium and xenon. Experimentally, it is however a challenge to fabricate such a system, especially as it is known that most of the real walls behave as diffuse surfaces.

1.4.2 Knudsen pumps used for fuel cell power generation systems

The first example of a self-sustaining, self-pressurizing combustor fueled by thermal tran-

spiration was reported by a group of researchers from Syracuse University and University of Southern California [34,35]. They designed a complete portable power generation system based on a KP; a catalytic propane combustion system and a thermal transpiration membrane were integrated to build a combustor with self-pumping ability (Fig. 1.13). The maximum power density generated was 0.04 W/cm^2 with a fuel cell area of 0.95 cm^2 and a propane flowrate of 0.5 mL/s corresponding to a chemical enthalpy flux of 41.4 W, which corresponds to an overall efficiency of less than 0.1 %. This very low performance can partly be attributed to the low temperature difference applied across the membrane.

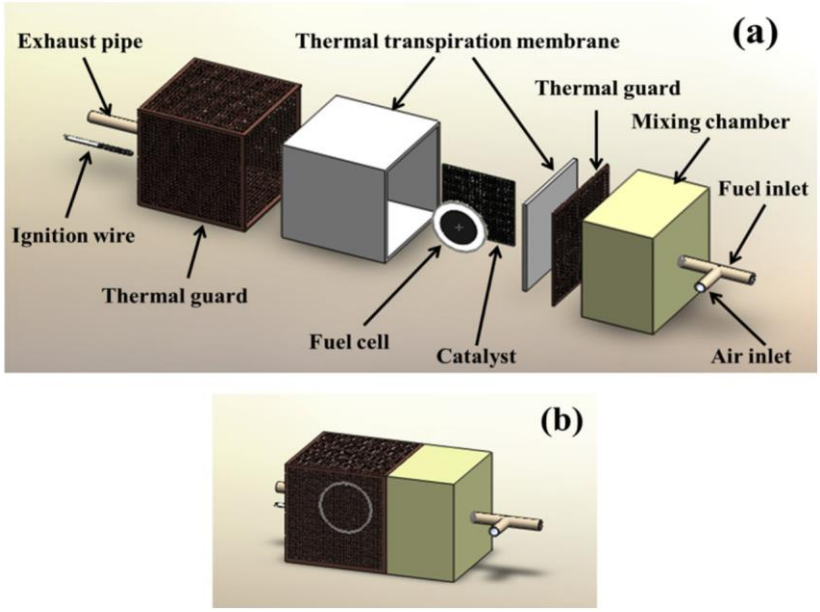

Figure 1.13 – Schematic of a thermal transpiration gas pump and fuel cell power generation system. a) Simplified exploded view; (b) Assembled view.

1.4.3 Knudsen pumps used for heat pumps

KPs can also be used as the pumping element of a heat pump. Kugimoto et al. introduced this idea in 2016 [37–39]. A KP composed of a porous medium glass fiber filter was used to pump water vapor from the evaporator towards the condenser of heat pump [37]. The porous medium was a glass fiber filter, 380 µm in thickness, and with an average pore size of 0.7 µm. The membranes were cooled on one side by coolant water and were heated on the other side by heated oil. The maximum pressure difference and mass flowrate obtained with a single-stage KP were 40 Pa and 0.039 mg s^{-1} cm^{-2}, respectively, for a temperature difference of 105 K [37]. A 30-stage KP was further numerically designed, but not experimentally tested [38]. It was equipped with glass-fiber filters with an area of 4 m^2 (in this case, the pump is definitely not a microsystem) and the simulation predicted interesting performances of the heat pump,

able to generate an output thermal power of 1.27 kW and a temperature difference of 6 K. A single-stage compact KP was also fabricated, the circular membranes with a diameter of 114 mm being heated by radiation from a halogen lamp. The output thermal power of the heat pump was 3.09 W, using a temperature difference for the KP of more or less 200 K, with a mean pressure of the order of 900 Pa.

1.4.4 Knudsen pumps used for gas chromatography

As a bidirectional gas flow can be created in KPs by only inverting the temperature gradients, KPs can be also employed in applications for gas chromatography requiring a bidirectional flow. Several works were conducted on this application by Qin et al. [41–44,83,84]. In a recent paper [83], a KP with a specific 3D-printed thermal management platform has been presented. This KP had reduced dimensions with a pumping area of 1.1 cm^2 and a total footprint, including the heat sink, of 64 × 64 mm^2. MCE membranes, 525 μm-thick and with 25 nm average pore diameter, as well as anodic aluminum oxide (AAO) membranes, with 0.2 μm average pore diameter and 531 μm in thickness, were both tested as porous media for the KP. With MCE, a maximum flow rate of 2.9×10^{-7} mol s^{-1} and a maximum pressure head of 818 Pa were obtained with a 2 W input power and a temperature difference of 40 K. When using AAO, the maximum flow rate was 5.6×10^{-7} mol s^{-1} and the maximum pressure head was 469 Pa with an input power of 9.8 W and a temperature difference of 121 K. These performances were obtained in the forward pumping. Similar performances, slightly lower, were obtained in the reverse pumping. The micro gas chromatography system, that included the KP, a preconcentrator, a separation column, and a capacitive detector successfully collected, separated and detected 6 volatile organic compounds: acetone, benzene, toluene, ethylbenzene, o-xylene and mesitylene.

1.4.5 Knudsen pumps used for vacuum generation

As previously explained, a KP can generate a difference of pressure by imposing a temperature difference starting from an initial state with the same pressure in the inlet and outlet of the pump. If the outlet is open and the inlet is closed by a reservoir, this reservoir can be vacuumed. Thus, the KP can operate as a vacuum generator.

A KP fabricated by deep reactive ion etching (RIE), wet thermal oxidation and anodic bonding processes, was recently proposed for achieving a vacuum environment. It was demonstrated that with only a temperature difference of 25 K, a compressed pressure ratio of 10 can be measured from atmospheric pressure in the evacuated chamber [16]. Besides, the investigations on a 48-stage KP and a 162-stage KP [8,9] have also illustrated that a high

compression ratio (844 in the case of the 162-stage KP) can be obtained from atmospheric pressure.

1.5 Efficiency estimation of different Knudsen pumps

The question of the efficiency of the KPs is generally not treated in the literature. The overall power consumption is low for a microsystem, and most of the authors did not focus on a power balance. However, in many emerging fields, even at the microscale, this question is becoming of great interest because energy management is more than ever a key issue for our planet and its inhabitants.

An estimation of the global efficiency of KPs is then necessary, to compare this efficiency to that of classical mechanical micropumps, and to have a clear idea of the degree of improvement that could be reached by optimizing KPs. Here, we tried to compare the global efficiencies of KPs described in the literature. As the information on these KPs can vary from one paper to another, it was decided to have an average estimation of the efficiency, defined as the ratio of a mean mechanical power delivered by the flow to the power required to actuate the pump. The real characteristic curve of each KP, which links the mass flowrate $\dot{m}$ to the pressure difference ΔP, is generally not provided in the articles. For this reason, the average mechanical power delivered by the pump is approximated by considering an operating point corresponding to half of the maximum pressure difference, *i.e.*, $\Delta P = \Delta P_{max} / 2$ and to half of the maximum mass flowrate, *i.e.*, $\dot{m} = \dot{m}_{max} / 2$, as shown in Fig. 1.14. This point is representative of the actual mean operating point, as for KPs the characteristic curve is usually close to a straight line.

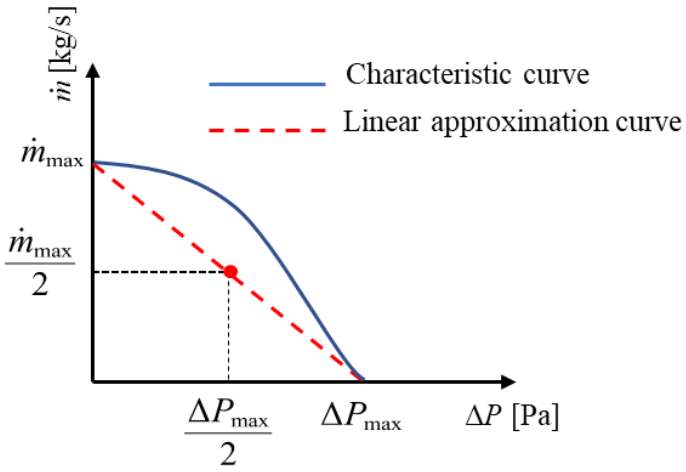

Figure 1.14 – Operating point considered to roughly estimate the mechanical power of a KP.

Thus, the efficiency η is defined as

$$\eta = \frac{\Pi}{\dot{Q}} = \frac{\Delta P\ \dot{m}}{\rho\ \dot{Q}} = \frac{\Delta P_{\max}\ \dot{m}_{\max}}{4\ \rho_m\ \dot{Q}} \tag{1.4}$$

where Π is an estimate of the mechanical power delivered by the KP, $\dot{Q}$ is the consumed power, and ρ_m is the mean gas density calculated by

$$\rho_m = \frac{P_m}{R_g\ T_m} \tag{1.5}$$

Here, $P_m = (P_o + P_i)\ /\ 2$ represents the mean pressure when $\Delta P = \Delta P_{\max}\ /\ 2$, R_g is the specific gas constant, $T_m = (T_o + T_i)\ /\ 2$ is the mean temperature, the subscripts *o* and *i* referring to the inlet and outlet of the KP, respectively.

The efficiency of various KPs is then estimated and tabulated in Table 1.1. In this table, n_c is the number of microchannels per stage and *N* is the number of stages. The characteristic dimensions of the pumping substage are the diameter *d* or the width *h* of the microchannels, or the characteristic diameter *d* of the pores, in case of porous media. All the listed KPs in Table 1.1 run with air, except KPs described in [19] and [20], which are designed for gas separation and have been tested with helium and argon, and helium and neon, respectively, and KPs analyzed in [38] and [39], which work with water vapor.

It can be seen that these global efficiencies are really very low, in the range $\left[8\times10^{-4} - 8\times10^{-10}\right]$. For prototypes, this parameter was not really considered, and the input power was limited, generally in the order of 1 W. But for further development requiring the implementation of a number of micropumps, the efficiency needs to be significantly improved, by taking much care to the local heating and to the use of low conductivity materials allowing to limit the conductive heat losses. Analyzing conjugate heat transfer in KPs by numerical simulations and experiments should be next field of research.

This is a key question for the future application of KPs in various domains. For comparison, the efficiencies of some mechanical micropumps pumping air are also approximately calculated by the same way and listed in Table 1.2. Although they are still lower than 1%, these mechanical pumps are one order of magnitude more efficient than the best KPs reported in the literature.

Table 1.1 – Efficiency estimation of different Knudsen pumps.

Ref.	Year	Material	Pumping sub-stage	$\dot{Q}$ (W)	P_i (× 10^3 Pa)	$\frac{P_i}{P_o}$	n_c	N	h or d (× 10^{-6} m)	$T_h - T_c$ (K)	η (%)
[8]	2012	Oxide–Nitride–Oxide (ONO) layer	microchannels	1.36	6.67	0.066	1	48	0.15	55	0.0000016
[9]	2014			0.39	0.12	0.0012		162	0.1 (1.0)	50	0.000052
[11]	2003	glass	microchannels	39	0.01	0.4	18	10	1600	150	0.00025
[12]	2005	polysilicon	microchannels	0.08	46.61	0.46	1	8	0.1	578	0.0000004
[15]	1999	silicon		0.192	0.4	0.02	19-795	16	0.099-4.11	300	0.000057
[19]	2015	MCE	Porous Medium (PM)	20	99.55	0.98		1	0.1	45	0.0044
[20]	2016			100	97.33	0.96				100	0.000000084
[38]	2018	glass fiber filter		2590	0.90	0.45		30	0.7	119	0.004
[39]	2019			3.09	0.88	0.94		1		200.31	0.077
[41]	2013	MCE	PM	1	100.33	0.99		1	0.025	60	0.00025
[42]	2014										0.00025
[43]	2016			3.2				2		28	0.000065
[44]	2017			2	100.45			1		20.92	0.00015
[81]	2008	zeolites	PM	18.09	51.33	0.51		2	21.1 – 27.8	36.11	0.00047
[82]	2010	MCE	PM	8.5	97.56	0.98		1	0.1	70	0.000061
[83]	2021		PM	2	100.51	0.99		1	0.025	37.7	0.000067
		AAO		9.8	100.83				0.2	121.2	0.000016
[84]		Glass – Si – Al_2O_3	microchannels	1.2	98.03	0.97	1800	4	1.2	84	0.00087

Table 1.2 – Efficiency calculation of micromechanical pumps.

Refs	Year	Material	$\dot{Q}$ (W)	P_i (× 10^3 Pa)	$\frac{P_i}{P_o}$	N	η (%)
[85]	2015	Si	0.057	101.325	0.85	18	0.45
			0.015		0.94	4	0.55
			0.009		0.98	2	0.31

1.6 Conclusions

Knudsen micropumps, which are non-mechanical micropumps, operate thanks to the thermal transpiration phenomenon. It just requires to impose a difference of temperature without any initial pressure difference. In the two last decades, an increasing number of numerical and experimental investigations have been conducting to optimization the performances of KPs. Applications of KPs in micro heat pumps, gas separators, gas micro chromatographs and vacuum micro generators have started to be explored. The two most important indexes for assessing the performances of KPs are the maximum pressure head (or blockage pressure) $\Delta P_{\max}$ and the maximum mass flowrate $\dot{m}_{\max}$. The global efficiency of the already fabricated KPs is poorly documented, and an estimate based on the data from the literature reveals very low efficiencies. With the recent improvement of microfabrication techniques, various prototypes of Knudsen pumps based on both micromachined channels and porous materials have been manufactured with a view to practical applications. Moreover, a variety of KP designs with various geometries of microchannels including uniform and non-uniform cross sections of channels, tapered channels, curved channels as well as the tapered channels, have been imagined, providing appealing tracks for potential designs and future optimization of Knudsen pumps.

Chapter 2 - Theoretical bases for the modeling of rarefied gas microflows

Introduction

As introduced in Chapter 1, Knudsen pumps elements were numerically simulated by several authors using simplified continuum approaches and more accurately with the kinetic theory of gases. The numerical simulations of gas microflows presented in the present work have the common final goal to design and optimize the performances of KPs with different configurations, as well as to model their transient behavior, which is of great interest for controlling actuators requiring specific response times. Different designs of KPs can include tapered microchannels with circular or square cross sections and several circular microchannels in parallel. The numerical method should then be adapted to treat steady and quasi-steady gas flows in the proposed geometries. Numerical simulations based on the fully developed linearized Shakhov model are implemented for purely diffuse boundary conditions and used for characterizing the theoretical performances of multistage KPs. The same method is used for modeling isothermal pressure-driven flows in constant-section or tapered microchannels that have been fabricated from different manufacturing techniques and tested in Chapter 3.

2.1 Kinetic theory of gases

The kinetic theory of gases is a classical approach for describing the thermodynamic behavior of gases in the different rarefied regimes. The kinetic theory of gases is based on statistical mechanics, and is able to describe the macroscopic properties, such as density, pressure, temperature, viscosity or thermal conductivity, through a statistical modeling of the microscopic properties of molecules and their interactions. The earliest concepts were based on the statement that the matter was composed of elements called atoms which were minuscule and indivisible. In about 50 BC, the Roman philosopher Lucretius proposed the atomistic idea that apparently static macroscopic bodies were composed of rapidly moving atoms in a small area, in which the atoms bouncing off each other. All these ideas on atomistic points of view were rarely considered in the subsequent centuries, until the Swiss mathematician and physicist Daniel Bernoulli published his chief work *Hydrodynamica* in 1738 [1], dedicated to fluid mechanics. In this work, Bernoulli assumed that gases consist of a large number of molecules composed of atoms and moving in all directions, that the pressure of gases was caused by the impact of these molecules on a surface, and that the heat increased the velocity of the mole-

cules while their average kinetic energy determined the temperature of the gas. With this work, a solid foundation of kinetic theory of gases was established. Following the initial theory developed by Bernoulli, other scientists made great contributions to develop his work. In the 19th century, the formulation for expressing the velocity distribution of gas molecules was provided by Maxwell [86]. Maxwell formulated the distribution probability of a particle with a specific velocity in an area at a particular time. Following the work of Maxwell, Boltzmann established in 1872 the transport equation of the distribution function with the assumption that the gas is in dilute conditions, *i.e.* with only binary intermolecular collisions. This transport equation of the distribution function is the well-known Boltzmann transport equation (BTE), or simply Boltzmann equation. It describes the statistical behavior of a thermodynamic system which is not in a state of equilibrium [87]:

$$\frac{df}{dt}+\boldsymbol{\xi}\cdot\frac{df}{d\mathbf{r}}+\mathbf{F}\cdot\frac{df}{d\boldsymbol{\xi}}=Q(f,f'). \tag{2.1}$$

In this equation, valid for a simple dilute gas, the velocity distribution function $f(\mathbf{r},\boldsymbol{\xi},t)$ is the probability density function defined so that

$$dn=f(\mathbf{r},\mathbf{v},t)\,d^3\mathbf{r}\,d^3\boldsymbol{\xi} \tag{2.2}$$

represents the number of molecules within a volume element $d^3\mathbf{r}$ around the position $\mathbf{r}(x,y,z)$ and within a very small region of velocity space $d^3\boldsymbol{\xi}$ around molecular velocity $\boldsymbol{\xi}(\xi_x,\xi_y,\xi_z)$ at time t.

The left-hand side of Eq. (2.1) describes the evolution of the velocity distribution function with time, as the gas molecules move in space according to their molecular velocities and due to an external force **F** per unit mass. The intermolecular collisions are considered in the right-hand side term, and are provided by the collision integral:

$$Q(f,f')=\iint(f'\,f_*'-f\,f_*)\,g_r\,\sigma\,d\Omega\,d\boldsymbol{\xi}_*. \tag{2.3}$$

Here, f' and f_*' are the velocity distribution functions of two molecules before collision and f and f_* are their velocity distribution functions after they have collided each other. The magnitude of their relative velocities $g_r=|\boldsymbol{\xi}-\boldsymbol{\xi}_*|=|\boldsymbol{\xi}'-\boldsymbol{\xi}_*'|$ is conserved after collision. Details on the differential cross-section $\sigma\,d\Omega$, where $d\Omega$ is the unit solid angle in which a molecule is deflected after collision, can be found for example in [88]. The collision integral calculates the effect of collisions on the distribution of molecules with velocity $\boldsymbol{\xi}$, investigating possible collisions with molecules having all other velocities $\boldsymbol{\xi}_*$. It should be noted that when the gas is in equilibrium, the solution of Eq. (2.1) gives the velocity distribution func-

tion introduced by Maxwell, which is a particular solution of the Boltzmann equation.

2.1.1 Dilute gas

As introduced previously, the Boltzmann equation is based on a dilute gas assumption. In the present work, the considered gas is a single gas, *i.e.* with single chemical species. In a dilute gas, the intermolecular collisions among the gas molecules are only binary collisions. Several characteristic length scales at molecular level should be considered to model the gas microflows in micro-size devices. The main characteristic lengths, such as the mean free path λ, the mean molecular diameter d_{mol}, and the mean molecular spacing D_S are presented in Fig. 2.1.

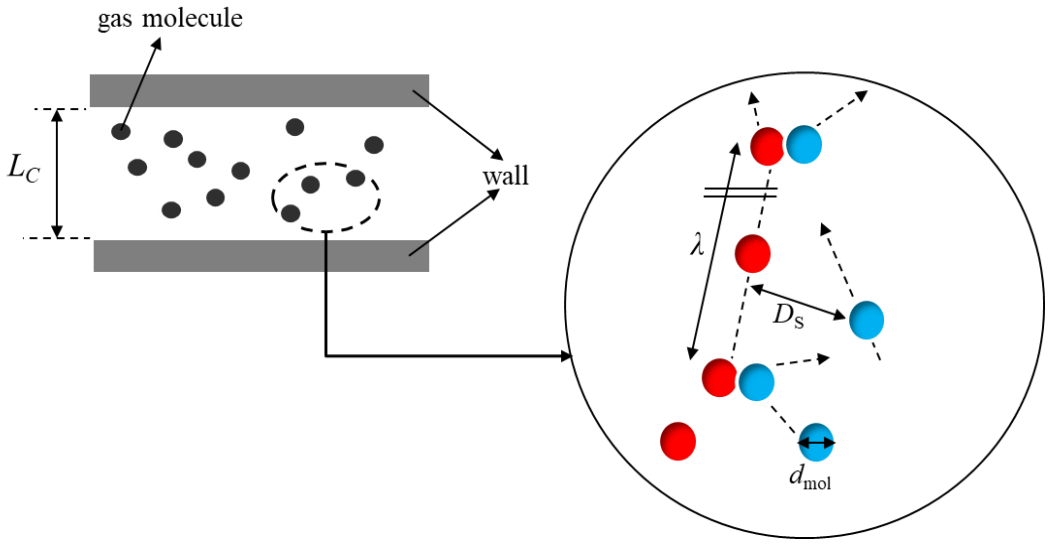

Figure 2.1 – Main characteristic length scales to be considered at the molecular level [89].

The mean molecular space D_S is related to the number density n_d through the simple relationship $n_d = D_S^{-3}$, as D_S^3 represents the mean volume available for a molecule. The mean free path λ is defined as the average distance that a molecule representing macroscopic motion travels between two successive intermolecular collisions in a relative local reference frame linked to the macroscopic flow field.

A gas can be treated as a dilute gas when the mean molecular diameter is small compared with the mean molecular space, *i.e.* if

$$d_{mol} \ll D_S \tag{2.4}$$

When the above condition is not satisfied, the gas is considered as a dense gas. With the dilute gas assumption, the mean free path λ of the molecule can be expressed by the ratio of the mean thermal velocity $\xi = \overline{|\boldsymbol{\xi}|}$, which is the mean molecular velocity magnitude, over the

mean collision rate υ :

$$\lambda = \frac{\xi}{\upsilon} \tag{2.5}$$

ξ depends on the specific gas constant R_g , the temperature T, the Boltzmann constant $k = 1.381 \times 10^{-23}$ J K^{-1}, and the mass m of the molecule [89]:

$$\xi = \sqrt{\frac{8R_g T}{\pi}} = \sqrt{\frac{8kT}{\pi m}} \tag{2.6}$$

For a specific gas, the collision rate υ and consequently the mean free path λ are determined by a collision model that describes the intermolecular binary elastic collisions.

2.1.2 Collision models

A collision model is required to model the behavior of the molecules during their binary collision and to obtain the related parameters, such as the mean diameter of molecule and the collisional cross section which are linked to the collision rate, the mean free path and the dynamic viscosity μ of the gas, a parameter that can be directly measured with a viscosimeter. In the past decades, different collision models including the hard sphere (HS) model, the variable hard sphere (VHS) model and the variable soft sphere (VSS) model, have been developed. All these models are based on the inverse power law (IPL) or point center of repulsion model that describes the force amplitude F between two colliding molecules [89]. This IPL model considers only the repulsive part of this force and assumes that

$$F = \frac{\kappa}{r_{i-j}^{\psi}} \tag{2.7}$$

where κ and ψ have a constant value and r_{i-j} denotes the distance between the two molecules' centers. One consequence of this collision model is that the dynamic viscosity μ is proportional to the temperature at the power of

$$\omega = \frac{\psi + 3}{2(\psi + 1)} \tag{2.8}$$

i.e., μ can be calculated at any temperature T from its value μ_0 at temperature T_0 :

$$\mu = \mu_0 \left(\frac{T}{T_0} \right)^{\omega} \tag{2.9}$$

HS model

The simplest model is the hard sphere model, which assumes that the total collisional cross section is constant and a constant coefficient independent of the gas species is induced due to the isotropic scattering. A consequence of the HS model is that the dynamic viscosity of the gas, which results from the intermolecular collisions of the molecules, is proportional to the square root of the temperature T:

$$\mu \propto \sqrt{T} \tag{2.10}$$

It can be seen that the HS model can be deduced from the IPL model with $\psi \to \infty$ (which explains why it is called a hard sphere) and $\omega = 0.5$. As a consequence, it is a quite good model only for specific gas species, as for example Ne for which the measured viscosity dependence with temperature reveals a factor $\omega = 0.66$. Most of the other gas molecules have higher values of ω.

VHS model

The variable hard sphere (VHS) model, proposed by Bird, was developed for the development of the direct simulation Monte-Carlo (DSMC) of gas flows. The application of this model illustrates that the scattering probability of molecules is isotropic as in the HS model, but with a variable total collisional cross section which is a function of the relative velocity between the two colliding molecules. Thus, the VHS model can be considered as an improved HS model, resulting in

$$\mu \propto T^{\omega} \tag{2.11}$$

with a coefficient ω that depends on the gas species and can be adjusted to match viscosity measurements.

VSS model

Another collision model based on IPL model is the variable soft sphere model was proposed Koura and Matsumoto [90], for both viscosity and diffusion cross section to be consistent with the IPL model. It can be considered as the simplest extension of the VHS model, demonstrating almost the same analytical and computational simplicity. The difference between VSS and VHS models is that for VSS model, both the collisional cross section and the deflection angle of the molecules after collision depend on the relative velocity between the molecules. It results in a complementary coefficient α than generally ranges from 1 to 2 and depends on the gas species. For $\alpha = 1$, the VSS model reduces to the VHS model [89].

Considering that the mean free path λ is determined by the collision model, each model can induce a different estimation of the mean free path of the molecules, which can be rewritten by some measurable macroscopic quantities multiply by a coefficient k_2 depending on the collision model:

$$\lambda = k_2 \frac{\mu}{\rho\sqrt{R_g T}} = k_2 \frac{\mu\sqrt{R_g T}}{P} \tag{2.12}$$

where ρ is the density of the gas considered as dilute and ideal. Table 2.1 tabulates the definition of coefficients k_2 for calculating the mean free path with different collision models.

Table 2.1 – Coefficient k_2 for calculating the mean free path for the different collision models.

Collision model	k_2
HS	$\frac{16}{5\sqrt{2\pi}} \approx 1.277$
VHS	$\frac{2(7-2\omega)(5-2\omega)}{15\sqrt{2\pi}}$
VSS	$\frac{4\alpha(7-2\omega)(5-2\omega)}{5\sqrt{2\pi}(\alpha+1)(\alpha+2)}$

In the present work, the VHS model is chosen for modeling the gas flows in microchannels in order to make a compromise between computational accuracy and time consumption. Therefore, the mean free path and the dynamic viscosity can be estimated by Eqs. (2.12) and (2.9) respectively, using the VHS model for calculating k_2, with values of μ_0 and ω taken from the literature [88].

2.1.3 Thermodynamic equilibrium

In classical fluid mechanics, with the continuum assumption, all considered macroscopic quantities, such as density ρ, pressure P, temperature T and velocity **u**, are variables that continuously vary within the flow. The continuum approach is applicable when the sampling volume, in which the local macroscopic quantities can be obtained when averaging the microscopic properties of molecules, is in thermodynamic equilibrium [88]. To respect this thermodynamic equilibrium, the intermolecular collision rate inside any sampling volume must be high enough. It means that the mean free path λ must be small compared to the characteristic length L_{sv} of the sampling volume, which is itself small in comparison to the characteristic

length L_C of the flow domain of interest [89]. On the contrary, if the frequency of the intermolecular collisions in the sampling volume is not high enough, the thermodynamic equilibrium will not be reached. Therefore, the local thermodynamic equilibrium requires that

$$\frac{\lambda}{L_C} \ll 1 \tag{2.13}$$

where the characteristic length L_C is generally the hydraulic diameter D_h or the minimum length (*e.g.* the depth of a rectangular microchannel) of the considered cross section of the flow.

2.1.4 Gas flow regimes

The ratio of the mean free path λ over the characteristic length L_C of the channel has already been introduced in Eq. (1.1) in the specific case where $L_C = D_h$. More generally,

$$Kn = \frac{\lambda}{L_C} \tag{2.14}$$

is the well-known Knudsen number *Kn*, which is a key dimensionless number for gas microflows that describes its rarefaction degree.

Generally, gas microflows can be classified in four different flow regimes according to the range of the Knudsen number, including the continuum or hydrodynamic flow regime, the slip flow regime, the transitional flow regime and the free molecular flow regime. Different models and methods can be used for modeling these flow regimes, as illustrated in Fig. 2.2.

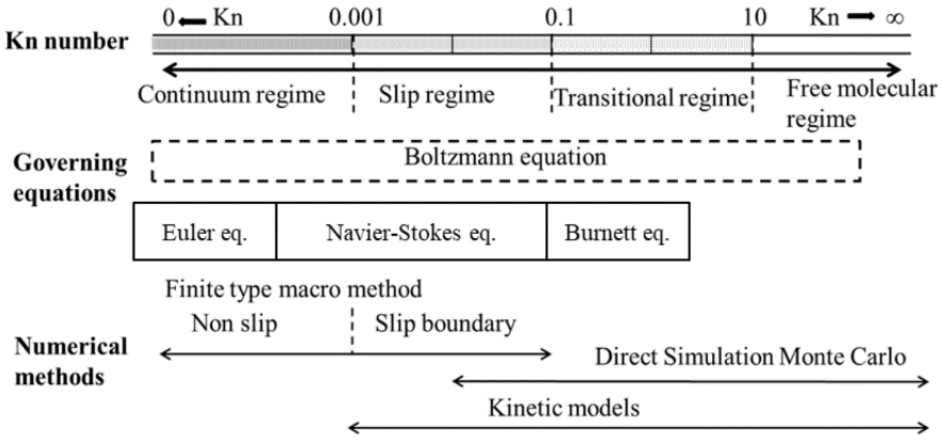

Figure 2.2 – Gas flow regimes and related methods classified by the value of Knudsen number *Kn* [1].

When $Kn < 10^{-3}$, the gas flow is in the ***continuum or hydrodynamic regime***, the gas is considered as a continuum medium and rarefaction effects can be ignored. The compressible

Navier-Stokes-Fourier equations with classic no-slip boundary conditions can be used to accurately model the flow.

When $10^{-3} < Kn < 10^{-1}$, the gas flow is in the ***slip regime***. Due to the decrease of the intermolecular collision rate compared to the collision rate between molecules and walls, the gas rarefaction effects start to be sensitive close to the solid boundaries. However, the Navier-Stokes-Fourier equations are still applicable in the bulk flow, provided they are coupled with appropriate velocity slip and temperature jump boundary conditions at the wall, that macroscopically take into account the local thermodynamic disequilibrium in the Knudsen layer defined in Section 1.2. Maxwell proposed the following expression for the slip velocity:

$$u_{slip} = u_s - u_w = \frac{2-\alpha}{\alpha}\lambda\left[\frac{\partial u_s}{\partial n} - \frac{3}{2}\frac{\mu}{\rho T}\frac{\partial^2 T}{\partial s\,\partial n}\right]_w + \frac{3}{4}\left[\frac{\mu}{\rho T}\frac{\partial T}{\partial s}\right]_w \tag{2.15}$$

The slip velocity is the difference between the macroscopic velocity u_s of the gas in the direction s parallel to the wall, and the velocity of the wall u_w. Here, α is the tangential momentum accommodation coefficient described further in Section 2.2.2, n refers to the direction normal to the wall and oriented towards the fluid, and s refers to the direction tangent to the wall which is parallel to the gas flow. Generally, Eq. is wrongly cited in the literature by omitting one term:

$$u_{slip} = u_s - u_w = \frac{2-\alpha}{\alpha}\lambda\left[\frac{\partial u_s}{\partial n}\right]_w + \frac{3}{4}\left[\frac{\mu}{\rho T}\frac{\partial T}{\partial s}\right]_w \tag{2.16}$$

The second term of the right-hand side is correlated with the thermal transpiration or creep phenomenon, exploited for the functioning of Knudsen pumps.

When $10^{-1} < Kn < 10^{1}$, the gas flow is in the ***transitional regime***, in which the intermolecular collisions have almost the same order of importance than collisions between the molecules and the walls. Therefore, the effects of rarefaction are significant and the Navier-Stokes-Fourier equations are no longer valid. Nevertheless, some extended continuum models such as the R13 moments methods or the Burnett equations have been proved to be applicable in this regime, at least in the early transitional regime ($Kn < 10^{0}$). For much higher Knudsen number ($Kn > 10^{0}$), the resolution of the Boltzmann equation is required, usually by either kinetic models or by DSMC methods.

In the ***free molecular regime***, for $Kn > 10^{1}$, molecules move freely between the walls and without any intermolecular collisions. Therefore, the flow in this regime can be depicted by the simplified Boltzmann equation without its collision term. Then, it can be solved by either analytical or numerical methods.

The above described classification, although more or less empirical, is generally accepted.

However, the limits of the four different regimes are not strict, and the range of the Knudsen number for each regime is indicative. Besides the Knudsen number, another parameter, frequently used to characterize the rarefaction of the gas flow, is the so-called rarefaction parameter δ, which is inversely proportional to the Knudsen number Kn, and can be expressed as:

$$\delta = \frac{L_C P}{\mu v} \tag{2.17}$$

where $v = \sqrt{2R_g T}$ is the most probable velocity of the molecules, slightly different from the mean molecular velocity $\bar{\xi}$.

Maxwell [7] theoretically explored the stresses in rarefied gases due to a temperature gradient, and he demonstrated that at a given point the pressure is not isotropic when the temperature is not uniform. He also showed that the transpiration effect described in Chapter 1 was not only dependent on the temperature gradient, but also on the rarefaction degree and on the gas nature itself. It should be noted that the nature and roughness of the walls also strongly affect rarefied gas flows [89]. Therefore, it is necessary to have an excellent knowledge not only on the gas but also on the walls properties for exploring the conjugate effects of thermally-driven and modelling pressure-driven rarefied gas flows.

Later, Knudsen [1] performed experiments on gas flows through small orifices. By imposing a difference of temperature between the two sides of an orifice, a pressure difference named thermomolecular pressure difference (TPD) could be measured as previously described by Reynolds and Maxwell. A model for calculating the TPD was also proposed by Knudsen. Thereafter, several kinetic models were developed by scholars for different gases, and these models analyzed the maximum value of TPD as a function of gas rarefaction [91–96].

2.2 Kinetic models and boundary conditions

For modeling gas microflows, kinetic models can describe the real behavior of the gas molecules, once associated with the appropriate boundary conditions imposed by the solid surface of the flow domain, linked to temperature, roughness, and properties of the wall. These models can cover a large range of Knudsen number, which is not the case of continuum models. It is the reason why they are preferred for modeling flows in Knudsen micropumps, that can operate in slip flow, transition and free molecular regimes.

2.2.1 Kinetic models

Various kinetic models have been developed to solve engineering problems involving rarefied gas flows. These models should satisfy the main properties of the Boltzmann equation,

including conservation of the collision invariants, should satisfy the *H*–Theorem which is equivalent to the second law of thermodynamics and describes the evolution of the gas towards equilibrium, and should provide correct transport coefficients.

BGK model

One typical and widely used simplified model is the Bhatnagar-Gross-Krook (BGK) model which was first proposed in 1954 for monoatomic gases [97]. In this model, the collision integral (2.3) is approximated by the following expression:

$$Q = \upsilon(f^M - f) \tag{2.18}$$

where the collision rate $\upsilon = P/\mu$ can be defined as the ratio of the local pressure to the dynamic viscosity. In this equation, f^M is the equilibrium value of f, *i.e.* the Maxwellian velocity distribution function. The BGK model is the simplest kinetic model, as the collision frequency does not depend on the velocity of the molecules. Besides, the BGK model assumes that the molecular velocities respect the local Maxwellian distribution after collision. Furthermore, it has been proven that the results provided by the BGK model in the whole range of the rarefaction parameter δ have a very good agreement with the results obtained from the complete Boltzmann equation [98]. Nevertheless, the BGK model has no ability to correctly express the thermal conductivity and the viscosity simultaneously. A consequence is that the Prandtl number predicted by the BGK model is equal to unity for ideal monoatomic gases, although the expected value is 2/3. Consequently, the BGK model is not applicable to problems with coupled hydrodynamics and heat transfer phenomena, such as thermal transpiration flows.

Shakhov model

Later, a generalization of the BGK model was developed by Shakhov [1,99]. This model has been validated for various pressure and temperature-driven flow problems. In this kinetic model, the collision term is expressed by:

$$Q = \upsilon\left\{f^M\left[1 + \frac{2(1-Pr)}{5}\frac{m}{N(kT)^2}\mathbf{Q}\cdot(\boldsymbol{\xi}-\mathbf{U})\left(\frac{m(\boldsymbol{\xi}-\mathbf{U})}{2kT} - \frac{5}{2}\right)\right] - f\right\} \tag{2.19}$$

where $\mathbf{Q}$ is the heat flux vector, and $\mathbf{U}$ the macroscopic velocity vector and N the number density. Here, the real value of Prandtl number Pr can be provided, and it can be seen that the BGK model is a specific case of the Shakhov model with $Pr = 1$. In addition, the expressions for the stresses and the thermal flux with the correct values of the viscosity and heat conduc-

tivity can be obtained from this model. However, it has not been rigorously proven that it satisfies the *H*-Theorem, since the distribution function may be negative under some certain conditions. In spite of all of this, the Shakhov model has been demonstrated very consistent and accurate, providing physically justified results of the macroscopic quantities. For these reasons, the Shakhov model is applied in the present work for the numerical simulation of coupled pressure and temperature driven flows generated by the thermal transpiration phenomenon, and necessary to characterize the performances of the Knudsen pumps.

2.2.2 Wall boundary conditions

Wall boundary conditions are required for the computational solution of the Boltzmann equation and the kinetic models. These boundary conditions describe the correlation between the distribution of molecules arriving to the wall and the distribution of molecules departing from the wall. The assumption of a velocity slip of the gas molecules at the surface was initially developed by Maxwell [7]. He considered two limit cases of reflection of the molecules after collision with the solid wall: either a specular reflection or a diffuse reflection (Fig. 2.3).

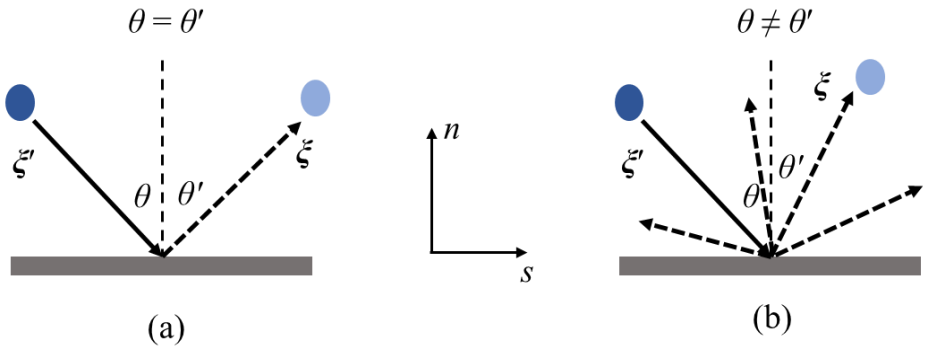

Figure 2.3 – Gas molecules departure from the wall after collision.
a) Specular reflection, and b) Diffuse reflection.

In the case of specular reflection, the molecule with an angle of incidence θ only changes the direction of the velocity component perpendicular to the wall after the collision, while keeping its initial velocity magnitude, and the angle of reflection θ' is equal to the angle of incidence θ. It results in the specular scattering kernel W_S expressed by:

$$W_{S\,(\boldsymbol{\xi}'\to\boldsymbol{\xi})} = \delta_{Dirac}\left[\boldsymbol{\xi}' - \boldsymbol{\xi} + 2\left(\boldsymbol{\xi}\cdot\mathbf{n}\right)\mathbf{n}\right] \tag{2.20}$$

A scattering kernel represents the probability of a molecule arriving at the wall with a velocity $\boldsymbol{\xi}'$ leaves the wall after colliding it with a velocity $\boldsymbol{\xi}$. In Eq. (2.20), δ_{Dirac} is the Dirac

delta distribution, and $\mathbf{n}$ is the unit vector perpendicular to the wall with a direction towards the flow domain.

In the case of diffuse reflection, the gas molecules are reflected with any random direction respecting the Maxwell distribution related to the properties of the wall, such as its temperature T_W and its velocity $\mathbf{U_W}$. The corresponding scattering kernel W_D is defined as follows:

$$W_{D\,(\xi'\to\xi)} = \frac{1}{2\pi}\boldsymbol{\xi}\cdot\mathbf{n}\left(\frac{m}{kT_W}\right)^2 \exp\left[-\frac{m\left(\boldsymbol{\xi}-\mathbf{U_W}\right)^2}{2kT_W}\right] \tag{2.21}$$

Maxwell treated the interaction between the gas molecules and the solid wall as a combination of diffuse and specular reflections. He defined β as the fraction of gas molecules reflected diffusely by the wall, while the complementary fraction $1-\beta$ is reflected specularly by the wall. This dimensionless coefficient is known as the tangential momentum accommodation coefficient (TMAC). When $\beta = 1$, the gas molecules totally experience a diffuse reflection, loose the tangential momentum and get in average the tangential momentum to the wall. Contrarily, when $\beta = 0$, the gas molecules undergo a specular reflection and there is no tangential momentum exchange between the gas molecules and the wall. Therefore, with the combination of specular and diffuse reflection, the Maxwell scattering kernel W_{DS} is given by the following expression:

$$W_{DS(\xi'\to\xi)} = \beta W_D + (1-\beta)W_S \tag{2.22}$$

2.2.3 Fully developed linear Shakhov model

As explained in Chapter 1, the thermal transpiration effect induces a thermally driven gas flow that results in an increase of pressure in the hot side and/or a decrease of pressure in the cold side if the pump is not open at its both ends. Thus, in the general case, the thermally-induced flow generates a pressure difference between cold and hot side called thermomolecular pressure difference (TPD). This difference of pressure generates a Poiseuille pressure-driven flow in the opposite direction, from hot side to cold side. Hence, models able to consider simultaneous temperature-driven and pressure-driven flows are required.

In the present work, the fully developed linear Shakhov model is implemented; it applies the infinite capillary theory that assumes a fully developed gas flow. This model does not consider the extremity effects, which is a reasonable assumption when the length of the microchannel is much higher than its hydraulic diameter.

The linear Shakhov model coupled with infinite capillary theory has been detailed in the thesis of Quesada [1]. By solving this model associated to complete diffuse boundary condi-

tions (β = 1), the dimensionless mass flowrates related to pressure and temperature-driven flows, namely, the kinetic coefficients G_P and G_T, can be calculated and the resulting mass flowrate $\dot{m}$ can be deduced as a function of the local pressure and temperature gradients.

2.3 Modeling thermal transpiration flows in Knudsen pumps

A basic Knudsen pump element is composed of one microchannel connected to two large reservoirs at different temperatures, T_c and T_h, resulting in transpiration flow from cold to hot reservoir. The boundary conditions in these reservoirs will condition the evolution of the flowrate through the microchannel and the pressure difference between the reservoirs.

2.3.1 Flow scenarios

Three different flow scenarios can be considered: a) open configuration; b) closed configuration; c) general configuration, as shown in Fig. 2.4. Each configuration can be characterized by its final stationary state, following the unsteady phase of the flow.

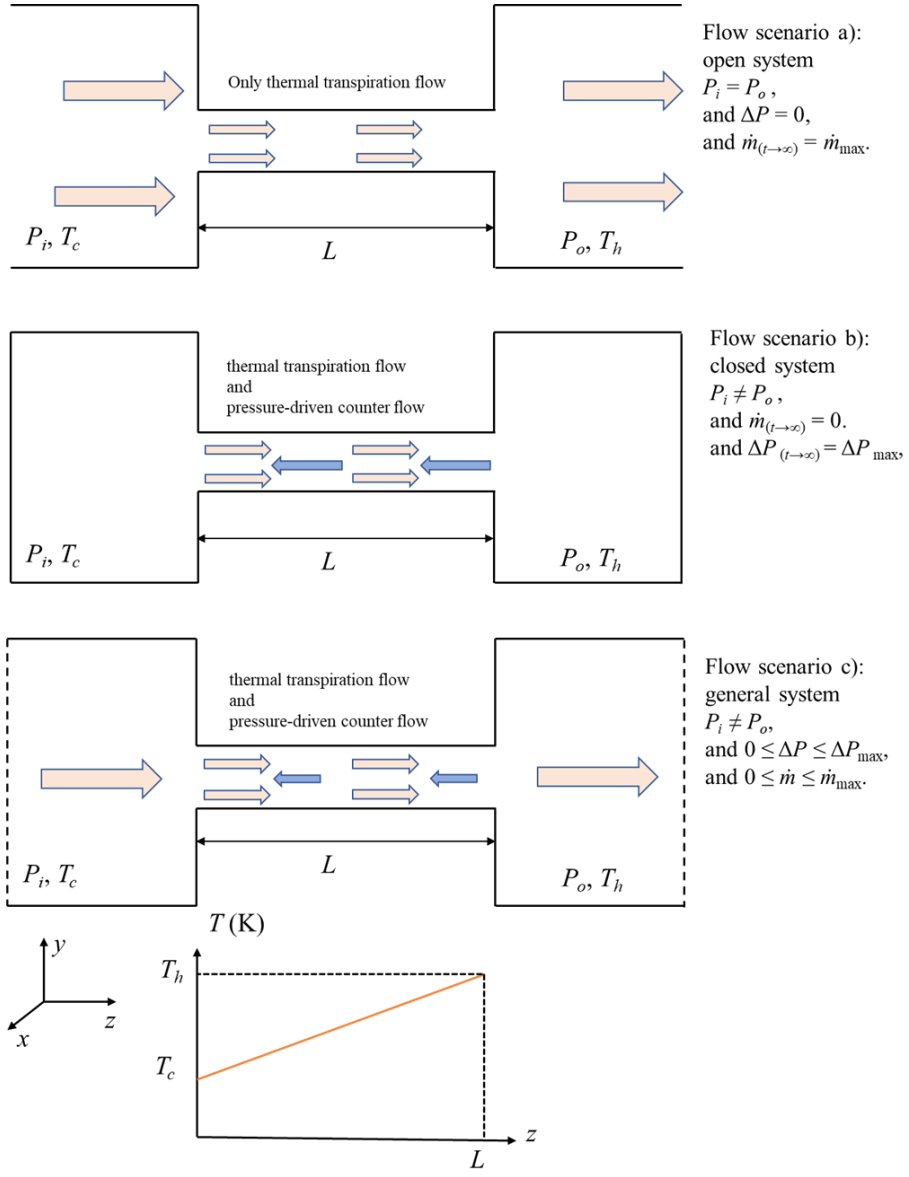

Figure 2.4 – Basic Knudsen pump element; flow scenarios in different configurations.

In the ***open configuration*** (a), the inlet and outlet pressures have always the same values ($\Delta P = P_o - P_i = 0$) and the final mass flowrate is maximal ($\dot{m}_{(t\to\infty)} = \dot{m}_{max}$).

In the ***closed configuration*** (b), the inlet and the outlet pressures are initially the same ($\Delta P_{(t=0)} = 0$), and the initial mass flowrate is only induced by thermal transpiration. Then the thermal transpiration flow increases the pressure in the hot side and decreases it in the cold side, resulting in a pressure-driven flow in the opposite direction (from the hot side to the cold side). The pressure driven counter-flow increases with time and a stationary state is finally reached, where the net mass flowrate is zero ($\dot{m}_{(t\to\infty)} = 0$) and the thermomolecular pressure difference is maximal ($\Delta P_{(t\to\infty)} = \Delta P_{max}$).

These two configurations correspond to the two limiting flow scenarios. However, in many practical cases, the flow scenario is ***intermediate*** (c) and the pump is delivering a net mass flowrate and has to face a counter pressure, during an unsteady operating phase or in the final stationary state ($0 \le \Delta P \le \Delta P_{max}$ and $0 \le \dot{m} \le \dot{m}_{max}$).

2.3.2 Numerical methods for thermal transpiration flows

Analytical and numerical studies have been developed by several researchers to obtain accurate solutions for thermal transpiration flows with different geometries under various rarefaction conditions. A complete analytical solution was performed by Méolans and Graur [100] in the slip flow regime in rectangular channels. Sharipov explored the solution of isothermal and non-isothermal flows through a long tube of uniform and variable radius [101–103] and through a long rectangular channel [104,105], and provided some guidance for further investigations on these kinds of channels. Later, theoretical analysis based on kinetic equations for pressure-driven and temperature-driven flows through a long rectangular channel with variable cross section were proposed [106]. Also, computational fluid dynamics (CFD) approaches based on the Navier-Stokes-Fourier equations associated with temperature jump and velocity slip boundary conditions were focused on the slip flow regime, and used for simulating transpiration flows in tapered, ratchet and curved microchannels [107].

2.3.3 Numerical procedure applied in the present work

The Discrete Velocity Method (DVM), which is one of the most accurate and reliable methods to solve the Boltzmann equation and the kinetic models [108,109], is used for our simulations. In this method, the discretization of continuous molecular velocity space induces a series of discrete molecular velocities. Afterwards, through the numerical integration of the distribution function at these considered discrete velocity points, the macroscopic quantities calculated from the moments of the distribution function can be computed. By the application of the DVM, the kinetic integral-differential equations are reduced to a system with one differential equation for each of the generated discrete molecular velocities. These ordinary differential equations can be calculated with finite element or finite volume approaches, resulting in a linear algebraic system, which can be solved using conventional methods.

For investigating the thermal transpiration flows in Knudsen pumps proposed in the present work, a fully developed gas flow in microchannel induced by both temperature and pressure gradients is considered. This problem has been extensively studied on the basis of the linearized kinetic model equations [98], and it was clearly demonstrated that the pressure and

the temperature-driven flows can be calculated separately from the kinetic coefficients G_P and G_T which are functions of the rarefaction parameter δ and the geometry of the cross section. These kinetic coefficients are obtained from the solution of the linearized Shakhov kinetic model and are available in the literature [1,98,101,110]. Thus, by superposing the solutions of both pressure and temperature-driven flows, the solution of the thermal transpiration flow coupled with a Poiseuille flow in the opposite direction can be obtained. The ordinary differential equation used for solving the pressure distribution along the channel as a function of the total mass flowrate has the following expression:

$$\frac{dP}{dz} = -\frac{v_{(z)}}{A_{S(z)} L_{C(z)} G_{P(\delta,z)}} \dot{m} + \frac{G_{T(\delta,z)}}{G_{P(\delta,z)}} \frac{P_{(\delta,z)}}{T_{(\delta,z)}} \frac{dT}{dz} \tag{2.23}$$

Equation (2.23) can be applied along the whole microchannel of length L, *i.e.* for $z \in [0, L]$. The most probable molecular velocity $v_{(z)}$ varies with the temperature $T_{(z)}$ along z-axis, and dP/dz and dT/dz are the local pressure and temperature gradients, respectively. $A_{S(z)}$ and $L_{C(z)}$ are the area and the characteristic length of the local cross section at the position z, respectively. The local gas rarefaction parameter δ defined in Eq. (2.11) is also a function of z.

An elementary one-stage Knudsen pump composed of one microchannel connected to one macrochannel (Fig. 2.5) is taken as an example to illustrate the calculation procedure based on Eq. (2.23). In this example, the geometries of both micro and macrochannels are straight circular channels with uniform cross section, but with different diameters D and lengths L. The diameter of the macrochannel (1) is higher than that of the microchannel (2). Consequently, the transpiration flow in z-direction in the microchannel is stronger than the transpiration flow in the $-z$-direction in the macrochannel, resulting in a net flow in z-direction. Considering a characteristic length $L_C = D/2$, Eq. (2.23) reads for both channels:

$$\frac{dP}{dz} = -\frac{8 v_{(z)}}{\pi D_{(z)}^3 G_{P(\delta,z)}} \dot{m} + \frac{G_{T(\delta,z)}}{G_{P(\delta,z)}} \frac{P_{(\delta,z)}}{T_{(\delta,z)}} \frac{dT}{dz} \tag{2.24}$$

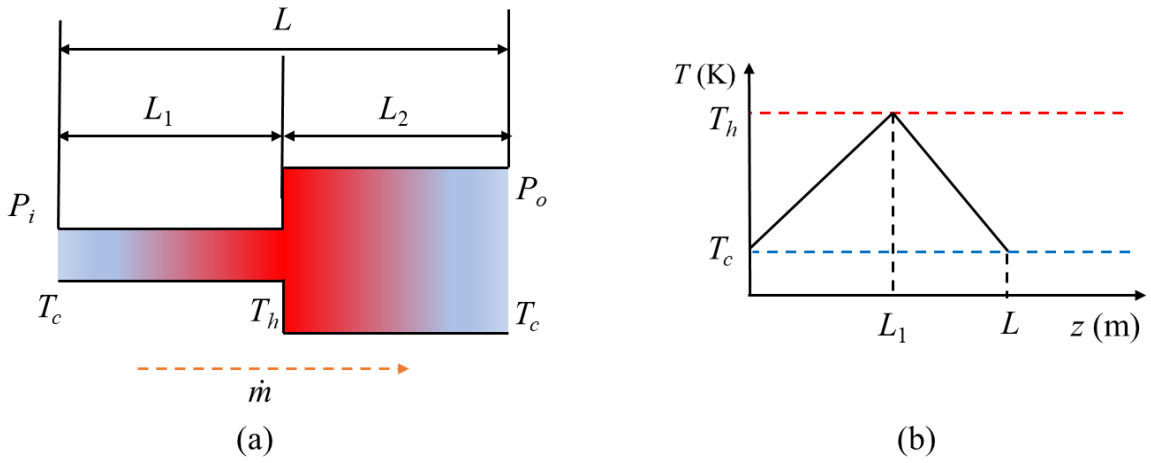

Figure 2.5 – a) A Knudsen pump composed of a microchannel connected to a macrochannel; b) Temperature distribution along the walls of the channels.

If we consider an open configuration (Fig. 2.4a), the inlet and the outlet pressures are known and equal ($P_i = P_o$), and the mass flowrate $\dot{m}$ can be calculated with a shooting method. An arbitrary positive initial mass flowrate is specified and Eq. (2.24) is integrated with the inlet condition $P_{(z=0)} = P_i$ along the length of the channel and, using Euler's method or a higher order integration scheme. The pressure at each node (or each cross section) can be calculated, from the values of G_P and G_T obtained from the local values of the parameters in each cross section. Then, the outlet pressure $P_{(z=L)}$ is obtained and compared to the given value P_o. A convergence condition is defined as a maximal threshold value of the difference between $P_{(z=L)}$ and P_o. If the convergence criterion is satisfied, the calculation is stopped and the mass flowrate is obtained. Conversely, if the convergence condition is not satisfied, the calculation is repeated with an adjusted mass flowrate value. A computational Fortran code has been written for these numerical simulations that follow the below flowchart (Fig. 2.6).

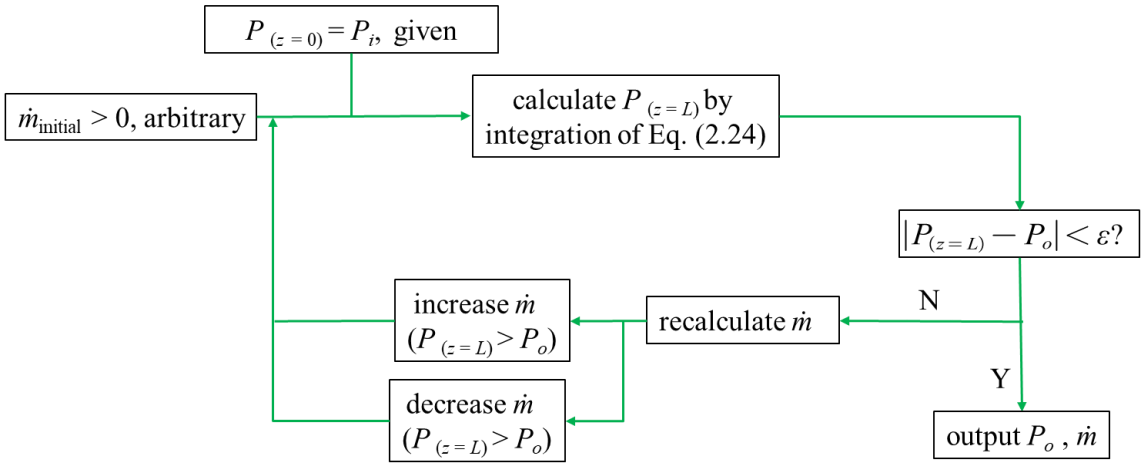

Figure 2.6 – Flowchart for calculating the mass flowrate for the open configuration of a single-stage KP.

If we now consider a general configuration (Fig. 2.4c), for which the mass flowrate $\dot{m}$ and either P_i or P_o are given, Eq. (2.24) can be easily solved to obtain the distribution of pressure P (z) along the channel, and the unknown parameter P_i or P_o can be calculated. A specific case corresponds to the closed configuration (Fig. 2.4b) in which the mass flowrate $\dot{m} = 0$. The maximum pressure difference ΔP_{max} for a given value of P_i or P_o can be calculated, and the unknow pressure P_o or P_i can accordingly be obtained. Figure 2.7 shows the calculation procedure for calculating the inlet or outlet pressures for a closed or general configuration.

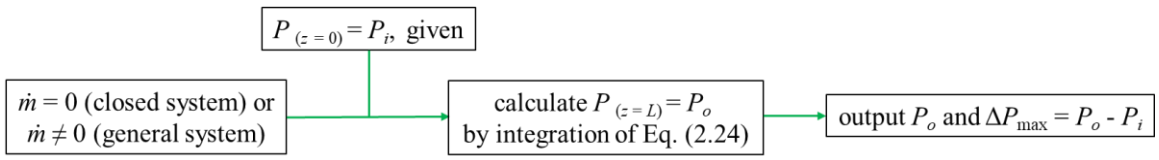

Figure 2.7 – Flowchart for calculating the outlet pressure for the closed or general configuration of a single-stage KP when the inlet pressure is known.

The above numerical method can be easily extended to simulate a multistage Knudsen pump composed of a series of monochannel stages similar to the above described one, and to optimize the performance of this kind of Knudsen pump. In the open configuration, it can be shown that the number of stages has no influence on the steady mass flowrate which is the same as in the single-stage configuration (provided of course that the applied temperature gradient is the same for each stage). As a consequence, designing a multi-stage KP with more or less the same inlet and outlet pressures has no interest. In other configurations, however, and more particularly in the closed configuration, the pressure difference increases as the number of stages increases. On the other hand, designing a KP with stages composed of

several parallel microchannels connected to one macrochannel increases the mass flowrate, but has no effect on the generated pressure difference.

As the objective is generally to design a KP able to generate both significant pressure differences and mass flowrates, it is necessary to envisage multistage configurations with stages associating several macrochannels in parallel.

2.4 Optimization of multistage Knudsen pumps

A *N*-stage KP with identical stages composed of n_c parallel microchannels with one macrochannel is now analysed. For this simple case study, all microchannels in the system are identical, and all macrochannels also have the same dimensions. Moreover, both microchannels and macrochannels are cylindrical with uniform circular cross sections (Fig. 2.8). In addition, the temperature gradients are the same for each stage.

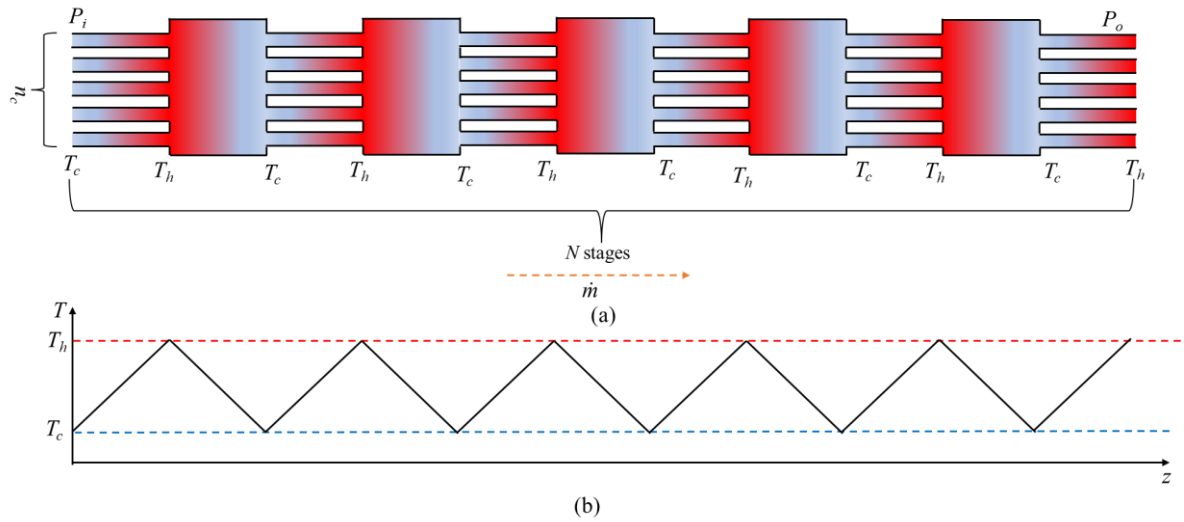

Figure 2.8 – Configuration of a multistage KP with stages consisting of several parallel microchannels with the same geometry connected to one macrochannel.
a) Configuration of the proposed KP; b) Temperature gradient along the wall of channels.

2.4.1 Calculation method for one stage

With this simple configuration involving identical stages, it is assumed that during steady operation of the KP, the individual mass flowrates $\dot{m}_{mic}$ are the same in each microchannel. The mass flowrate $\dot{m}_{mac}$ in the macrochannel correspond to the effective mass flowrate $\dot{m}$ of the KP and is simply given by $\dot{m} = \dot{m}_{mac} = n_c\, \dot{m}_{mic}$.

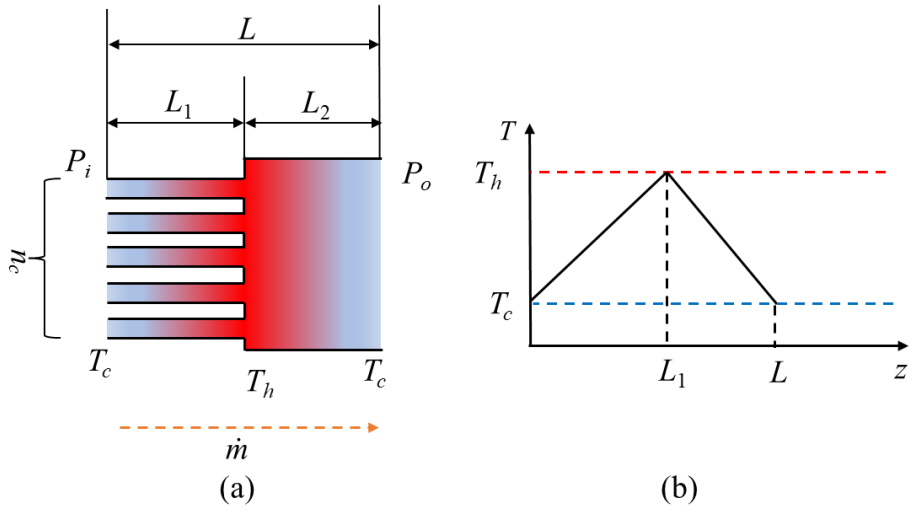

Figure 2.9 – a) One stage of KP composed of n_c parallel microchannels connected to one macrochannel; b) Temperature distribution along the wall of the channels.

One stage of KP can be divided into two segments (Fig. 2.9), the first one corresponding to the microchannels with an inlet pressure P_i, an inlet temperature T_c and an outlet temperature T_h, which are considered as given data for this stage. The calculation procedure is similar to the case of one microchannel per stage. Assuming an initial value of $\dot{m}_{mic} = \dot{m}/n_c$, or knowing it according to the considered configuration, the pressure at the outlet of the microchannels, $P_M = P_{(z=L_1)}$, can be calculated with the method described in Section 2.3.2. With the same equation, $P_{(z=L)}$ is obtained considering the macrochannel with an inlet pressure P_M, an inlet temperature T_h and an outlet temperature T_c. For an open configuration, $P_{(z=L)}$ is compared to P_o and the process is iterated, and for a closed of general configuration, as $\dot{m}$ is zero or given, P_o is directly obtained (Fig. 2.10).

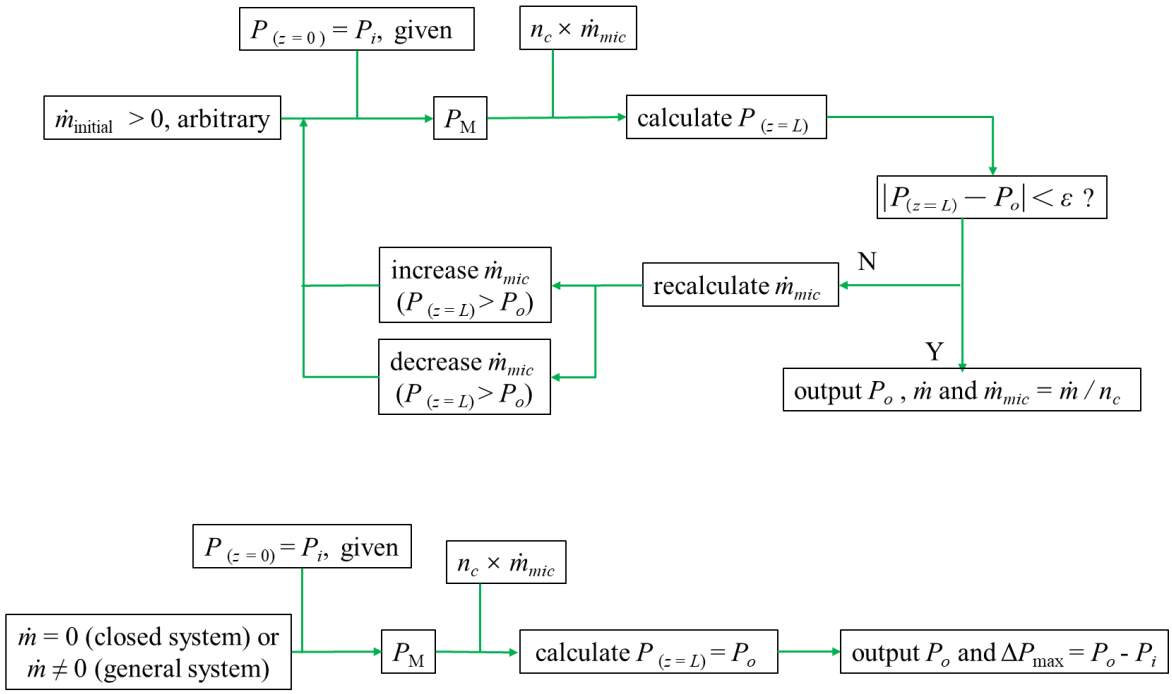

Figure 2.10 – Flowchart of calculation procedure for a stage of a multistage KP.
Up: calculation for the open configuration; Bottom: calculation for closed or general configurations.

2.4.2 Calculation method for a series of stages

For a multistage KP, the outlet pressure of the macrochannel in the preceding stage is regarded as the inlet pressure of the microchannel in the subsequent stage. This assumption is made while considering that the individual mass flowrate $\dot{m}_{max}$ in each stage remains constant. The pressure distribution along the channels can be calculated using the method detailed in Section 2.3.2, progressing until the final outlet pressure of the entire KP is determined. In an open configuration, this outlet pressure is compared against the predetermined value P_o. If the system is closed or of a general configuration, where the predetermined value of $\dot{m}$ is either zero or given, the outlet pressure P_o is directly obtained without further iteration.

2.4.3 Numerical results

The single-stage with one microchannel configuration shown in Fig. 2.5 is first chosen for analyzing the influence of different parameters on the performance of a KP working with helium. The parameters for this simple investigation are tabulated in Table 2.2. The gas is helium.

Table 2.2 – Parameters for the sensitive analysis of a single-stage single-channel KP

Parameter	r (μm)	$\frac{L_1}{r}$	$\frac{R}{r}$	$\frac{L_2}{r}$	P_i (kPa)	T_c (K)	$\Delta T = T_h - T_c$ (K)
Value	5, 10, 20	25, 50, 100	1.25, 2.5, 5	25, 50, 100	0.1 100	300	100, 200, 300

The following figures (Figs. 2.11 to 2.16) display three sets of data. The maximal pressure difference $\Delta P_{\max}$ (corresponding to the closed configuration) and the maximal mass flowrate $\dot{m}_{\max}$ (corresponding to the open configuration) are analyzed as a function of the inlet pressure P_i. The characteristic curves displaying the mass flowrate $\dot{m}$ versus the pressure difference ΔP (corresponding to the general configuration) are also drawn for a specific inlet pressure $P_i = 10$ kPa.

In Fig. 2.11, the influence of the temperature difference $\Delta T = T_h - T_c$ is shown for $r = 5$ μm, $R = 25$ μm, $L_1 = L_2 = 500$ μm. It can be readily seen that for any inlet pressure P_i, both $\Delta P_{\max}$ and $\dot{m}_{\max}$ logically increase as the temperature difference ΔT increases from 100 to 300 K. A maximum of $\Delta P_{\max}$ is obtained for an inlet pressure that slightly increases with ΔT (Fig. 2.11a). This maximum corresponds to the following values of the mean Knudsen number $\overline{Kn} = \left(Kn_{(z=0)} + Kn_{(z=L_1)} \right) \Big/ 2$ based on the diameter $d = 2r$ of the microchannel: 0.23, 0.27 and 0.24 for $\Delta T = 100$, 200 and 300 K, respectively. In the open configuration, the maximum mass flowrate is not yet reached at $P_i = 100$ kPa, a pressure that corresponds to $\overline{Kn} =$ 0.047, 0.055, and 0.064 for $\Delta T = 100$, 200 and 300 K, respectively (Fig. 2.11b). The characteristic curves of the pump, obtained from simulations corresponding to the general configuration at $P_i = 10$ kPa are linear for this single-stage and single-microchannel KP. The slopes of these characteristic curves depend on the temperature. As T increases, $\Delta P_{\max}$ increases more rapidly than $\dot{m}_{\max}$.

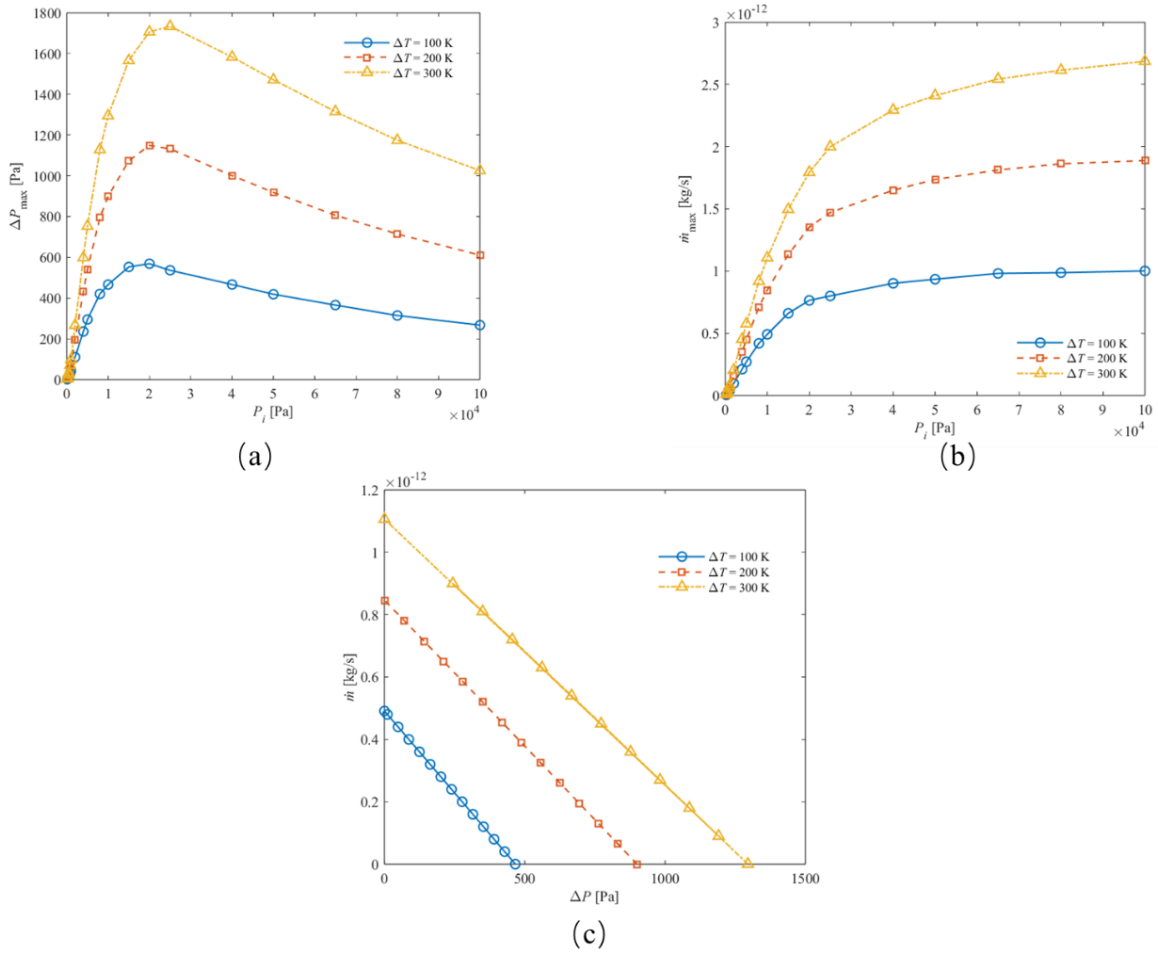

Figure 2.11 – Influence of the applied temperature difference $100\,\mathrm{K} \leqslant \Delta T \leqslant 300\,\mathrm{K}$ on the performances of a single-stage and single-microchannel KP with the following geometrical parameters: $r = 5\,\mu\mathrm{m}$, $R = 25\,\mu\mathrm{m}$, and $L_1 = L_2 = 500\,\mu\mathrm{m}$.

a) maximum pressure difference $\Delta P_{\max}$ vs inlet pressure; b) maximum mass flowrate $\dot{m}_{\max}$ vs inlet pressure; c) characteristic curves providing mass flowrate $\dot{m}$ vs pressure difference ΔP for $P_i = 10\,\mathrm{kPa}$.

Figure 2.12 shows the influence of the radius r of the microchannel for $\Delta T = 100$ K, $R = 25$ µm, $L_1 = L_2 = 500$ µm. As r decreases from 20 to 5 µm, $\Delta P_{\max}$ increases (but the mean Knudsen number $\overline{Kn}$ = 0.231 corresponding to the peak value of $\Delta P_{\max}$ does not change) and $\dot{m}_{\max}$ naturally decreases (Fig 2.12a). Besides, it can be seen from Fig. 2.12b that for $r = 20$ µm, the variation of $\dot{m}_{\max}$ with P_i exhibits a non-monotonic behavior when $P_i > 20$ kPa. This could be due to the very small value of the R over r ratio in this case, leading to a non-negligible temperature-driven counterflow in the macrochannel that can strongly affect the maximum mass flowrate. This point, however, should be discussed more in detail from simulations involving additional values of r and R (see further the discussion on Fig.

2.15). For $r = 10$ µm, a maximum of $\dot{m}_{max}$ is observed at P_i = 80 kPa, which corresponds to $\overline{Kn}$ = 0.029. As previously, the characteristic curves at $P_i = 10$ kPa are linear with a slope that significantly increases with the microchannel radius r. At $P_i = 70$ kPa, a pressure for which Fig. 2.12b exhibits an unusual shape, these curves are still linear with a slope that remains higher when the microchannel radius r is higher.

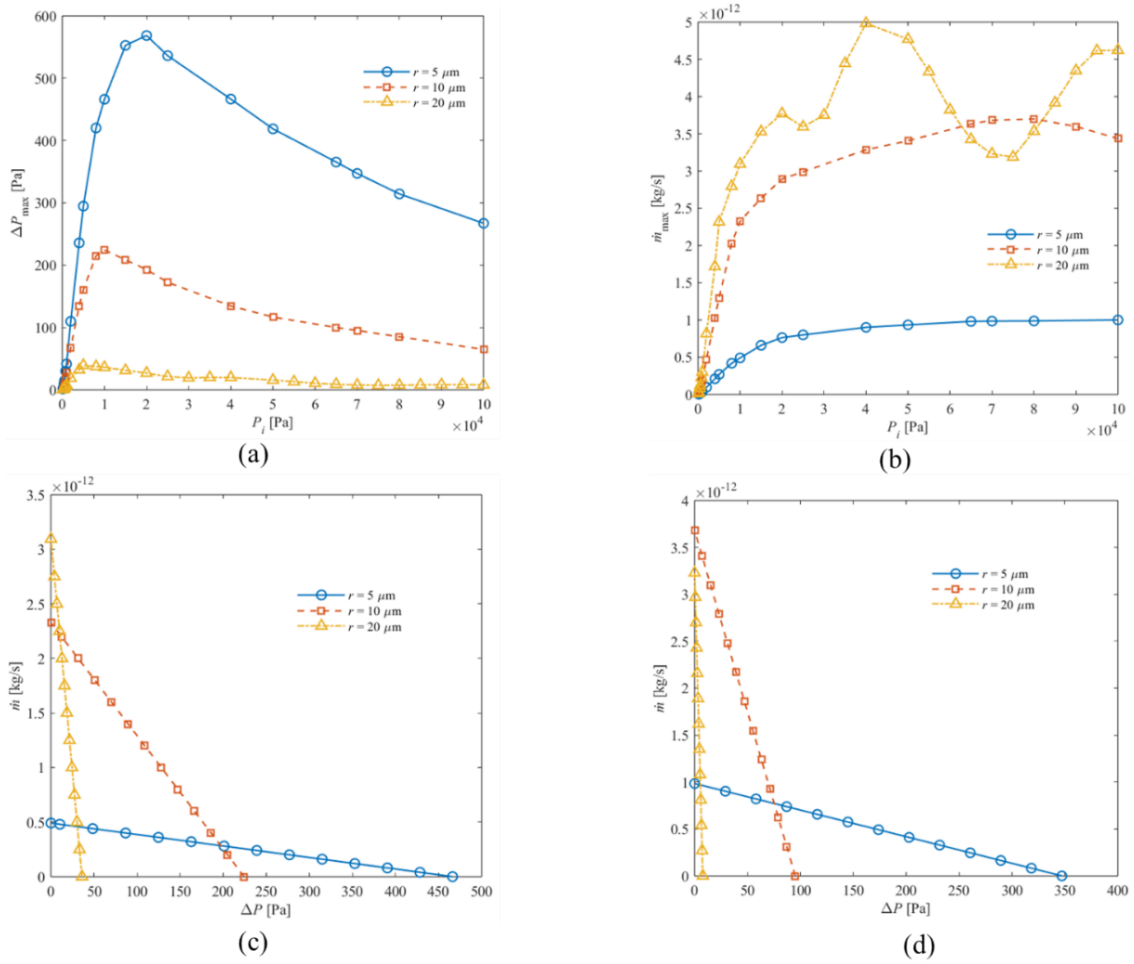

Figure 2.12 – Influence of the microchannel radius $5\ \mu m \le r \le 20\ \mu m$ **on the performances of a single-stage and single-microchannel KP with the following other geometrical parameters:** $R = 25\ \mu m$ **and** $L_1 = L_2 = 500\ \mu m$**. The applied temperature difference is here** $\Delta T = 100$ K **. a) Maximum pressure difference** ΔP_{max} **vs inlet pressure; b) maximum mass flowrate** $\dot{m}_{max}$ **vs inlet pressure; c) characteristic curves providing mass flowrate** $\dot{m}$ **vs pressure difference** ΔP **for** $P_i = 10$ kPa **; d) characteristic curves providing mass flowrate** $\dot{m}$ **vs pressure difference** ΔP **for** $P_i = 70$ kPa **.**

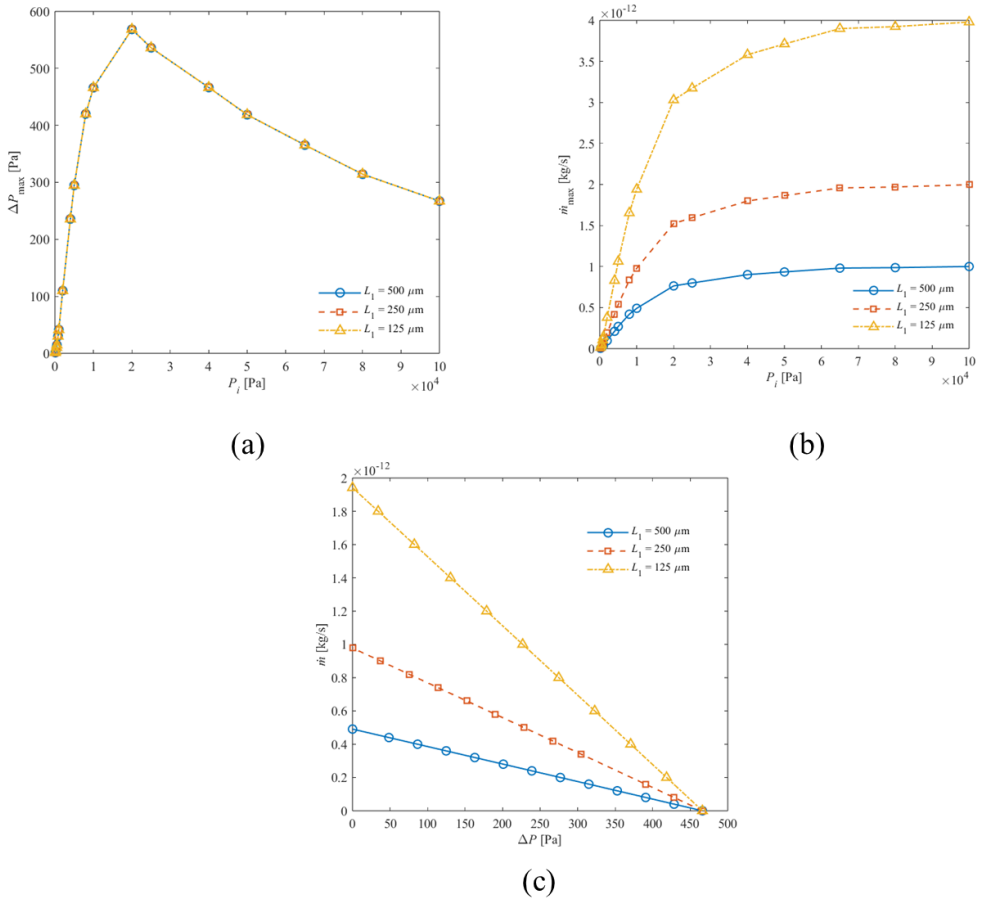

Figure 2.13 – Influence of the microchannel length $125\ \mu m \leq L_1 \leq 500\ \mu m$ **on the performances of a single-stage and single-microchannel KP with the following other geometrical parameters:** $r = 5\ \mu m$, $R = 25\ \mu m$, **and** $L_2 = 500\ \mu m$**. The applied temperature difference is here** $\Delta T = 100\ K$**.**

a) maximum pressure difference ΔP_{max} **vs inlet pressure; b) maximum mass flowrate** $\dot{m}_{max}$ **vs inlet pressure; c) characteristic curves providing mass flowrate** $\dot{m}$ **vs pressure difference** ΔP **for** $P_i = 10\ kPa$**.**

In Fig. 2.13, the influence of the length L_1 of the microchannel is investigated for $\Delta T = 100\ K$, $r = 5\ \mu m$, $R = 25\ \mu m$ and $L_2 = 500\ \mu m$. It is clear from Fig. 2.13a that ΔP_{max} is not affected by the value of L_1. This was expected because when $\dot{m} = 0$, Eq. (2.24) shows that the local pressure difference dP is directly linked to the temperature difference dT, whatever the value of dz. The integration of Eq. (2.24) consequently shows that ΔP_{max} depends on the temperature difference ΔT but not on the temperature gradient, *i.e.* ΔP_{max} does not depend on L_1. On the contrary, when the pressure is uniform, it can be seen from Eq. (2.24) that the mass flowrate is proportional to the temperature gradient and consequently,

$\dot{m}_{max}$ is proportional to $1/L_1$ (Fig. 2.13b). A consequence of these two conclusions is that the characteristic curves are homothetic with a multiplying factor equal to $1/L_1$.

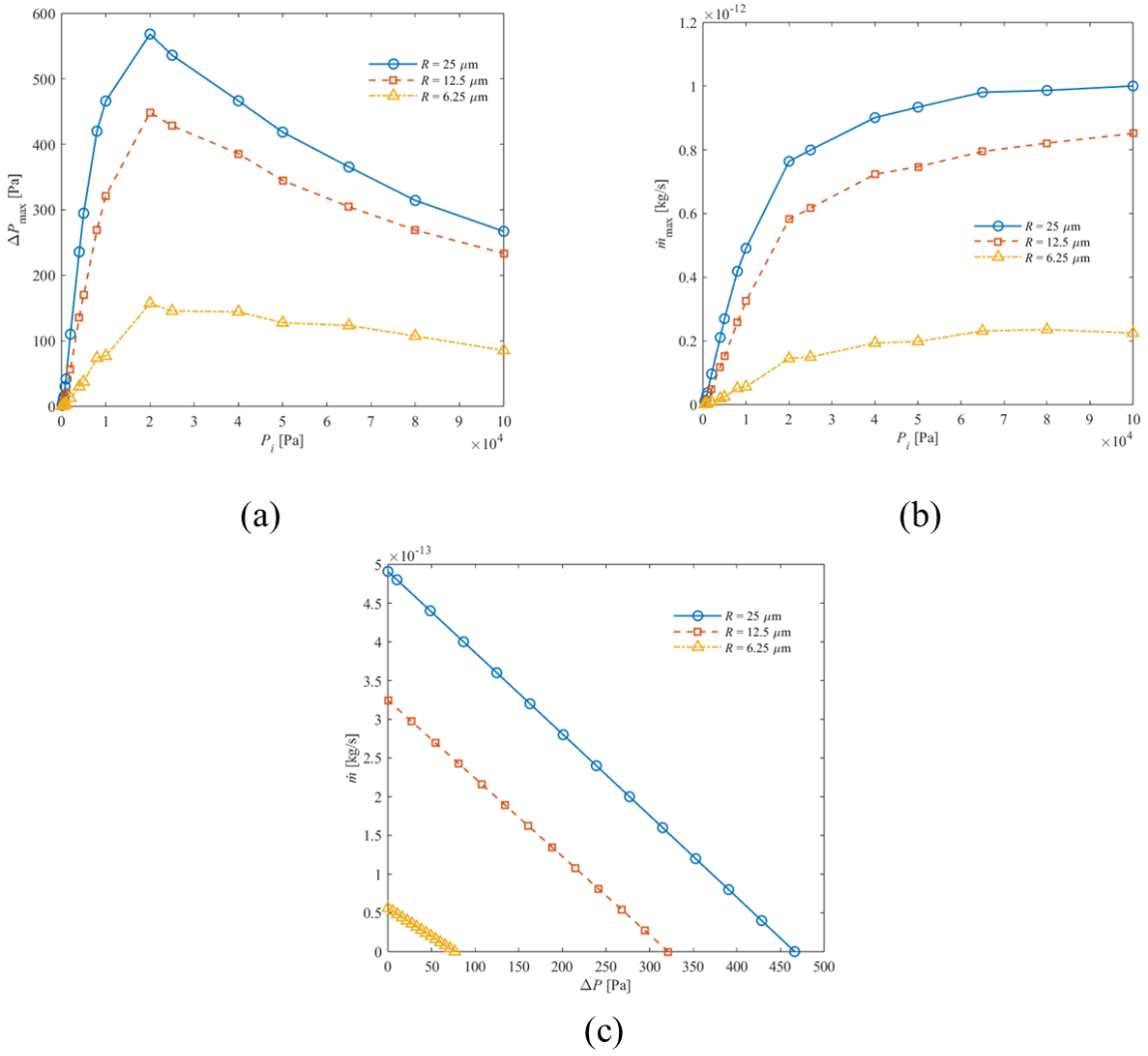

Figure 2.14 – Influence of the macrochannel radius $6.25\ \mu m \le R \le 25\ \mu m$ on the performances of a single-stage and single-microchannel KP with the following other geometrical parameters: $r = 5\ \mu m$ and $L_1 = L_2 = 500\ \mu m$. The applied temperature difference is here $\Delta T = 100\ K$. a) maximum pressure difference ΔP_{max} vs inlet pressure; b) maximum mass flowrate $\dot{m}_{max}$ vs inlet pressure; c) characteristic curves providing mass flowrate $\dot{m}$ vs pressure difference ΔP for $P_i = 10\ kPa$.

Figure 2.14 shows the influence of the radius R of the macrochannel for $\Delta T = 100\ K$, $r = 5\ \mu m$, and $L_1 = L_2 = 500\ \mu m$. As it increases, here between 6.25 and 25 µm, both ΔP_{max} (Fig. 2.14a) and $\dot{m}_{max}$ (Fig. 2.14b) increase, as the counterflow in the macrochannel is reduced. Also, when the value of R is multiplied by 2, first from 6.25 to 12.5 µm, the increase of ΔP_{max} and $\dot{m}_{max}$ is significant but when it is multiplied again by 2, from 12.5 to 25 µm, this

increase is significantly reduced and the two cubes will reach and asymptotic limit for $R \to \infty$, which corresponds to the solution of the flow in the microchannel alone. This trend is confirmed with the characteristic curves in Fig. 2.14c, showing that the maximum value of the ratio R/r is beneficial for the performance of the KP.

Additional values of the ratio $10 \leqslant R/r \leqslant 100$ have been used for the simulations shown in Fig. 2.15, for $5\ \mu\text{m} \leq r \leq 20\ \mu\text{m}$. Figures 2.15a to 2.15c provide the values of $\Delta P_{\max}$ while Figs. 2.15d to 2.15f provide the values of $\dot{m}_{\max}$. These figures show that when the ratio R/r is higher than 10 (whatever the value of *r*), $\Delta P_{\max}$ and $\dot{m}_{\max}$ have almost reached their maximum asymptotic values. Thus, $R/r = 10$ can be chosen for optimizing the KPs. It can also be seen (Fig. 2.15f) that the non-monotonic behavior observed in Fig. 2.12b for $r = 20\ \mu\text{m}$ is still present for high values of *R* (for which the Knudsen number in the macrochannel is lower than 10^{-3}), showing that the value of the ratio R/r is not enough to explain this specific trend.

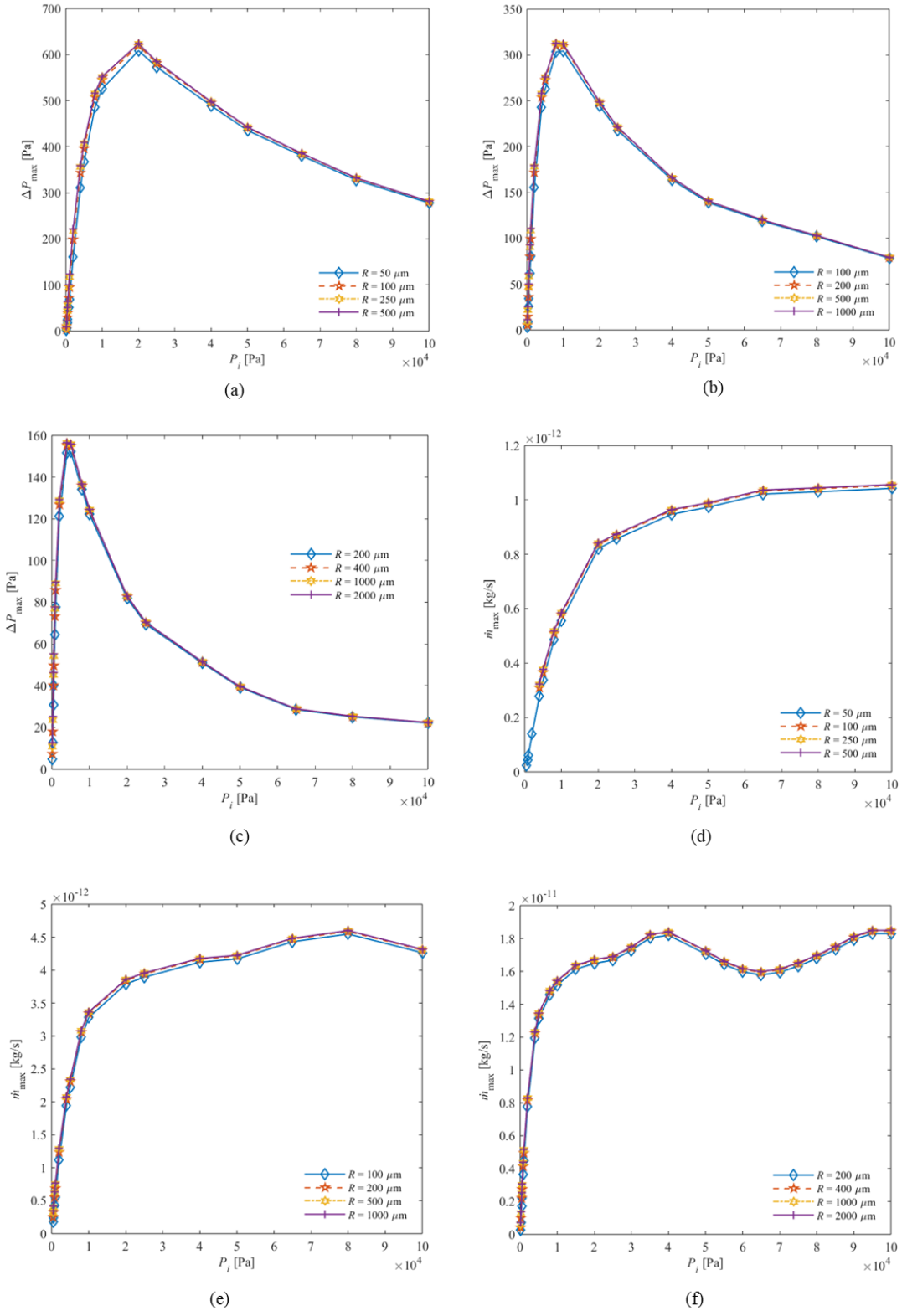

Figure 2.15 – Influence of the ratio $10 \le R/r \le 100$ on the performances of a single-stage and single-microchannel KP with the following other geometrical parameters: $L_1 = L_2 = 500$ μm. The applied temperature difference is here $\Delta T = 100$ K. Maximum pressure difference ΔP_{max} vs inlet pressure for a) $r = 5$ μm; b) $r = 10$ μm; c) $r = 20$ μm. Maximum mass flowrate $\dot{m}_{max}$ vs inlet pressure for d) $r = 5$ μm; e) $r = 10$ μm; f) $r = 20$ μm.

Finally, the length of the macrochannel L_2 does not affect the performance of the KP, as shown in Fig. 2.16. Regarding the maximal pressure difference (Fig. 2.16a), the reason is the same as for Fig. 2.13a. In addition, $\dot{m}_{max}$ is also independent of L_2 (Fig. 2.13b), which leads to a unique characteristic curve (Fig. 2.13c). Thus, $L_2 = L_1$ could be considered for further optimization.

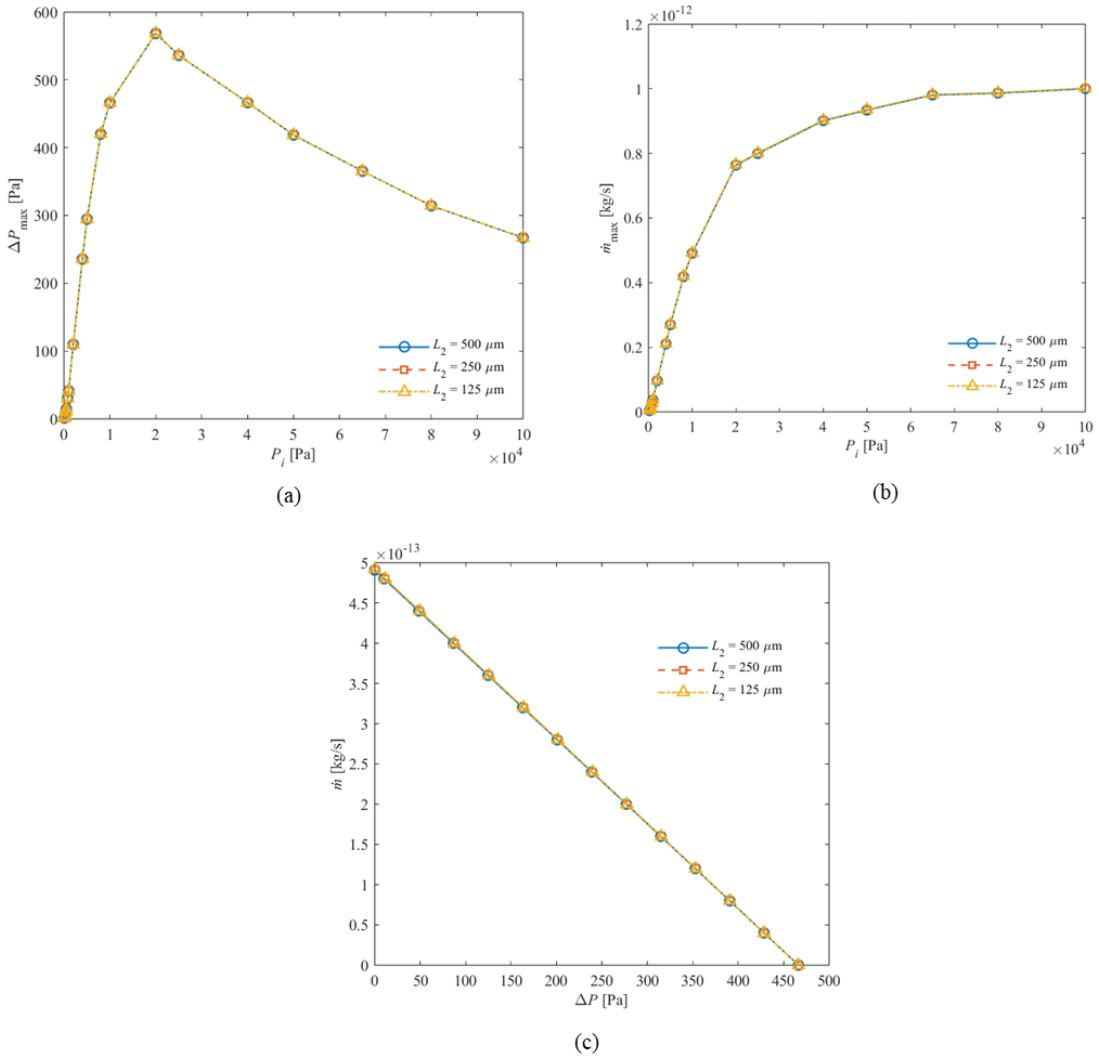

Figure 2.16 – Influence of the macrochannel length $125\ \mu m \le L_2 \le 500\ \mu m$ **on the performances of a single-stage and single-microchannel KP with the following other geometrical parameters:** $r = 5\ \mu m$, $R = 25\ \mu m$, **and** $L_1 = 500\ \mu m$**. The applied temperature difference is here** $\Delta T = 100\ K$**.**

a) maximum pressure difference ΔP_{max} **vs inlet pressure; b) maximum mass flowrate** $\dot{m}_{max}$ **vs inlet pressure; c) characteristic curves providing mass flowrate** $\dot{m}$ **vs pressure difference** ΔP **for** $P_i = 10\ kPa$**.**

Following the above results and discussion on a simple single-stage KP with a unique microchannel, the performance of multistage KPs, with a number $1 \leq n_c \leq 10$ of microchannels per stage and a number $1 \leq N \leq 1000$ of stages, is numerically investigated for an inlet pressure P_i ranging from 0.1 to 100 kPa. In this analysis, the microchannels have a radius $r = 5$ µm, and the macrochannels a radius $R = 50$ µm, the length of all channels is $L_1 = L_2 = 50$ µm, and the working gas is helium (Table 2.3).

Table 2.3 – Inlet parameters for the numerical simulations of a multi-stage KP

Parameter	P_i (kPa)	T_c (K)	$\Delta T = T_h - T_c$ (K)	N	n_c	Gas
Value	0.1 – 100	300	100	1 – 1000	1 – 10	helium

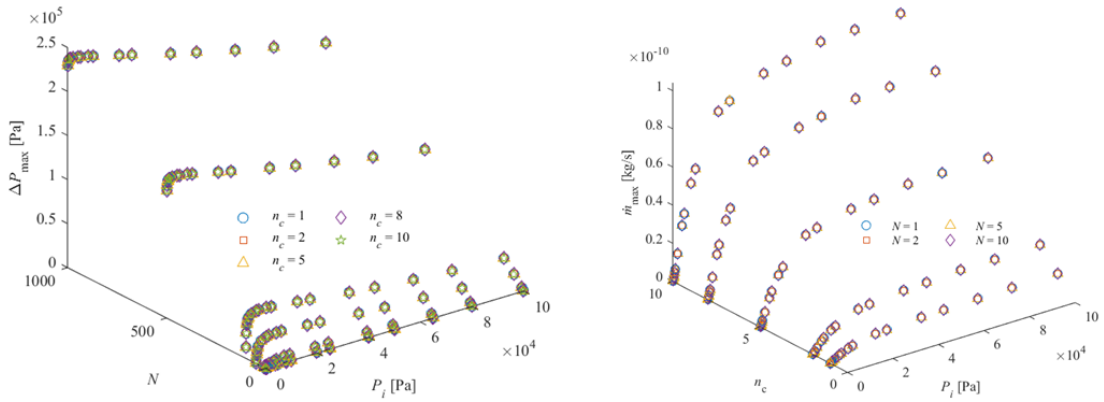

(a) (b)

Figure 2.17 – Influence of $1 \leq n_c \leq 10$ and $1 \leq N \leq 1000$ on a) ΔP_{max} and b) $\dot{m}_{max}$ for a multistage KP.

It can be readily seen that, as expected, an increase of N results in an increase of ΔP_{max} but has no influence on $\dot{m}_{max}$ (as in this case the pressure difference is zero for each stage and each stage has exactly the same behavior and provides the same mass flowrate). In contrast, the increase of n_c results in the increase of $\dot{m}_{max}$ but has no influence on ΔP_{max}. Thus, in order to simplify the problem analysis and reduce the calculation time, we can limit the simulations to $n_c = 1$ for investigating the performance of a N-stage KP in terms of ΔP_{max}, and to $N = 1$ for the performance in terms of $\dot{m}_{max}$. These two cases are illustrated in Fig. 2.18. The

first figure (Fig. 2.18a) provides $\Delta P_{\max}$ vs P_i for various values of N between 1 and 1000. The maximum pressure can be highly increased by increasing the number of stages and the peak value corresponds to an inlet pressure that decreases as N increases (Fig. 2.18c).

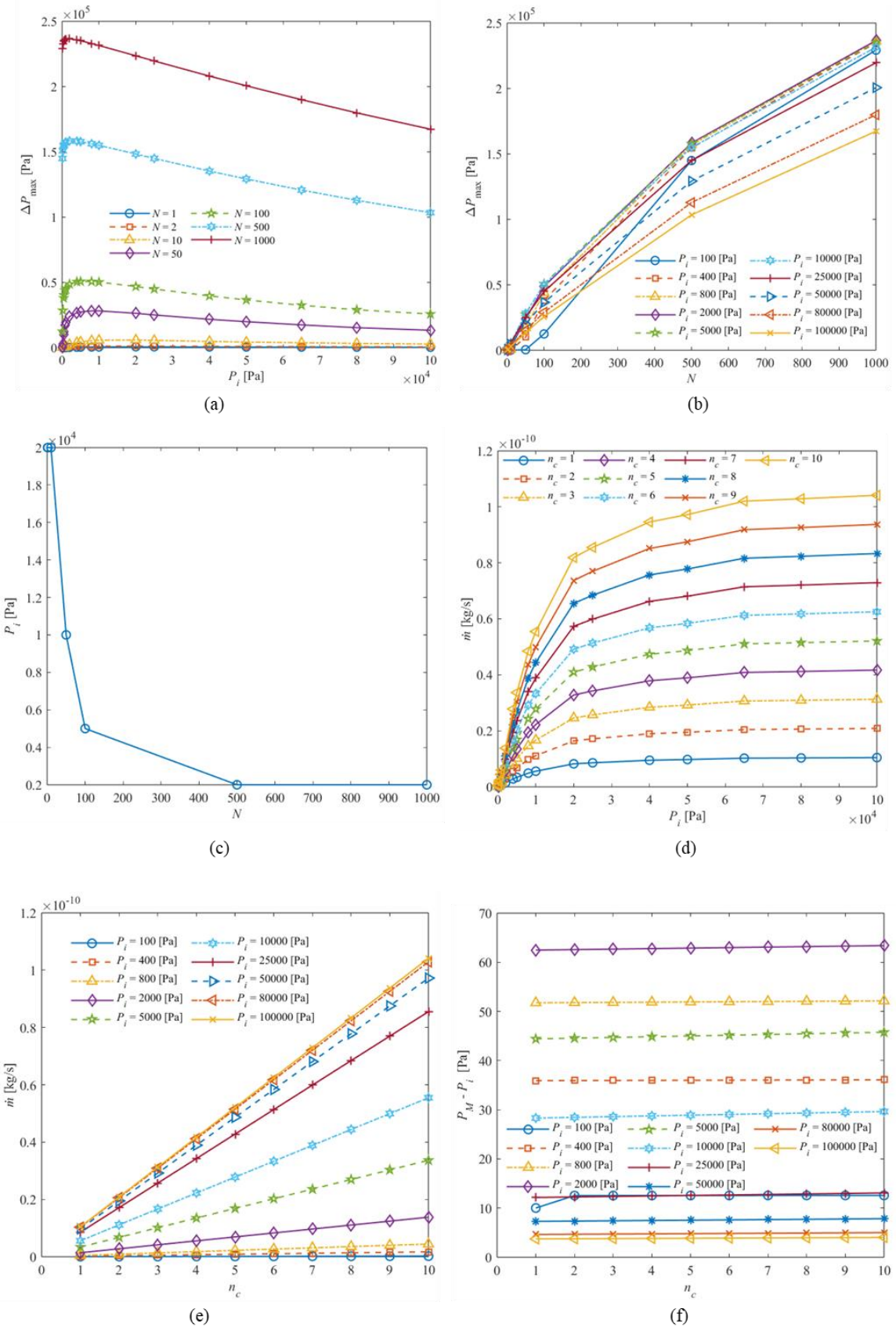

Figure 2.18 – Influence of $1 \le N \le 1000$ for $n_c = 1$ on ΔP_{max} : a) ΔP_{max} vs P_i ; b) ΔP_{max} vs N and c) P_i vs N at the peak value of ΔP_{max} . Influence of $1 \le n_c \le 10$ for $N = 1$ on $\dot{m}_{max}$: d) $\dot{m}_{max}$ vs P_i ; e) $\dot{m}_{max}$ vs n_c and f) $P_M - P_i$ vs n_c .

According to the inlet pressure, the way ΔP_{max} increases with N can be different, as illustrated by Fig. 2.18b, with an inflexion point clearly visible for $P_i = 100$ Pa. The maximum mass flowrate is proportional to the number of parallel microchannels (Fig. 2.18e) and increases with P_i up to an asymptotic value, visible in both Figs. 2.18d and 2.18e. The increase of n_c can a priori affect the counter flow in the macrochannel (as the flow rate increases in this channel) and have a consequence on the value of the intermediate pressure P_M but as can be seen in Fig. 2.18f, this effect is quite negligible.

From the above results, it is clear that increasing simultaneously N and n_c significantly improve the performance of a multistage KP. Therefore, for controlling some actuators such as artificial micro-muscles, increasing the mass flowrate will reduce the response time, and increasing the pressure difference will allow larger contraction ratios.

As an illustration, the characteristic curves of a specific multistage KP (r = 5 µm, R = 25 µm, $L_1 = L_2$ = 500 µm, ΔT = 100 K, P_i = 10 kPa) with a number of stages between 1 and 1000 and a number of parallel microchannels per stage between 1 and 10 are shown in Fig. 2.19. The results show that for the lowest values of N (1 and 5), ΔP is inversely proportional to $\dot{m}$. When N increases, this linear relationship gradually decreases, and for the highest values of N (500 and 100), $\dot{m}$ starts increasing as ΔP decreases but reach its maximum value for a value of ΔP that increases with N. As explained previously, the maximum value $\dot{m}_{max}$ of $\dot{m}$ does not depend on the number of stages.

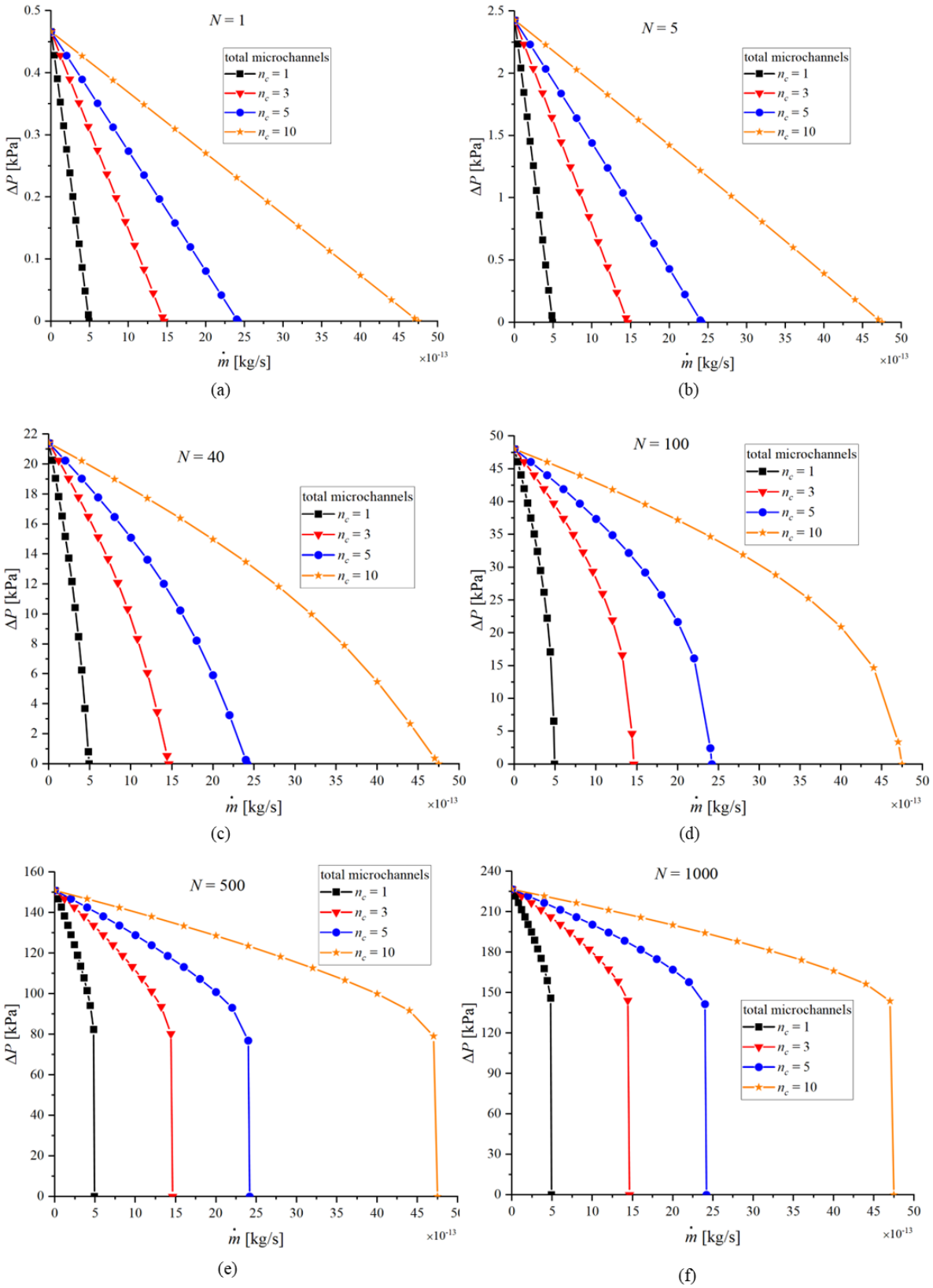

Figure 2.19 – Characteristic curves of a specific multistage KP, for which $r = 5\,\mu\text{m}$, $R = 25\,\mu\text{m}$, $L_1 = L_2 = 500\,\mu\text{m}$, $\Delta T = 100\,\text{K}$, $P_i = 10\,\text{kPa}$. Influence of the number of stages and number of parallel microchannels per stage.

2.5 Towards Knudsen pumps with microchannels of non-uniform cross-sections

As the fabrication techniques have rapidly progressed in the past years, it is now conceivable to design KPs with microchannels having non-uniform cross-sections (see Chapter 3) that could improve the performance of the KP's stages due to a diodic effect in such microchannels [77] For this reason, tapered microchannels have been fabricated and tested (Chapter 3), first with pressure-driven rarefied flows. The isothermal models used for the analysis of the experimental data are provided in the present section.

2.5.1 Isothermal gas flow in microchannels with uniform circular cross section

The simplest microchannel for isothermal pressure-driven flow is a straight circular channel with uniform cross section of radius $r = d/2$. Considering a simple case in which the two ends of the microchannel are connected to two big tanks with two different pressures and the same temperature, the gas flows from the high-pressure side to the low-pressure side through the microchannel (Fig. 2.20).

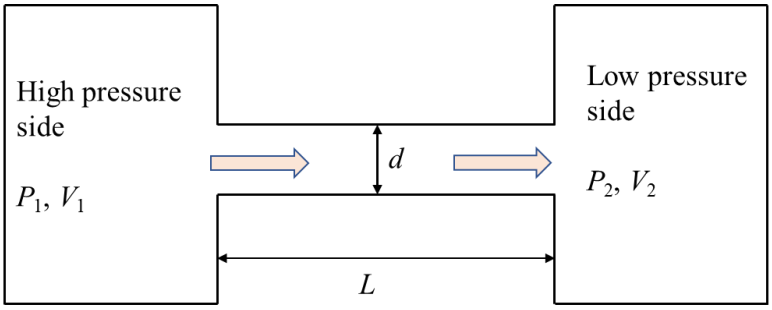

Figure 2.20 – Diagram of the system used for measuring and simulating the isothermal pressure-driven flowrate through a microchannel with uniform circular cross section.

The gas is dilute and respects the ideal gas law and the mass conservation law, and considering a long tube of diameter d ($d \ll L$), Eq. (2.24) reduces to

$$\frac{dP}{dz} = -\frac{v}{\pi r^3 G_{P(\delta,z)}} \dot{m} \tag{2.25}$$

as the most probable molecular velocity v is constant when the temperature is constant, and can be integrated as

$$\dot{m} = G_{P(\delta_m)} \frac{\pi d^3 \left(P_1 - P_2\right)}{8 \nu L} \tag{2.26}$$

where the dimensionless mass flowrate $G_{P(\delta_m)}$ can be expressed by [111] in the case of complete (diffuse) accommodation of the molecules at the wall:

$$G_{P(\delta_m)} = \frac{8}{3\sqrt{\pi}} \frac{1 + 0.025\delta_m^{0.7} \ln\left(\frac{\delta_m}{2}\right)}{1 + 0.448\delta_m^{0.8}} + \left(\frac{\delta_m}{8} + 1.018\right) \frac{\delta_m}{2 + \delta_m} \tag{2.27}$$

This parameter is only a function of the mean rarefaction parameter

$$\delta_m = \frac{P_m D}{\mu v} \tag{2.28}$$

where $P_m = \frac{P_1 + P_2}{2}$ is the average pressure of the tanks and the dynamic viscosity μ is constant in an isothermal gas flow.

The transient behavior of the gas flow considered as a succession of quasi-steady states is characterized by the pressure variation in both tanks or by the mass flowrate variation with time. By application of the ideal gas law, along with the constant volume technique [112], the mass flowrate entering each tank can be correlated to the pressure variation with time, thus for an isothermal gas flow:

$$\dot{m}_i = \frac{V_i}{R_g T} \left(\frac{dP_i}{dt}\right) \tag{2.29}$$

where i = 1, 2 is the index denoting the tank, V_i is the tank volume and dt will be considered as a time step. The flowrate leaving Tank 1 is equal to the flowrate entering Tank 2, so that $-\dot{m}_1 = \dot{m}_2 = \dot{m}$. Thus, the pressure variation dP_i at each time step dt is:

$$dP_i = \frac{R_g T}{V_i} \dot{m}_i \, dt \tag{2.30}$$

and one can deduce the pressures in the tanks at each time from:

$$P_i^{j+1} = P_i^j + dP_i^j \tag{2.31}$$

Here, superscript j denotes the time $j\,dt$. The isothermal gas flowrate can be numerically calculated until the final equilibrium state is reached, according to the flowchart shown in Fig. 2.21.

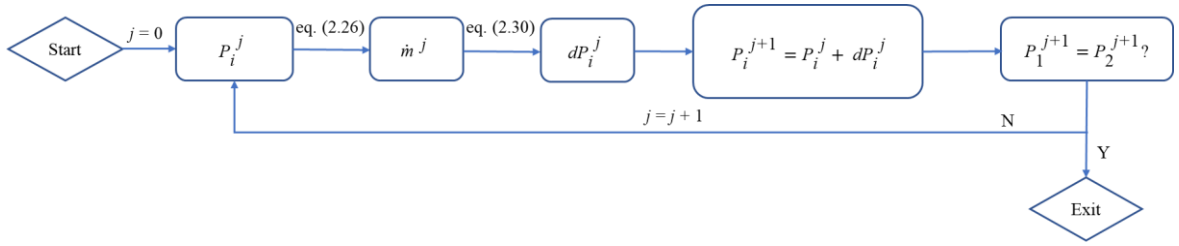

Figure 2.21 – Flowchart of the calculation procedure for transient behavior of an isothermal gas flow.

The isothermal gas microflows in this kind of microchannels are numerically simulated by requiring only the pressures in both tanks without requiring the pressure distribution along the channel. Experimentally, it is then easy to compare the pressure evolutions in both tanks to compare them with the theoretical expectations and discuss the limits of the model (that assumes $d \ll L$) and/or the exact internal geometry of the channel that can differ from the expected one before manufacturing.

2.5.2 Isothermal gas modeling flows in tapered microchannels

Tapered channels (Fig. 2.22) were developed for either thermal transpiration flows [62,77] or isothermal pressure-driven flows [113,114]. Previous works have demonstrated that the predicted mass flowrate through a tapered channel was higher in the converging direction rather than in the diverging one, for the same pressure difference imposed, under moderate rarefaction conditions. This is the so-called gas flow diode effect, affected by the angle of the tapered channel, the properties of the gas, the flowrate and the rarefaction degree [114].

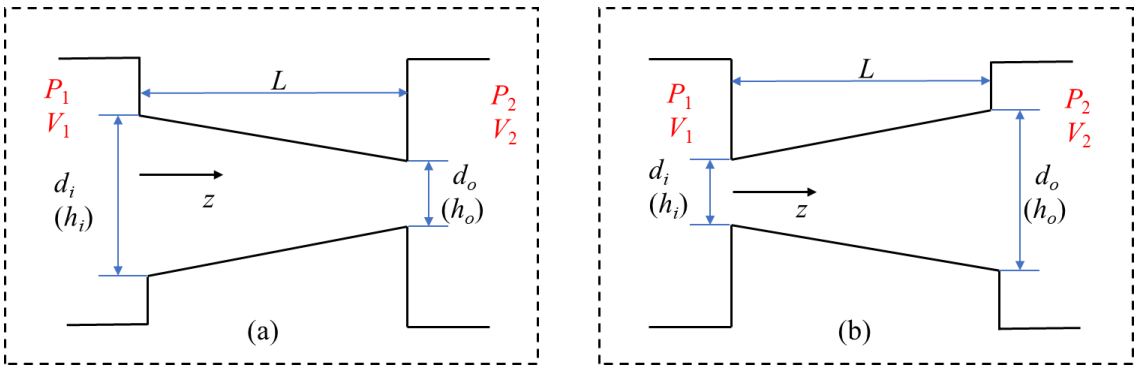

Figure 2.22 – Design of a tapered microchannel. a) Converging and b) diverging configurations.

In this work, two different tapered channels, the first one with a circular cross section (Fig. 2.23a), and the second one with a square cross section (Fig. 2.23b), have been designed and fabricated, in order to explore the diode effect. In this section, the numerical method using the kinetic model introduced in Section 2.2.3 is described for both geometrical configurations.

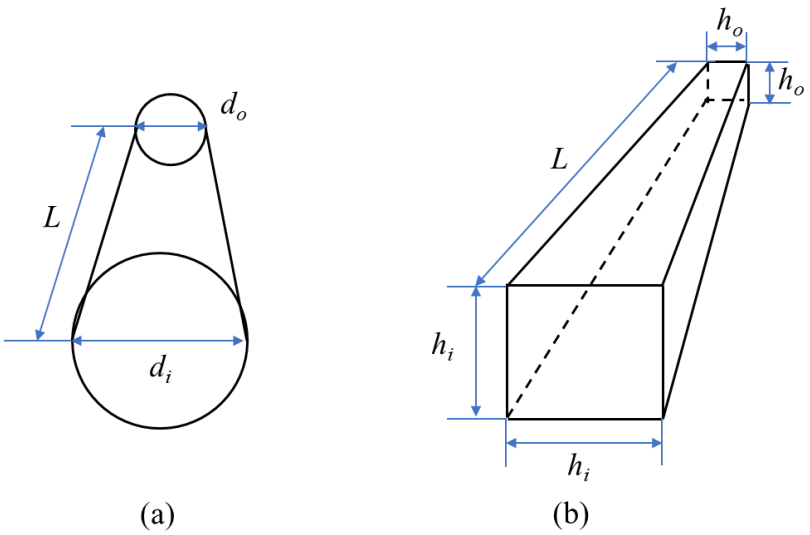

Figure 2.23 – Geometrical parameters of tapered microchannel with a) circular cross section, and b) square cross section.

Microchannel with circular cross section

For tapered channel with circular cross section, the diameter in each section varies linearly along the *z*-axis from inlet to outlet, resulting in different rarefaction parameters $\delta_{(z)}$ in each local cross section, and accordingly to different dimensionless mass flowrate $G_{P(\delta_{(z)})}$. Thus, contrarily to the constant cross section case, it is necessary to calculate the pressure distribution along the channel to compute the mass flowrate through the channel. For each section Eq. (2.25) reads:

$$\frac{dP}{dz} = -\frac{8\sqrt{2R_gT}}{\pi d^3_{(z)} G_{P(\delta_{(z)})}}\dot{m} \tag{2.32}$$

Microchannel with square cross section

For a tapered channel with a rectangular cross section, the dimensionless mass flowrate G_P is not only determined by a local characteristic length, but also by the local aspect ratio [1]. For example, in one cross section with local width $w_{(z)}$ and height $h_{(z)}$, the characteristic length can be defined by the smallest of these two parameters, $L_{C(z)} = \min(w_{(z)}, h_{(z)})$, and its local aspect ratio defined as $\beta_{(z)} = \dfrac{\min(w_{(z)}, h_{(z)})}{\max(w_{(z)}, h_{(z)})}$. Therefore, the pressure distribution and the mass flowrate can be calculated from:

$$\frac{dP}{dz} = -\frac{v_{(z)}}{w_{(z)} h_{(z)} L_{C(z)} G_{P(\delta_{(z)},\beta_{(z)})}} \dot{m} \tag{2.33}$$

In the specific case of a square cross section for which the aspect ratio $\beta_{(z)}$ is always equal to 1, this equation is simplified as:

$$\frac{dP}{dz} = -\frac{v_{(z)}}{h^3_{(z)} G_{P(\delta_{(z)})}} \dot{m} \tag{2.34}$$

For both tapered channels with circular or square cross sections, the dimensionless flowrate G_P is obtained through the linearized Shakhov model for purely diffuse boundary conditions [98,103,106]. Equations (2.32) and (2.34) are treated in the same way as described in Fig. 2.6 considering the problem of each time step as an open configuration (the inlet and outlet pressure are fixed during *dt*). For investigating the transient gas flows in the tapered channels, the method developed in Section 2.3 is still applicable.

The results for the 3 microchannels (with constant and linearly varying cross sections) will be compared in Chapter 3 with experimental measurements.

2.6 Summary

In this chapter, the basis of the theory of rarefied gas flows has been presented. In the present work, the VHS collision model has been chosen for the numerical simulations. The linearized Shakhov kinetic model and a purely diffuse condition were used for simulating both steady and transient gas flows induced by differences of temperature and pressure in microchannels.

For analyzing thermal transpiration flows in KPs, three different flow scenarios were considered: i) an open system in which the pressure difference $\Delta P = 0$ and the mass flowrate $\dot{m} = \dot{m}_{\max}$ is maximal, ii) a closed system in which the pressure difference $\Delta P = \Delta P_{\max}$ is maximal, and the mass flowrate $\dot{m} = 0$, and iii) a general system in which the pressure difference ΔP and the mass flowrate $\dot{m}$ are both different from zero. Later, a multistage KP consisting in several parallel microchannels connected to one macrochannel at each stage was numerically simulated for characterizing the performance as a function of various parameters. The analysis showed that the pressure difference is influenced by the number of stages and not by the number of microchannels, and that the mass flowrate is affected by the number of the microchannels rather than by the number of the stages. This gives an initial guidance for optimization of KPs by playing simultaneously on the number of microchannels and stages.

Additionally, three different straight microchannels with uniform circular cross section,

and linearly varying circular or square cross sections have been considered, first for isothermal pressure-driven flows. The mass flowrate and the pressure distributions along the wall of the two tapered channels have been computed. The numerical method for steady state or transient flows considered as a succession of quasi-steady states has been developed and will be used in the next chapter to analyze specific microchannels obtained from different manufacturing techniques.

Chapter 3 - Manufacturing and test of microchannels

Introduction

Microchannels with uniform and non-uniform cross sections, that could be used as unit elements of Knudsen micropumps, have been presented in Chapter 2 with the numerical associated models for both temperature and pressure driven flows. Experimental measurements of gas microflows in these microchannels are necessary to check the accuracy of the models, the capability of microfabrication techniques to generate microchannels with the desired dimensions and the robustness and tightness of the samples in various low pressures conditions.

In this chapter, we present different kinds of samples fabricated by using two manufacturing methods through a collaboration with two different groups. The first method is based on maskless ultraviolet (UV) light lithography of dry film (DF) photoresist layers on poly (methyl methacrylate) (PMMA) substrate. It was implemented in the framework of a collaboration with the Laboratoire de Physique et Chimie des Nano-Objets (LPCNO) in Toulouse, and several microchannel samples with rectangular cross-sections were manufactured. The second method is the two-photon-polymerization (TPP) fabrication technique realized in the Karlsruhe Nano Micro Facility (KNMFi) laboratory in Germany. With this technique, four different microchannels with uniform circular cross sections were successfully manufactured, as well as two tapered microchannels with circular and square cross sections.

All the manufactured samples have been submitted to pressure-driven isothermal flows with various rarefaction conditions. The experimental measurements were performed with a constant volume technique able to obtain the mass flowrate through the microchannel, thanks to the pressure variation with time measured inside reservoirs connected at both ends of the microchannel. Finally, the experimental results were compared to the numerical results obtained via the kinetic theory of gases (Chapter 2). The two fabrication processes, the experimental setup, the experimental data and their comparison with numerical simulations are presented in Sections 3.1, 3.2, 3.3 and 3.4.

Additionally, temperature-driven flows were also tested in micro glass tubes. The results are presented in Section 3.5.

3.1 Manufacturing based on photolithography of DF layers

This fabrication method was chosen for its advantages including simplicity, speed, good bonding and low thermal conductivity of involved materials. However, it requires certain standards and detailed procedures to achieve the desired resolution. This manufacturing process can be used for manufacturing microchannels along the surface of a surface, as well as through the film thickness by maskless UV light lithography. Following extensive efforts, certain guidelines have been provided to improve the standard procedures at LPCNO in order to achieve a perfect lamination, expected resolutions and strong bonding power. The manufacturing of the rectangular channel samples in a DF layer has been accomplished and preliminary experimental work has been performed. Also, with the improvements of the manufacturing process performed and the new guidelines provided, it is strongly believed that some other prototypes should be completed soon in the short future.

3.1.1 Introduction to the photolithography technique

The maskless photolithography process is mainly performed by exposing the DF photoresist to UV. The pattern is transferred to a PC connected to SMART PRINT^{UV} machine (Fig. 3.1) and controlling a digital micromirror device (DMD). UV light is projected onto the DMD, which reproduces the pattern by orienting micro-mirrors (each one corresponding to a pixel) in order to transmit the light on the surface of the DF or to an absorbent surface whether the pixel has to be reflected or not.

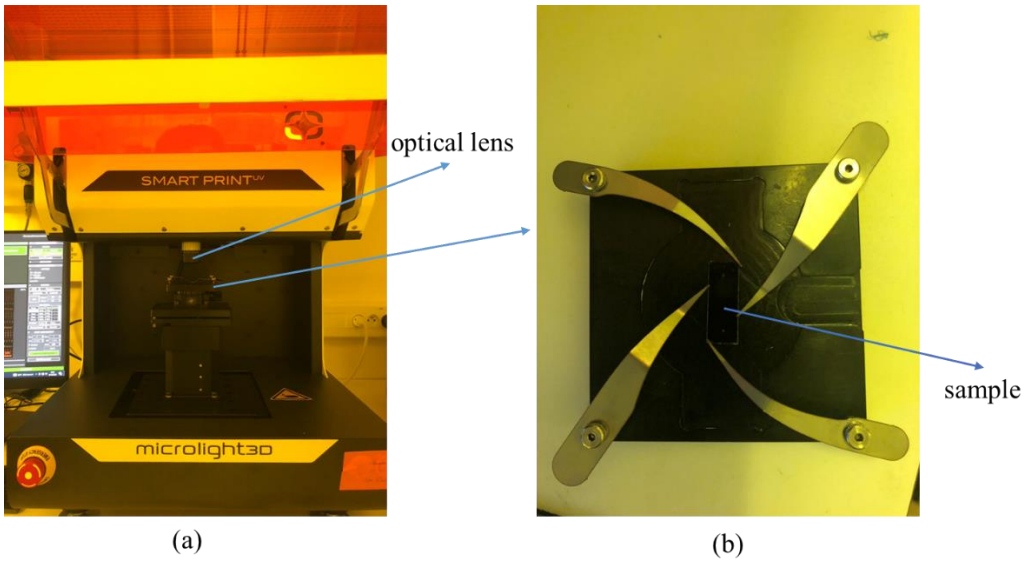

Figure 3.1 – a) Smart print machine for lithography, and b) Support to hold the sample.

The UV light passes then through an optical lens to reach the DF surface. The insolation causes a chemical reaction on the photoresist material (DF layer in this work) that either makes it more or less soluble to certain solvents corresponding to positive and negative photoresists respectively (Fig. 3.2). The solvent used for developing the pattern in the DF layer, as well as the particular wavelength required for the activation of the photosensitive reaction, depend on each particular photoresist material [115].

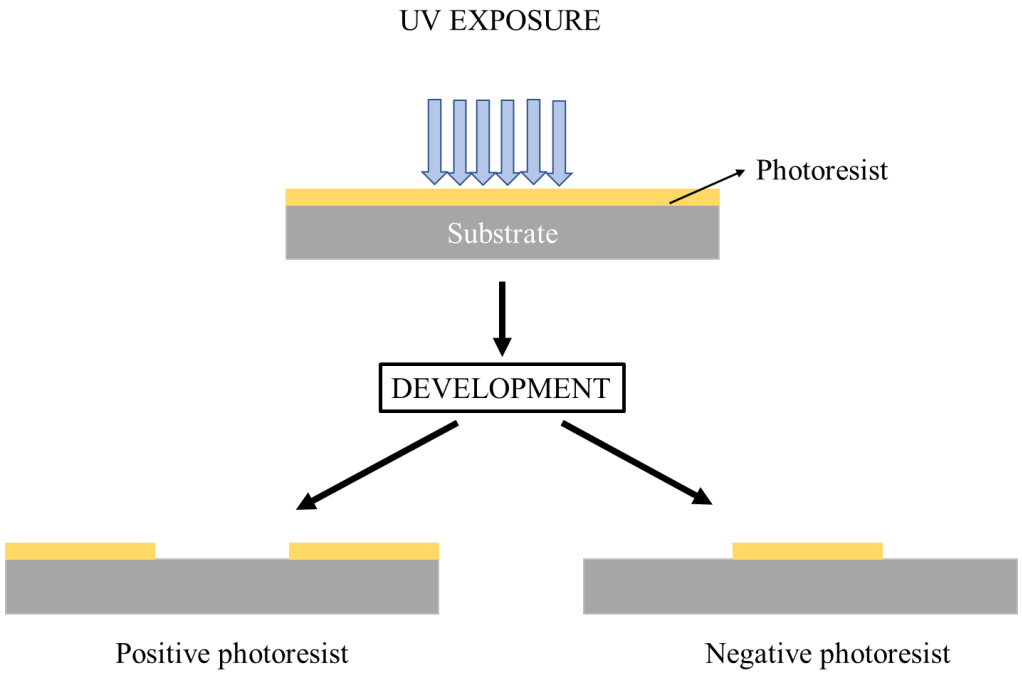

Figure 3.2 – Illustration of the maskless photolithography process with either positive or negative photoresists.

In the present work, a negative photoresist was chosen for the fabrication of samples. It is a low-cost material that can be used as DF layer laminated on a substrate with a specific pressure and temperature, and combined with standard photolithography procedures. The DF layer is laminated on a PMMA substrate previously prepared with two drilled orifices. It is then exposed to UV light to create the designed microchannel by removing on the desired zone all the thickness of the DF layer. Another DF layer is also laminated on a PMMA substrate without any orifice, and finally, these two DF layers are bonded together via plasma activation for closing the microchannel. A scheme of the designed sample fabricated with this simple technique is showed in Fig. 3.3. The two orifices drilled in the top substrate will be connected to high and low-pressure sides, respectively, in order to generate an isothermal pressure-driven gas flow inside the microchannel.

Concerning the substrate on which the DF photoresists are laminated, PMMA was chosen due to its high strength, high transparency, low price, easy machining and other advantages: the PMMA will be kept intact following the application of quite high pressure and temperature during lamination in order to provide an excellent adhesion between substrate and DF layer. In addition, for the experimental measurements, the sample will be installed into a casing able to press the sample with a high pressure to prevent leakages and the mechanical resistance of PMMA to compression is welcome. Thus, PMMA is a suitable choice both for the manufacturing process and experimental measurements.

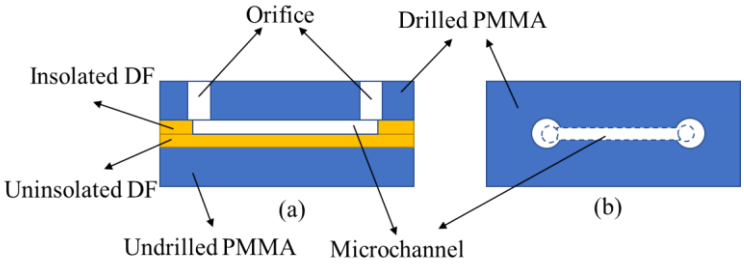

Figure 3.3 – Scheme of a sample manufactured by photolithography technique.
a) Sectional view of the sample; b) Top view of the sample.

From the above figure, we can see that the height of the microchannel is the nominal thickness of the DF. The manufacturing of the proposed structure was performed after several tries. The fabrication process can be mainly summarized as follows: i) lamination of the uninsolated DF photoresist layer onto a planar PMMA substrate; ii) following standard maskless photolithography procedures, the DF layer is exposed to UV light, polymerizing the monomers composing the photoresist (insolated DF); iii) the DF layer is developed in a bath of solvent (sodium carbonate) for removing the material of the non-exposed areas during the photolithography process (the DF layer is a negative photoresist). This process is repeated for each sample, enabling the production of different patterns. Here, two different DF layers (E9200 and Ordyl 355 DFs) were used for manufacturing samples with this fabrication method. The detailed manufacturing process is presented in the following section, including the preparation of the drilled PMMA substrate.

3.1.2 Standard process of manufacturing for different materials of DF

The parameters for each step of the standard process developed at LPCNO depend on the thickness of the DF layers, since the photolithographic process to polymerize the DF and etch the patterns strongly depends on this parameter. According to the thickness, different expo-

sure doses, baking times and development baths are required [116]. For the present work, the thickness of the DF photoresists is 50 µm; thus, through several trials, the specific parameters for this value of thickness were fixed in order to get a good adhesion, a perfect lithography and a correct development of the microchannels. The description of the manufacturing process is detailed below.

1. **Preparation of the drilled PMMA substrate**: the PMMA substrate was micro-drilled with two orifices, 800 µm in diameter, with a distance between both centers of 18 mm. Then, the drilled substrate (top substrate) was cleaned with ethanol then water, and it was dried with a nitrogen blower. Then, the PMMA substrate was put on a hot plate at 65 °C for 5 min for a quick dehydration, and finally, the PMMA substrate was spin-coated with Ti Prime from MicroChemicals, which is a titanium based adhesive promotor, at a speed of 2000 rpm during 30 s for increasing the adhesion with the DF layer.
2. **Lamination**: the equipment used for this step is a Fortex Laminator (Fig. 3.4). For the lamination of the DF layer on the PMMA substrate, a roll speed of 1 cm/s and a temperature of 100 ºC were fixed in order to avoid the collapsing of DF and to obtain a complete adhesion of DF without any wrinkle.

(a) (b)

Figure 3.4 – Lamination of a DF layer onto a PMMA substrate.
a) Before lamination; b) After lamination.

3. **Exposure**: the photolithography process has been performed with a SMART PRINT^{UV} machine (Fig. 3.1). The DF layer was insolated following the pattern shown in Fig. 3.3b with an exposure time of 1 s and a UV light power of 15 %. The smallest achievable resolution is 1.5 µm (Fig. 3.5a) and the 385 nm wavelength of UV light of the machine

is suitable for both E9200 and Ordyl 355 DF layers.

4. **Development**: the DF was developed in a bath of solvent (aqueous solution of sodium carbonate at 0.85 % mass concentration) with the use of a pipette for 10 to 15 min, until a good development of the microchannel was obtained by optical observations, and it was rinsed with distilled water to clean the solvent. Then, the optical profilometer measured the height of the channel, with a 50 µm theoretical value of thickness of DF layer.

Figure 3.5 – Plasma activation of DF layers for bonding. Following the plasma treatment, the surface of the material is rich in polar molecules. UV radiation and active oxygen species generated by the plasma disintegrate separating agents, silicones, and oils on the surface. The vacuum system efficiently removes these byproducts. Concurrently, the active oxygen species, or radicals, in the plasma, adhere to active surface sites across the material, resulting in a highly receptive surface for bonding agents.

5. **Preparation of bottom substrate**: the bottom PMMA substrate was used for sealing the sample with the top substrate. The treatment of this substrate was therefore the same as for the drilled one.
6. **Lamination between DF layer without channel and bottom substrate**: it was done with the same process as for previous lamination (step 2). Some of the bottom layers were completely exposed during 30 s under a 365 nm UV light, whereas others were not. It was also observed that there was a better sealing when the bottom layers were not insolated before the sealing.
7. **Bonding of two pieces**: after finishing the steps described above, the two DF layers were exposed to plasma during several minutes for activation in order to increase bonding power (Fig. 3.5). The top piece was put above the bottom piece, and the sandwich was left for several hours under compression.

8. **Sealing**: The full sandwich was then insolated during 30 s under a 365 nm UV light to improve the sealing.

The manufacturing process proved to be quite fast and straightforward. Following the standard procedures at LPCNO, within a couple of days, six samples with two DF layers were completed with straight rectangular channels fabricated in a 50 µm thickness DF layer with the inlet and outlet. This clearly demonstrates the potential of this low-cost technique for rapid manufacturing.

3.1.3 Samples obtained by DF lamination and photolithography technique

Six samples with two different DF layers (E9200 and Ordyl 355, showed in left and right sides of Fig. 3.6, respectively) were successfully manufactured. The rectangular microchannels were ended with two small cylinders in the top DF layers, that were aligned with the two orifices of the top PMMA substrate.

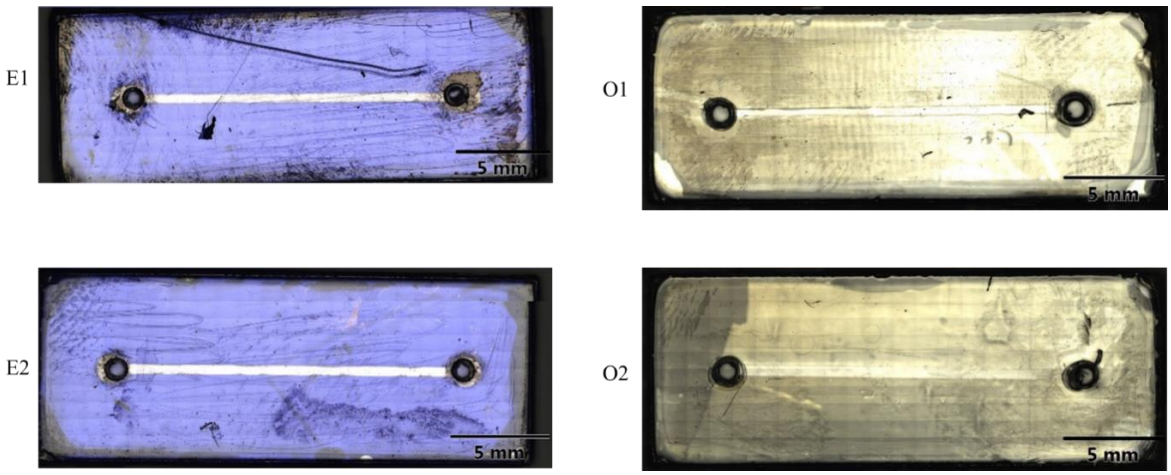

Figure 3.6 – Samples successfully manufactured via maskless UV light lithography technique. Left: E9200 DF; Right: Ordyl 355 DF.

The samples' dimensions, including the diameters of two orifices drilled in the substrate, the length and the width of the rectangular microchannel, were measured by a digital microscope with a dispersion along the channel of ± 5 µm. The resolution of the digital microscope was 0.01 µm. These dimensions are reported in Table 3.1. In this table, *L*, *H* and *W* represent the length, height and width of the channel, respectively.

In addition, the real structures of two orifices and the microchannel of each sample before any gas flow measurements were also visualized by microscope, shown in Fig. 3.7.

Table 3.1 – Dimensions measured by digital microscope of each sample.
The height given by the provider is 50 µm.

sample	microchannel			diameters of orifices in PMMA (µm)	
	L (µm)	*H* (µm)	*W* (µm)	left	right
E1	15715.14 ± 5	49.67	470.16 ± 3.5	691.57 ± 5	792.44 ± 5
E2	16403.77 ± 3	50.12	470.60 ± 3	762.79 ± 4	704.43 ± 4
O1	16096.12 ± 4	44.75	494.11 ± 4	870.73 ± 5	1053.16 ± 5
O2	16106.70 ± 4	46.22	507.42 ± 5	857.81 ± 5	930.62 ± 5

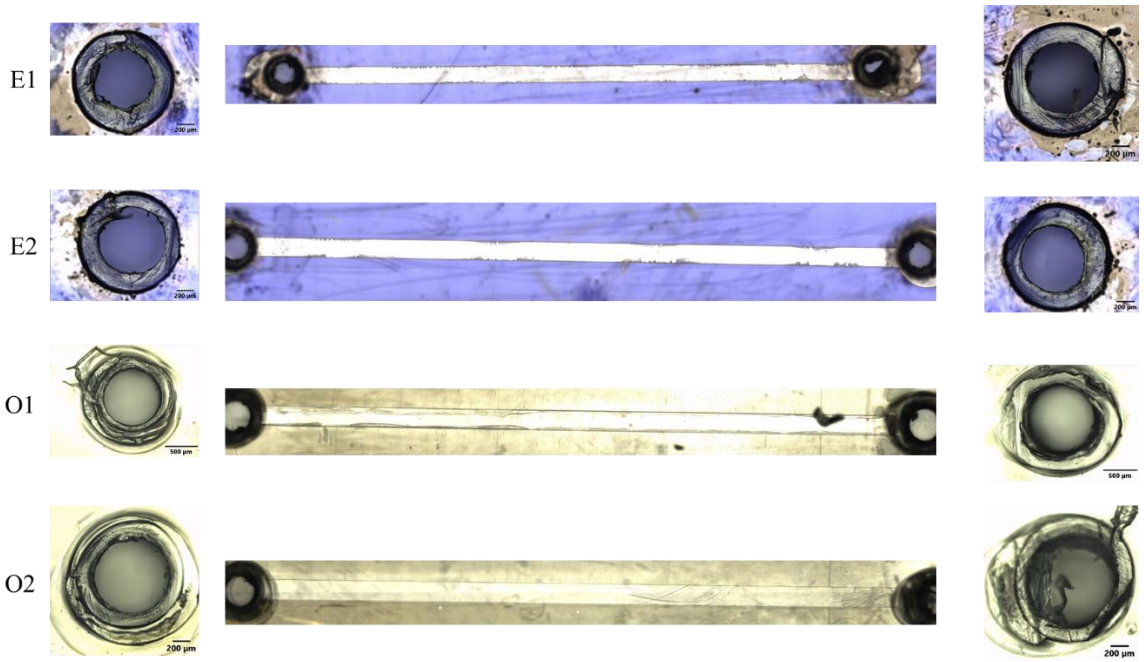

Figure 3.7 – Real structures of the DF-layer based microchannels observed by digital microscope, with details on the two orifices, before gas flow measurements.

It's evident that the microchannels have been developed effectively, and the orifices connected to the microchannels were correctly drilled in PMMA. However, some imperfections occurred during the manufacturing process. In sample E1, the left orifice wasn't a perfect circle, while the right orifice was circular, indicating some inaccuracies in the drilling process. This was confirmed with three other samples, especially in the case of the left orifice in sample O2. Additionally, in sample O1, there is residue on the top piece but not in the microchannel, primarily because of incomplete cleaning.

3.2 Experiments on isothermal pressure-driven flows through DF-layer based microchannels

The experimental measurements of isothermal pressure-driven flows through the different DF-layer based microchannels described in Section 3.1 were performed with a simple experimental setup. An existing setup has been slightly modified by changing different casings in order to allow the rapid and easy replacement of the channel samples. The volume of both high and low-pressure reservoirs were calculated for the different casing with and without connection of a small gas tank with a given volume. Also, the well-known constant volume technique [112] was applied to correlate the mass flowrate through the channel to the pressure variation with time in each reservoir, as described in Chapter 2. It should be mentioned that the experimental system needed to be vacuumed for several hours for avoiding leakage and outgassing, to make a highly pure single-phase gas flow inside the channel and to improve the accuracy of measurements. In addition, nitrogen was chosen for the working gas in all experiments.

3.2.1 Description on experimental setup

The main test section of the experimental setup was mainly composed of two tanks connected to the microchannel (Fig. 3.8).

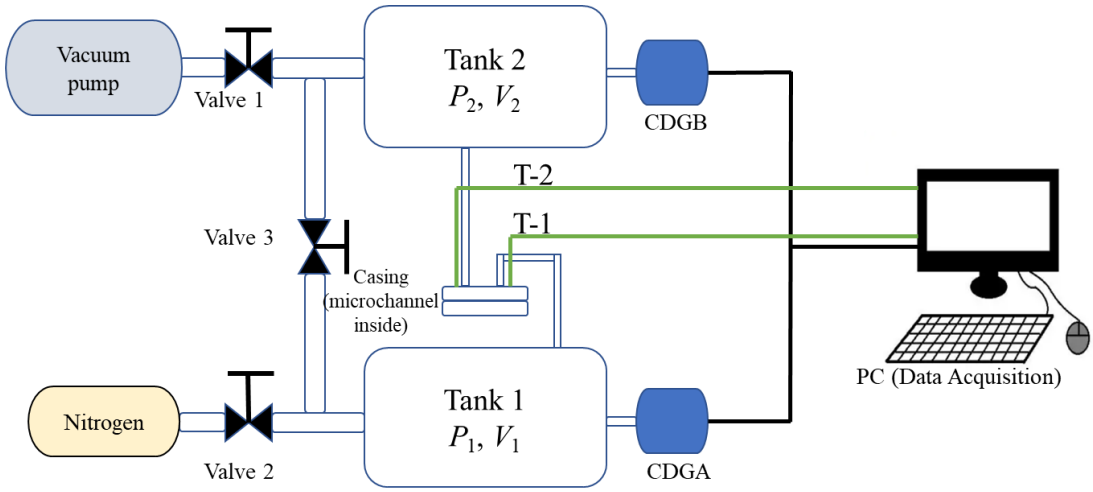

Figure 3.8 – Diagram of the experimental setup. Two tanks are separated by Valve 3 in order to generate a gas flow through the microchannel with an initial pressure difference between the two tanks. Thermocouples T-1 and T-2 are used for checking the temperature.

Thus, it is possible to generate a gas flow through the microchannel by imposing an initial pressure difference ($\Delta P = P_1 - P_2 > 0$) between the two tanks with Valves 1, 2 and 3 closed.

During time evolution, P_1 decreases and P_2 increases, until a final equilibrium state is reached with a constant and uniform pressure in the whole test section ($\Delta P = 0$), and a zero mass flowrate ($\dot{m} = 0$). The pressure variation with time was monitored by means of two independent absolute capacitance diaphragm gauges connected to Tank 1 (CDGA) and Tank 2 (CDGB). As a function of the nominal pressure in the tanks, sensors of four different full scales (FS), 133 330 Pa, 13 330 Pa, 1 330 Pa and 133.3 Pa, with a resolution 0.015 % of the full scale and a precision of 0.2 % of the reading, were used. The pressure in both tanks was regulated through Valves 1 and 2 and a vacuum pump.

3.2.2 Experimental procedure

The experimental procedure for the isothermal pressure driven flow consists in measuring the pressure variation with time in the two tanks and to correlate them to the mass flowrate through the microchannel. The procedure for each measurement of these isothermal pressure-driven flow experiments includes the following steps:

1. **Vacuuming the system**: at the beginning of the experiment, Valves 1, 2 and 3 are open. The vacuum pump is activated and the system is evacuated reaching pressures below 1 Pa. This vacuuming procedure is kept for a long time to avoid outgassing and completely empty the setup from any gas species. Also, vacuum-pumping and gas-filling are performed several times by closing Valve 1 and opening Valve 2 to fill the system with the single gas species of the experiment and to wash the inner surfaces of the setup from other gas species.
2. **Filling the system**: by having Valve 1 closed and Valves 2 and 3 open, the whole circuit of the experimental setup is filled with a particular gas species, nitrogen in this experiment. Once the desired pressure at which the experiment will take place is reached, the pressures measured by CDA and CDB are the same. Then, Valves 2 and 3 are closed.
3. **Generating the initial pressure difference**: following Step 2, the pressure in the whole system is uniform. By opening Valve 1 very slowly and keeping Valves 2 and 3 closed, the pressure in Tank 2 is decreased and the pressure in Tank 1 is kept constant. Once the desired initial pressure difference between the two tanks is reached, Valve 1 is closed.
4. **Recording the experiment**: the recording system is started 1 or 2 min after Step 3, in order to have a stable gas flow through the microchannel. During time, the pressure in Tanks 1 and 2 measured by CDGA and CDGB are getting closer, until the final equilibrium state.
5. **Leakage measurement**: once the final equilibrium state is reached in the system, the

pressure in the whole system starts to increase in a linear manner due to leakages, that cannot be completely neglected compared with the flowrate through the microchannel. This leakage has to be quantified to properly post-process the data acquired from the experiments. The pressure in Tanks 1 and 2 is measured during 30 min while Valve 3 is closed. The pressure increase in both tanks may be different due to the different volumes and the location of the leakages. Consequently, in data processing, the leakage corresponding to each side of the microchannel should be extracted to obtain more accurate gas flow experimental data.

3.2.3 Volume calculation

For the experiments, among the most important parameters are the volumes V_1 and V_2 of Tank 1 and Tank 2, respectively. These volumes include all connections up to the valves and the microchannel inlet or outlet. The volume measurements can be divided into two steps: in the first step, an isothermal pressure-driven gas flow through the microchannel from Tank 1 to Tank 2 is measured. Different initial pressures, P_1^0 and P_2^0, are set for the two tanks at the initial time $t = 0$, and at a random time t_1 during the experiment, the pressures P_1^1 and P_2^1 are measured in both tanks (Fig. 3.9a). Considering the ideal gas law and the mass conservation in isothermal conditions, the following equation can be deduced:

$$P_1^0 V_1 + P_2^0 V_2 = P_1^1 V_1 + P_2^1 V_2 \tag{3.1}$$

In the second step, another gas flow generated with the same method is also measured (Fig. 3.9b), after having connected to Tank 2 a reference tank with a known volume V_0. In this case, the initial inlet and outlet pressures are denoted by P_3^0 and P_4^0, respectively, and the pressures measured at time t_1 by P_3^1 and P_4^1. A second equation can then be written:

$$P_3^0 V_1 + P_4^0 (V_0 + V_2) = P_3^1 V_1 + P_4^1 (V_0 + V_2) \tag{3.2}$$

The volume V_0 = 302 ml of the reference tank is measured by comparing the weight of the empty tank with the weight of the tank filled by water. Then, with the combination of Eqs. (3.1) and (3.2), the volumes V_1 and V_2 can be calculated. In the present work, five experiments with different initial inlet pressures were carried out for each of the two steps.

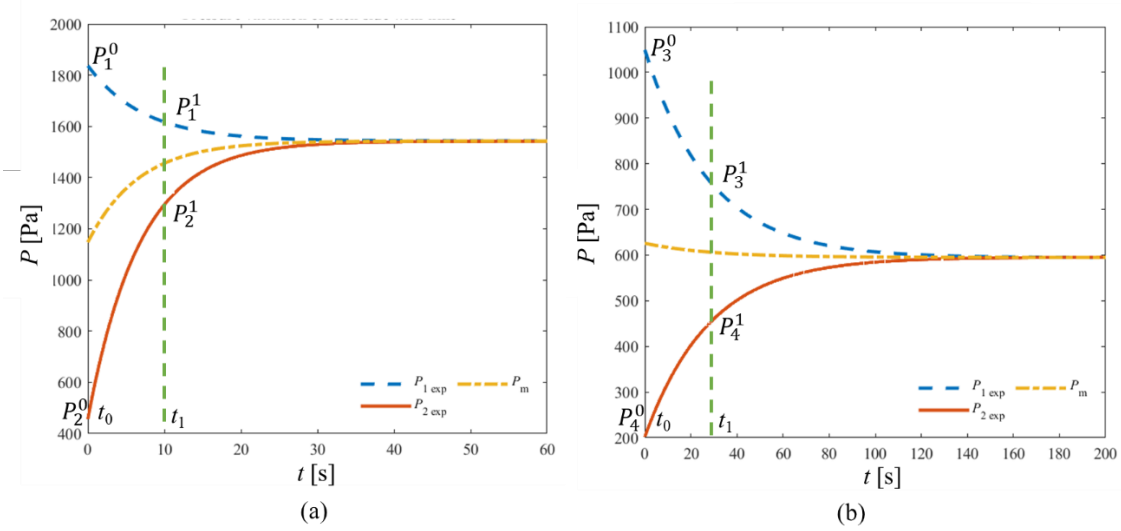

Figure 3.9 – Typical experiment carried out for the two steps required for the measurement of the tanks volumes. Inlet (blue dashed line) and outlet (red plain line) pressures vs time. The mean pressure value is also represented (orange dotted dashed line).

a) Only V_2 in the low-pressure side; b) (V_0 + V_2) in the low-pressure side.

3.2.4 Temperature measurement

The experiments are run in isothermal conditions, at the room temperature around 293 K. The two type K thermocouples are placed in the setup to provide the temperature measurements at the inlet connected to Tank 1 and at the outlet connected to Tank 2 (Fig. 3.8). They were calibrated by measuring the temperature on a heater at various temperature levels using a reference sensor. This calibration process established a linear relationship between the voltage and temperature. (Fig. 3.10).

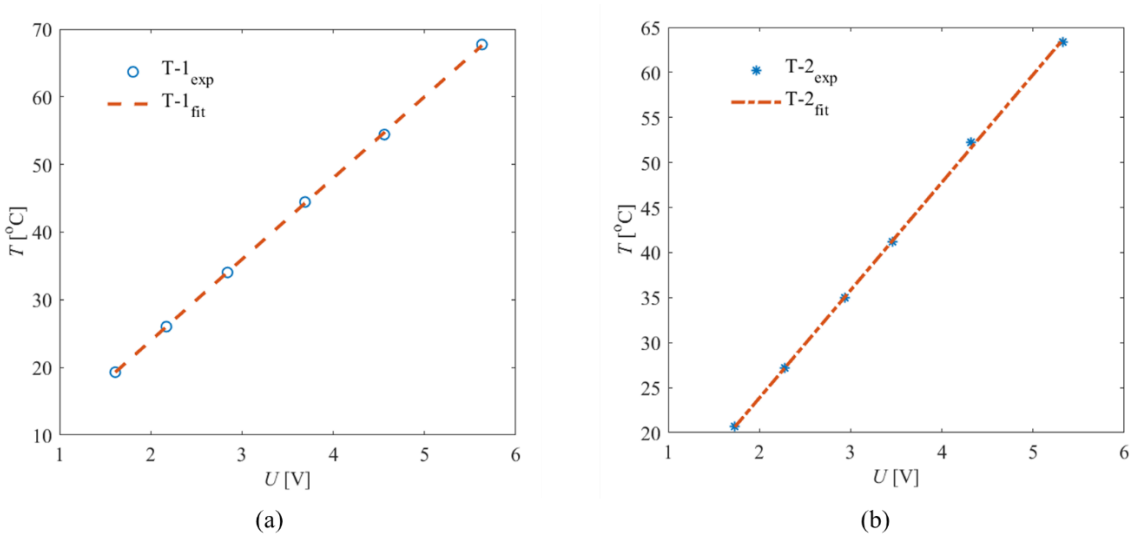

Figure 3.10 – Calibration of temperature sensors. Temperature vs tension. a) T-1, b) T-2.

Thus, these two linear fitting functions provide the temperature in °C for Tanks 1 (T_1) and 2 (T_2):

$$T_1 = 12.0118 \times U_1 - 0.0478 \text{ °C} \tag{3.3}$$

$$T_2 = 11.9599 \times U_2 - 0.0494 \text{ °C} \tag{3.4}$$

To validate the accuracy of the temperature measurements obtained from the two thermocouples after calibration, both T-1 and T-2 were utilized to measure the room temperature at the same location. The results are depicted in Fig. 3.11. It is evident that both sensors effectively capture the minor temperature fluctuations over the course of an hour. Their noise levels are similar, and the disparity between the mean values (after noise reduction) provided by both sensors is on the order of 0.1 K.

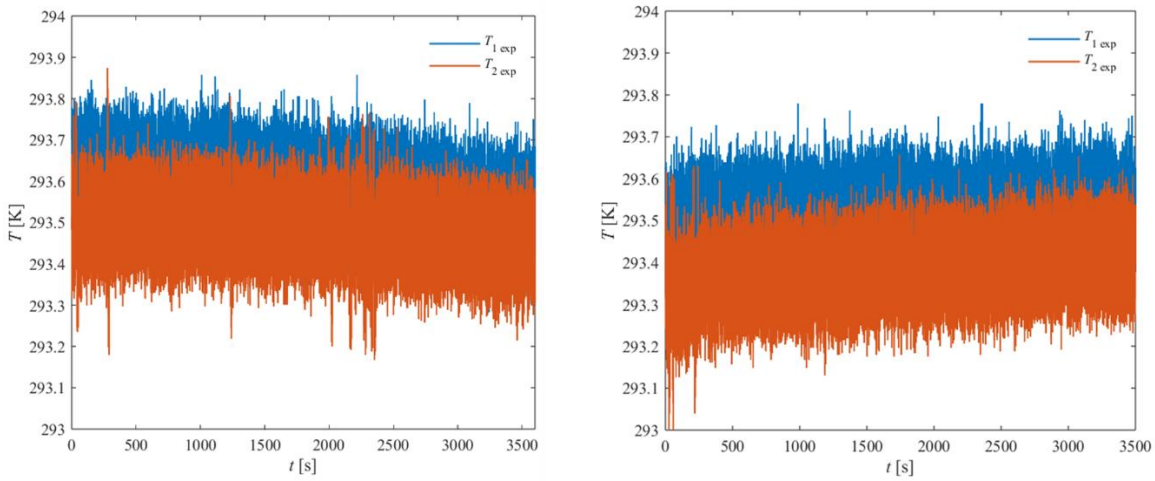

Figure 3.11 – Temperature measurements for two different experiments.

The whole system being at room temperature, it is assumed that the air convection has no influence on the temperature within the setup.

3.2.5 Results and discussion

Since the mass flowrate of gas microflows is typically very small, attention should be paid to accurately extract this small value. As mentioned in Chapter 2, the constant volume technique allows to correlate the mass flowrate through the microchannel to the pressure variation with time in the two tanks with Eq. (2.29). As the methodology is intrinsically correlated to an unsteady evolution with time of the mass flowrate, it is assumed that the evolution is a succession of quasi-steady states, each one corresponding to a short time interval [117,118].

In order to verify the precision of the manufacturing technique, the experimental results in terms of pressure vs time, mass flowrate vs time and conductance of the microchannel were compared with numerical data obtained via the kinetic theory of gases. The main parameter used to calculate these numerical data was the dimensionless mass flowrate G_P inside a long tube. For a long tube, the dimensionless mass flowrate depends solely on the mean rarefaction parameter of the flow. The G_P databases obtained via different kinetic models are reported in several publications [98,103,106,110] for different channels with uniform and non-uniform cross sections.

Only sample E2 was subjected to tests involving isothermal pressure-driven flows, as the other samples unfortunately suffered damage after being subjected to extended periods of vacuuming. The casing for holding the sample and the inner structure of the casing are showed in Fig. 3.12. In this test, the calculated volumes were V_1 = 145.1 ml and V_2 = 84.01 ml, and the same initial pressure difference $\Delta P = 300$ Pa was applied for different experiments.

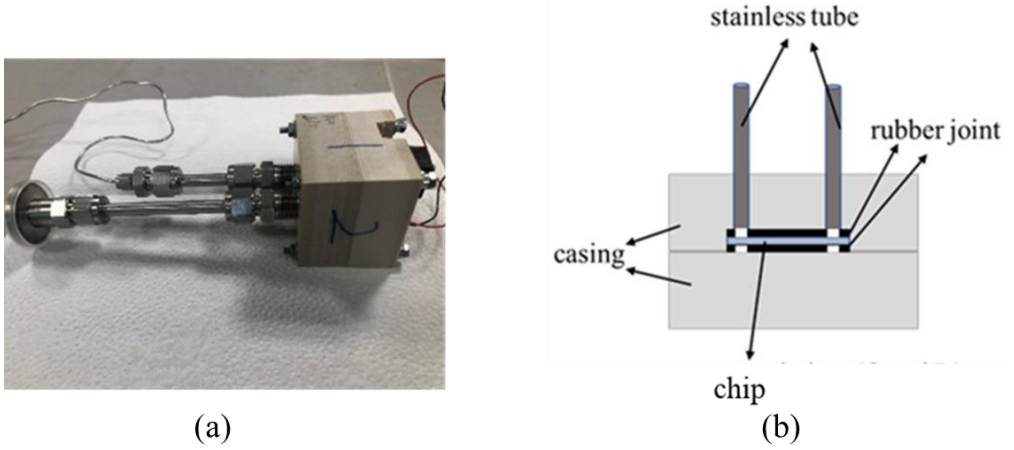

Figure 3.12 – Casing for holding the chip. a) Global view; b) Inner structure.

Tests were conducted starting with lower pressures (around 250 Pa) and progressing to higher pressures (around 13 kPa). At low pressures, the numerical results from simulations of a 50 μm height microchannel showed significantly higher flowrates compared to the experimental measurements. This discrepancy was attributed to the assumption that the bottom DF partially filled the channel created in the top DF, resulting in a significant reduction in the average depth of the channel.

To address this issue and achieve better agreement between numerical simulations and experimental data, the height of the channel in the simulations was gradually decreased while maintaining the measured length and width of the microchannel. The simulations yielded the

best fit with a channel depth of 28 µm. With this adjusted value, numerical and experimental data were compared for the other initial pressures, as shown in Fig. 3.13.

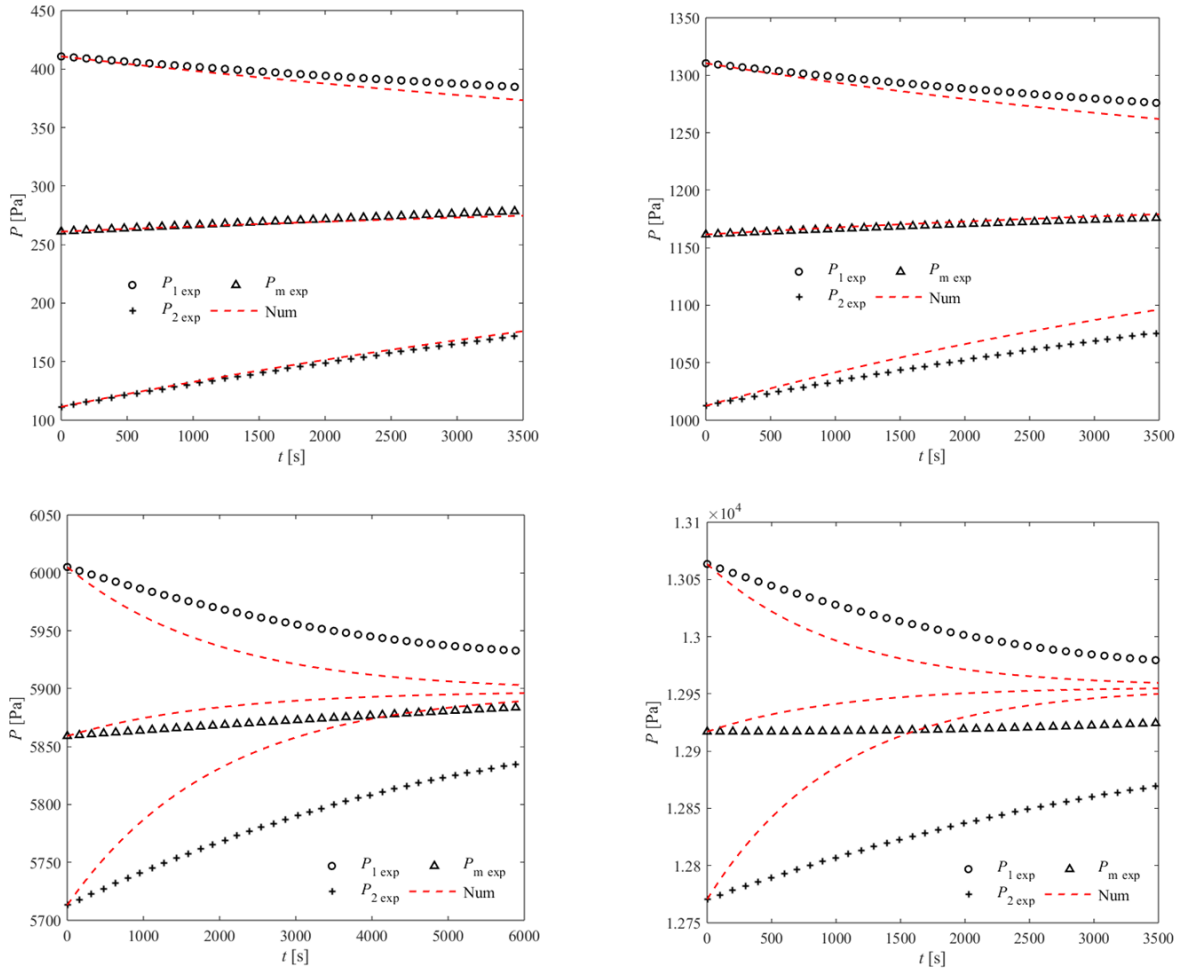

Figure 3.13 – Inlet pressure P_1 (o) and outlet pressure P_2 (+), as well as mean pressure P_m (Δ) vs time for different initial pressures. The numerical results were simulated with a 28 µm deep microchannel.

At low pressure, with a mean pressure P_m ranging between 250 and 300 Pa, the agreement between the theoretical predictions and experimental data is quite good. However, as the initial pressure increases, it becomes evident that the deviation between numerical simulations and experimental results significantly grows. This deviation could be attributed to the instability of the microchannel structure. After each test, the microchannel was subjected to vacuum, which may have led to partial collapsing or deformation of the microchannel. This could explain why a better agreement with the simulations was achieved with a lower depth in each subsequent experiment.

The results can also be analyzed through the conductance defined by

$$C = \frac{\sqrt{2R_g T}}{2L} H^2 W G_P \tag{3.5}$$

and plotted as a function of the mean rarefaction parameter δ_m as shown in Fig. 3.14.

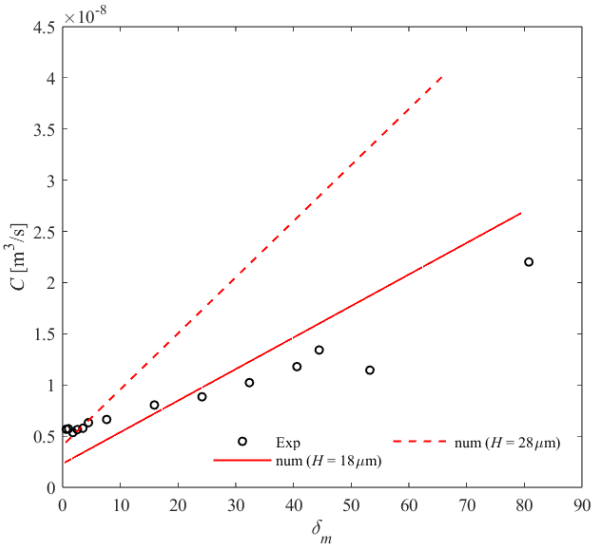

Figure 3.14 – Conductance vs rarefaction parameter for sample E2 fabricated on DF.

Some visualizations of the sample were captured using a microscope after conducting gas flow experiments in the microchannel. These images were then compared with the ones obtained prior to the flow experiments (Fig. 3.15). The purpose was to determine whether the microchannel exhibited any deformations after undergoing the tests. It is evident from the images that the aspect of the channel has changed and that some residues are present after the tests, which could potentially be causing blockages within the microchannel. These residues may have formed due to the compression of the casing and the vacuuming process applied to the microchannel.

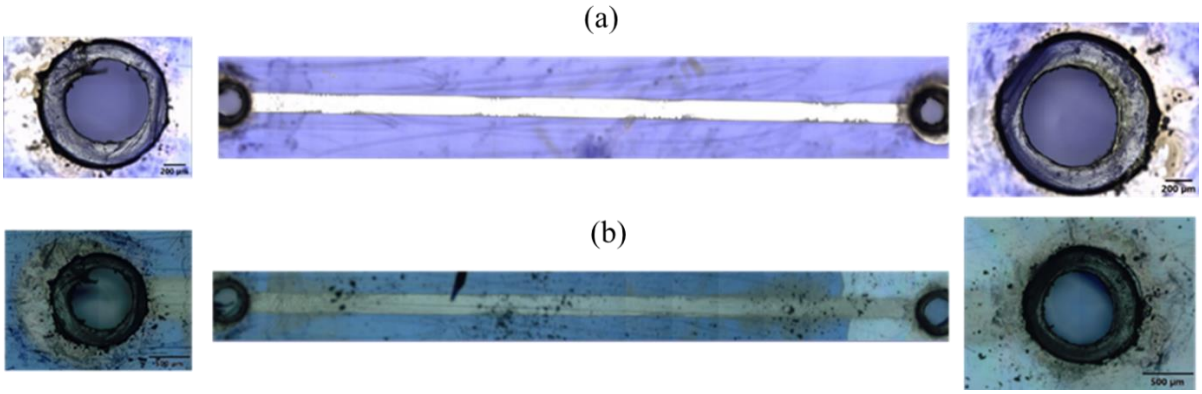

Figure 3.15 – Digital microscope test of orifices and microchannel of sample 2. (a): Before any gas flow measurements; (b): After several gas flow experiments.

These modifications of the microchannel structures were obviously not recoverable and additional work is still necessary to manufacture reliable and stable microfluidic structures based on DFs.

Therefore, a new but more complex manufacture technique should be proposed for fabricating the elements of operating 3D KPs. This is the objective of the next section.

3.3 Manufacturing of microchannels by TPP

Two-photon-polymerization (TPP), also called 3D direct laser writing (3D-DLW), is an additive manufacturing technique based on the two-photon polymerization of a photoresist with ultra-short laser pulses. This technique has been originally developed for the rapid, cheap and customizable fabrication of nanostructures [119–121]. Recently, it has been proposed for the development of new bio-medical applications at the microscale [122] and biomimetic surfaces [123]. Following these developments, the technique has been modified to achieve larger writing fields with high precision and for manufacturing leak proof microfluidic devices working with rarefied gas flows. The samples have been manufactured in the KNMFi facilities in Karlsruhe, Germany, in the framework of a long-term grant agreement “2022-027-031254” and a short-term grant agreement “2020-024-029397” financed by KNMFi and the Helmholtz Gemeinschaft (HGF).

3.3.1 TPP manufacturing process

In comparison with other additive 3D-printing methods, two-photon-polymerization offers an outstanding precision and resolution. It is also interesting for its ability to work without the need of supporting structures, which allows for the manufacture of especially complex 3D-structures with various internal details. The manufacturing was realized by means of the photonic Professional GT 2 (Nanoscribe GmbH) setup, which relies in a laser system combined with an inverted microscope, synchronized and controlled by a personal computer (PC). The manufacturing procedure consisted in focusing a laser beam into a viscous liquid photosensitive material (IP-Q Nanoscribe GmbH) in order to activate a photochemical reaction in the laser focus volume, which is a high intensity spot. This was achieved via a build-in monochromatic erbium-doped femtosecond-laser from Toptica (λ_T = 790 nm) and a tight focusing objective, a modified Zeiss Objective by Nanoscribe with 10 × and NA 0.3, which leads to 2-photon absorption [121]. The pulsed femtosecond-laser frequency was 80 MHz, the pulse duration was 100 fs and the maximal power output was 60 mW. The beam was guided through the objective and focused inside the photoresist deposited over an aluminum substrate which was mounted on the sample holder of the system. The sample holder could be translat-

ed via a piezo-actuator along the three dimensions of space. The manufacturing laser power and the scan-speed were set to 48 mW and 50 mm/s, respectively. The 3D-model was obtained from a STL-format model by imposing a slicing (layer distance) of 5 μm and hatching (lateral line distance) of 1 μm. For better definition, 5 contour lines that follow the outer shape of the structure, also with a line distance of 1 μm, were added. While printing, the material was directly polymerized upon the substrate without the need of chemical adhesion promotion, and the lower part of the structure remained attached to the substrate. In addition, a galvano scanner unit was used for fast writing in the field of view of the objective. To achieve large structures, these fields were stitched together by a lateral movement of the motor stage. This combination (Objective and adjusted IP-Q photoresist), also called Large Feature Set (LF-Set) by Nanoscribe, was optimized to provide a good resolution and at the same time allowed for the fabrication of reasonable large parts. As a function of the laser power, the voxel size can have a diameter from 1.6 up to 5 μm and an aspect-ratio of 16, providing a writing field of 1 mm. For the current setup, a film with surface $w^2 = 1$ mm^2 and thickness $l =$ 300 μm could be written without the need of stitching. It can be noted that, for other applications, the manufacturing technique can reach voxel diameters down to 150 nm but with a maximum writing field of 140 μm, by using higher focusing objectives (100 ×).

The 3D-structure polymerization via femtosecond-laser exposure took about 8 and 16 min for the 150 and 300 μm thickness samples, respectively. Afterwards, a two-step development process was achieved via a washing step with propylene glycol methyl ether acetate (PGMEA) during 45 min to remove the unexposed photoresist, followed by a rinsing step during 2 min with nonafluorobutyl methylether, an extreme low viscosity perfluorinated engineering fluid (Novec 7100; 3M). The sample was left to dry at a controlled 7 °C temperature for 10 min. Since the development of small cavities is highly challenging, additional washing and rinsing were performed over the sample, during 2 hours and 10 min, respectively [124].

The single microchannels were placed at the center of a wider photoresist structure, which corresponds to a film of surface with different dimensions for different microchannels (for example, for uniform microchannels, surface $w^2 = 1$ mm^2 and thickness $l = 300$ or 150 μm; for tapered microchannels, $w^2 = 1$ mm^2 and $l = 1$ mm.). As previously mentioned, the structure was printed on top of an aluminum metal plate ($10 \times 10 \times 0.5$ mm^3 and $25 \times 25 \times 0.5$ mm^3 for uniform and tapered microchannels, respectively). It should be noted that being able to 3D-write over a metal plate could be of great interest for other works as well, since the materials which are often used for substrate purposes are mainly silicon or glass. In the present experiments, the metal plate was also used as a fluidic connector via which the microchannels were

connected to the experimental setup (see Section 3.2.1). The advantage of using a metal connector in respect to a silicon or glass substrate is easier manipulation of the device, and easier fluidic connections, *e.g.* by mechanical clamping. A 200 μm diameter orifice was milled at the center of the metal plate. The manufactured patterned 3D-film covered the orifice which served as an inlet or outlet for the gas flowing through the micro-channel.

3.3.2 Visualization of samples manufactured via TPP

In this study, two kinds of single straight microchannels were designed and fabricated via the TPP fabrication technique, namely, cylindrical microchannels a circular cross section, and circular and square tapered microchannels with a cross section varies linearly along the length of the channel.

Cylindrical microchannels with circular cross section

The characterization of the four samples was realized through a focus-variation 3D optical measurement microscope (Alicona Infinite Focus SL), a digital microscope (VHX 7100, Keyence) and an EasyTom XL tomograph (RX Solutions). Thanks to the focus-variation 3D optical measurement, it is possible to appreciate the 3D nature of the structure. The translucid parallelepipeds structures correspond to the TPP polymerized matter which contains the micro-tubes (Fig. 3.16: left column). The support metal substrate is also captured in these images. A reference system was chosen in order to represent the obtained measurements of the geometry of the micro-tubes: z is directed along the axis of the channel, while the *x*-*y* plane is perpendicular to this axis. The inlet of the tube ($z = 0$) is located at the interface between polymer and metal substrate. The digital microscope images provide a view of the outer section of the microtubes (Fig. 3.16: center column). The measurements obtained from these images can be largely deceptive, since they do not represent the inner dimensions of the micro-tubes fabricated through TPP. The dimensions obtained through the microscope at the outlet sections are always larger than the measured mean diameter. In addition, the *x*-*y* outlet section images reveal an unsatisfactory circular shape of the tube, especially for the thinner samples (Samples 2 and 4). These effects, which are not present in the inner sections of the tube, could be explained by inhomogeneous residual shear stress created at the surface during polymerization.

The inner structure of the 3D-TPP structure was characterized through the EasyTom XL tomograph. Acquisition of the X-ray radiographs was made using a 160 kV nanofocus X-ray source. Image acquisition was performed at a 40 kV voltage and a 140 μA amperage. The exposure time on the flat panel sensor was 3 s for each radiograph and 1440 radiographs were

acquired as the sample rotated through 360 °. Reconstruction was carried out using the X-Act software (RX Solutions), leading to the obtention of the tomographic slices on three different planes. The isotropic voxel size depends on the exact positioning of the sample with regards to the X-ray source output window and the flat panel. In the present study, it was either 1.5 (Samples 1, 2 and 3) or 1.2 µm (Sample 4).

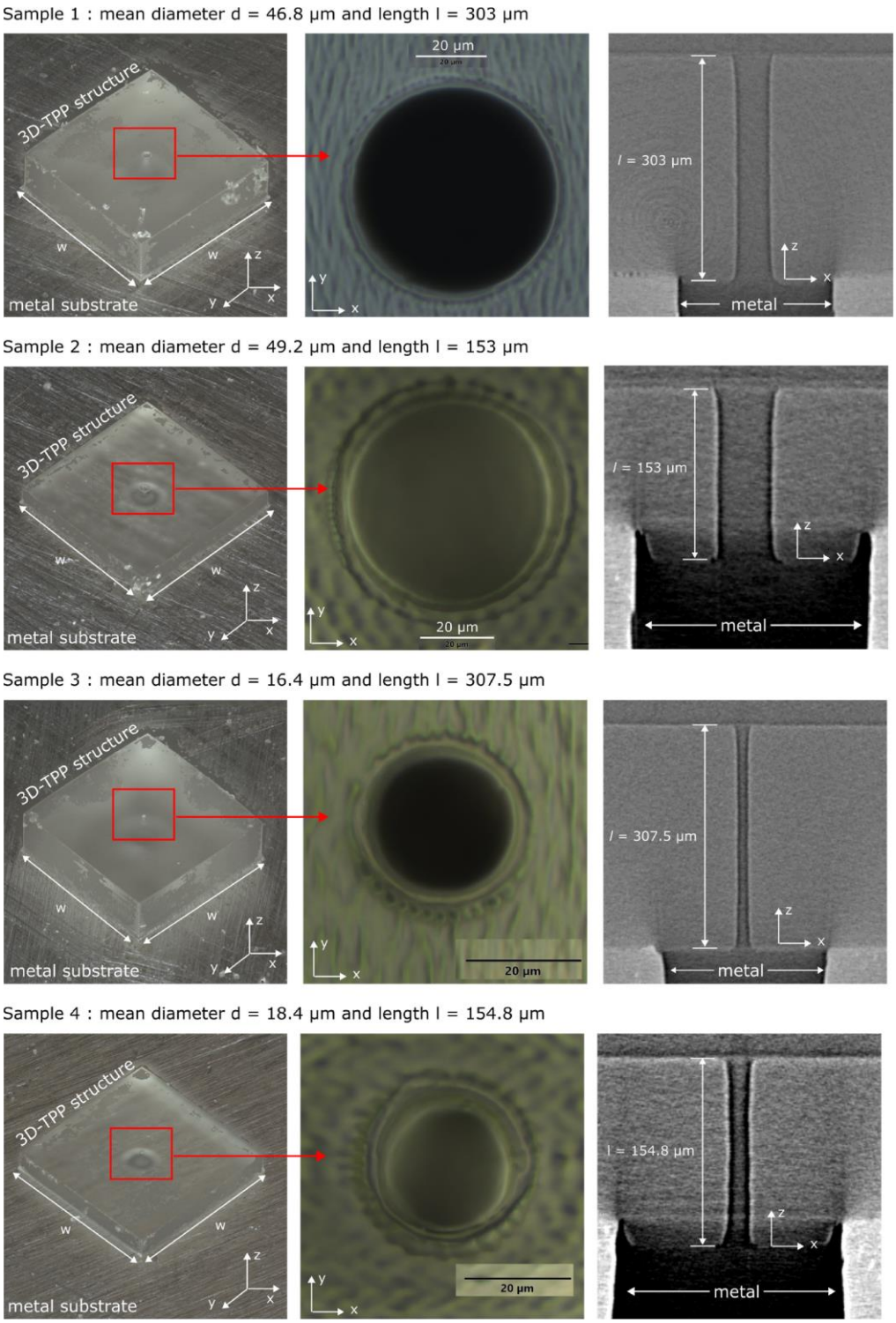

Figure 3.16 – Micro-tubes manufactured via TPP over a metal plate. Left images: focus-variation 3D optical measurement of the full 3D-DLW structure. Center images: Digital microscope measurements of the top surfaces of the 3D-DLW structure with focus on the outlet orifice of the micro-tube (*y*-*x* plane). Right images: EasyTom tomograph measurements along the full length of the microtube (*z*-*x* plane).

The acquired images in the *x*-*z* plane show the diameter variation along the *z*-axis, the maximum diameters being located at the outlet and inlet sections, while the minimum diameter is located in the central part of the channel (Fig. 3.16: right column). These images also show

the great quality of the polymer deposition over the metallic structure, which ensures the leak tightness along the whole structure for rarefied gas flows applications. Finally, it should be noted that for the thinner samples, that is Samples 2 and 4, the polymer enters inside the orifice drilled on the metal substrate. This effect does not seem to impact the geometry of the channel. In order to measure the diameters of the inner sections of the micro-tubes, a Matlab code was developed on the basis of the Hough transform circle extraction technique and applied to the *x-y* plane images. A very thorough investigation of the inner sections of the micro-tubes was realized through these images. The small isotropic voxel size led to more than 200 and 100 acquired exploitable images for the 300 and 150 μm length samples, respectively. For each image, a diameter measurement was extracted. Through the data treatment of the complete set of images in the *x-y* plane, the mean diameter of each micro-tube was calculated. The nominal dimensions and the measured dimensions of each sample are listed in Table 3.2.

Table 3.2 – Summary of the tested samples with nominal lengths and diameter and respective measured dimensions.

Microchannel	Nominal diameter (μm)	Nominal length (μm)	Measured Mean Diameter (μm)	Measured length (μm)
Sample 1	50	300	46.8 ± 1.5	303.0 ± 1.5
Sample 2	50	150	49.2 ± 1.5	153.0 ± 1.5
Sample 3	20	300	16.4 ± 1.5	307.5 ± 1.5
Sample 4	20	150	18.4 ± 1.2	154.8 ± 1.2

It should be noted that the aspect ratio between the outlet section and the mean diameter is quite large, that is approximately 19.6 % for Sample 1, 27.0 % for Sample 2, 32.3 % for Sample 3 and 26.1 % for Sample 4.

Circular and square tapered microchannels

The dimensions of the tapered microchannels are approximately l = 973 μm, d_i = 32 μm and d_o = 426 μm for the circular channel and l = 968 μm, h_i = 33 μm and h_o = 440 μm for the square channel, respectively. The microchannels were created inside a polymerized cube of approximately 1 mm^3 (Fig. 3.17a).

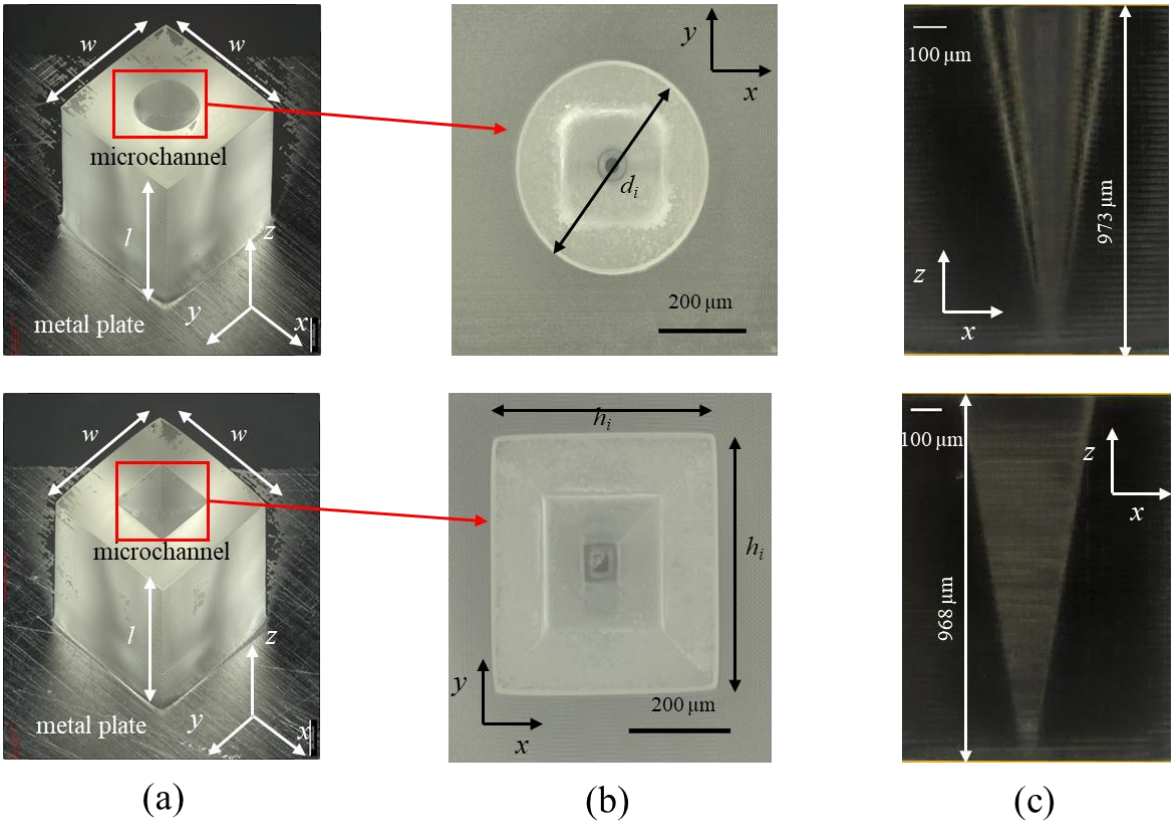

Figure 3.17 – Tapered microchannels with circular (top) and square (bottom) cross sections mounted on an aluminum metal plate.
a) 3D structure of the full microdevice, b) Top view of the microchannel measured by digital microscope, and c) Side view of the microchannel measured along the length by digital microscope.

3.4 Experiments on microchannels fabricated via TPP

In the present section, pressure-driven flows in microchannel fabricated via TPP submitted to a pressure difference between their two extremities are investigated.

3.4.1 Experiments on microtubes fabricated via TPP

The four samples described in the first part of Section 3.3.2 have been tested with isothermal pressure-driven flows using the same method as in Section 3.2, with a constant initial pressure difference of 200 Pa and different initial inlet pressures for each experiment, to cover different rarefaction parameters defined by Eq. (2.28). In addition, for practical purposes, the dimensionless mass flowrate G was here computed via a fitting equation expressed by Eq. (2.27) obtained via the Bhatnagar-Gross-Krook (BGK) model. The numerical results presented for different rarefaction conditions of the flow are valid for a complete diffusive accommodation at the wall only.

In these experiments, the calculated volumes of both tanks are V_1 = 342.2 ml and V_2 = 95.13 ml, while the temperature of the gas is T = 293.5 K. Other parameters including leak rate at each side (lk_1 at the inlet and lk_2 at the outlet) and measured average diameters d_m are listed in Table 3.3. For details on leak rate, see Section 5.3.3.

Table 3.3 – Average diameter for each sample and inlet and outlet leak rates.

Sample	d_m (μm)	l (μm)	lk_1 (Pa / s)	lk_2 (Pa / s)
1	46.8	303	2.42×10^{-4}	1.32×10^{-3}
2	49.2	153	4.36×10^{-4}	4.54×10^{-3}
3	16.4	307.5	5.95×10^{-5}	1.6×10^{-3}
4	18.4	158.4	5.95×10^{-5}	1.75×10^{-3}

Representative curves of pressure variation with time for one experiment (the inlet initial pressure in Tank 1 is 350 Pa for each sample) are presented in Fig. 3.18.

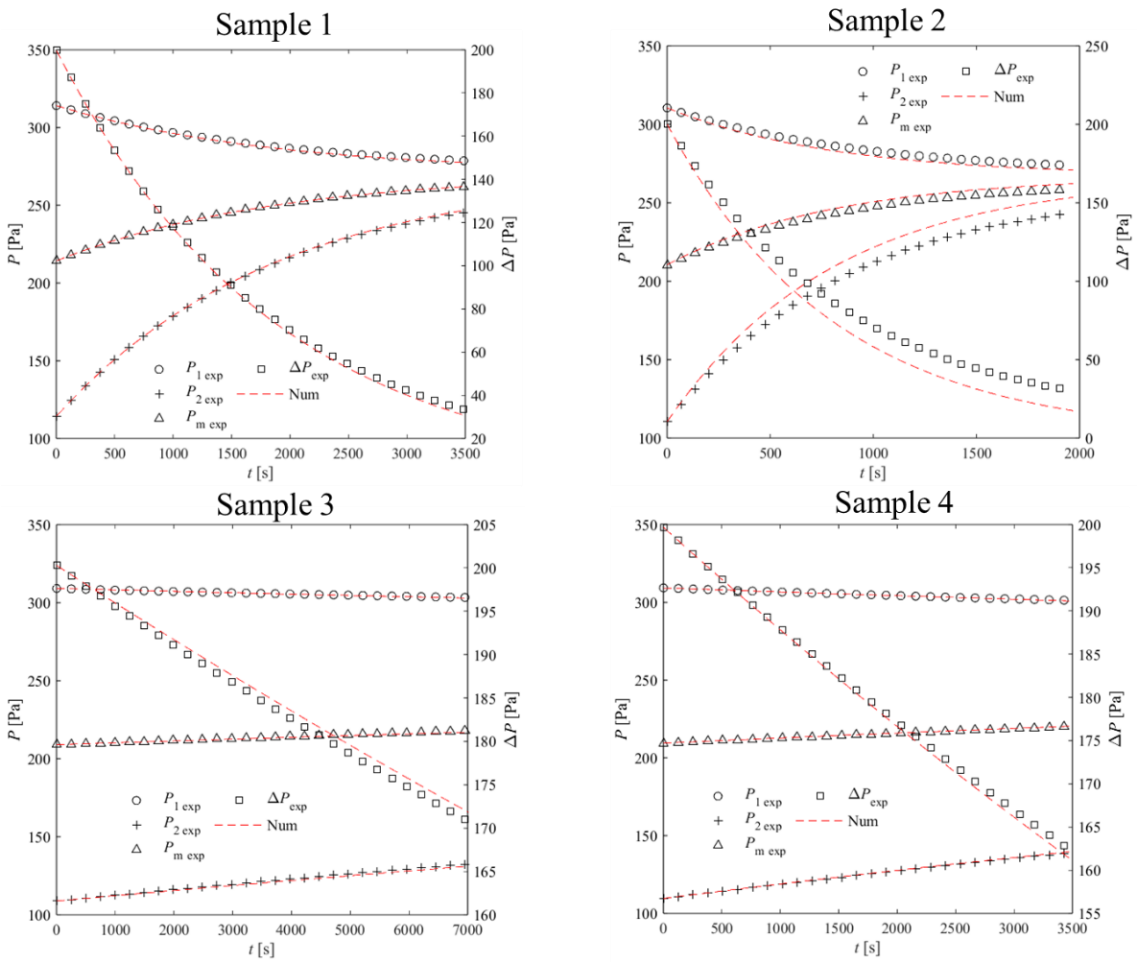

Figure 3.18 – Nitrogen flow tests. Experimental and numerical (on kinetic theory basis) pressure vs time for the 4 microtube samples with the same initial pressure difference.

Experimental: (○) P_{1exp} **inlet tank, (+)** P_{2exp} **outlet tank, (△)** $P_{m\,exp}$ **mean pressure, (□)** ΔP_{exp} **difference of pressure between inlet and outlet tanks. Numerical kinetic theory counterparts (-).**

Numerical data obtained for: Sample 1: $d_m = 46.8$ μm **and** $l = 303$ μm**; Sample 2:** $d_m = 49.2$ μm **and** $l = 153$ μm**; Sample 3:** $d_m = 16.4$ μm **and** $l = 307.5$ μm**; Sample 4**: $d_m = 18.4$ μm **and** $l = 154.8$ μm**.**

As it can be readily seen, the comparison between numerical and experimental data is of great quality, especially for Samples 1, 3 and 4. The pressure variation with time is highly dependent on the diameter of the microchannel, resulting thus in the very different relaxation times of Samples 1 and 2 ($d \approx 50$ μm) in respect to Samples 3 and 4 ($d \approx 20$ μm). The dependence to the length of the tube is also evident, as it can be observed by comparing the results obtained from Samples 1 and 3 ($l \approx 300$ μm) in respect to Samples 2 and 4 ($l \approx 150$ μm). From these experiments it is thus possible to extract the pressure variation with time speed (dp / dt), which is linked to the mass flowrate in the microchannel (Eq. (2.29)).

For a constant geometry and isothermal flow, the gas rarefaction varies only with the mean pressure inside the flow according to Eq. (2.29). For a specific pressure difference imposed

between inlet and outlet of the microchannel, it is possible to compute the numerical flow conductance C via the G_P function as [112]:

$$C = \frac{\dot{m} R_g T}{P_1 - P_2} = \frac{\pi \sqrt{2 R_g T}}{16} \frac{d^3}{l} G_P \tag{3.6}$$

From the above equation, it is can be readily seen that in isothermal flows, keeping the same working gas, the conductance C relies on the geometry of the channel and the initial conditions of the flow. This relation between conductance and mass flowrate has also been used in order to compute the experimental conductance of the microchannel.

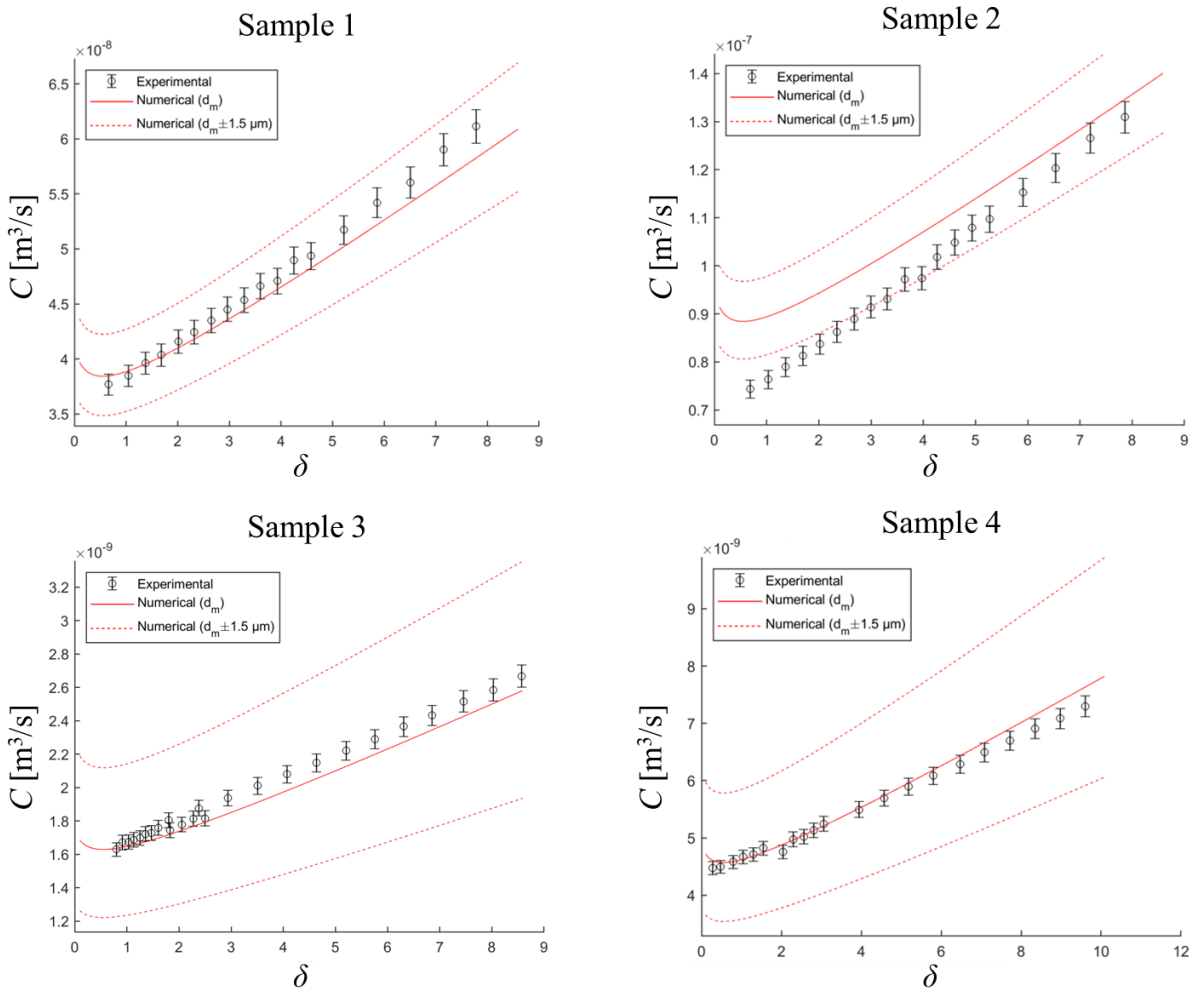

Figure 3.19 – Conductance of each sample vs rarefaction parameter.

(○) Experimental data; (—) Numerical data computed with the measured mean micro tube diameter d_m;

(-) Numerical data for $d_m \pm 1.5$ μm. Sample 1: $d_m = 46.8$ μm and $l = 303$ μm; Sample 2: $d_m = 49.2$ μm and $l = 153$ μm; Sample 3: $d_m = 16.4$ μm and $l = 307.5$ μm; Sample 4: $d_m = 18.4$ μm and $l = 154.8$ μm.

A large conductance experimental scan was performed for a wide range of rarefaction for the 4 samples (Fig. 3.19). The mass flowrate measurements were obtained for the initial time of each experiment (t = 0, ΔP = 200 Pa). The uncertainties associated to the conductance measurements are related to the volumes of the tanks, temperature fluctuations and pressure variations with time [118]. The uncertainty on the conductance has been estimated at ± 2.5 %.

The experimental results of Sample 1 (d_m = 46.8 μm and l = 303.0 μm), Sample 3 (d_m = 16.4 μm and l = 307.5 μm) and Sample 4 (d_m = 18.4 μm and l = 154.8 μm) match the expected numerical results obtained for the measured lengths and mean diameters. However, Sample 2 (d_m = 49.2 μm and l = 153 μm) exhibits a slight deviation from the long tube theory (here, l / d = 3.1 is not large enough), since the inlet and exit effects of the flow are neglected in the numerical model [98]. Another possible explanation of this divergence could be attributed to entrance and exit effects introduced by the varying cross-section through the tube, which for the specific case of Sample 2 is indeed more significant. As can be seen from the numerical/experimental comparison, the long tube theory is adequate if one considers the average diameter of the tube for Samples 1, 3 and 4. As previously mentioned, the experimental results were compared to numerical results calculated with the average diameter of the microtubes. However, additional numerical conductance curves were added for diameters of d_m ± 1.5 μm. This comparison was introduced in order to give a better idea of the uncertainties related to the fabrication process. If the l / d aspect ratio is sufficiently large (Samples 1, 3 and 4), the end effects can be neglected and thus the theory matches the experimental results well beneath the uncertainty of the optical measurements. This confirms the precision of the fabrication method in terms of straightness and constant cross section of the channels even for long aspect ratios. Let us point out that the highest aspect ratio investigated in this study corresponds to Sample 3 (l / d = 18.7) and that even for such high aspect ratios, the manufacturing precision is maintained.

3.4.2 Experiments on tapered microchannels fabricated via TPP

The tapered microchannel with a circular cross-section was subjected to isothermal pressure-driven flows, and both the converging and diverging directions of the flow were investigated both numerically and experimentally. The experiments were conducted with the same initial pressure difference $\Delta P = 200\,\mathrm{Pa}$ between the inlet and outlet tanks, considering various rarefaction conditions. The results are presented as a function of the inlet pressure in Fig. 3.20.

In a first step, the numerical simulations were carried out using externally measured inlet and outlet diameters d_{meas}, while in a second step, the numerical simulations employed inlet and outlet diameters adjusted by a shrinking coefficient to better match the experimental data ($d = 0.86 d_{\text{meas}}$). The observed ratio is attributed to the presence of rounded edges at the extremities of the microchannel. These rounded edges create a local increase in the diameter of the channel, which ultimately results in a diameter that is lower than what is measured at the surface of the sample. This variation in diameter can impact the flow behavior in the microchannel and explains the need to adjust the numerical model to better match the experimental results. The length l and inclination ratio α of the channel remained constant.

As expected, the experimental data in the first step exhibit significantly lower mass flowrates across the entire range of inlet pressures compared to the numerical results (Fig. 3.20a). However, when the numerical simulations use diameters that are 86 % of the external diameters, there is relatively good agreement with the experimental data. Some deviations can be observed as rarefaction increases, which may be attributed to extremity effects not considered in the numerical model, especially for very short channels.

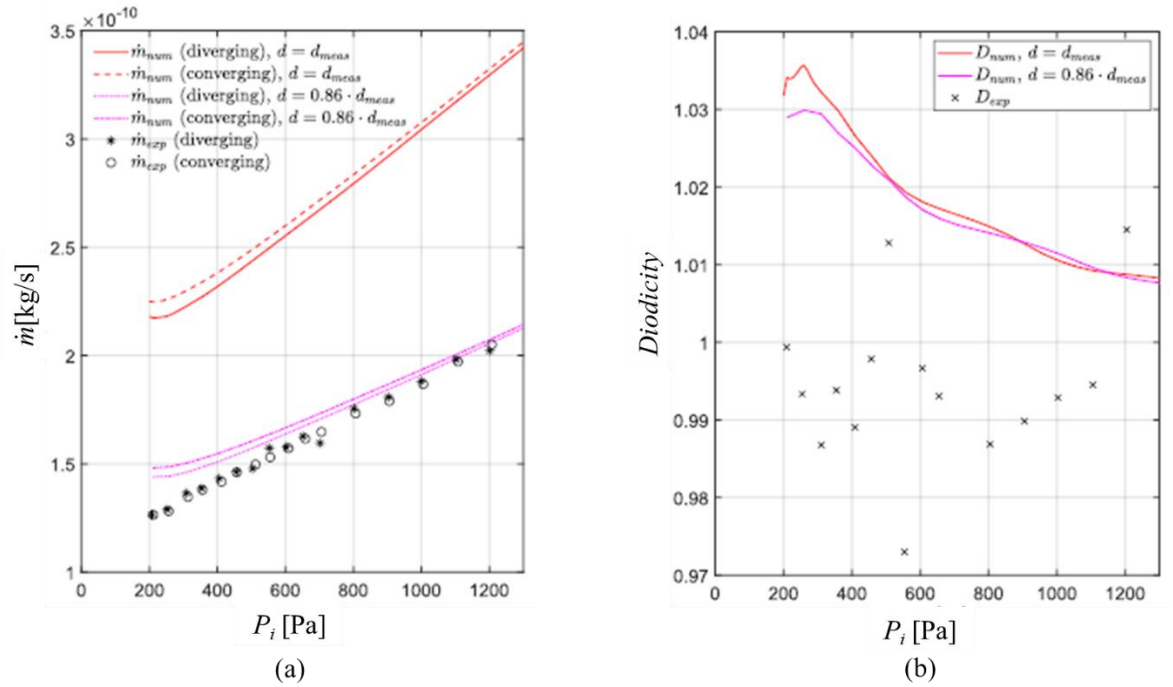

Figure 3.20 – Tapered microchannel with circular cross section. Left: Mass flowrate vs inlet pressure for converging and diverging directions; Right: diodicity versus inlet pressure.

For the numerical results it can be noted that the mass flowrate in the converging direction is always slightly higher than in the diverging direction. This is more clearly noticeable by

plotting the diodicity, which is defined as

$$Diodicity = \frac{\dot{m}_{con}}{\dot{m}_{div}} \tag{3.7}$$

The numerically expected diode effect is observed to increase within a small range of the transitional flow regime, specifically for pressures ranging from 200 Pa (δ = 3.14) to 260 Pa (δ = 5.03), and to decrease from the transitional to the slip-flow regime, occurring for pressures ranging from 260 Pa (δ = 5.03) to 1110 Pa (δ = 31.7). It's important to note that this diode effect is not particularly significant, with a diodicity always remaining lower than 1.035.

The experimental results (Fig. 3.20b) indicate that there isn't a clear difference between the measured mass flowrates in the converging and diverging directions. The fluctuations in measured diodicity fall within the experimental uncertainties of the measured mass flowrates, which have an error margin of approximately +/5 %.

However, it's worth noting that the absence of a significant diodicity effect could also be attributed to potential fabrication defects at the inlet and outlet of the device, which may not have been accounted for in the numerical simulations. Further investigations are required to accurately characterize the inner geometry of the sample, and to analyze square tapered microchannels as well.

3.4.3 Conclusions on samples fabricated via TPP

It has been proven that TPP is a manufacturing technique of great potential for the fabrication of a new generation of 3D-microfluidic devices for rarefied gas flows applications. Inherent adhesion of the polymerized material to the natural aluminum oxide surface layer and the absence of volatile compounds from the polymer material allow a wider use of this material combination for low pressure applications. Furthermore, great novelty has been introduced in this work in respect to the very different l / d aspect ratios obtained for the manufactured micro-tubes. The TPP writing voxel size had a diameter ranging from 1.6 up to 5 μm and an aspect-ratio of 16, providing a writing field up to 1 mm. This is a major breakthrough for the manufacturing options for developing 3D micro devices handling rarefied gas flows with well controlled designs, since conventional microfabrication techniques for rarefied flows are often limited to two-dimensional geometries. The results described in Section 3.4.1 have been published in Vacuum [125] and the results described in Section 3.4.2 have been presented at NEGF23 Conference [126].

The next step should consist in including heaters in the manufacturing process to perform thermally-driven flows. This work was not feasible during the present thesis, due to a lack of

time, but temperature-driven flows were tested in simpler glass microtubes. They are presented in the next section.

3.5 Temperature-driven flows in glass microtubes

In the present section, temperature-driven flows in glass microtubes submitted to a temperature difference between their two extremities are investigated.

3.5.1 Experimental setup

The experimental setup for thermally-driven flows is more or less the same as that for pressure-driven flows, the main difference being that a high temperature is generated at one extremity of the channel via a heater connected to a power supply, as shown in Fig. 3.21. The dimensions of the glass microtube is 77.29 mm in length and 499.4 μm in diameter. Besides, the volumes of Tank 1 and Tank 2 for this experiment are V_1 = 76.99 ml and V_2 = 397.15 ml, respectively. Temperatures for hot side and cold side measured by T-1 and T-2 are T_h = 357 K and T_c = 319 K.

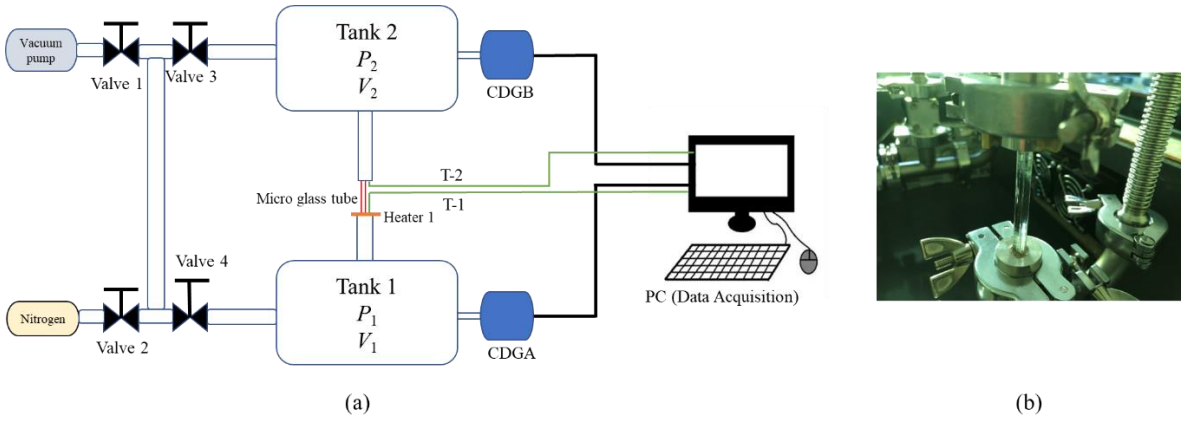

Figure 3.21 – a) Diagram of experimental setup for temperature-driven flows in a glass microtube; b) Close view of the glass microtube connected to the setup.

3.5.2 Experimental procedure

The experimental procedure follows 4 main steps:

1. **Vacuuming the setup**: Valves 1, 3 and 4 are open, Valve 2 is closed, and the vacuum pump is activated to clean the system in order to limit outgassing.
2. **Feeding gas inside the system**: after vacuuming the system for several hours, Valve 1 is closed, and Valves 3 and 4 are kept open. Then Valve 2 is opened slightly to feed the setup with gas and assure the same pressure in the whole system.

3. **Starting the thermally driven flow**: once the pressure inside the system has reached a specific value, Valve 2 is closed, then Valves 3 and 4 are closed simultaneously. The thermal transpiration flow will start at this moment, and the experimental data is recorded. The experiment runs at least one hour to reach the final equilibrium state.
4. **Stopping current experiment and preparing the next one**: data recording is stopped and Valves 3 and 4 are opened, while Valve 2 is kept closed. Then the above steps can be repeated to perform the next experiment.

3.5.3 Data treatment

An example of data treatment is shown in this Section. For this example, the initial pressure P_i = 105.4 Pa, and the raw data are shown in Fig. 3.22a. First, the raw data of pressure variation in the hot and cold sides are fitted by two 2-degree exponential functions (Fig. 3.22b).

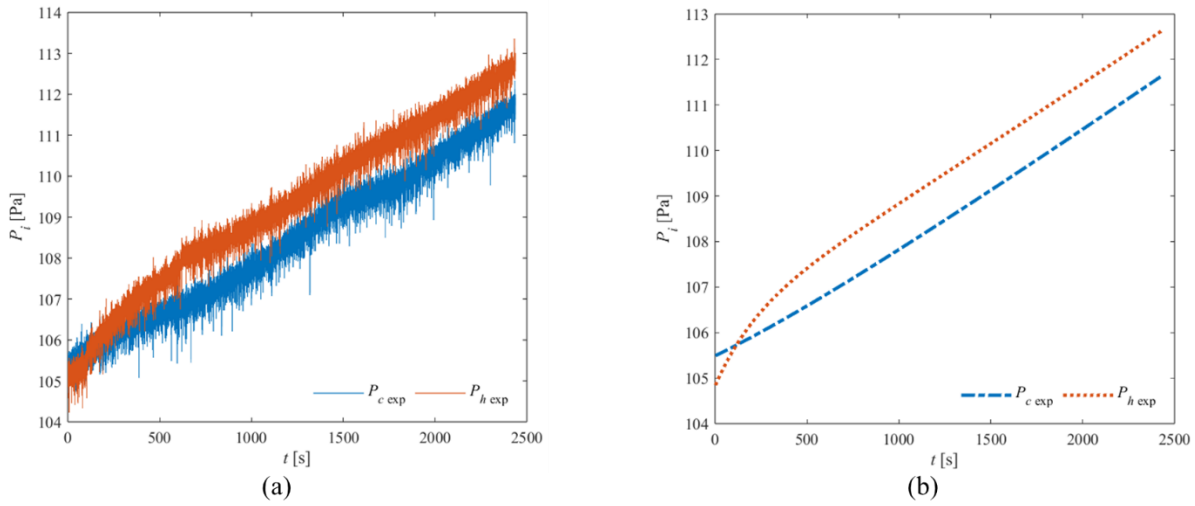

Figure 3.22 – Pressure evolution in hot and cold sides of the microchannel for P_i = 105.4 Pa. a) Raw data of the experiments; b) Experimental results after 2-degree exponential fitting.

As can be seen from the fitting curves, after a non-linear increase in this hot side and decrease in the cold-side, the pressures in both sides increase linearly after roughly 1000 s. This means that the system is almost in the final equilibrium state with zero-mass flowrate inside the tube, and that the observed linear increase of pressure in both sides is due to leakage. Therefore, the leakage rate of each side is evaluated from the fitting curve, through the slope of the linear variation in pressure. In this experiment, the leakage rates are L_h = 0.002656 Pa/s and L_c = 0.002585 Pa/s, for hot and cold sides, respectively. Then, the data are plotted in the Fig. 3.23a after substraction of the leakage. In addition, an intersection point is

observed between cold side and hot side curves. Before this point, the pressures in the cold side is a bit higher than in the hot side (0.2 Pa). The data before the intersection are not considered and the starting point of the experiment is taken when $P_h = P_c$, as shown in Fig. 3.23b.

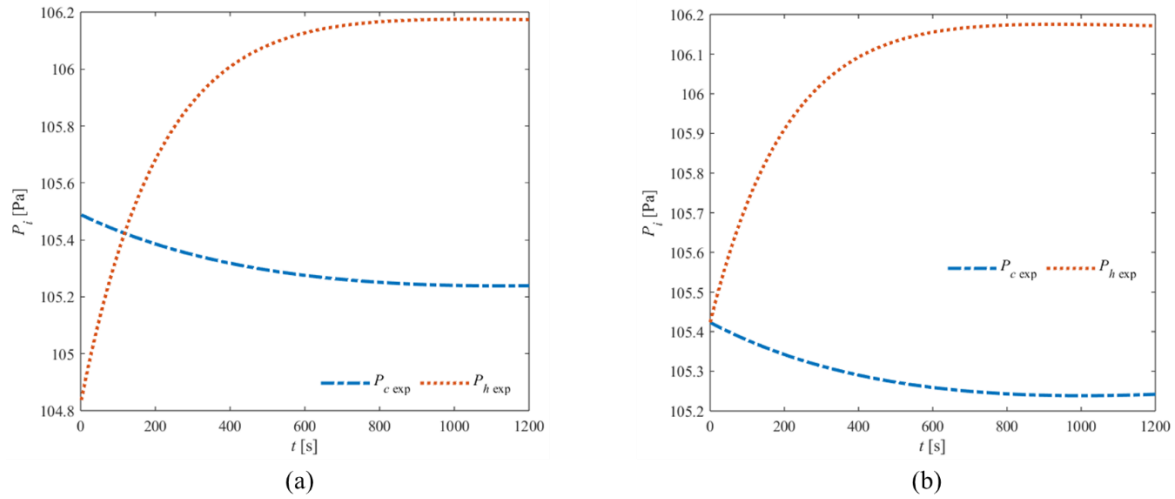

Figure 3.23 – a) Experimental fitting data after substraction of the leakage; b) Experimental results with a starting point when pressures are equal in both sides of the channel.

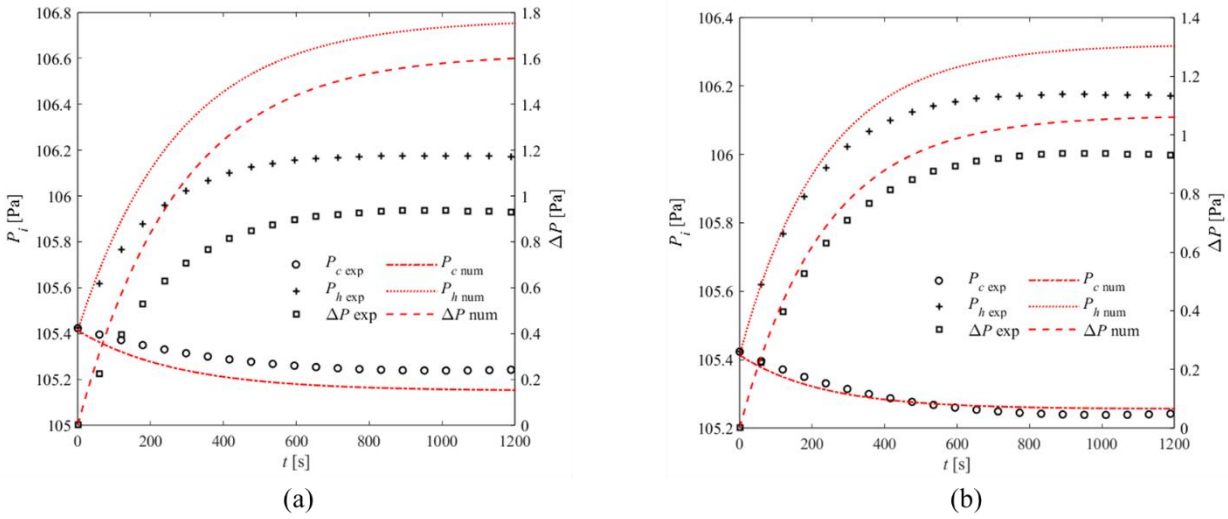

Figure 3.24 – Comparison between numerical and experimental results.
a) the numerical simulation was performed with T_h = 357 K and T_c = 319 K;
b) the numerical simulation was performed with T_h = 350 K and T_c = 320 K.

Later, the numerical simulations for the experiment are performed with T_h = 357 K and T_c = 319 K for hot and cold sides, respectively, corresponding to the temperatures measured by the thermocouples. The results with these temperature conditions are shown in Fig. 3.24a.

Obviously, the simulated pressure increase in the hot side is much higher than the experimental one, and the simulated pressure in the cold side is lower than the experimental one. Hence, the simulated pressure difference overestimates the experimental data. This is due to the fact that the thermocouples measured the temperatures of the metal supports connected to both ends of the glass tubes, rather than the gas temperature itself. Therefore, a complete simulation of heat transfer (including internal and external convection, conduction and radiation) would show that the temperature of the gas is lower than that measured.

Following numerical simulations with a lower temperature in the hot side and a bit higher temperature in the cold side, it was found that when T_h = 350 K and T_c = 320 K, a much better agreement between experimental and numerical results can be obtained (Fig. 3.24b). The remaining observed deviations can be explained by the fact that leakage was significant compared to the flowrate in the microchannel and that it substraction was imperfect. The ratio of pressure variation with time due to leakage (dP_{leak}/dt) over that due to gas flow through the microchannel (dP_{flow}/dt) is displayed in Fig. 3.25, which shows that the dP_{leak}/dt is several times higher than dP_{flow}/dt, especially in the cold side.

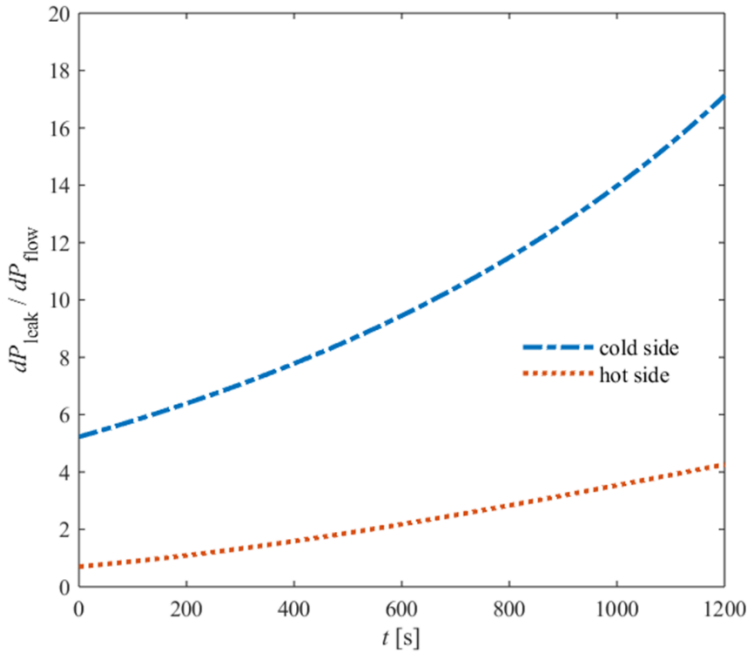

Figure 3.25 – Variation of ratio of the ratio dP_{leak} over dP_{flow} with time.

Following the above data processing, various experiments were compared to numerical simulations, and the results are analyzed in the next section.

3.5.4 Results and discussion

Through the above steps, several experiments were performed with different initial pressures. The processed experimental data have been compared with numerical results obtained from Eq. (2.24) and simulated as described in Section 2.3.3. When comparing with numerical simulations, a better agreement is observed for temperatures T_c = 320 K and T_h = 350 K, which are a bit different from the experimental values provided by the thermocouples (319 and 357 K respectively). This should mainly be due to the conductive and convective heat transfer that decrease the hot temperature applied to the inner wall at the outlet and increase the cold temperature applied to the inner wall at the inlet. Four results corresponding to different initial pressures (80.9 95.5 105.4 and 120.1 Pa) are showed in Fig. 3.26.

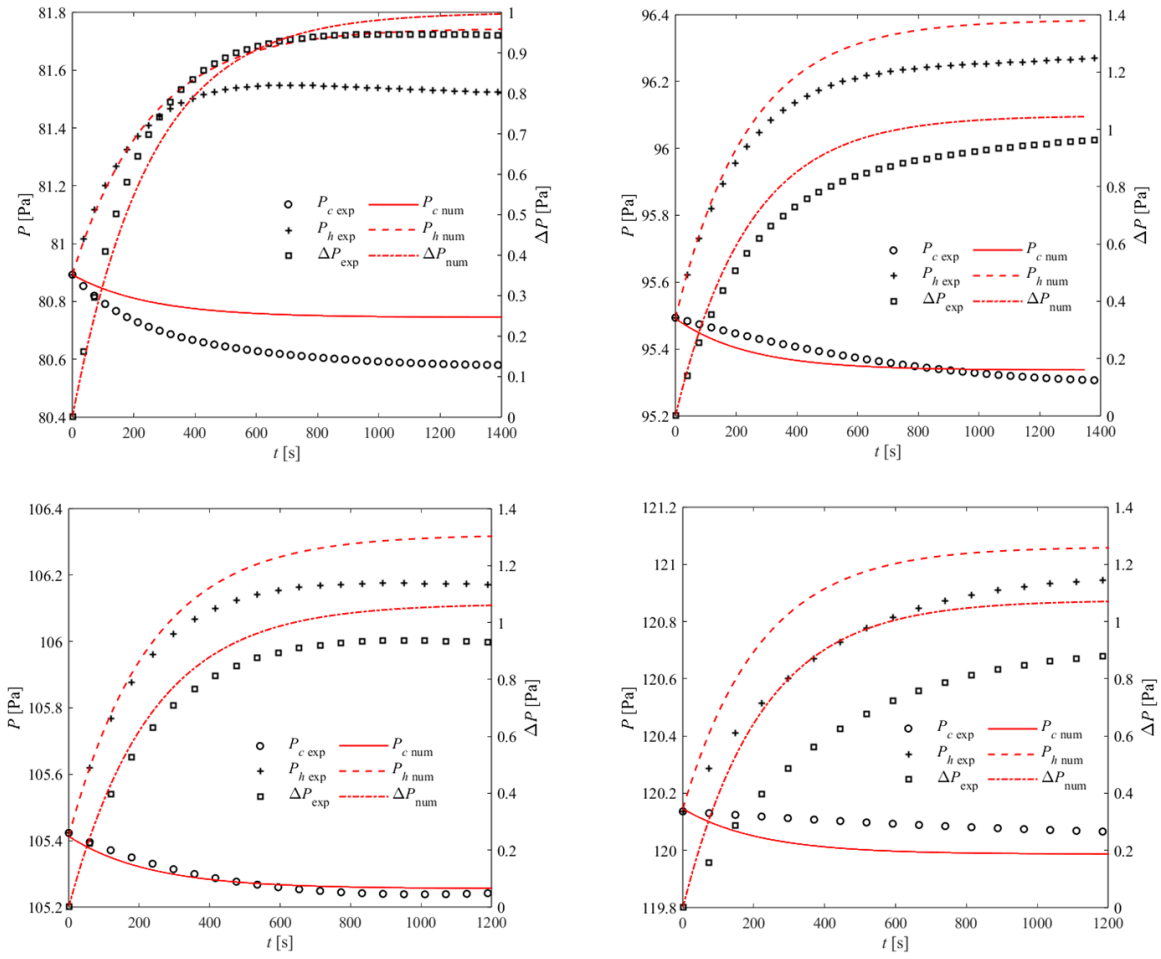

Figure 3.26 – Inlet (P_c – cold side) and outlet (P_h – hot side) pressures vs time for thermally-driven flows through a glass microtube with different initial pressures (80.9 95.5 105.4 and 120.1 Pa). The pressure difference ΔP is also plotted. The numerical results were obtained with T_c = 320 K and T_h = 350 K.

In addition, the maximum pressure difference ΔP_{max} and the maximum mass flowrate $\dot{m}_{max}$ of each experiment are also extracted and both are plotted vs the inlet pressure P_i and compared to the numerical data (Fig. 3.27).

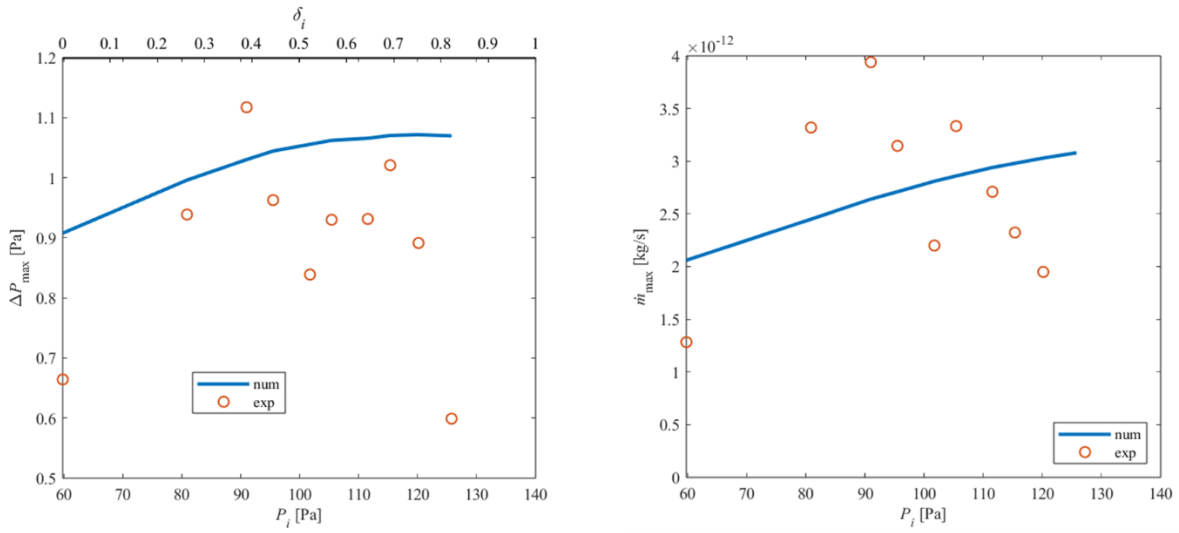

Figure 3.27 – Thermally-driven flows through a glass microtube. a) Maximum pressure difference vs inlet pressure and inlet rarefaction parameter; b) Maximum mass flowrate vs inlet pressure.

It can be readily seen that there even if the trends are well captured, and that the order of magnitude measured for ΔP_{max} and $\dot{m}_{max}$ are correct, but there are non-negligible deviations between numerical and experimental results. One explanation is that the pressure due to leakage in the experiments is much higher than the pressure variations induced by the thermal transpiration (that are typically below 1 Pa), especially in the hot side where leakage leads to pressure variations one order of magnitude higher than those due to the flow through the tube. The other reason is that convective and conductive heat transfer cannot be neglected in the experiments and that a more complete model considering conjugate heat transfer would be necessary to accurately reproduce the complex experimental conditions.

3.5.5 Conclusions on thermally-driven flows through a microtube

Temperature-driven flows with a temperature difference of about 30 K have been successfully generated in a glass microtube. The observed inlet and outlet pressure evolutions are qualitatively in agreement with the model presented in Chapter 2. However, the agreement between experiments and simulations could be significantly improved by i) reducing leakage in the experiments, ii) considering conjugate heat transfer in the simulations.

3.6 Summary

The application of the maskless UV light lithography technique, a low-cost fabrication method, has been applied to the manufacturing of rectangular microchannels in DF layers laminated on PMMA substrates. Several samples were fabricated with different DFs with of thickness 50 μm and experimentally tested. A more powerful technique, the two-photon-polymerization (TPP) fabrication technique has been for the first time successfully implemented to manufacture fluidic microdevices with three-dimensional structure suitable for confined rarefied gas flows. Several microchannels with uniform circular cross section and tapered channels with circular or square cross sections were successfully fabricated on an aluminum metal plate with a drilled orifice.

In order to properly assess the precision and reliability of the manufacturing of both TPP and maskless UV light lithography techniques, several samples were submitted to isothermal nitrogen gas flows on a setup based on the constant volume technique. Different inlet pressures were imposed for each sample while keeping a fixed initial pressure difference to cover a large range of the rarefaction parameter while measuring the conductance of the microchannels. Current limitations of the maskless UV light lithography have been observed, concerning the integrity of the channels when submitted to low-pressure gas flows, that require further investigation. On the other hand, the TPP technique is a very promising additive technique able to deliver high precision complex microfluidic structures, suitable for gas applications and potentially integrable in a complete Knudsen micropump.

Additionally, thermally driven gas microflows have been successfully generated inside a glass microtube, and several experiments were performed with the same difference of temperature. The agreement between experimental and numerical data requires more investigation on both the experimental and numerical points of view.

Chapter 4 - Vacuum-actuated artificial muscles

Introduction

Artificial muscles, also known as muscle-like actuators, are devices that mimic natural muscles and can change their stiffness, reversibly contract, expand, or rotate within one component due to a physical or a chemical stimulus (such as voltage, current, pressure or temperature) [127]. With external stimuli, artificial muscles can experience different deformations, such as contraction, rotation, bending, expansion, etc. They can grip and lift objects with different masses, work under unstructured and extreme environment, and operate safely with humans. Contrarily to rigid actuators, artificial muscles have a variety of potential applications due to their high flexibility and compliance, high power-to-weight ratio, ease of fabrication, low cost. This chapter presents a short overview of the main concepts of pneumatically-actuated artificial muscles.

4.1 Context of vacuum-actuated artificial muscles

Since the occurrence of artificial muscles, scholars have been attracted by the high research value of artificial muscles. Until now, various types of artificial muscles have already been designed. They can be divided into different classifications according to actuation mechanisms: artificial muscles with tethered power source (dielectric elastomer actuators, electrohydrodynamic and electro-aerodynamic actuators, electrochemical actuators, fluidic elastomer actuators) and artificial muscles with untethered power source (magnetic actuator, thermally actuated polymers) [128]. Detailed features on each kind of artificial muscle can be found in the literature [128]. Among them, the fluidic elastomer actuators (FEAs) are widely investigated and used actuators. This is especially true for the pneumatic artificial muscles (PAMs) [129], with their highly attractive features in terms of high compliance, easy fabrication and operation, relatively higher output force, etc.

PAMs are devices that can be compressed or expanded thanks to pressurized air filling in a pneumatic bladder. PAMs were first developed in the 1950s for helping the move of a polio patient [130]. The McKibben artificial muscle (Fig. 4.1a) is a prominent example of PAMs that operate via positive pressure, offering a unique ability to replicate the behavior of biological muscles in soft robotics. This innovative pneumatic design has found widespread use in various technological applications and research fields.

Two other extensively studied PAMs [131] that also operate using positive pressure are the

fiber-reinforced actuator (Fig. 4.1b) and the PneuNets bending actuator (Fig. 4.1c). The fiber-reinforced actuator employs advanced materials and a tailored design to achieve a combination of strength, lightweight performance, and customizable actuation properties. These characteristics make it an attractive choice for applications requiring precise, powerful, and adaptable motion control. On the other hand, the PneuNets bending actuator stands out for its innovative use of pneumatic chambers to achieve controlled bending motion. Its flexibility, compliance, and adaptability open up new possibilities for applications in robotics, automation, and fields demanding gentle and precise motion.

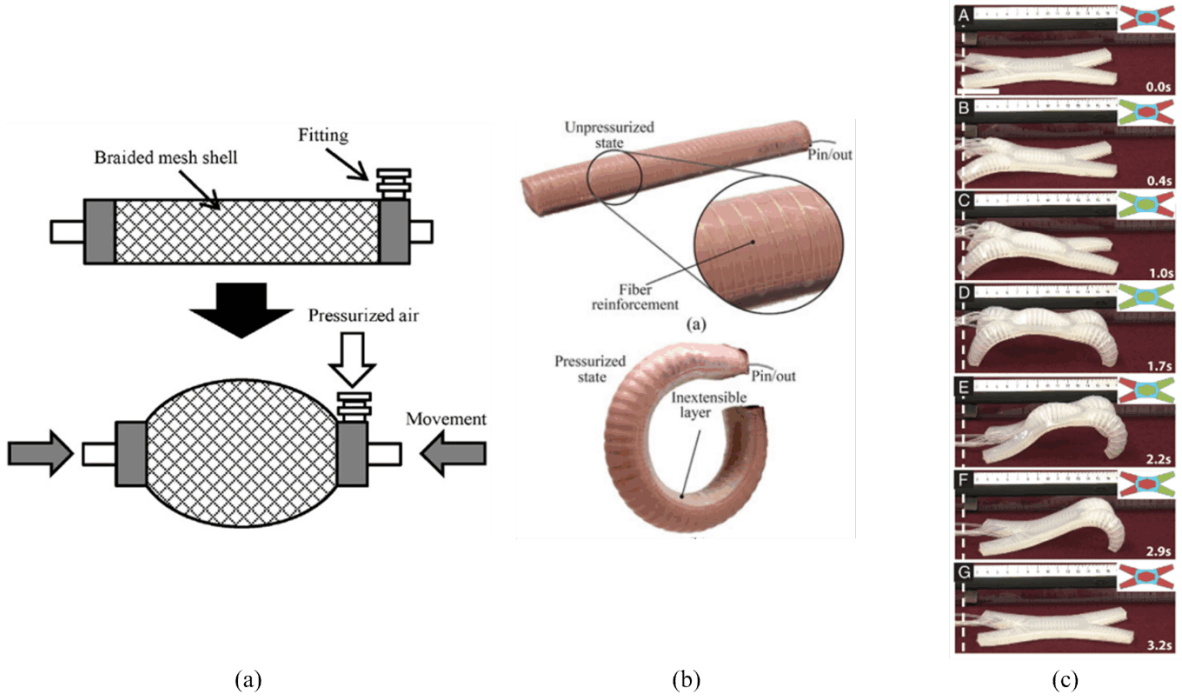

Figure 4.1 – Three extensively studied soft pneumatic positive-pressure actuators.
a) McKibben artificial muscle [132]**, b) Fiber reinforced actuator** [133]**, and c) PneuNets actuator** [134]**.**

Although positive pressure soft pneumatic actuators can generate significant functions upon activation and a wide variety of motions (contraction, bending, extension, twisting), they also have some limitations. For example, McKibben artificial muscles can only generate a contraction ratio of the order of 30% to 35%, fiber reinforced and PneuNets actuators require more complex fabrication processes, which make them fail to be the ideal actuators for numerous applications.

With the improvement of the properties of elastic materials, however, in the recent years, an emerging field of research for investigation of artificial muscles made of flexible materials and driven by negative pressure or vacuum, with little exploration before, has attracted the attention of scholars. The actuation mechanism of these kinds of artificial muscles relies on

the use of negative pressure difference between the inner and outer surfaces of the chamber (the external pressure is then always higher than the internal one) to collapse the structure, so that the different and new deformations can be generated for various applications. The deformation of an elastomeric structure is reversible since the actuator can come back to its original state when the applied vacuum is stopped, which is similar to the working process of a spring.

Inspired by this effort, a few related papers have described studies on vacuum-actuated muscle-inspired pneumatic structures (VAMPs) focusing on cheaper cost, easier fabrication and better performance compared to positive pressure artificial muscles. Stimulated by these innovative designs, some potential applications at the microscale including actuation with μKPs, could be realized in a short future. This thesis was designed with the objective of laying the first bricks necessary for the upcoming manufacture of such pneumatic microactuators.

4.2 Different types of vacuum-actuated muscle-inspired pneumatic structures

A VAMP can generate different deformations when a negative pressure difference between the internal and external pressures of a close elastic structure is applied. These deformations can be divided into linear motions including contraction [135–149] along an axis, allowing the lift of weighty objects and nonlinear motions among which bending [136,142,144,150–155], twist [136,156,157] and rotation [136,156], in order to grasp some fragile objects without any damage. Locomotion combining linear (in the sense of 1D, not in the sense of proportional) and nonlinear deformations can be generated, leading for example to the multifunction of grasping, lifting and rotating objects with one single system actuated by vacuum. Different structures have then been designed to realize different deformations, and these structures can be classified into diverse types, such as buckling-type structures made of elastic materials, origami-inspired structures, as well as bellow types structures.

4.2.1 Buckling-type elastic structures

For most structural materials, buckling is associated to a damage of the material's properties, and is usually avoided in practical applications. With soft materials, buckling can be a rapid but revertible phenomenon. Thus, this could be an advantage for artificial muscles requiring a short response time to generate diverse deformations under external stimuli, with the capacity to come back to the original state when the stimuli are stopped.

Inspired by the above consideration, buckling of elastic materials under vacuum have been

used for realizing the functions of lifting and grasping objects with contraction [135,137,139] and torsion [158]. A typical actuator is made with a structure comprising several air chambers connected with horizontal and vertical beams (Fig. 4.2a), as developed by Yang et al. [135]. When a certain level of vacuum is applied to the actuator, the horizontal beams experience a significant buckling, while the vertical beams undergo little deformation (Fig. 4.2b), resulting in a quite large contraction in the vertical direction (the observed final contraction ratio is around 40%). Therefore, with this linear compression, objects with a weight of 20 to 500 g can be lifted under a level of vacuum of around 18 kPa, for actuators (34 × 28 × 46.5 mm^3) made of Ecoflex and Elastosil, respectively. The difference is mainly due to the different Young modulus of these two materials [135].

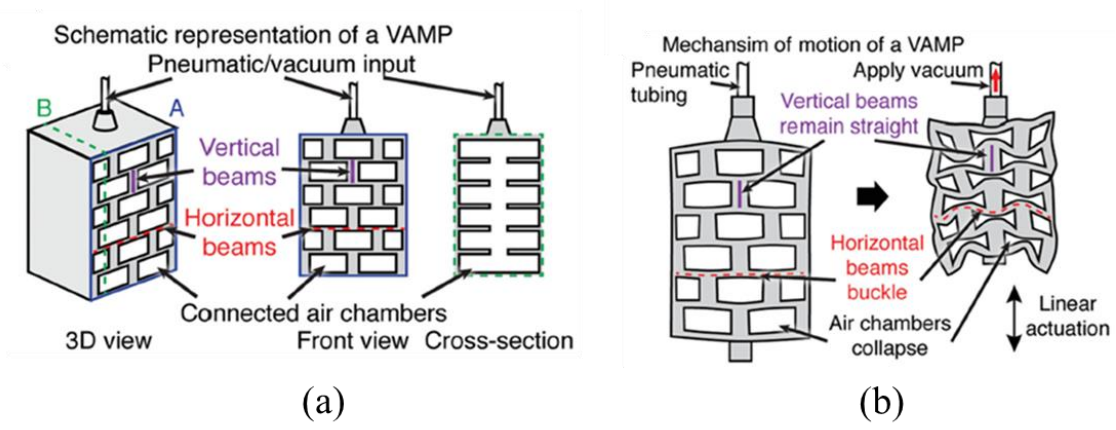

Figure 4.2 – Example of VAMP.

a) 3D view and cross-sectional views of the actuator. b) Linear actuation resulting from buckling [135]**.**

Based on a similar structure and operation principle, another linear actuator designed with a mechanical advantage (*i.e.* a magnification of the applied force) was proposed by the same group [137]. This so-called shear-VAM is made of two inextensible but flexible strips place on the lateral borders of some connected chambers (Fig. 4.3). Vacuuming the chambers results in a parallel movement of the strips with an amplification due to the geometry of the structure. In this study, shear-VAMs connected either in series or in parallel were able to lift different weights, as well as to move a paddle when two shear-VAMs were placed in an agonist-antagonist arrangement.

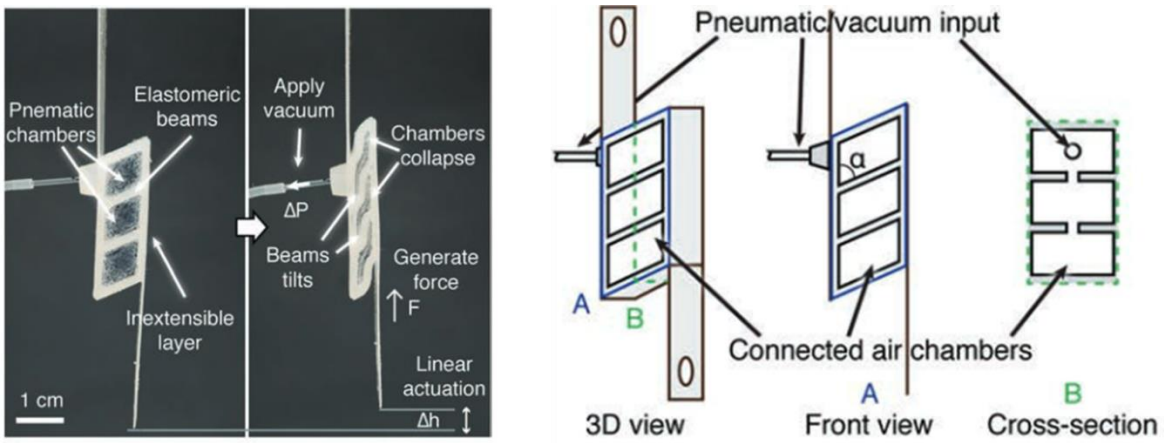

Figure 4.3 – Schematic description of a shear-mode vacuum-actuated machine (shear-VAM). a) Mechanism of motion of a shear-VAM. b) Schematic representation of a shear-VAM [137]**.**

In addition, there is another noteworthy linear actuator [139] employed in a climbing robot designed for navigating within confined tubes. This remarkable actuator possesses the capability to displace obstacles that are several times heavier than the actuator itself. Moreover, it exhibits the remarkable ability to alter its direction of movement even within tubes characterized by varying inclinations, diameters, and complex turns (as illustrated in Fig. 4.4).

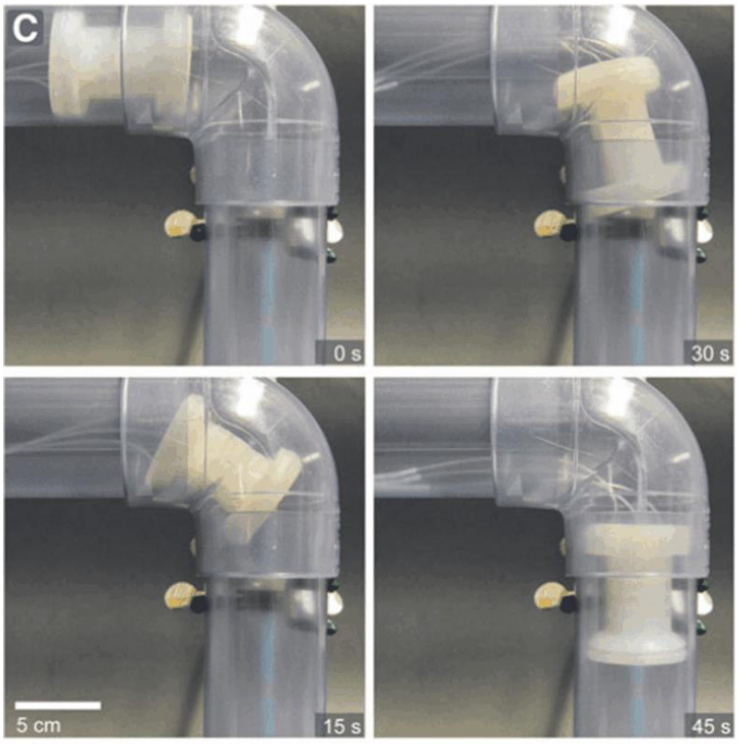

Figure 4.4 – A climber robot can change the direction of the movement at a corner in a tube [139]**.**

A non-linear actuator generating torsion under vacuum was also developed by the same

team. The elastic structure in this design comprises several interconnected air chambers that are linked to buckling pillars, featuring a non-buckling center area [158]. With a single center area structure and a maximum pressure difference of ΔP = 5 kPa, the actuator was capable of achieving a torsion angle of 30° when fully actuated. By increasing the center area to two, this versatile actuator found application as a swimmer robot and a walking trolley. Additionally, it demonstrated its adaptability as a soft gripper, allowing for the clockwise and anti-clockwise collapse of two central actuators, which could be employed, for instance, to grasp objects such as chalk, as illustrated in Fig. 4.5.

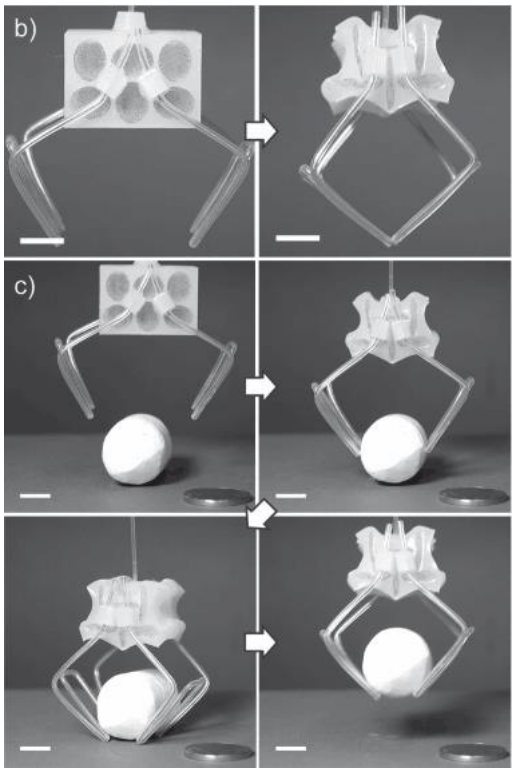

Figure 4.5 – A soft gripper made of a buckling actuator picks up a piece of chalk [158]**.**

4.2.2 Origami-inspired structures

Origami structures are very common in our daily life in art, mechanics, biology, mathematics, medical science, etc. Possessing characteristics of ease of fabrication, low cost, and simple geometries, origami structures can be used as VAMPs. Like buckling structures, origami structures can generate motions with different degrees of freedom thanks to an imposed vacuum. Recently, artificial muscles constructed by origami structures have been investigated. The reported functions of each actuator were lifting [136,140,141,148,149,159], grasping objects with different geometries [136,152,159,160], as well as mimicking the behavior of humans or

biological element.

A very simple structure (Fig. 4.6) fabricated using 3D printing, machining, casting, forming and manual techniques was reported by Li et al. [136].

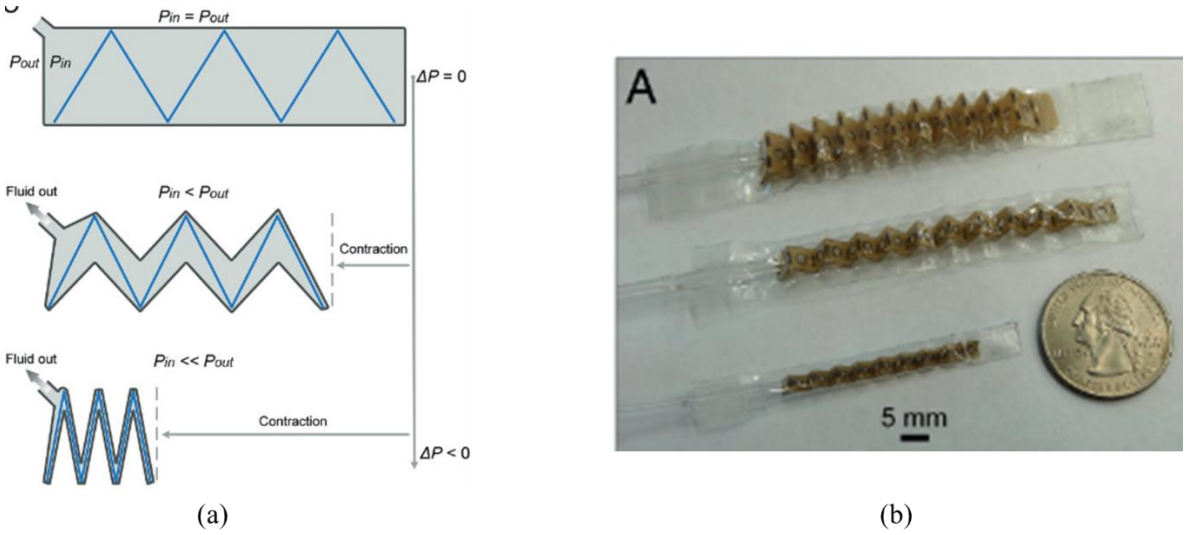

Figure 4.6 – a) Working principle of a linear origami VAMP. b) Miniature artificial muscles composed of biocompatible materials [136]**.**

Furthermore, this origami-inspired design also exhibited impressive contraction ratios in one, two, or three directions, typically falling within the range of 91% to 92%. These remarkable results were achieved by applying a negative pressure difference ranging from −60 to −80 kPa [136]. Additionally, origami-based structures like these have the potential to perform various functions, including the creation of artificial fingers that can bend in response to vacuum application.

An optimized origami VAMP was designed by Lee et al. [140,141] to achieve a large contraction ratio (Fig. 4.7). It was demonstrated that this actuator made of thin films and plastic is able to lift weights up to 8 kg with a contraction ratio of 89 % at a vacuum level of 10 kPa.

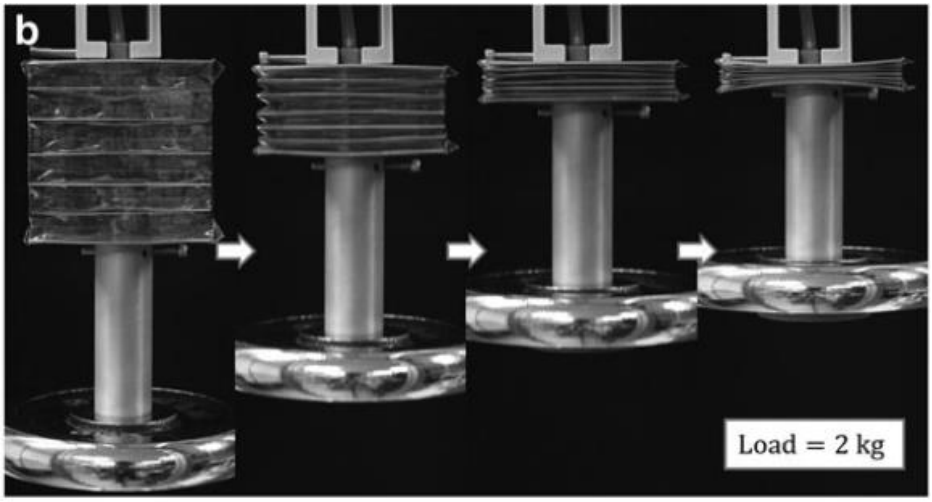

Figure 4.7 – Origami-based vacuum pneumatic artificial muscles lifting a load of 2 kg [141].

Lin et al. [159] introduced a relatively intricate structure consisting of two parallel actuators designed for grasping, twisting, and releasing a light bulb. This innovative system also demonstrated the capability to navigate through both straight and curving tubes filled with water. In this actuator design, both the central chamber and its four double-wall sides have the capacity to be subjected to vacuum. When the sides are vacuumed, it leads to an increase in their stiffness. This vacuum-induced stiffness alteration is a key factor in achieving various controlled deformations and motions in the artificial muscle. The paper elaborated on four fundamental shape-morphing mechanisms achievable through vacuum actuation (Fig. 4.8a):

- No Vacuum Pressure (mode 1): In the absence of vacuum pressure applied to any of the side chambers, the internal chamber exposed to vacuum undergoes an approximate inward buckling of its four sides.
- Vacuum on Two Opposing Sides (mode 2): When vacuum pressure is applied to two opposing sides, the muscle exhibits linear contraction deformation while being actuated.
- Vacuum on Three Sides: By reinforcing three sides, only one side of the device undergoes buckling, resulting in a bending deformation.
- Buckling and Reinforcement: In cases where one side has buckled, and the two adjacent sides are strengthened, the muscle's deformation alternates between a bending state and a contraction state.

Consequently, by harnessing these four mechanisms and applying vacuum pressure, this artificial muscle can seamlessly transition between different deformation states (Fig. 4.8b).

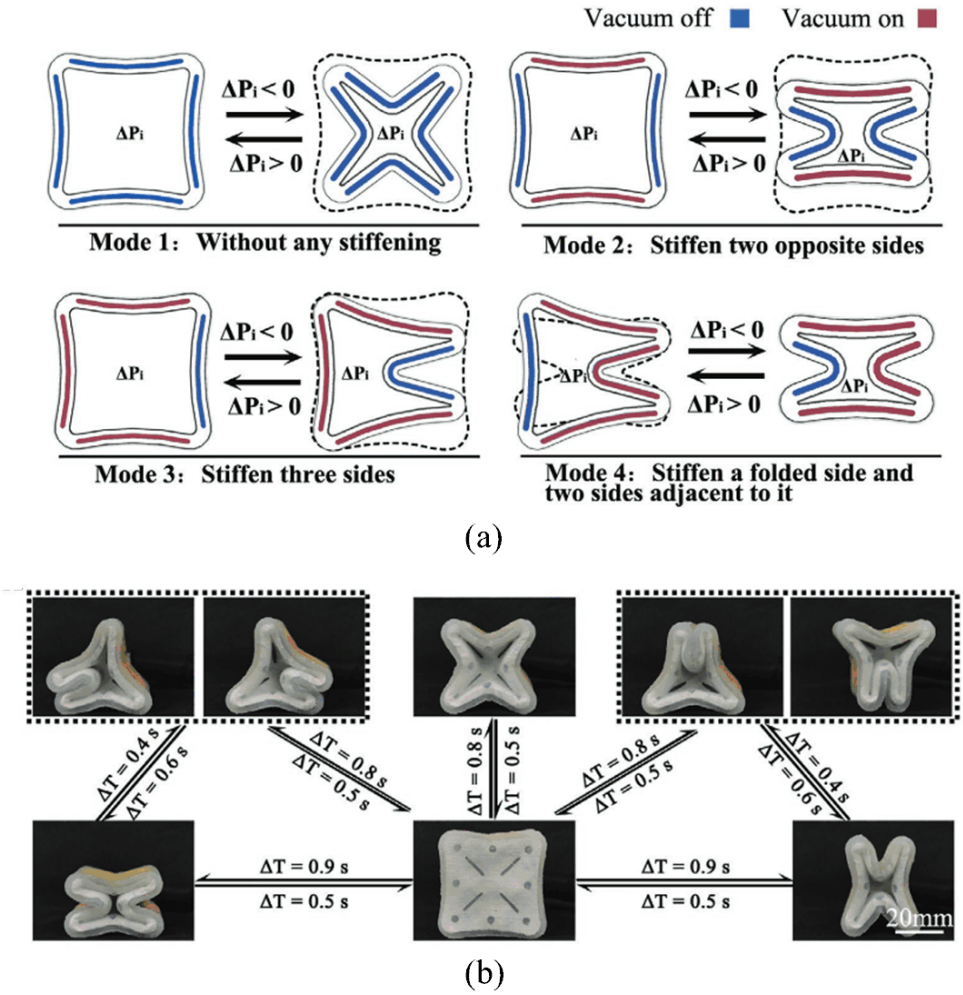

Figure 4.8 – a) Four basic shape-morphing mechanisms of elastic material artificial muscle; b) Different states of deformation with four shape-morphing types [159].

These artificial muscles have demonstrated their versatility in various applications. For instance, two hyper-redundant arms composed of artificial muscles were employed to manipulate and transfer a bulb from one socket to another. The artificial muscles underwent controlled bending and contraction when a vacuum was applied, enabling this transfer process (Fig. 4.9a).

Additionally, these artificial muscles were utilized in the creation of a pipe-climbing robot. The robot featured interconnected adhesive artificial muscles and was equipped with silicone feet, allowing it to move nimbly and freely within a pipe configuration (Fig. 4.9b). The robot's operation involved a sequence of steps: it began with all eight feet (four at the front and four at the rear) maintaining contact with the inner surface of the pipe. Then, the rear muscle folded, causing the four rear feet to detach. Subsequently, the middle muscle contracted, propelling the rear muscle forward. The rear muscle unfolded, re-establishing contact between its four feet and the inner pipe surface. Next, the front muscle folded, leading to the detachment

of the four front feet. Finally, the middle muscle elongated, pushing the front muscle forward. The front muscle unfolded, completing a full cycle of motion. This intricate sequence of actions allowed the robot to effectively climb within the pipe, demonstrating its potential for a wide range of practical applications.

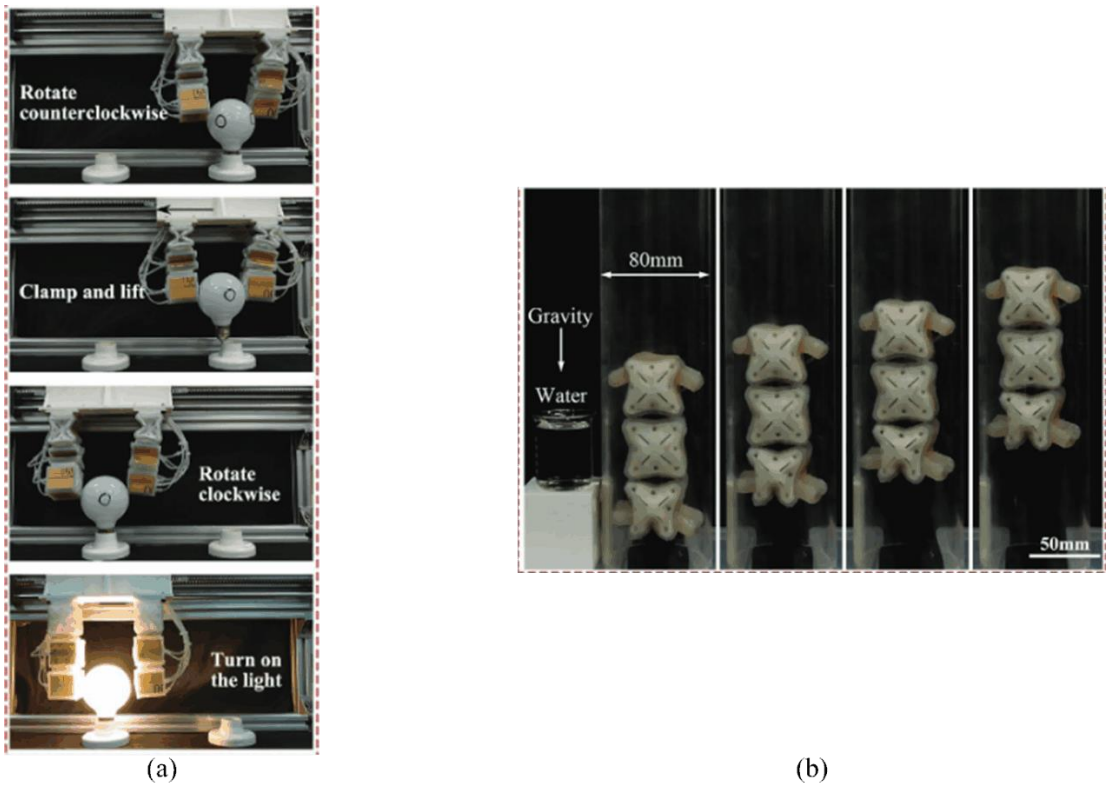

Figure 4.9 – Versatility exhibited by interconnected artificial muscles with "skeletons". a) Two hyper-redundant arms are employed to detach a bulb from one socket and subsequently affix it onto another socket; b) The "caterpillar" robot designed for pipe climbing, demonstrates the ability to ascend pipes of diverse geometries [159]**.**

The development of re-foldable bidirectional twisting actuators inspired by origamis, as demonstrated by Jiao et al. [157], enables the replication of complex biological motions such as those observed in the human neck, wrist, ankle, and biceps, as well as the ability to achieve multimode morphing. These actuators rely on different crease patterns inspired by origami to achieve diverse motions.

The working principle of these re-foldable artificial muscles is illustrated in Fig. 4.10 and is controlled by applying vacuum inside two chambers, namely, chamber A and chamber B, in the following steps:

- When vacuum is applied to chamber B, it collapses, causing pillar 3 (connected to chamber B) to buckle, resulting in a certain clockwise inclination of the buckled pillar

3. However, since chamber A is not actuated, the other three pillars do not buckle, and there is no twisting motion (Fig. 4.10C).

- When vacuum is applied to both chambers A and B, a different scenario unfolds. In this case, the buckling of the remaining three pillars occurs as chamber A collapses. This generates an anticlockwise torque that causes the remaining three pillars to buckle in the anticlockwise direction. Consequently, the twisting motion of the top facet is initiated, which drives the buckled pillar 3 to twist anticlockwise (Fig. 4.10D).

Additionally, it has been observed that the collapsed artificial muscle exhibits a distinct bi-stable feature when both chambers are collapsed (Fig. 4.10E). This bistability allows for the reversible transition of pillar 3 from the clockwise-buckled state to the anticlockwise-buckled state when chamber A is actuated. As a result, the bistability of the collapsed artificial muscle facilitates the switch between two different steady states, enabling bidirectional torsional movements of the artificial muscle.

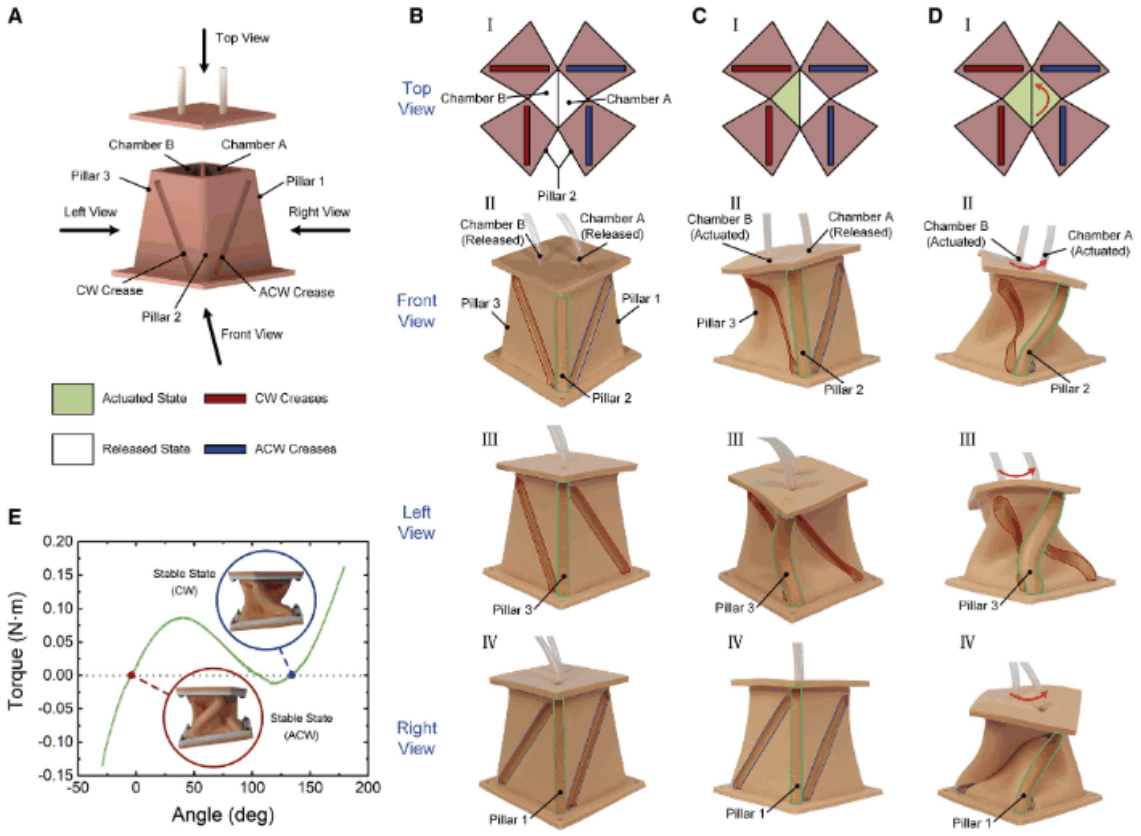

Figure 4.10 – Working principle of a re-foldable square-twist artificial muscle.
(A) Diagram of re-foldable square-twist artificial muscle. (B) Initial state of the muscle from different views. (C) Chamber B is actuated. (D) Chamber A is actuated. (E) Torque–angle curve exhibiting a bistable structure [157]**.**

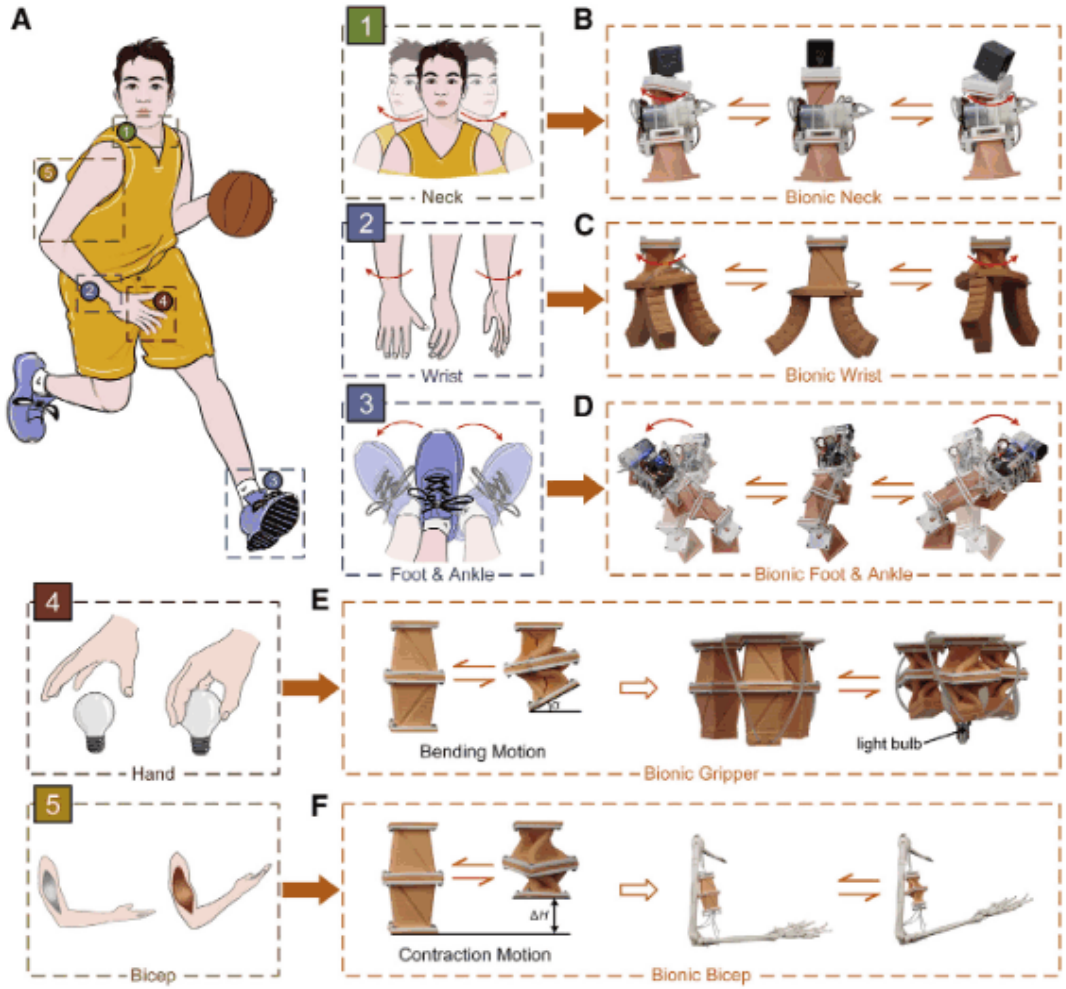

Figure 4.11 – Multifunctional bionic locomotion of re-foldable square-twisting artificial muscles. (A) An individual doing varied biological maneuvers while playing basketball. (B) Re-foldable square torsion artificial muscle is used as a bionic neck to rotate its onboard camera. (C) A re-foldable square twisting artificial muscle is attached to the flexible hand to function as a bionic wrist. (D) A re-foldable square-twisting artificial muscle is used as bionic feet and ankles to enable crawling robots to turn in place. (E) Two re-foldable square torsion artificial muscles combined to form a flexor muscle for assembling a bionic grasping hand. (F) Two re-foldable square-twisting artificial muscles combined to form a contractile muscle used as a bionic biceps to pull the lower arm up [157].

The re-foldable square-twist artificial muscle, as demonstrated in the paper, finds extensive applications in mimicking a variety of bionic motions in soft robots, as depicted in Fig. 4.11. Leveraging its bidirectional twisting function, this artificial muscle enables the replication of important torsional organs found in biology:

- Bionic Neck (Fig. 4.11B): By employing the bidirectional twisting feature of the re-foldable square-twist artificial muscle, it can replicate the torsional movement of a biological neck, allowing soft robots to achieve similar motions.
- Bionic Wrist (Fig. 4.11C): The artificial muscle can mimic the twisting motion of a

wrist, demonstrating its versatility in replicating complex biological movements.

- Bionic Foot and Ankle (Fig. 4.11D): Similarly, the muscle can imitate the motions of a foot and ankle, showcasing its potential in achieving lifelike locomotion.

Additionally, the re-foldable square-twist artificial muscles are capable of performing bionic flexion and contraction movements, which can be selectively decoupled by using multiple muscles in combination:

- Bionic Gripper (Fig. 4.11E): By combining several of these artificial muscles, they can replicate the flexion and contraction actions observed in biological grippers, enabling soft robots to grasp and manipulate objects effectively.
- Bionic Bicep (Fig. 4.11F): The artificial muscles can imitate the flexing and contracting motions of a bicep muscle, further expanding their applicability in creating lifelike robotic structures.

These diverse bionic motions highlight the adaptability and potential of re-foldable square-twist artificial muscles for soft robotics applications, where the replication of biological movements is crucial.

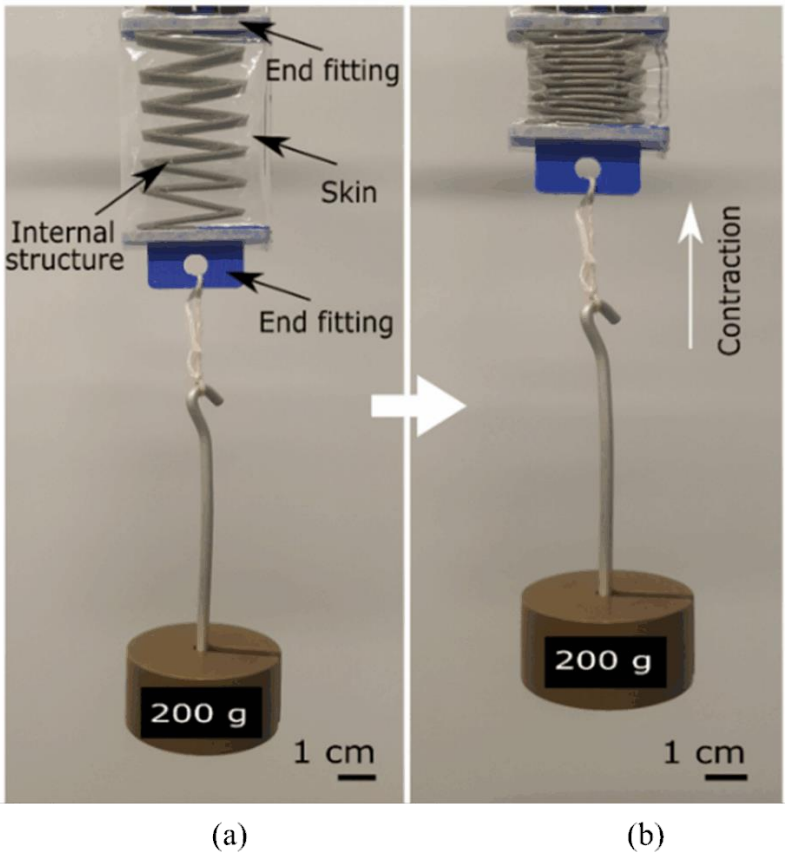

Figure 4.12 – Low-profile vacuum-powered manual muscle LP-VPAM, directly driven by an electric vacuum pump, load capacity 0.2 kg ($\Delta P = -40$ kPa). (a) Unactuated state and (b) actuated state [148].

A medical application of vacuum-powered artificial muscles, known as the low-profile vacuum-powered artificial muscle (LP-VPAM), was specifically designed to assist infants with limb disabilities. This innovative LP-VPAM (Fig. 4.12) comprises three key components:

- Zigzag Structure or Skeleton: This forms the core of the artificial muscle, providing a structural framework.
- End Fittings: These components are crucial for connecting the artificial muscle to the load or limb that needs assistance.
- Skin: The outer layer that encapsulates the artificial muscle, offering protection and facilitating the muscle's function.

Remarkably, this LP-VPAM was capable of lifting a load of 0.2 kg using a pressure difference of –40 kPa. Furthermore, experimental results, including characterization and dynamic response assessments, indicated that the LP-VPAM had the potential to assist infants in moving their legs. This agonistic-antagonistic configuration allowed infants to undergo rehabilitation with encouraging results, demonstrating the effectiveness of such artificial muscles in aiding the mobility of infants with limb disabilities (Fig. 4.13).

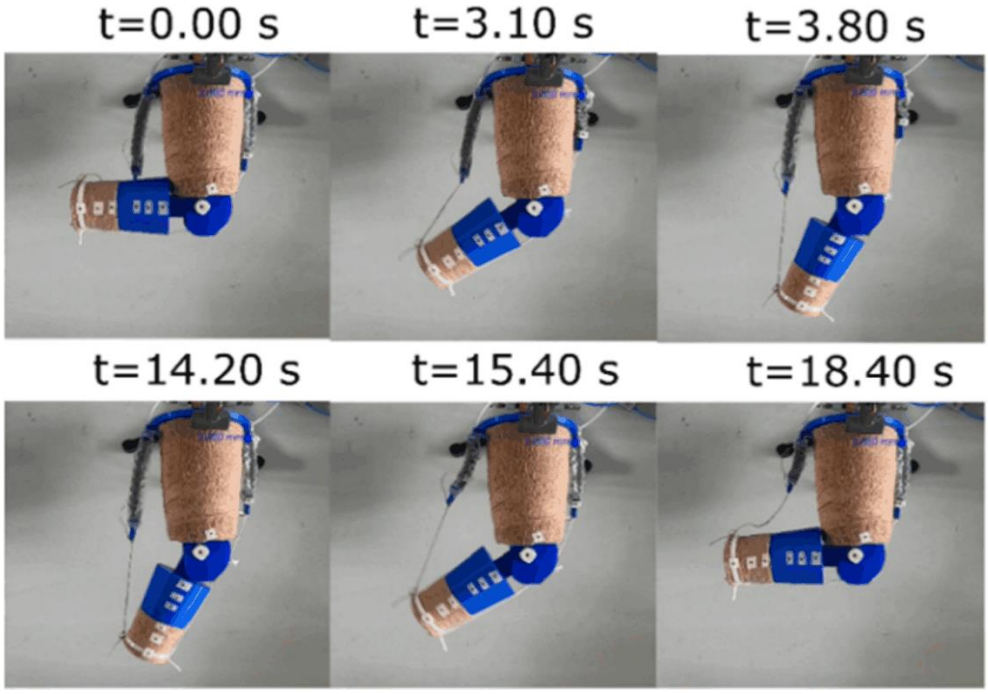

Figure 4.13 – Time series images of infant leg models demonstrating rehabilitation movements in extension (upper three frames) and flexion (lower three frames) states [148]**.**

4.2.3 Bellows-type actuators

Bellows, as the folded structures, are also widely used in practical life. Used as VAMPs, a large reduction in the length of the bellow can be obtained.

A concept and the modeling of bellows actuators with optimal mechanical performance was proposed by Felt et al. [138]. This kind of bellows consists of a series of parallel rigid rings connected to an inextensible tubular membrane (Fig. 4.14). It was demonstrated that by increasing the number of rings, a higher contraction ratio could be achieved, and by increasing the ring spacing, the work output of the actuator can be concentrated in the initial part of the stroke.

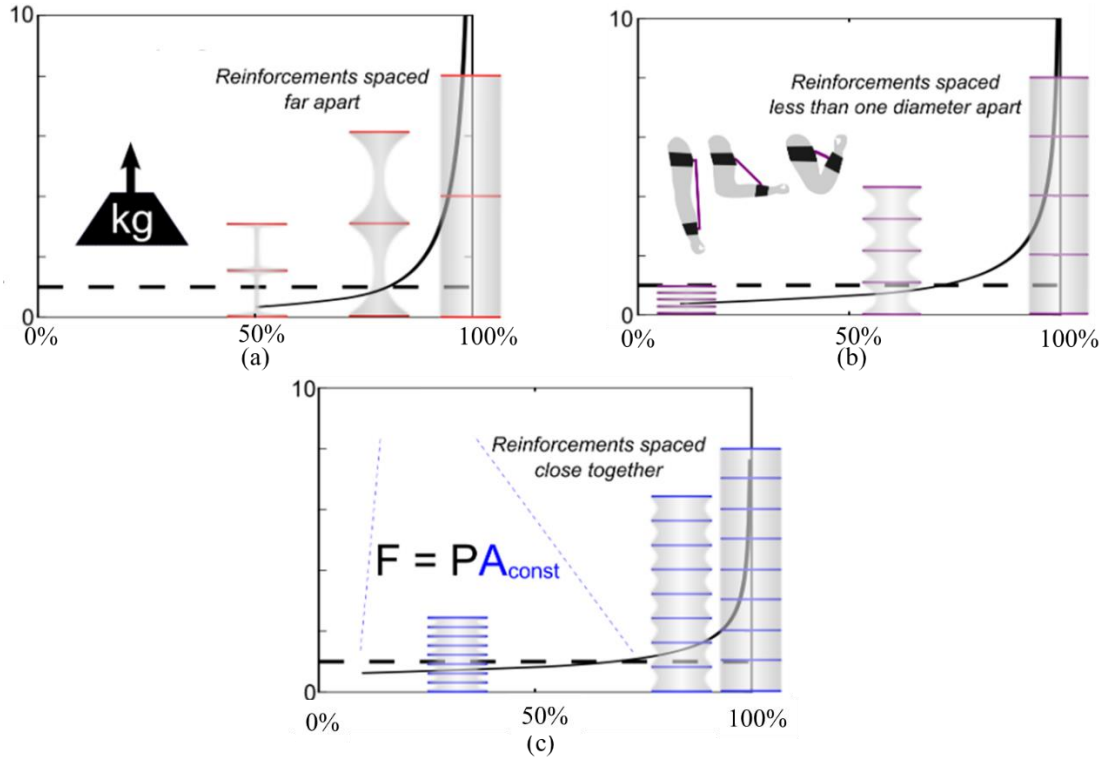

Figure 4.14 – This bellows is a tubular membrane connected to evenly spaced internal rigid reinforcing rings. By changing the spacing of the rings attached to the inside of a membrane tube, the force profile can be customized to obtain (a) high peak forces, (b) high contraction ratios and (c) an approximately constant force-per-unit-pressure [138]**.**

By using a low-cost open-source fused deposition modeling 3D printer, several linear soft actuators (Fig. 4.15) activated through vacuum were directly manufactured [144]. The modeling, performance, and applications of these actuators were explored. From a combination of numerical and experimental investigations, several advantages of these actuators were demonstrated, including high bandwidth, high output force and long lifetime (around 21500 cycles).

Moreover, analytical and finite element models were able to accurately predict the blocked force (*i.e*. the maximum force or load that the muscle can exert) and linear stroke of the actuator. Besides, it was also demonstrated that the thickness of the wall of these bellows plays a significant role on the performance of actuators. Measurements during practical applications of weights lifting by connecting the actuator to elbow joints, and grasping objects with different surface and geometries were successfully performed.

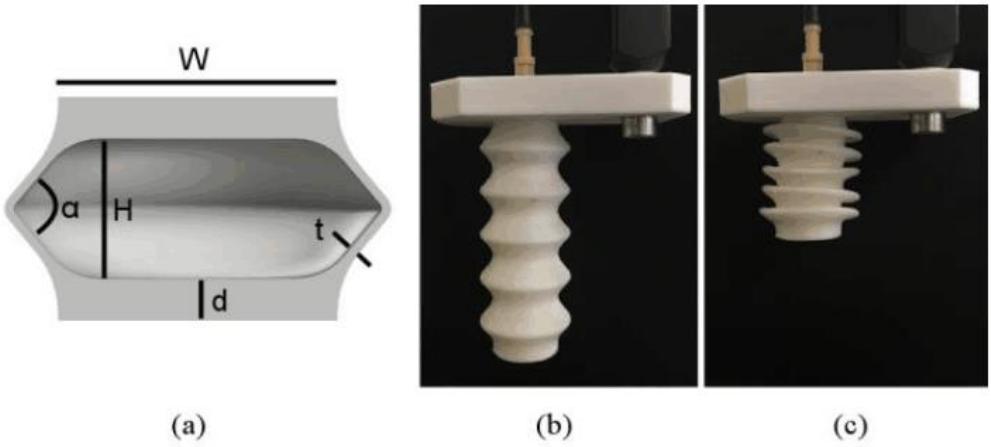

Figure 4.15 – a) Dimensions and cross-sectional view of a soft vacuum actuator. $W = 20$ mm, $H = 10$ mm, $d = 3$ mm, $t = 0.90$ mm, $\alpha = 110°$**; b) Initial position when no vacuum is applied; c) Final position when 95.7 % of vacuum is applied** [144]**.**

To predict the output force of vacuum-actuated artificial muscles as a function of their contraction ratio, Gollob et al. [146] proposed a generalized modeling tool. This tool utilizes the virtual work principle and a simplified geometrical approach. Essentially, it aims to provide a predictive model that relates the contraction ratio of these muscles to the force they can generate. Such modeling tools are essential for understanding and optimizing the performance of vacuum-actuated artificial muscles in various applications. This modeling tool was applied to origami structure and bellow type actuators (Figs. 4.16a and b). An analytical method and finite element modeling were implemented. Some fabricated actuators were experimentally tested, showing the versatility and the efficiency of the proposed model. The experiments on bellow type actuator confirmed that a high contraction ratio of 80 % was achievable.

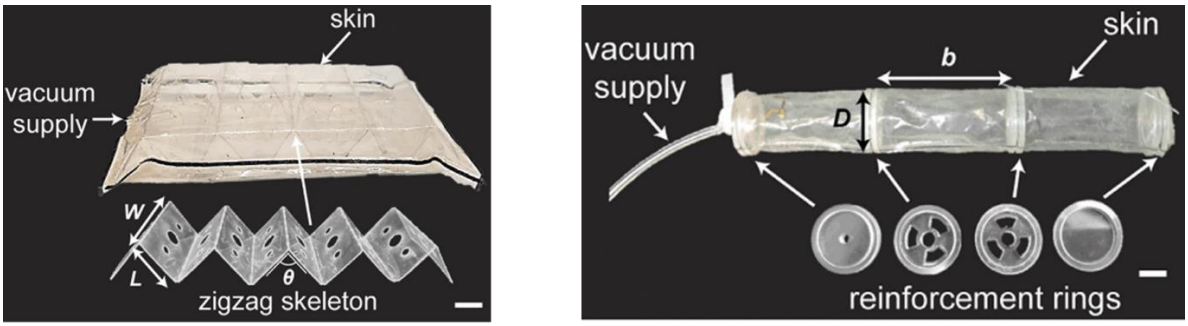

(a) (b)

Figure 4.16 – Actuator prototypes fabricated in by Gollob et al. [146]**.**
a) A fluid origami artificial muscle; b) a vacuum bellows actuator.

Recently, a novel ultralight hybrid pneumatic artificial muscle (UH-PAM) (Fig. 4.17a) was explored by Joe et al. [147]. It was composed of three main parts: a hyperelastic skin that encases the other two parts including open-cell foam cylindrical segments and plastic rings. The bellows-type structure allows the actuator to achieve high contraction, and the open-cell foam is able to ensure structural stability during actuation. In addition, the plastic rings are capable of enhancing stiffness of the structure along the longitudinal axis (or axial stiffness) to avoid undesired deformation. It was analyzed by combining numerical, analytical and experimental approaches. The results illustrated that an actuator only 20 g in weight could lift a payload of 3 kg, with an achieved maximal contraction ratio is around 50 %. Furthermore, the configuration of the actuator was optimized for its static and transient behaviors. Meanwhile, the approach has potential applications such as manipulation of 3 degrees-of-freedom platforms (Fig. 4.17b). The device is mainly composed of three actuators separated from each other by $120°$. At the top side, each actuator supported by a Plexiglas© frame was linked to a vacuum line. In the bottom side, a plastic cone embedding the localization probe of the tracking system was attached to each actuator. As a result, various displacements or orientations of the bottom cone can be smoothly generated by adjusting vacuum in each actuator. Finally, the tracking system acquires the 3D coordinates of the cone tip.

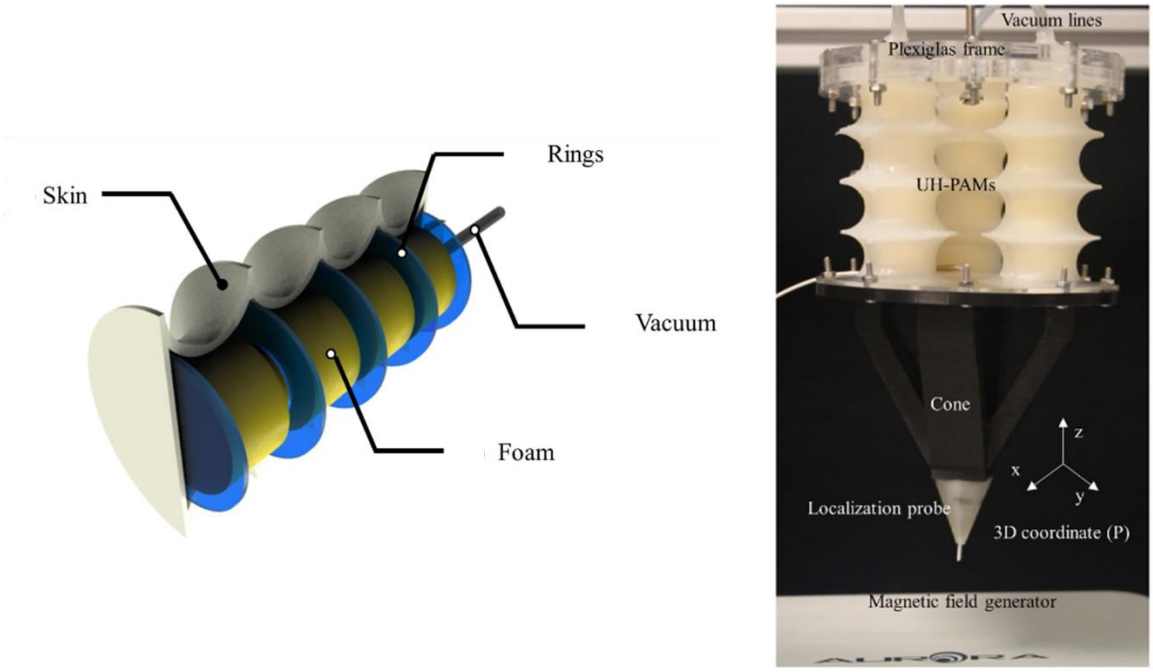

Figure 4.17 – a) Concept design of the bellow-type pneumatic artificial muscle; b) Configuration of a 3 degrees of freedom Stewart platform integrating 3 actuators [147]**.**

This section provides an overview of different types of vacuum-actuated artificial muscles, highlighting their varying deformations at different levels of vacuum and the diverse materials used in their construction. The information (including dimensions) for each type of actuator discussed in this section is summarized in Table 4.1. It's important to note that all of them operate under atmospheric conditions, using air as the working gas.

Future research in this field should focus on optimizing the performance of these soft vacuum-actuated artificial muscles, aiming to enhance their capabilities and broaden their applications.

Table 4.1 – Information of each actuator described in the chapter.

Ref	Year	Material	Deformation	Vacuum level	Type of the actuator	Dimensions
[135]	2016	Ecoflex/Elastosil	Linear contraction	90 kPa	Buckling	34 × 28 × 46.5 mm^3
[137]	2016					17 × 13 × 1.8 mm^3
[139]	2018			95 kPa		34 × 28 × 46.5 mm^3
[158]	2015	Silicone elastomer	Torsion	5 kPa		22 × 22 × 78 mm^3
[136]	2017	PEEK/PVC film	Contraction/bending	80 kPa	Origami	NA
[141]	2019	Polyvinyl chloride	Linear contraction	10 kPa		150 × 150 × 150 mm^3
[159]	2020	Ecoflex00-30		10 – 80 kPa		NA
[148]	2021	Filaflex		40 kPa		38 × 5 × 60 mm^3
[138]	2018	Acrylic/polythene		4.6 – 6 kPa	Bellows-type	48 mm in diameter 205 mm in length
[144]	2019	NinjaFlex		20 kPa		20 mm in diameter 80 mm in length
[146]	2021	Fibreglast/McMaster-carr		25 kPa		20 × 40 × 0.05 mm^3
		McMaster-carr		15 kPa		25 mm in diameter 150 mm in length
[147]	2021	McMaster-carr/plexiglass		80 kPa		34 mm in diameter 78 mm in length

4.3 Summary

As a new field recently developed, research on artificial muscles activated by negative pressure difference is of the great interest owing to a series of advantages such as ease of fabrication, flexibility, light weight, safe for human applications, operation under extreme environments, etc. Compared to inflated pneumatic artificial muscles, the deflated ones are able to have higher contraction ratios with much lower pressure difference. Different types based on the bulking of flexible materials, origami structures, and bellow shape have been developed, sometimes inspired by practical life. Furthermore, multifunctional vacuum-actuated artificial muscles have been proposed with functions including grasping, lifting and twisting objects which various shapes, mimicking biological motions, swimming in liquids and walking like a trolley.

For the existing artificial muscles actuated by vacuum, however, the working gas is always air, and the external pressure of the structure is atmospheric pressure. It should be possible to use some other working safety gas such as nitrogen, to explore specific applications. Anyhow, the proposed designs provide a solid foundation for further investigations on potential applications, particularly at the microscale, that was little investigated up to now.

Considering that Knudsen micropumps can be used as miniaturized vacuum generators, combination of μKPs with μVAMPs is a challenging area of research. Each VAMP part of a complex micro-actuator could be controlled by its own KP in order to provide complex movements at the microscale. To investigate this idea, Chapter 5 presents the design, fabrication and test of bellow-type VAMPs at a mini-scale and a first attempt to produce them at the microscale by the TPP technique. Some preliminary calculations are then presented in Chapter 6 to assess the dynamics of this μVAMP and the possibility to actuate it thanks to a μKP.

Chapter 5 - Numerical simulations and experiments on artificial pneumatic mini-muscles and fabrication of pneumatic micro-muscle

Introduction

Controlled by negative pressure or vacuum, artificial muscles, with different structures fabricated from various materials mentioned in Chapter 4, can generate diverse deformations covering contraction, bending, twisting, and torsion, as well as combinations of two or more deformations. Thus, the performance of artificial muscles can possibly be characterized by contraction ratio, tortuosity, and torsion angle determined by the pressure difference. On the other hand, the speed required to achieve the target deformation is the time response dominated by the mass flowrate. It is also one of the vital parameters for evaluating the performance of artificial muscles. Precisely, the pressure difference and the mass flowrate are the two most important indices to characterize KPs. Therefore, considering the combination of artificial muscles and KPs is a relatively innovative concept. The first step is taken to explore this goal in the present work.

In this chapter, the structure of artificial mini-muscles is designed in the shape of bellows, and the deformation is initially limited to linear contraction instead of complex locomotion to simplify the model in the ABAQUS software. Three identical samples, each composed of three bellows and one soft tube, are fabricated using 3D printing techniques. A simple experimental workbench is also developed for practical tests with different pressure differences between the inner pressure of the muscle and atmospheric pressure.

The contraction ratios of the mini-muscles under diverse pressure differences are extracted from images and videos using a Python code, and a comparison between experimental and numerical results is then performed. The work presented in this chapter was greatly aided by a group of students who completed their internship in the microfluidic group. They are Elek Bogaers, Lea Decroix, Pablo Mir, Lucia Vicente-Martinez, and Thomas Villemez.

The chapter is completed by a first partially successful attempt of fabrication of a micro-muscle by the TPP technique.

5.1 Statement of the problem

A bellows-like artificial muscle composed of several bellows in series operates in a com-

pression manner when negative pressure is imposed inside the muscle [144,148,149,161]. In this type of structure, the only deformation that occurs is a linear contraction along the axis of the muscle. The primary working principle is as follows: In the initial state with no pressure difference, the muscle remains undeformed while maintaining its maximum length. As the deflation process begins, the bellows are compressed simultaneously, leading to a reduction in length. Eventually, the muscle becomes completely compressed at a specific pressure difference, referred to as the critical pressure difference. This critical pressure difference represents the minimum pressure required for the muscle to achieve full compression. Beyond this point, the muscle will not contract any further, regardless of any increase in pressure difference.

When the pressure difference is released, following the relaxation of the deflation process, the muscle gradually returns to its initial state over a period of time. Therefore, the linear contraction of a bellows-like artificial muscle, characterized by the contraction ratio, is dependent on the critical pressure difference, naturally linked to the material properties of the muscle.

From the initial state of the muscle at initial time $t_0 = 0$ and the maximum initial length L_0 (Fig. 5.1a), at time $t > t_0$, the length of the muscle is reduced to L (Fig. 5.1b); the contraction ratio e can be readily defined as the ratio of the reduction of length ΔL over L_0:

$$e = \frac{\Delta L}{L_0} = \frac{L_0 - L}{L_0} = 1 - \frac{L}{L_0} \tag{5.1}$$

Therefore, the contraction ratio varies with time between 0 and $e_{max} = 1 - L_{min}/L_0$ for with the length reaches its minimal value L_{min}.

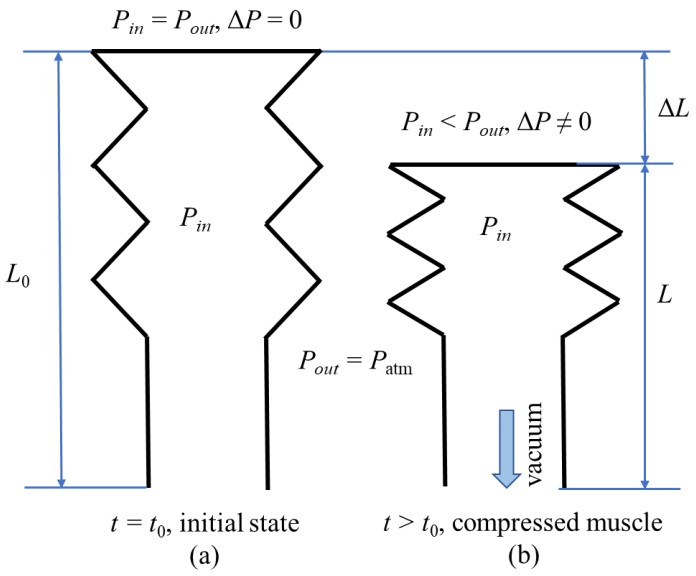

Figure 5.1 – Illustration of the deformation of a bellows-like artificial muscle.

The objective of this work is to fabricate a mini-muscle, to test its ability to work under negative pressure actuation and to model and measure its static characteristics $e = fct(\Delta P)$ and dynamic characteristic $e = fct(t)$ when a pressure difference step ΔP is applied.

5.2 Manufactured bellows-like artificial mini-muscles

In this work, three identical samples of bellows-like artificial mini-muscles with three bellows (Fig. 5.2a) were 3D-printed by the company Protolabs Ltd, Le Bourget-du-Lac, France, using the Polyjet technology able to print a deformable structure made of Protolabs white photopolymer.

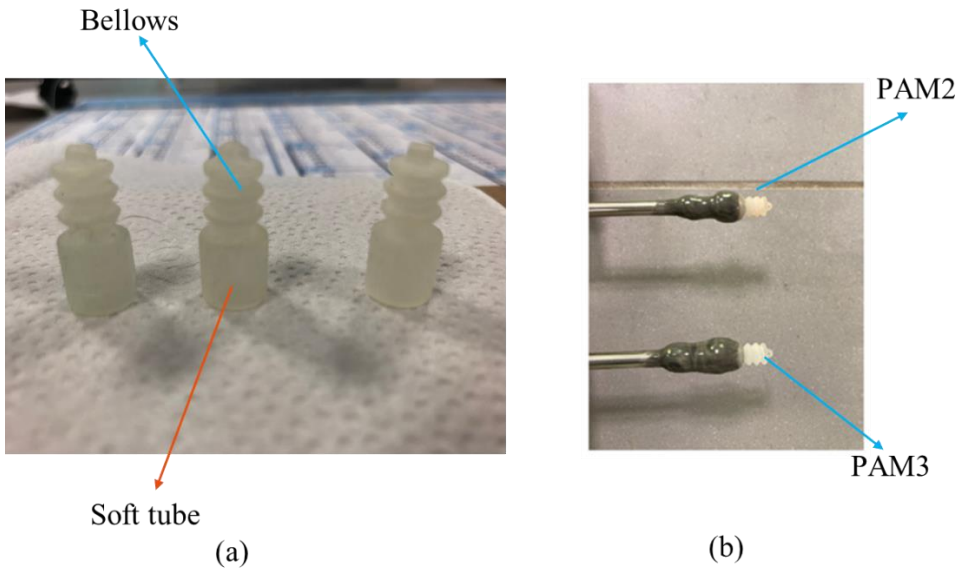

Figure 5.2 – 3D-printed bellows-like artificial muscles. a) Three fabricated samples; b) Samples PAM2 and PAM3 glued to stainless tube (inner diameter: 3.8 mm, outer diameter: 6 mm)

Details on the dimensions of the mini pneumatic artificial muscles (PAMs) are given in Section 5.3.2. Their bottom part is a circular cylinder 6 mm in diameter and 10 mm in length, able to be glued on a stainless tube (Fig. 5.2b) for being connected to the experimental bench. The bellows part of interest of the PAMs at rest are 11.5 mm in length and 4.4 mm in radius. The hardness of the material was characterized by its Shore A index. The smaller the Shore A, the more flexible the material. The muscles were printed with a Shore A index equal to 30, which is the smallest index offered by the company for this kind of material, the properties of which are summarized in Table 5.1.

Table 5.1 – Properties of white photopolymer from Protolabs Ltd.

White Photopolymer Shore A 30	
Tensile tear strength (kN/m)	5.0 − 7.0
Elongation at break (%)	220 − 270
Shore hardness (Scale A)	30 − 35
Tensile strength (MPa)	2.4 − 3.1

The properties listed in the table have specific physical meanings, which are defined as follows:

- Tensile Tear Strength: This property is a force per unit of specimen thickness that measures a material's ability to resist tearing when it is stretched. It is typically used for non-metallic materials such as rubber, polymers, fabrics, etc. The test gives a measure of how the test specimen resists the growth of any cuts when under tension.
- Elongation at Break: Elongation at break is a measure of a material's ductility. It is defined as the ratio of the elongation of a specimen when stretched to the point of fracture to the initial length of the specimen. It is expressed as a percentage and provides information about how much a material can be stretched before breaking.
- Shore Hardness: Shore hardness is a parameter commonly used to assess the softness or hardness of a material, as well as its abrasion resistance. It quantifies the material's resistance to indentation or penetration by a harder object. Shore hardness values are determined using specific tests, such as the Shore durometer test.
- Tensile Strength: Tensile strength is the maximum tensile (pulling) force that a material can withstand when subjected to a tensile force. It is a measure of the material's strength and durability and indicates how much force it can endure without breaking or deforming significantly.

These properties are crucial for understanding the mechanical behavior and performance of materials, especially in applications where materials are subjected to forces, stretching, tearing, or abrasion.

5.3 Numerical modeling on Abaqus

To comprehensively assess the performance of the mini-PAMs, a numerical modeling approach was employed using Finite Element Analysis (FEA) software, specifically Abaqus. The complex geometry of the mini-PAMs was initially simplified by adopting an axisymmetric model. Additionally, two supplementary muscle models were developed: one incorporated

a 3D-shell approximation for the membrane, while the other featured the complete 3D geometry. These diverse models enabled numerical simulations with practical assumptions, enabling the exploration of a broader range of geometries for study.

5.3.1 Material model

In terms of the deformation of PAMs, hyperelastic models capable of analyzing large deformations are suitable for numerical modeling of highly nonlinear materials. These nonlinear materials exhibit an instantaneous elastic response to significant deformations [162]. They can sometimes be stretched up to 1000 %. Additionally, they are nearly incompressible since deformation results from the straightening of the material's molecular chains. As a result, there is minimal volume change under applied stress. Furthermore, hyperelastic materials demonstrate a highly nonlinear stress-strain relationship. Several models, including the Neo-Hookean model, the Mooney-Rivlin model, the Ogden model, the Arruda-Boyce model, and the Yeoh model, have been proposed to approach the behavior of hyperelastic materials, which find applications in predicting and analyzing the mechanical properties of items like rubber products (such as rubber seals) or biological materials (like muscles) [162].

In this chapter, we have opted for the simplest among the commonly used hyperelastic models, the Neo-Hookean model, to model the behavior of the white photopolymer (Shore A = 30) from Protolabs. This choice is based on several advantages of the Neo-Hookean model [162]:

1. The model is well-suited for predicting the mechanical behavior of geometries with compression ratios ranging from approximately 30 % to 40 %.
2. Although this model typically requires two input parameters (initial shear modulus and bulk modulus), only the initial shear modulus is necessary here since the material is nearly incompressible.
3. Parameters derived from one strain-stress curve can be applied to predict the material's behavior under various strain conditions, rendering the model compatible for our purposes.

To employ the Neo-Hookean model for quantifying the behavior of PAM in Abaqus simulations, two parameters are essential: the material constant C_{10} and the material incompressibility parameter D_1 [6]. These parameters, which are temperature-dependent, can be derived from the equation of strain energy potential that governs the Neo-Hookean model [163]:

$$U = C_{10}\left(\bar{I}_1 - 3\right) + \frac{1}{D_1}\left(J^{el} - 1\right)^2, \tag{5.2}$$

where U is the strain energy per unit volume, J^{el} the elastic volume ratio and $\bar{I}_1$ is the first deviatoric strain (trace of the right Cauchy-Green deformation tensor), defined by

$$\bar{I}_1 = \bar{\lambda}_1 + \bar{\lambda}_2 + \bar{\lambda}_3 . \tag{5.3}$$

Here, $\bar{\lambda}_i = J^{-1/3}\lambda_i$ are the deviatoric stretches, J being the total volume ratio and λ_i the principal stretches. The coefficients C_{10} and D_1 are essential to determine the initial shear modulus μ_0 (or 2nd Lamé coefficient) and the bulk modulus K_0 (or 1st Lamé coefficient) of the Neo-Hookean model:

$$\mu_0 = 2C_{10} \qquad K_0 = \frac{2}{D_1} \tag{5.4}$$

In our simulations, $D_1 = 0$ since the considered hyperelastic materials are supposed incompressible. Moreover, for calculating C_{10}, the initial shear modulus μ_0, expressed by

$$\mu_0 = \frac{\tau_s}{\sigma_s} , \tag{5.5}$$

should be derived. In Eq. (5.5), τ_s is the shear stress linked to the tensile strength $N_t = 2\,\tau_s$, and σ_s is the limit shear strain. For the PAM's material of the present work, $N_t = 2.4$ MPa, and consequently $\tau_s = 1.2\,\text{MPa}$. In addition, the limit shear strain, defined the relative elongation reached at break of the material, is given around 2.2 (220 %), therefore, the shear modulus $\mu_0 = 0.545\,\text{MPa}$, and $C_{10} = 0.272\,\text{MPa}$.

5.3.2 Models of bellows-like artificial mini-muscles

The muscle's geometry, which dimensions are detailed in Fig. 5.3 and Table 5.2, was replicated for modeling purposes. Three distinct models were formulated to characterize the muscle, each serving a specific purpose: an axisymmetric model, a shell model, and a full 3D model.

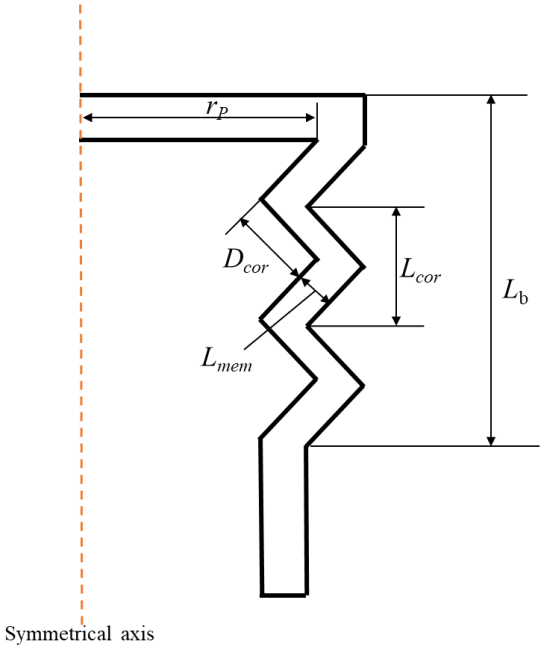

Figure 5.3 – Definition of the dimensions of the mini-muscle tested in the present work.

Table 5.2 – Dimensions of the bellows-like artificial mini-muscles.

Corrugation			L_{mem} (mm)	r_P (mm)	L_b (mm)
Number	L_{cor} (mm)	D_{cor} (mm)			
3	3	1.9	0.57	4.44	11.43

Axisymmetric model

Given the axisymmetric structure of the proposed muscle, an axisymmetric numerical model was created (as shown in Fig. 5.4a) to simplify the actual model and reduce computational costs. Additionally, due to the need to accurately depict the large deformations of the PAM under vacuum, contact interactions were introduced. Specifically, "Self-contact" interactions were established to account for contact points between various areas of the surfaces. This approach offers a straightforward yet powerful way to define contacts, enabling efficient and economical calculations.

Subsequently, loading and boundary conditions (as illustrated in Fig 5.4b) were applied to the model to replicate the muscle's behavior. The process of depressurization within the cavity of the artificial mini-muscle was simulated using negative pressure forces acting perpendicular to the inner surfaces of the model. These pressure forces ranged from –5 kPa to –50 kPa, with increments of 5 kPa.

The sealing of the PAM with the tube was simulated by embedding the end of the PAM into the tube, replicating the real-world configuration.

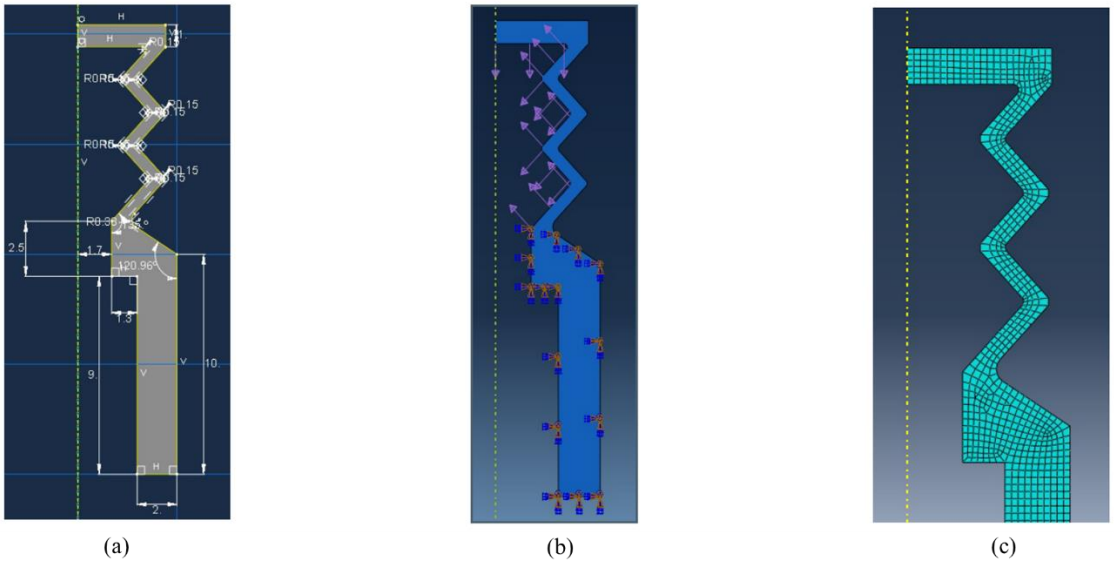

Figure 5.4 – Axisymmetric modeling of the mini-PAM. a) Geometrical model; b) Imposed pressure load (pink) and boundary conditions (orange and blue); c) Mesh.

Hybrid elements were employed to address the incompressibility of the material and establish the mesh for Finite Element Analysis (FEA) calculations. To ensure accurate results without compromising precision while optimizing calculation time, the mesh was refined in the most constrained regions of the muscle (as depicted in Fig 5.4c). Consequently, the model incorporated "Quad-dominated" elements along with a "medial axis" resolution algorithm. This approach was chosen to effectively handle the meshing process and accommodate the characteristics of the material's incompressible behavior.

Shell model

The purpose of this model is to achieve results similar to the first model under axisymmetric conditions. One of the advantages of this model is its adaptability to study geometries that lack axial symmetry. The shell model simplifies calculations by considering the membrane to have no thickness, and the membrane's thickness was incorporated using Abaqus parameters.

As in the first model, only two-dimensional elements were utilized to construct the mesh for this structure. This approach is interesting in terms of computational costs since it reduces mesh complexity by employing 2D elements instead of 3D ones. Significantly fewer elements were needed to mesh the component compared to a model where the thickness would be re-

tained. However, due to the bellows-like shape of the artificial muscle being considered in three dimensions, the calculations took longer compared to the axisymmetric model.

Given the complexity of the geometry, the most straightforward approach to designing it was through Computer-Aided Design (CAD) software, specifically CREO. Using CREO, the 3D structure of the bellows-like artificial muscle was created (as shown in Fig. 5.5a). The dimensions of the geometry tested in the laboratory were maintained according to Table 5.2. This 3D structure from CREO was then imported into Abaqus as a "Part". The "remove" tool in Abaqus was employed to eliminate certain surfaces and create a shell model of the muscle by removing the external surfaces of the 3D shape. Additionally, it was assumed that the attachment at the top of the muscle had minimal impact on the overall compression ratio of the muscle. Therefore, it was removed from the model. This decision was guided by the removal of the external surfaces of the muscle, which necessitated the removal of the attachment to achieve a realistic model.

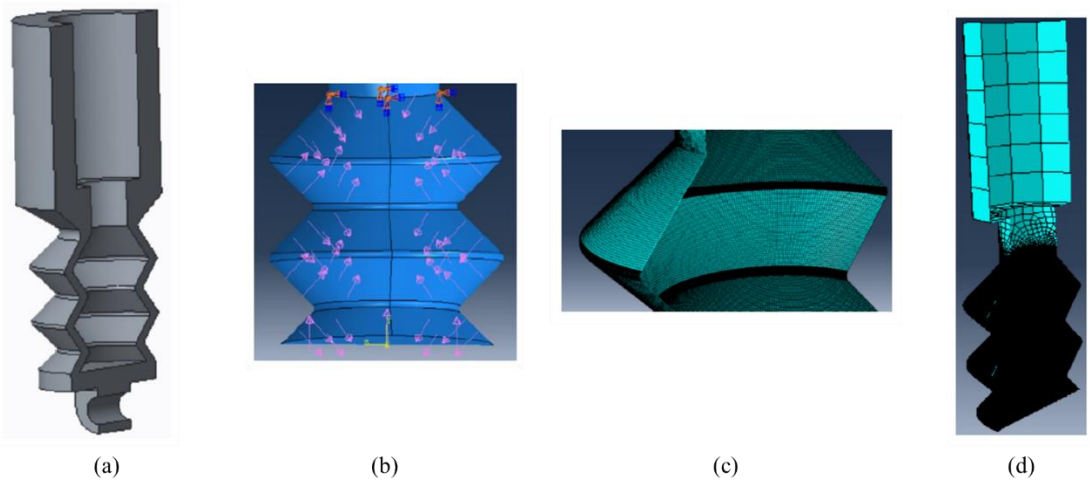

Figure 5.5 – Shell modeling of the mini-PAM. a) Cross-sectional view of the designed artificial muscle; b) Loads and boundary conditions imposed; c) Refined mesh on the bellows; d) Coarse mesh on the soft tube.

The material model and contact interactions were incorporated in a manner consistent with the axisymmetric model. The process of depressurization was also simulated by applying pressure forces to the internal surfaces. The muscle's end remained embedded as a boundary condition, as illustrated in Fig. 5.5b. To ensure precision in the calculation, a highly detailed mesh was implemented along the edges of the muscle, where deformations are most prominent (shown in Fig. 5.5c). This refinement was chosen to enhance calculation accuracy. Conversely, for the cylindrical end (soft tube) of the muscle, which experienced negligible deformations, a coarser mesh was employed (depicted in Fig. 5.5d).

The mesh utilized S4R elements, quadratic with reduced integration, specifically designed for shell models involving incompressible hyperelastic materials. The model consisted of a total of 166,931 elements.

The 3D model

The comprehensive 3D model representing the entire studied geometry demands substantial computing power due to the requirement for a high-element count mesh. As such, it's more advisable to resort to an axisymmetric or shell model when feasible. However, for certain 3D geometries, adopting a shell model can exacerbate complexity rather than streamline simulations. Consequently, directly importing and meshing the geometry designed in CAD software within Abaqus becomes necessary.

In cases where a geometry features planes of symmetry, the 3D model could be streamlined. For instance, in the current model, retaining only a quarter of the bellows-like PAM shape can enhance mesh precision. It's important to note that the proposed bellows-like artificial mini-muscle featured an infinite number of symmetry planes, all intersecting along the same axis. Thus, for the 3D model, an even smaller section of the PAM was retained, adhering to a commonly used simplification approach for this type of model.

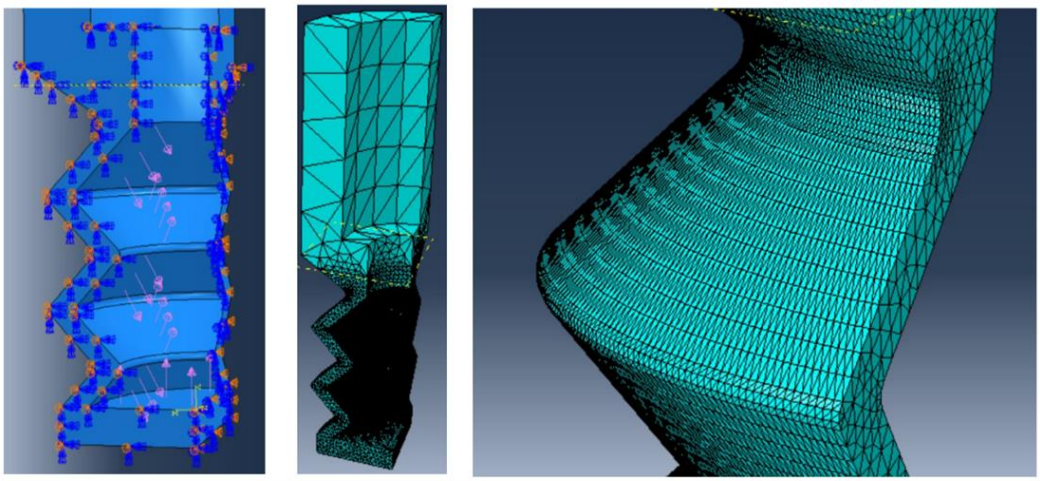

Figure 5.6 – 3D modeling of the mini-PAM. a) Loads and boundary conditions; b) Coarse mesh of the tube; c) Refined mesh of the bellows.

The interactions were modeled consistently with the approaches in the previous models, and the cylindrical end of the PAM was simulated as being embedded. Similarly, pressure

forces were applied perpendicular to the inner surfaces, with variations to match experimental conditions (as illustrated in Fig. 5.6a).

Leveraging the symmetry of the geometry necessitated the application of appropriate boundary conditions. Given symmetry on the *x*-*y* plane, translation along the *z*-axis was restricted, along with rotations around the *x* and *y*-axes. These boundary conditions were imposed on two symmetry planes. To enhance accuracy, the mesh of the structure was refined in regions where the geometry experienced the most significant deformation (depicted in Fig. 5.6b and c). This refinement utilized a C3D4H mesh consisting of 4-node tetrahedral elements in a linear hybrid formulation. These elements were chosen for their suitability with incompressible hyperelastic materials. The final mesh comprised 246,450 elements, considering that the Abaqus solver's maximum allowable element count was 250,000.

5.4 Experimental measurements

The practical behavior of the three bellows-like artificial mini-muscles was explored through experimentation using a dedicated workbench. The aim was to observe how they responded to negative pressure. A set of measurements, involving varying pressure differences, was carried out to determine the maximum contraction achievable for each case. This procedure was documented using a smartphone, recording the compression process.

Subsequently, image processing was employed, facilitated by Python code, to extract the displacement of the artificial mini-muscles. This approach allowed for quantifying the extent of contraction based on the recorded images and translating it into measurable data for analysis.

5.4.1 Description on the experimental workbench

Initially, the first sample, referred to as PAM1, underwent testing on a straightforward workbench setup. This setup primarily comprised one capacitance diaphragm gauge (CDG) pressure sensor, three valves, and a smartphone, as depicted in Fig. 5.7a. The components of the setup were configured as follows:

1. **Valve A**: This valve served to isolate the vacuum pump from the system, allowing the pressure inside the system to be reduced.
2. **PAM1 with stainless-steel tube**: PAM1, affixed to a stainless-steel tube, was connected to the system via Valve B. Valve B facilitated the generation of a pressure difference between the interior and exterior of the muscle.
3. **Valve C**: This valve was responsible for introducing air into the system, thereby causing the muscle to return to its non-compressed state.

4. **CDGA pressure sensor**: This CDG pressure sensor was installed to monitor fluctuations in system pressure.
5. **3D-printed support**: A support structure, 3D-printed and affixed to the testing bench, was utilized to secure the smartphone in place for recording purposes.

This arrangement allowed for controlled manipulation of pressure conditions within the system and enabled the monitoring of pressure changes through the CDG sensor. The smartphone, positioned on the 3D-printed support, was employed to record the experimental procedure.

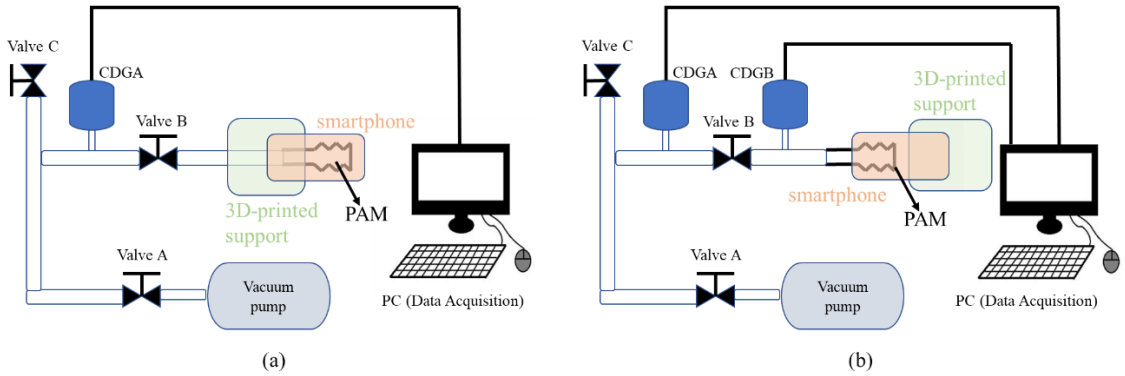

Figure 5.7 – Experimental workbench for measurements of artificial mini-muscles.
a) PAM1 was tested on this workbench with only one pressure sensor;
b) PAM2 and PAM3 were tested on this workbench with two pressure sensors.

The initial experimental workbench setup, (Fig 5.7a), was focused on tracking pressure variations on the left side of Valve B using a single pressure sensor. However, when Valve B was rapidly opened, pressure changes occurred on both sides of the valve due to the pressure difference. Therefore, measuring pressure variations on both sides became essential for understanding muscle behavior accurately.

To achieve this, another pressure sensor, CDGB, was introduced and connected to the right side of Valve B (Fig 5.7b). This arrangement enabled the simultaneous measurement of pressure changes on both sides of the valve. This dual-sensor setup was particularly useful for tasks like estimating the time required to achieve maximum contraction for a specific pressure difference, which could be approximated when pressures on both sides are equal. Given that Valve B was operated manually, vibrations from the test bench could affect the stability of the smartphone and consequently the recording process. To address this, the 3D-printed support was relocated and secured to the table holding the test bench, providing greater stability for the smartphone during recording. This improvement is depicted in Fig. 5.7b. Samples PAM2 and PAM3 were subjected to testing using this updated setup.

In addition, the pressure sensors had a full-scale range of 1000 torr (equivalent to 133 kPa). For the current experiments, the maximum pressure monitored by the sensors was atmospheric pressure (100 kPa). The resolution of the sensors was 0.015 % of the full scale, and their precision was 0.2 % of the reading. The ideal operating temperature for these sensors was set at 25 ℃.

5.4.2 Experimental procedure

To provide a clear understanding of the experimental procedure conducted at standard atmospheric pressure, here is a step-by-step description:

1. **Pressure difference generation**: The experiment started with running the vacuum pump. Valve A was manually and slowly opened while keeping Valve B and Valve C closed. This action led to a decrease in pressure on the left side of Valve B, while the pressure on the right side remained constant. Once the desired pressure level, monitored by CDGA, was achieved, Valve A was closed. As a result, a pressure difference between the left and right sides of Valve B was established.
2. **Start recording**: Before opening Valve B, the recording video function of the smartphone was activated. The data acquisition system was initiated to capture the practical pressure variation within the system.
3. **Actuation of artificial mini-muscle**: Valve B was rapidly opened while Valves A and C remained closed. This allowed the artificial mini-muscle to start compressing due to the pressure difference until it reached its maximum compression. This process lasted a few seconds, during which the pressure on both sides of Valve B gradually converged. Meanwhile, the pressure variations on both sides and the mini-muscle's contraction process were recorded. Valve B was closed once the mini-muscle could no longer be compressed, and recording was stopped.
4. **Recovery to initial state**: Valve A was kept closed, Valve B remained open, and Valve C was opened to introduce air into the system. This action brought the system's pressure back to standard atmospheric conditions. During this process, the artificial muscle reverted to its initial state. Once the pressure was restored, Valve C was closed in preparation for the next experiment.

By repeating the above steps for a series of experiments, different dynamic behaviors and the maximum contractions of the artificial mini-muscles were obtained for various pressure differences. Image processing was then employed to extract the maximum contraction from the recorded images. This data was used to calculate the contraction ratio of the mini-muscles.

5.4.3 Image-processing and extraction of PAM's contraction

The process of extracting the observed deformations of the PAM from video recordings proved to be a time-consuming endeavor. Each muscle tested involved processing between 25 and 30 videos, with each video being approximately 10 s in duration. The Python program was designed to extract all images within each video, resulting in around 29 images per second.

To comprehensively analyze the PAM's performance under negative pressure, both dynamic and static behaviors were examined through image processing. The dynamic behavior referred to the changes in PAM contraction over time, while the static behavior involved characterizing the final contraction of the PAM subjected to vacuum conditions and studying how this final contraction ratio varied with the pressure difference.

In the context of this analysis, the first image of each video, representing the PAM's initial state (as depicted in Fig. 5.8a), was utilized as a reference point. For dynamic behavior assessment, the compression variation over time was tracked by processing every frame of the video (Fig. 5.8b). This allowed for the calculation of the transient contraction ratio of the PAM for each frame, using the first image as the baseline reference. On the other hand, to investigate the static behavior of the PAM, the last image of each video, indicating the equilibrium state of the PAM (Fig. 5.8c), was taken as a reference. Using this equilibrium state, the global compression ratio of the PAM was calculated. The difference in terms of pixels between the top of the PAM in the initial state and the top of the PAM in the equilibrium state was used to derive the global contraction ratio of the PAM for each depressurization condition. This thorough analysis approach aimed to capture both the time-dependent and equilibrium behaviors of the PAM under varying pressure differences.

Figure 5.8 – Different states of PAM extracted from a video of contraction. a) Initial state, b) General state, and (c) Final equilibrium state.

The complete Python program to process the images isn't fully detailed in this chapter, but an illustrative example of an image in a general state of the PAM processed by the program is provided in Fig. 5.8b to explain how the contraction ratio is calculated using pixel information.

The white PAM was surrounded by a dark area to maximize contrast for better analysis. The process of identifying the origin of the PAM (at the top of the image) involved scanning the image pixel by pixel from top to bottom. For each pixel, the average RGB value (ranging from 0 to 255) was computed to determine whether the pixel was light or dark. The first light pixel encountered defined the origin of the PAM, and its vertical position was recorded. The scanning continued until the last light pixel was identified, determining the top of the PAM. In Fig. 5.8a, the origin and top of the PAM in the initial state can be observed, as well as in Fig 5.8c for the final state.

The boundary between light and dark pixels corresponded to an RGB value. It's worth noting that a higher RGB value indicated a lighter pixel. Depending on the lighting conditions during the experiment, the value of this boundary could vary. In practice, this value typically fell between 75 and 110. If the average RGB value of a pixel was lower than this boundary value, the program considered the pixel to be dark, and vice versa.

5.5 Results and discussion

Using the experimental approach described earlier, a series of experiments were conducted on the three artificial mini-muscles. Through the image processing method, both the dynamic and static behaviors of the muscles during the contraction process were analyzed. These behaviors were also simulated on the models that had been created and previously described. In the culmination of the study, the experimental results were compared with the numerical re-

sults obtained from simulations. This comparison allowed for a comprehensive assessment of how well the simulations captured the real-world behavior of the artificial mini-muscles under negative pressure conditions.

Static behavior

The initial phase of experimentation involved testing PAM1 under various pressure difference conditions. For each case, three tests were conducted. The results of these tests were used to create a plot in Fig. 5.9a, illustrating the maximum contraction ratio as a function of the pressure difference.

The relationship between pressure difference and compression ratio exhibited a logarithmic function-like trend. The curves in the plot appeared to converge towards two asymptotes, effectively dividing the graph into two sections. When the pressure difference ΔP was less than 30 kPa, the static contraction ratio e_{max} followed an asymptote corresponding to a linear relationship. As ΔP increased beyond 30 kPa and approached 50 kPa, e_{max} exhibited slight variation. This behavior suggested that ΔP was gradually nearing the critical pressure difference required to achieve the maximum contraction ratio.

To assess the repeatability of the manufacturing process for the bellows-like PAMs, the three samples were tested. The deflection behavior of a PAM is intricately linked to the material properties of its membrane. Therefore, if any of the PAMs were produced with defects in their membranes, discrepancies among the static behaviors of the three samples would have been evident. This analysis is depicted in Fig. 5.9b, demonstrating the importance of consistent manufacturing for reliable results that lead here to little deviations between the behaviors of the three samples.

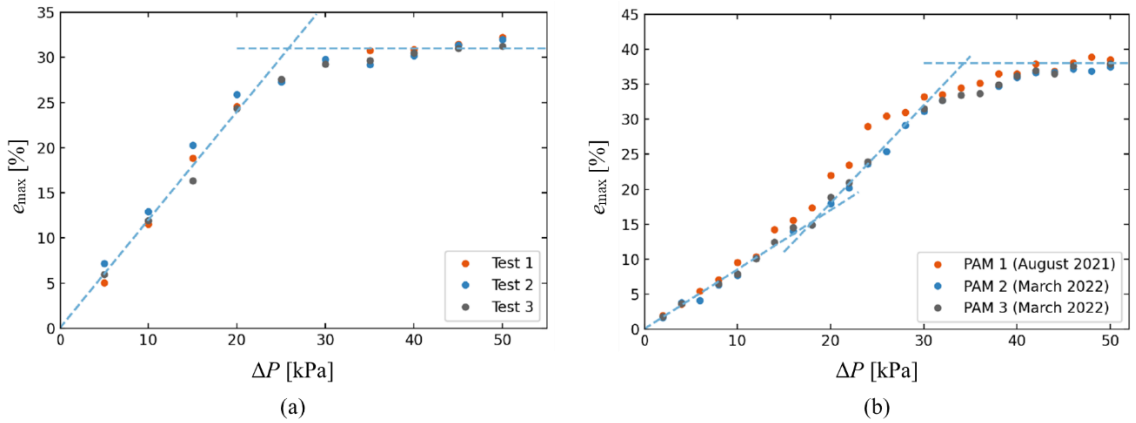

Figure 5.9 – Contraction ratio vs pressure difference.

a) Static behavior of PAM1 for 3 different tests; b) Static behavior of the three PAMs.

By increasing the number of measurements within the same depressurization interval, more accurate curvature profiles were obtained. The curves displayed in Fig. 5.9b exhibited three distinct asymptotes, indicating that the curvature appeared less logarithmic compared to the curves in Fig. 5.9a. Notably, a pronounced asymptote was observed as the depressurization varied between 15 and 35 kPa. This phenomenon is directly linked to the behavior of hyperelastic materials.

The contraction ratios of the three PAMs converged around 38 % when tested on the improved workbench illustrated in Fig. 5.7b (as seen in Fig. 5.9b). This value is 6 % higher than the contraction ratios obtained from the series of tests presented in Fig. 5.9a, conducted on the setup of Fig. 5.7a. This discrepancy could potentially stem from the enhancement of the experimental setup. However, it's important to note that the two series of tests were not carried out under identical experimental conditions in terms of lighting, temperature, and ambient pressure. Consequently, it remains somewhat challenging to definitively conclude whether the actual final compression ratio aligns closer to 32 or 38 %. This range of results offers a comprehensive overview of the characteristic behavior of these samples.

Furthermore, a more detailed analysis revealed that the curve representing PAM1 was slightly above the curves of the other two samples. This divergence might be attributed to PAM1 having undergone multiple tests, potentially altering the material properties of its membrane and resulting in a more flexible membrane. The responses of PAM2 and PAM3 to depressurization were very similar, confirming the repeatability of the manufacturing process for these two samples.

Dynamic behavior

The static analysis of the PAM's behavior yielded valuable insights that paved the way for the subsequent dynamic study. However, exploring the dynamic behavior of the PAMs proved to be a time-intensive endeavor. Additionally, the data generated by the program was substantial due to the number of video recordings processed.

Given the notable similarity between the behaviors of PAM2 and PAM3, as evidenced by Fig. 5.9b, a decision was made to focus the dynamic study solely on the video recordings of PAM2. This choice was made to streamline the analysis and reduce the data volume. Furthermore, the dynamic behavior of PAM1 was also examined to facilitate a comparative assessment of the behaviors of both PAMs. This approach allowed for a comprehensive evaluation of the differences and similarities in dynamic responses between these two PAMs (PAM1 and PAM2).

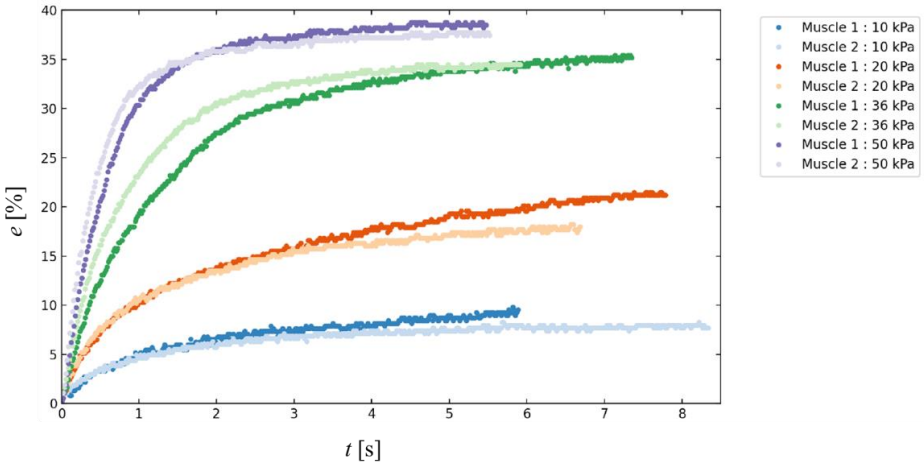

Figure 5.10 – Dynamic behaviors of the PAM1 (dark color) and the PAM2 (light color): contraction ratio vs time for various pressure differences.

The results presented in Fig. 5.10 were acquired using the enhanced test bench illustrated in Fig 5.7b. This figure displays the change in contraction ratio over time for both PAM1 (dark points) and PAM2 (light points). Notably, for each depressurization condition, the curvature profiles corresponding to both PAMs are quite close.

Across all the pressure differences depicted in the graph, it is evident that the maximum contraction ratio of PAM1 was consistently equal to or higher than that of PAM2. This finding aligns with the observations from Fig. 5.9b, where PAM1 consistently exhibited greater final contraction ratios compared to PAM2 and PAM3. However, along the first asymptote of the curve, particularly for a specific pressure level, the compression ratio of PAM2 often slightly exceeded that of PAM1. This phenomenon is likely linked to the varying material properties due to the testing process. As previously explained with regards to the static behavior, it's conceivable that the material properties of PAM1 changed in a way that reduced its rigidity after undergoing multiple tests. Conducting aging tests on the fabricated structures, subsequent to cycles of pressurization and depressurization, would be essential for assessing the lifespan of the PAMs.

The initial segments of the curves are associated with the dynamics of air evacuation from the cavity and fluidic connections. The stabilization of the curves is indicative of the membrane's dynamics and its process of flattening. An interesting observation is that PAM2 seemed to react more swiftly to vacuuming in the initial part of the graph, while PAM1 exhibited a tendency to flatten more than PAM2 later on. This dynamic behavior shift could be attributed to various factors, including the material properties and structural characteristics of the PAMs.

Numerical results

The simulation of the axisymmetric model of the bellows-like PAM yielded an approximate depiction of the PAM's response under vacuum conditions. This simulation facilitated the collection of compressed PAM lengths. Within the Abaqus software, users have the option to designate a specific point within the mesh and monitor its displacement along an axis throughout the simulation. In this study, the displacement of the PAM was gauged by tracking the position of a designated node situated at the top of the PAM.

The variation in the contraction ratio of the PAM with respect to pressure difference, as derived from simulations, is illustrated in Fig. 5.11a. This plot demonstrates that the contraction ratio approached 35 % with increasing pressure difference. Notably, within the range of ΔP from 0 to 35 kPa, the contraction ratio $e_{\max}$ exhibits a significant and nearly linear variation. However, for ΔP values surpassing 35 kPa, the variation of $e_{\max}$ becomes more gradual, eventually stabilizing at a constant value. Remarkably, this trend closely parallels the findings from the experimental results.

Regarding the software's requirement for the inclusion of the material model's coefficients C_{10} and D_1, an investigation into their influence on curvature is necessary. However, in the current study, the impact of coefficient D_1, associated with material compressibility, was not explored due to the assumption of material incompressibility in the simulation. Consequently, the investigation solely focused on the influence of coefficient C_{10} on the static behavior of the PAM, as depicted in Fig. 5.11b.

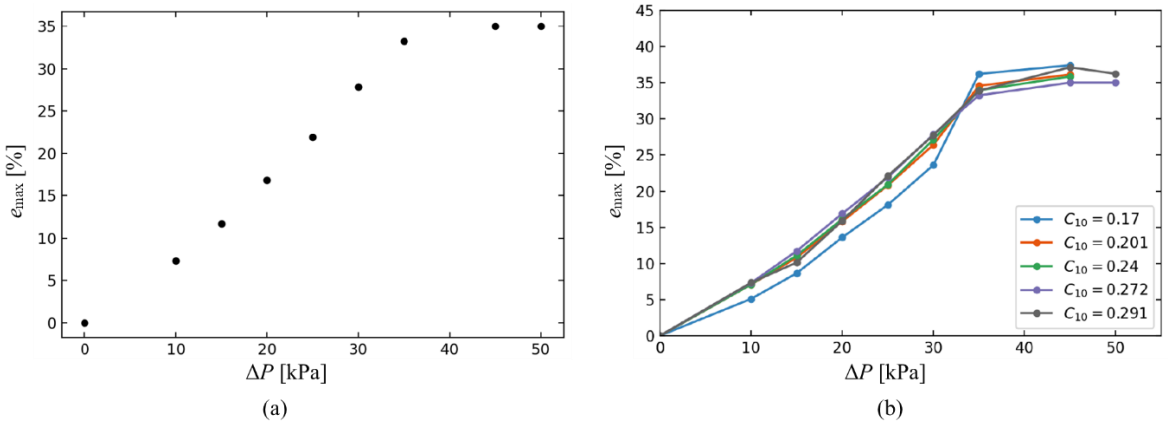

Figure 5.11 – a) Static behavior of the bellows-like PAM according to the axisymmetric model; b) Influence of coefficient C_{10} of the Neo-Hookean model on the static behavior of PAM.

Figure 5.11b clearly illustrates that a decrease in the C_{10} coefficient results in a higher maximum static contraction ratio e_{max}. This coefficient also exerts influence over the slopes of the curve. Notably, when C_{10} is set at 0.17 MPa, the variation curve deviates notably from those corresponding to the other coefficient values. Except for this specific value, when C_{10} assumes values below the analytically determined value of 0.272 MPa (see Section 5.3.1), or slightly above, the behavior curves align closely.

Comparison between experimental and numerical results

The comparison between experimental and numerical results was conducted to underscore the authenticity of the numerical models, which are capable of accurately simulating the practical behavior of the fabricated artificial mini-muscles.

The outcomes depicted in Fig. 5.12 highlight the striking similarity between the variations of contraction ratio as a function of pressure difference obtained from experimental findings and numerical simulations. A noteworthy observation is that the numerical results closely aligned with the behavior of PAM2 and PAM3, exhibiting better agreement than with the behavior of PAM1. Additionally, the outcomes from the 3D model displayed less deviation from experimental data in comparison to the axisymmetric model, especially for pressure differences below 30 kPa.

In the context of characterizing the bellows-like PAM, the axisymmetric model tended to predict a slightly smaller contraction ratio compared to the experimental curves as the pressure difference increased. Nonetheless, while numerical models inherently entail some level of error, the axisymmetric model still provided a comprehensive overview of the experimentally obtained contraction ratios. As for the 3D model, to affirm its overall accuracy, an extended validation would require a model capable of simulating the PAM's behavior up to a pressure difference of 50 kPa.

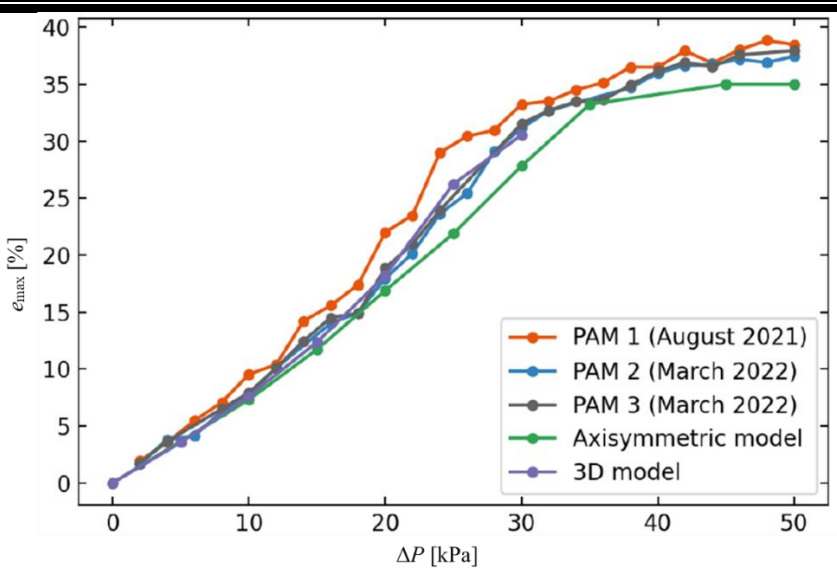

Figure 5.12 – Comparison of experimental and numerical data on static contraction parameter vs pressure difference.

5.6 Conclusions on mini-PAMs fabrication, simulation and tests

Three bellows-like artificial mini-muscles (PAMs) were conceptualized, fabricated using 3D printing, and subjected to both experimental and numerical investigations under the influence of negative pressure. The aim was to study their behaviors when actuated by negative pressure. The dynamic behavior of the samples was captured using image processing on video recordings, which depicted the contraction ratio over time for specific depressurization conditions. For numerical explorations of the mini-PAMs influenced by negative pressure, three distinct models – an axisymmetric model, a shell model, and a 3D model – were constructed within the Abaqus software. The Neo-Hookean hyperelastic material model was utilized to emulate the response of the PAMs, replicating real-world behavior. Both experimental and numerical studies employed air as the working gas.

A simple experimental setup, accompanied by a well-defined protocol, was devised to characterize the PAMs. This setup incorporated pressure sensors to track system pressure changes over time and smartphones for recording the muscle contraction process during actuation. The bellows-like PAMs exhibited compression upon the application of negative pressure within the cavity. Results from both numerical simulations and experimental tests revealed that the maximum (or static) contraction ratio for each specific negative pressure differed, increasing significantly as the pressure difference exceeded the critical value (approximately 50 kPa). Beyond this point, the maximum contraction ratio stabilized at a constant value (around 35 – 37 %, observed from both experimentation and modeling).

Additionally, the experimental and numerical results demonstrated a notable alignment, indicating that the modeling effectively mirrored the practical PAM behavior. However, despite the meticulous construction of the experimental setup, certain sources of potential error persisted. For instance, video recordings might lack sufficient resolution to capture small displacements accurately. Lower depressurizations exhibited more significant point mismatches than higher ones due to the difficulty in precisely capturing small displacements. Improving measurement precision could involve using a higher-resolution camera and ensuring its stability during recording. Enhanced contrast between the muscle and background could be achieved by altering the material properties of the PAM or using a matte background to minimize light reflection. For testing micro-muscle, it is quite clear that the current setup is inappropriate to capture displacements at the microscale.

Moreover, to accurately implement the Neo-Hookean model, the material properties would require determination through basic traction and compression tests. Another avenue for improving numerical accuracy is measuring the PAM dimensions directly from the test bench. Variability in the 3D printing process could result in discrepancies between the actual PAM dimensions and the CAD model. By creating an Abaqus model that precisely matches the experimentally tested PAM, even closer alignment between experimental and simulated outcomes could be achieved.

Finally, simulating the dynamic behavior of the muscle would require considering all connecting elements between the PAM and the valve and imposing the actual pressure difference variation with time.

5.7 Artificial micro-muscle fabricated via TPP technique

To couple the Knudsen pump with an artificial muscle, the dimensions of the artificial muscle must be scaled down to the microscale. Building on this idea and leveraging the valuable measurements obtained, a bellows-type artificial micro-muscle was meticulously designed. Figure 5.13 illustrates the structure and dimensions of this micro-muscle. To test the ability of the TPP technique to manufacture complex shapes, it was decided to replace the axisymmetric geometry of the mini-muscle with a 6th-order rotational symmetry, as shown in Fig. 5.14.

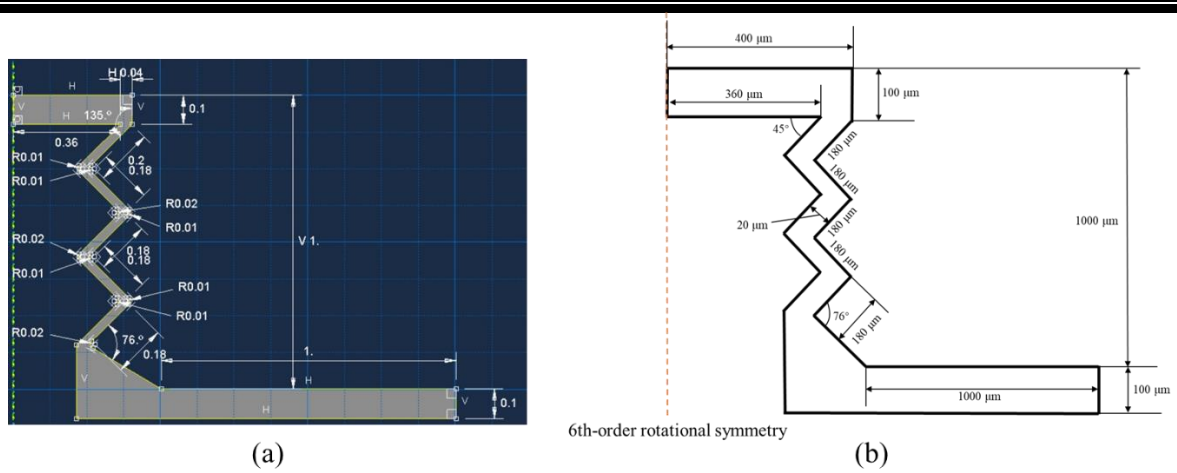

Figure 5.13 – Bellows-type artificial micro-muscle. a) CAD design; b) Diagram of the dimensions.

Using the TPP technique, the designed artificial micro-muscle was successfully manufactured, as depicted in Fig. 5.14. This micro-muscle is affixed to an aluminum plate measuring 25 mm × 25 mm × 0.5 mm. The chosen material for the micro-muscle is IP-PDMS, which boasts a Young's modulus of 15.3 MPa. IP-PDMS is a novel photoresin engineered for 3D freeform printing of elastomers via TPP. It exhibits key attributes such as softness, remarkable flexibility, and elasticity. However, even if the outer shape was successfully reproduced in agreement with the CAD design, exploration of the sample with a tomograph revealed that the micro-muscle was full of polymer, meaning that the unrevealed material was not properly removed. It was then impossible to make some vacuum tests on this preliminary sample and additional investigation should be conducted at KNMFi to solve this issue.

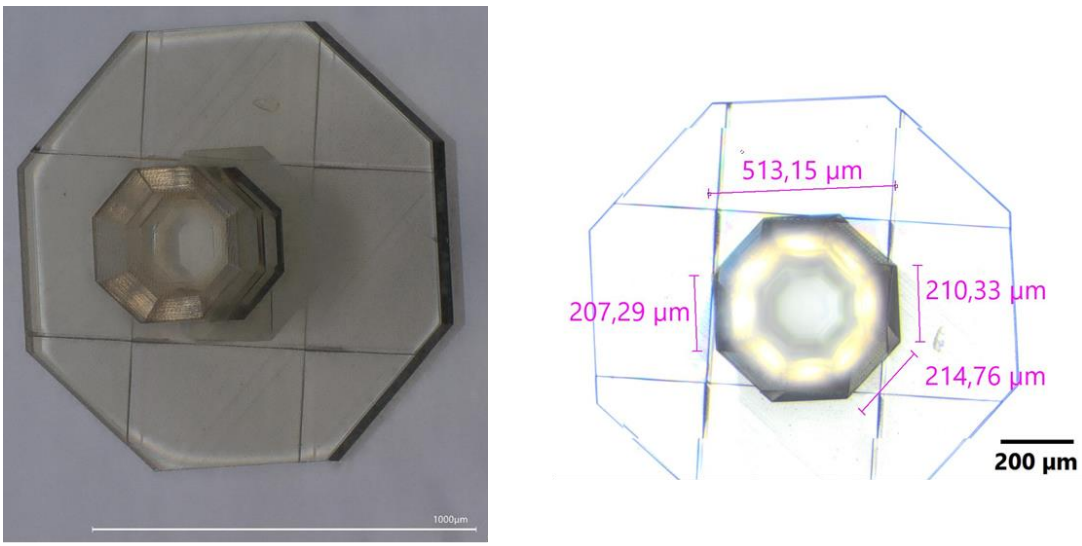

Figure 5.14 Bellows-type artificial micro-muscle successfully fabricated via the TPP technique. a) 3D structure of the whole microdevice; b) Top-view of the micro-muscle by digital microscope.

5.8 Summary

This chapter focuses on the characterization of the dynamic and static behaviors of three artificial bellows-like mini-muscles that are actuated by negative pressure. The contraction analysis program managed to collect displacement data in terms of pixels and determine the contraction ratio by dividing displacement by the initial length of the PAM. Employing more precise tools like lasers would enhance displacement measurement accuracy and allow characterization of micro-PAMs.

Overall, the results highlight the efficiency of using an axisymmetric model to approximate PAM behavior. Such models are preferable due to their cost-effectiveness and computational efficiency. Complex models aren't always necessary to achieve accurate results. Therefore, if geometry allows simplification, it should be utilized in FEA modeling.

This initial investigation lays the foundation for a more comprehensive study into how different geometries and materials with varying stiffness impact PAM behavior at the mini scale. The ultimate goal is to characterize contraction and load behaviors solely based on a PAM's geometry and material properties through Abaqus models.

The insights gained from this mini scale study of PAMs can be extrapolated to microscale structures. Future possibilities include creating a micro-actuator with a miniaturized PAM for connection to a Knudsen pump. By understanding the displacement or load developed by the PAM, one could deduce the required vacuum pressure. Moreover, the inspiration from this study opens doors for the development of micro-actuators with applications in fields like medicine and micro-robotics. As a first step to reach this goal, an artificial micro-muscle potentially compatible with a Knudsen pump was proposed and successfully manufactured through the TPP technique.

This initial sample was fabricated using a polymer with excessively high rigidity. Attempts to fabricate with more flexible polymers have so far proven unsuccessful, resulting in structures that do not match the designs and collapse during polymerization, and these efforts will need to be continued. Nevertheless, this first sample, despite its excessive rigidity, was accurately produced with external dimensions in excellent agreement with the desired dimensions. This is highly encouraging for the future fabrication of micro-muscles using TPP and controlled by Knudsen pumps.

Chapter 6 - Coupling of Knudsen pumps and artificial pneumatic micro-muscles

Introduction

In the previous chapter, we briefly discussed the performance of artificial mini-muscles actuated by negative pressure. We highlighted the significant role of pressure difference in determining the maximum contraction ratio of these muscles. This suggests that at the microscale, it is possible to utilize Knudsen micropumps to actuate pneumatic artificial micro-muscles (PAμMs). Moreover, the characteristic curves presented in Chapter 2 for the KPs, each stage of which consisting of multiple parallel microchannels connected to one macrochannel, demonstrate a quasi-linear relationship between two key parameters (pressure difference ΔP and masse flowrate $\dot{m}$), at least up to a certain number of stages. More generally, ΔP increases as $\dot{m}$ decreases. This behavior aligns with the deformation behavior of the artificial muscle. Initially, when the muscle starts to deform, the pressure difference is zero and the mass flowrate is at its maximum. When the muscle is fully deformed, the pressure difference is at its maximum while the mass flowrate becomes zero. This analysis lays the foundation for the concept of using Knudsen micropumps to actuate artificial micro-muscles.

Consequently, the main objective of this chapter is to theoretical analyze the possible integration of a KμP with a PAμM by performing preliminary calculations for the coupled microsystem. Towards the end of the chapter, we also provide a glimpse into the potential implications and future prospects of this concept.

6.1 Initial concept

As highlighted in Chapter 5, achieving maximum deformation of an artificial micro-muscle requires a high-pressure difference. Additionally, considering the time response of deformation, a higher mass flowrate results in a faster response time. These two factors can be simultaneously enhanced by increasing the number of stages and of parallel microchannels in each stage of the KμP, as elucidated in Chapter 2. Consequently, for the analysis and calculations in this chapter, we opt for a multistage with multichannel KμP.

Figure 6.1 illustrates a straightforward and uncomplicated connection between the KμP and the PAμM. Notably, in this concept, all microchannels are identical and with the same number in each stage. Similarly, the macrochannels are identical as well. This configuration

simplifies the system and facilitates analysis.

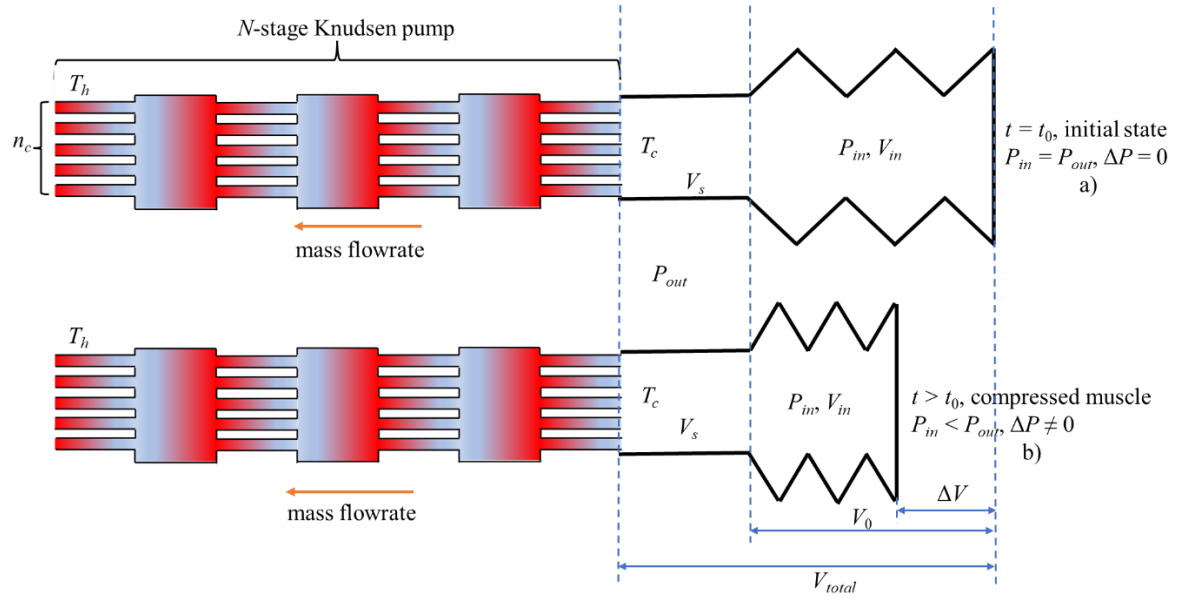

Figure 6.1 – A simple diagram representing a KµP connected to a bellows-like PAµM.

The operational principle of the depicted system lies in the generation of a thermal transpiration gas microflow. This flow emerges due to an induced temperature difference along the channels of the KµP. The flow originates from the cold side, which is linked to the internal cavity of the artificial muscle, and travels towards the hot side, connected to atmospheric pressure. Consequently, the pressure within the internal cavity (P_{in}) gradually decreases over time, resulting in the simultaneous compression of the artificial micro-muscle.

Throughout this process, both P_{in} and the internal variable volume of the cavity V_{in} undergo changes with respect to time, until the PAµM reaches a fully compressed state. At this point, P_{in} and V_{in} remain constant, and the pressure difference ΔP equals its maximum value $\Delta P_{\max}$.

6.2 Analytical model

As depicted in Fig. 6.1, when the muscle is subjected to compression via vacuum, both the volume and pressure within the internal cavity will undergo changes over time. Additionally, the parameters corresponding to the initial state, without any deformation of the muscle, are known, with the exception of the initial volume of the muscle, denoted as $V_{total} = V_0 + V_s$, that should be calculated. Here, V_0 represents the initial internal volume of the deformable portion

of the PAμM, while V_s signifies the dead volume that remains constant during contraction. These two volumes can be computed based on a micro-muscle's structural characteristics, similar to that elucidated in Chapter 5, but simplified with an axisymmetric shape (Fig. 6.2). The process for calculating V_0 and V_s is elucidated through the schematic of a micro-muscle shown in Fig. 6.2.

Within this figure, specific dimensions ($r_1 = r_3 = r_5 = 360\,\mu\text{m}$, $\varphi = 45°$, $l_{total} = 1000\,\mu\text{m}$, and $l_1 = l_2 = l_3 = l_4 = l_5 = 180\,\mu\text{m}$) are defined as per the micro-muscle's design (see Fig. 5.13). Furthermore, the initial volume V_0 can be determined through the sum of individual volumes V_i for $i \in \{1;5\}$. The calculation of each small volume is obtained from:

$$V_i = V_1 = \frac{1}{3}\pi l_1 \sin\varphi\,(r_1^2 + r_2^2 + r_1 r_2) \tag{6.1}$$

with

$$r_2 = r_1 - l_1 \cos\varphi \tag{6.2}$$

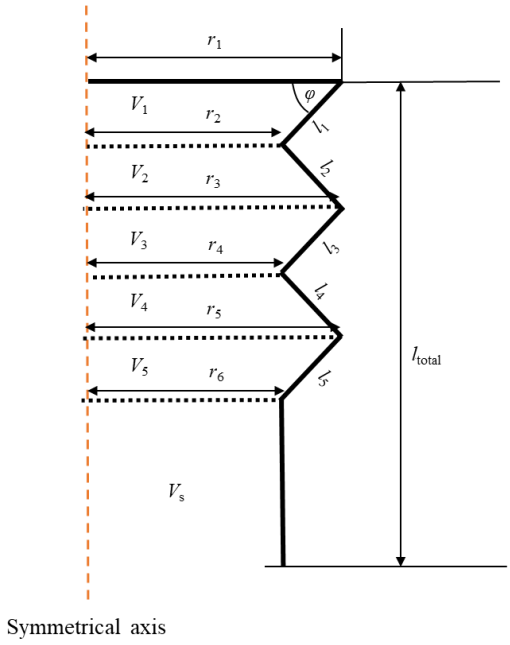

Figure 6.2 – Diagram of micro-muscle and parameters for volume calculation.

Moreover, the dead volume V_s can also be calculated by

$$V_s = \pi r_6^2 \left[l_{\text{total}} - (l_1 + l_2 + l_3 + l_4 + l_5) \sin\varphi \right] \tag{6.3}$$

Using the above equations, the initial volume of the PAμM without any deformation can be obtained: V_{total} = 22 × 10^{-11} m^3, with $V_0 = 16.75 \times 10^{-11}$ m^3, and $V_s = 5.25 \times 10^{-11}$ m^3. According to the fabrication process, the dead volume can be kept as such, or the KμP can enter inside the PAμM and this dead volume disappears (see further Cases 2 and 1, respectively).

To compute the contraction ratio of the micro-muscle coupled with a multistage KμP, an assumption is made that the micro-muscle follows the same characteristic curve as the mini-muscles discussed in Chapter 5. Consequently, an identical relationship between the contraction ratio and pressure difference, as shown in Fig. 6.3a, can be extrapolated. As already seen in Fig. 5.8a, this relationship is close to linear until a plateau at $e = 32\%$:

$$e = \frac{\Delta V}{V_0} = \varepsilon \ \Delta P \tag{6.4}$$

Here, $V_{in} = V_0 - \Delta V$ (see Fig. 6.1), and $\varepsilon = 1.2 \times 10^{-5}$ Pa^{-1} represents the slope of the curve linear fitting. Of course, this value of α is arbitrary because i) the PAμM have a smaller thickness than the mini PAMs, and ii) the polymer should have different elastic properties, both conditions impacting the slope.

In addition, for a given choice of KμP, its characteristic curve can be calculated as:

$$\dot{m}_{\text{K}\mu\text{P}} = fct_{\text{K}\mu\text{P}}\left(\Delta P_{\text{K}\mu\text{P}}\right) \tag{6.5}$$

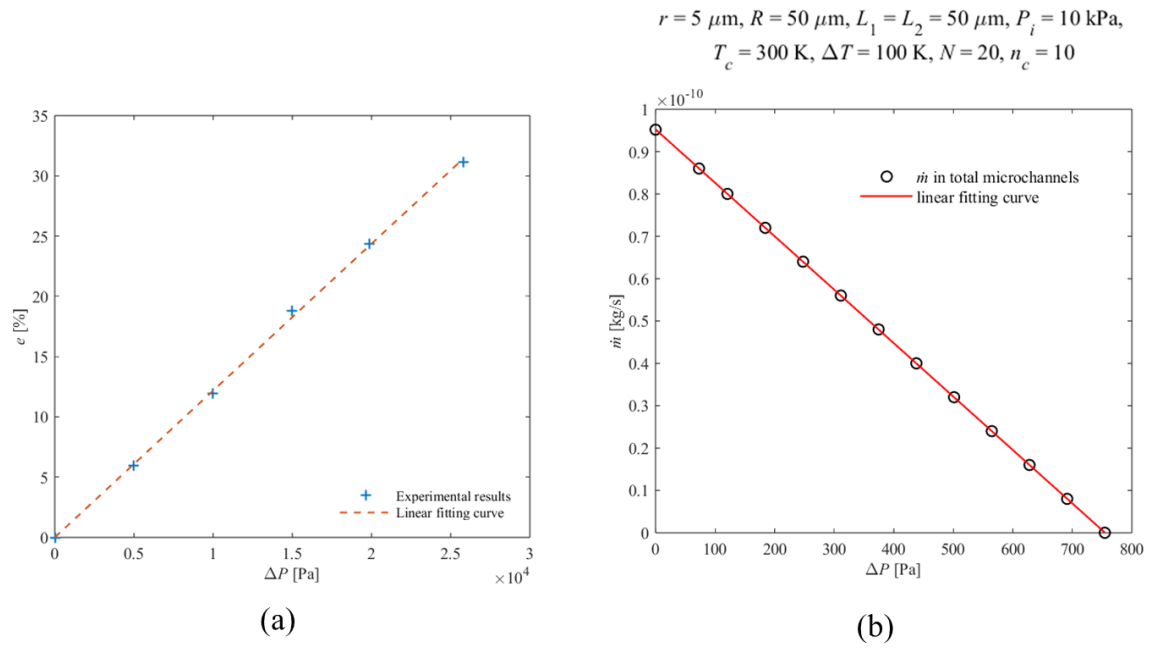

Figure 6.3 – a) Contraction ratio *e* vs pressure difference Δ*P* adapted from mini-muscles experiments; b) Characteristic curve of a specific multistage KμP with only 20 stages and 10 microchannels per stage.

For example, for a KµP with 20 stages and 10 microchannels per stage, this function, which is represented in Fig. 6.3b, is linear. For the simulation with air as the working gas, the following parameters, adapted to the size of the PAµM, have been chosen for the KµP considered for the coupling with the muscle: 10 microchannels per stage with a radius $r = 5$ µm and a length $L_1 = 50$ µm, a macrochannel with a radius of $R = 50$ µm and a length $L_2 = 50$ µm. The temperature difference was set to 100 K and the inlet pressure to 100 kPa. For the simulations presented in Section 6.3, all these parameters are conserved but the number N of stages and the number n_c of microchannels per stage is varied. For a large number of stages, as elaborated in Chapter 2, the characteristic curve expressed by Eq. (6.5) is no longer linear.

This transient problem is solved with a quasi-steady assumption, calculating at time step the following parameters:

- *m*: the mass of gas inside the PAµM
- P_{in}: pressure inside the PAµM
- T_{in}: temperature inside the PAµM assumed constant
- R_g: specific gas constant
- V_g: volume of gas inside the PAµM

Regarding this last parameter, two cases were considered: Case 1 for which there is no dead volume between the KµP and the deformable part of the PAµM ($V_g = V_{in}$, meaning that both elements are optimally integrated and the KµP enter inside the PAµM), and Case 2 for which there is a dead volume between the KµP and the deformable part of the PAµM ($V_g = V_{in} + V_s$).

The initial conditions at step $i = 0$ corresponding to $t = 0$ are the following:

$$P_{in(0)} = 100 \text{ kPa} \tag{6.6}$$

$$V_{(0)} = V_0 = 16.75 \times 10^{-11} \text{ m}^3 \text{ (Case 1) or } V_{(0)} = V_0 + V_s = 22 \times 10^{-11} \text{ m}^3 \text{ (Case 2)} \tag{6.7}$$

$$m_{(0)} = \frac{P_{in(0)} V_{(0)}}{R_g T_{in}} \tag{6.8}$$

$$\dot{m}_{(0)} = \dot{m}_{\max} \tag{6.9}$$

obtained from the simulation of the KµP in the open configuration. A time step Δt is then chosen and for each step $i \geq 1$ corresponding to $t = i\,\Delta t$, the following set of equations is solved:

$$P_{in\,(i+1)} = P_{in\,(i)} + \Delta P_{in\,(i)} \tag{6.10}$$

$$\Delta P_{(i+1)} = \Delta P_{(i)} + \Delta P_{in\,(i)} \tag{6.11}$$

$$m_{(i+1)} = m_{(i)} - \dot{m}_{(i)}\ \Delta t \tag{6.12}$$

$$V_{(i+1)} = V_{(i)} + \Delta V_{(i)} \tag{6.13}$$

In the above equations, the flow rate is calculated from the KµP characteristics:

$$\dot{m}_{\mathrm{K\mu P}\,(i)} = fct_{\mathrm{K\mu P}}\left(\Delta P_{\mathrm{K\mu P}\,(i)}\right) \tag{6.14}$$

which also writes for the PAµM with the same function:

$$\dot{m}_{(i)} = fct_{\mathrm{K\mu P}}\left(\Delta P_{(i)}\right) \tag{6.15}$$

as the mass flowrate entering the PAµM is opposite to the mass flowrate entering the KµP ($\dot{m}_{(i)} = -\dot{m}_{\mathrm{K\mu P}\,(i)}$) and $\Delta P_{\mathrm{K\mu P}\,(i)} = P_{out\,(i)} - P_{in\,(i)} = -\Delta P_{(i)}$.

In addition, by deriving the ideal equation of state of the gas

$$\dot{m}_{(i)}\ \Delta t = \frac{P_{in\,(i)}\ \Delta V_{(i)} + \Delta P_{in\,(i)}\ V_{(i)}}{R_g\ T} \tag{6.16}$$

and from the characteristic curve of the PAµM

$$\frac{\Delta V_{(i)}}{V_0} = \varepsilon\, \Delta P_{in(i)} \tag{6.17}$$

we can deduce:

$$\Delta P_{in(i)} = \frac{\dot{m}_{(i)}\ \Delta t\ R_g\ T}{P_{in(i)}\ V_0\ \varepsilon + V_{(i)}} \tag{6.18}$$

and

$$\Delta V_{(i)} = \frac{\dot{m}_{(i)}\ \Delta t\ R_g\ T\ V_0\ \varepsilon}{P_{in(i)}\ V_0\ \varepsilon + V_{(i)}} \tag{6.19}$$

Finally, the contraction ratio *e* at each time step is expressed as:

$$e_{(i)} = \frac{V_{(0)} - V_{(i)}}{V_0} \tag{6.20}$$

6.3 Preliminary simulation of the transient behavior of a PAµM coupled with a KµP

Using the aforementioned analysis, the transient behavior of a PAµM actuated via a multi-stage KµP is examined. The parameters utilized for the preliminary calculations are outlined in Table 6.1. The working fluid considered for these analytical investigations is air.

Table 6.1 – Parameters for preliminary calculation.

Parameters	T_c (K)	ΔT (K)	P_i (kPa)	r (µm)	L_1 (µm)	R (µm)	L_2 (µm)	N	n_c
Value	300	100	100	5	50			10 – 700	1, 5, 10

First, Case 1 was examined for varying values of N (Fig. 6.4), while keeping n_c constant at 10. The results show that the contraction ratio increases as N increases, since ΔP_{max} increases with N. In order to approach the maximum contraction ratio of the PAµM (32 %), 700 stages are required, and the final contraction is reached in about 3 s.

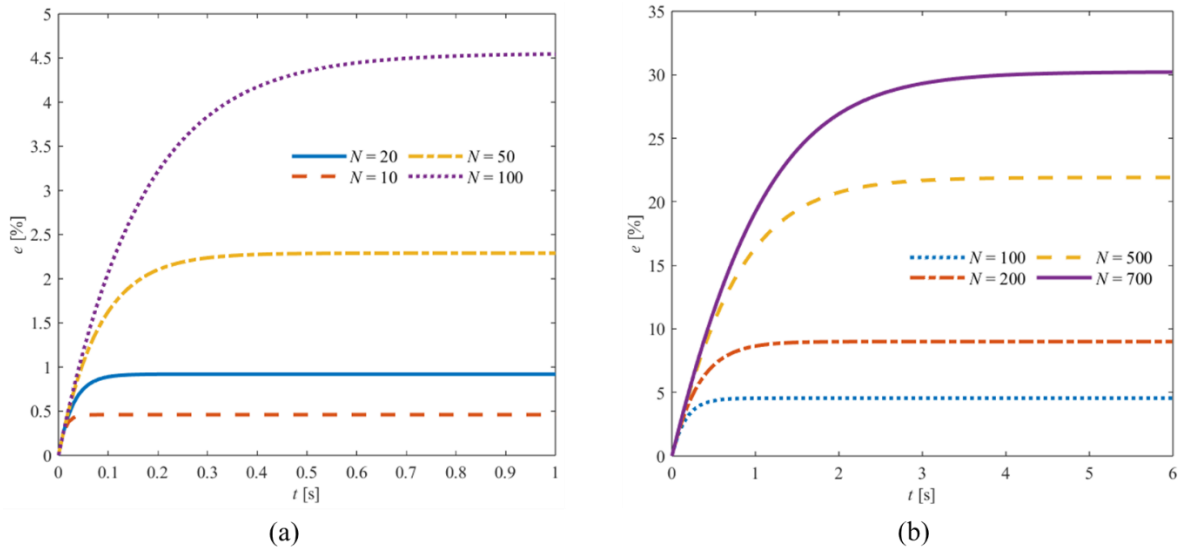

Figure 6.4 – Transient contraction of a PAµM actuated via a multistage KµP, according to Case 1 for $n_c = 10$ and a) for a number of stages $10 \leq N \leq 100$, and b) for $100 \leq N \leq 700$.

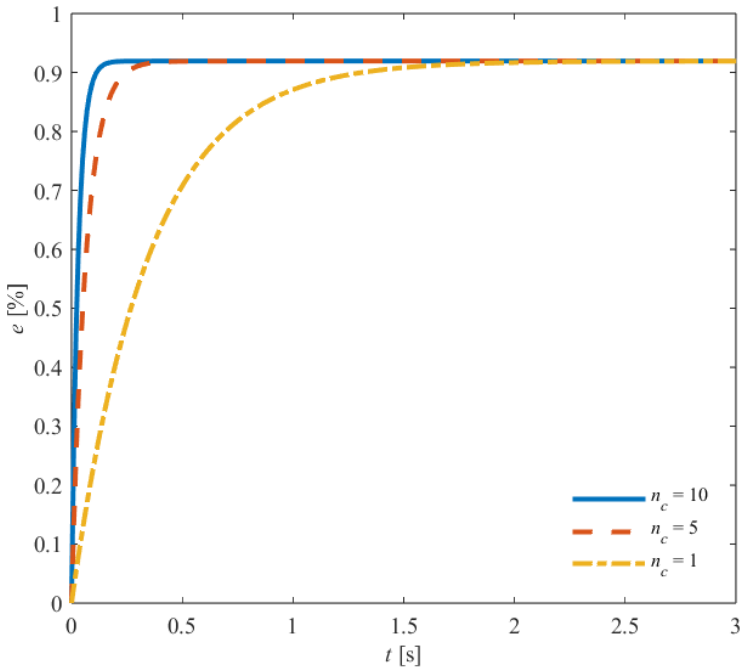

Figure 6.5 – Transient contraction of a PAμM actuated via a multistage KμP, according to Case 1 for $N = 20$ and for a number of microchannel in each stage $1 \leq n_c \leq 10$.

In a second step, the number of microchannels per stage was varied from 1 to 10, while keeping the same number of stages $N = 20$. As expected, increasing the number of microchannels per stage reduces the response time (see Fig. 6.5), as the mass flowrate is increased. It can be readily seen that the maximal contraction ratio does not depend on n_c, as the final pressure difference is not linked to the number of microchannels per stage, at least as long as the counter flow in the macrochannels is not significantly affected by the increase of mass flowrate.

Case 2 was also investigated for various values of N and n_c, and the results were compared to Case 1, as shown in Fig. 6.6. The presence of the dead volume V_s is clearly visible: it delays the contraction of the PAμM, resulting in a longer response time.

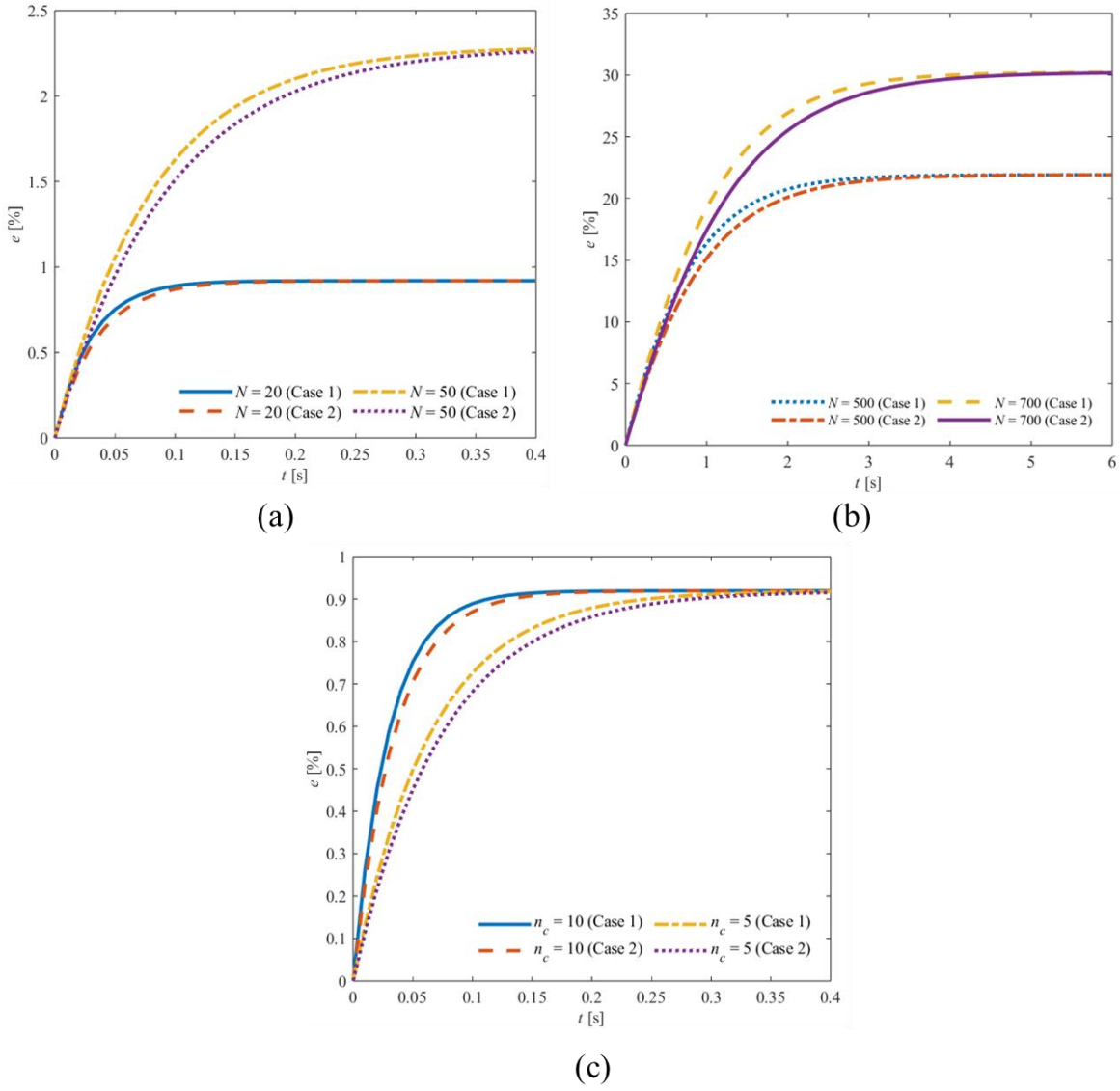

Figure 6.6 – Transient contraction of a PAμM actuated via a multistage KμP, according to Cases 1 and 2, stressing the influence of the dead volume. a) for $n_c = 10$ and $10 \le N \le 50$, b) for $n_c = 10$ and $500 \le N \le 700$, and c) for $N = 20$ and $5 \le n_c \le 10$.

Overall, we can see that with a limited number (less than 20) microchannels in parallel, response times of the order of 1 ms are reached. As the TPP microfabrication technique should allow manufacturing of KμP with much higher n_c, it is reasonable to expect a significant reduction of this response time in the future.

6.4 Conclusions and perspectives

The transient behavior of micro-muscles actuated through a multistage Knudsen micropump has been theoretically explored, involving the analysis and comparison of two distinct cases. The obtained results reveal that as the number of stages increases, the contraction ratio

also rises, while the time required to attain the maximum contraction ratio diminishes with a higher number of parallel microchannels in each stage of the KμP. In addition, when comparing Cases 1 and 2, it is evident that Case 2, with a constant dead volume, experiences a time delay due to the increased duration needed to reduce pressure and reach the peak differential pressure.

Further calculations are essential to refine the present model before its application to more intricate models, adapted to multistage Knudsen pumps featuring varying numbers and arrangements of microchannels in each stage, optimizing each stage as a function of the local Knudsen number. These models also need to encompass diverse deformations beyond linear contractions generated by artificial micro-muscles under vacuum. Moreover, the behavior of artificial micro-muscles –both static and dynamic– is contingent upon factors like the muscle's material, structure, and the performance of the employed KμP. Thus, achieving an optimal synergy between appropriately designed artificial micro-muscles and corresponding Knudsen pumps remains a challenging field of research.

Exploring different structural variations of artificial muscles can lead to multifunctional micro-muscles capable of mimicking diverse biological movements, addressing challenges in microscale applications where conventional macro-muscles might not be functional. Moreover, ensuring the stability of artificial micro-muscles within their operating environment is crucial for safe and effective performance.

Finally, it's worth noting that the current artificial muscles driven by negative pressure operate with air as the working gas, mostly functioning at atmospheric pressure levels. This observation may inspire further investigation into the performance of muscles operating with different gases and under varying pressure conditions distinct from atmospheric levels.

6.5 Summary

In this chapter, we introduced the concept of integrating Knudsen micropumps with artificial micro-muscles. We outlined an initial method for simulating the behavior of this integrated microsystem and presented a preliminary analysis. Finally, we provided a glimpse into the potential prospects of this innovative concept.

While we took the first steps towards exploring this concept by integrating Knudsen micropumps with artificial micro-muscles, it's important to note that the preliminary analysis was conducted on a straightforward Knudsen pump structure. Consequently, the scope of our results is limited in predicting the performance of more complex system configurations. Subsequent research should expand to encompass various designs for both Knudsen pumps and

artificial micro-muscles. This will provide a comprehensive evaluation of different system configurations. We strongly believe that the integrated system of Knudsen pumps and artificial micro-muscles holds promise across diverse applications in the near future.

Conclusions

The current study represents an initial step towards the development of pneumatically actuated micro-muscles controlled by Knudsen micropumps. It involves both numerical and experimental investigations, as well as the development and implementation of reliable fabrication techniques for microchannels that will be integrated into Knudsen gas micropumps. The experimental characterization was specifically focused on isothermal gas flows through these microchannels subjected to pressure gradients. Furthermore, we conducted numerical simulations using Abaqus software and carried out experimental measurements on artificial mini-muscles actuated by negative pressures. Subsequently, we performed preliminary calculations to pave the way for the further design and optimization of a complex microsystem that integrates the Knudsen pumps and artificial micro-muscles.

The theoretical and computational investigation of microchannels is grounded in the kinetic theory of gases and remains valid across the entire Knudsen number spectrum. Experimental work, both for microchannels and artificial mini-muscles, took place at the Clément Ader Institute (ICA). In the former case, we employed the constant volume time-dependent methodology, and we achieved good agreement with corresponding numerical results for microchannels with constant cross-sections. In the latter case, we applied various pressure differences to compress the artificial mini-muscles, and we compared the experimental and numerical results. The manufacturing of microchannels was conducted at KNMFi in KIT, Germany (using the TPP technique), and LPCNO in Toulouse, France (via maskless lithography). I participated to the fabrication campaign at LPCNO, while the fabrication campaign at KNMFi was conducted by the local KIT team. These two fabrication methodologies, in conjunction with the numerical and experimental results, will be applied in the future for the development of multistage micropumps.

I. Summary and Major Contributions

The research presented in this work has made significant contributions in the following areas:

1. **Improvement of a Kinetic Code**: A kinetic code, previously developed by Lopez-Quesada, has been extended to assess the performance of multistage Knudsen pumps. These pumps consist of numerous identical and parallel microchannels connected to a macrochannel in each stage. The code is founded on the linear Shakhov kinetic model,

subject to purely diffusive boundary conditions, and incorporate the infinite capillary theory. A parametric study of the multistage Knudsen pump's impact on thermal transpiration flow was conducted. This study characterized the system's performance, considering variables such as the number of stages and parallel microchannels. It provided insights into mass flowrate and pressure difference, along with characteristic curves relating pressure difference to mass flowrate at the same operating pressure, with respect to the number of stages and parallel microchannels in the assembly.

2. **Implementation of TPP Technique**: The TPP (Two-Photon Polymerization) fabrication technique was applied to manufacture single microchannels with both constant and variable circular cross-sections, as well as a single microchannel with a variable square cross-section. All microchannels were visually examined under a microscope, and isothermal pressure-driven flow experiments were conducted on microchannels with constant and tapered circular cross-sections using the constant volume technique. The experimental results exhibited a noteworthy agreement with numerical results, confirming the suitability of the TPP fabrication technique for producing 3D microdevices designed for rarefied gas flows.
3. **Alternative Manufacturing Process**: Another manufacturing process was proposed for fabricating elements of Knudsen micropumps, involving the lamination of dry film photoresist layers to create microchannels with constant rectangular cross-sections. Two different dry film photoresist materials were employed to fabricate 3D structures through maskless lithography. While manufacturing certain channels with precise and accurate geometry was achieved after extensive efforts, it was observed that under high vacuum conditions, microchannels might collapse or become blocked.
4. **Thermally Driven Flow Experiments**: Experiments were conducted on thermally driven flow in micro glass tubes with a fixed temperature difference, starting from zero initial pressure difference. Notably, there was a significant deviation between the experimental data and simulated results due to substantial leakage, which was several times greater than the actual gas flows inside the tube. Nevertheless, the measured data for the maximum pressure difference and the maximum mass flowrate as functions of input pressure demonstrated a similar trend to the numerical results.
5. **Artificial Mini-Muscles**: Three bellows-like artificial mini-muscles were manufactured using 3D printing technology. These mini-muscles were examined both experimentally and numerically in terms of their static and dynamic behaviors when actuated by negative pressure. The results revealed that the maximum contraction ratio increased as the

pressure difference rose within a critical range. Beyond this critical value, the maximum contraction remained constant.

6. **Integration of Knudsen Pumps and Artificial Micro-Muscles**: This work introduced the novel concept of integrating Knudsen micropumps with artificial micro-muscles. The study provided the first steps toward the development of a metamodel for optimization purposes, considering parameters such as the ratio of pressure difference to inlet pressure and the volume variation of artificial micro-muscles during deformation, as functions of three dimensionless parameters defined by the microchannel diameter. Preliminary calculations were conducted on a simplified configuration of a multistage Knudsen micropump, and promising response times were obtained.

II. Future Work

We hope that the outcomes of this research are of some significance, motivating the continuation of the ongoing work in modeling, manufacturing, and experiments to further advance technological knowledge in the field and create promising gas microfluidic devices for various applications. Within this research line, the following steps are proposed:

1. **Simulation of Thermal Transpiration Gas Flows**: Future work may include simulations of thermal transpiration gas flows in multistage Knudsen pumps with rectangular cross-sections. These simulations can assess performance and provide characteristic curves for this type of Knudsen pump.
2. **Experimental Testing of Tapered Microchannels**: Isothermal pressure-driven flows through tapered square microchannels, as proposed in Chapter 3, will be experimentally tested. This evaluation will explore the existence of diode effects, and results will be compared with numerical calculations. Additionally, experimental investigations into thermal transpiration flows in both straight and tapered channels may be conducted in the near future.
3. **Expanding TPP Fabrication Technique**: The TPP fabrication technique can be extended for the manufacturing of several parallel microchannels positioned over the center of a metal plate. Following this, experiments on both pressure and temperature-driven flows can be performed, if feasible. Moreover, microchannels fabricated using DF lamination and maskless lithography, after improvement of the process to produce more reliable samples, will undergo experimental measurements for isothermal pres-

sure-driven flows using the constant volume technique.

4. **Enhanced Preliminary Calculations**: Preliminary calculations should be expanded to incorporate more complex models to validate the analytical method. This will allow for the exploration of more precise simulated data, and the development of metal models based on an numerical experience plan to ease the optimization. As a result, an initial integration of Knudsen pumps and artificial micro-muscles could be achieved in the near future.
5. **Diverse Artificial Mini-Muscles**: The research can involve the creation and experimental measurement of various artificial mini-muscles with different structures. These mini-muscles can be designed to achieve different deformations, including contraction, bending, twisting, and more.

These proposed steps should advance our understanding of gas microfluidics and contribute to the development of innovative devices for a wide range of applications.

References

[1] G.L. Quesada, Thermally Driven Vacuum Micropumps, PhD thesis, (University of Toulouse, 2019).

[2] J. Fluitman, Microsystems technology: objectives, Sensors and Actuators A: Physical. 56 (1996) 151–166.

[3] P. Irving, L. Allen, Q. Ming, T. Healey, Novel Catalytic Fuel Reforming Using Micro-Technology with Advanced Separations Technology, (2002).

[4] C.P. Ellington, The novel aerodynamics of insect flight: applications to micro-air vehicles, Journal of Experimental Biology. 202 (1999) 3439–3448.

[5] X. Wang, T. Su, W. Zhang, Z. Zhang, S. Zhang, Knudsen pumps: a review, Microsyst Nanoeng. 6 (2020) 26.

[6] O. Reynolds, XVIII. On certain dimensional properties of matter in the gaseous state. Part I. Experimental researches on thermal transpiration of gases through porous plates, and on the laws of transpiration and impulsion, including an experimental proof that gas is not a continuous plenum. Part II. On an extension of the dynamical theory of gas which includes the stresses, tangential and normal, caused by a varying condition of the gas, and affords an explanation of the phenomena of transpiration and impulsion, Philos. Trans. R. Soc. London, Ser. A. 170. (1879) 727–845.

[7] J.C.Maxwell, III. On stresses in rarefied gases arising from inequalities of temperature, Proc. Royal Soc. Lond. 27 (1879) 304-308.

[8] N.K. Gupta, S. An, Y.B. Gianchandani, A Si-micromachined 48-stage Knudsen pump for on-chip vacuum, J. Micromech. Microeng. 22 (2012) 105026.

[9] S. An, N.K. Gupta, Y.B. Gianchandani, A Si-Micromachined 162-Stage Two-Part Knudsen Pump for On-Chip Vacuum, J. Microelectromech. Syst. 23 (2014) 406–416.

[10] H. Sugimoto, Vacuum Pump without a Moving Part Driven by Thermal Edge Flow, in: AIP Conference Proceedings, AIP, Bari (Italy), 2005: pp. 168–173.

[11] Y. Sone, Vacuum Pump without a Moving Part and its Performance, in: AIP Conference Proceedings, AIP, Whistler, British Columia (Canada), 2003: pp. 1041–1048.

[12] S. McNamara, Y.B. Gianchandani, On-chip vacuum generated by a micromachined Knudsen pump, J. Microelectromech. Syst. 14 (2005) 741–746.

[13] S.E. Vargo, Initial results from the first MEMS fabricated thermal transpiration-driven vacuum pump, in: AIP Conference Proceedings, AIP, Sydney (Australia), 2001: pp. 502–509.

[14] S.E. Vargo, E.P. Muntz, G.R. Shiflett, W.C. Tang, Knudsen compressor as a microand macroscale vacuum pump without moving parts or fluids, Journal of Vacuum Science & Technology A: Vacuum, Surfaces, and Films. 17 (1999) 2308–2313.

[15] R.M. Young, Analysis of a micromachine based vacuum pump on a chip actuated by the thermal transpiration effect, J. Vac. Sci. Technol. B. 17 (1999) 280.

[16] N. Van Toan, N. Inomata, N.H. Trung, T. Ono, Knudsen pump produced via silicon deep RIE, thermal oxidation, and anodic bonding processes for on-chip vacuum pumping, J. Micromech. Microeng. 28 (2018) 055001.

[17] S. McNamara, Y.B. Gianchandani, A micromachined Knudsen pump for on-chip vacuum, in: TRANSDUCERS '03. 12th International Conference on Solid-State Sensors, Actuators and Microsystems. Digest of Technical Papers (Cat. No.03TH8664), IEEE, Boston, MA, USA, 2003: pp. 1919–1922.

[18] S. Nakaye, H. Sugimoto, N.K. Gupta, Y.B. Gianchandani, Thermal method of gas separation with micro-pores, in: IEEE SENSORS 2014 Proceedings, IEEE, Valencia, Spain, 2014: pp. 815–818.

[19] S. Nakaye, H. Sugimoto, N.K. Gupta, Y.B. Gianchandani, Thermally enhanced membrane gas separation, European Journal of Mechanics B/Fluids. 49 (2015) 36–49.

[20] S. Nakaye, H. Sugimoto, Demonstration of a gas separator composed of Knudsen pumps, Vacuum. 125 (2016) 154–164.

[21] S. Takata, H. Umetsu, Numerical study on effective configurations of the Knudsen pump for separation and compression, in: Pacific Grove, California, (USA), 2011: pp. 998–1003.

[22] S. Takata, H. Sugimoto, S. Kosuge, Gas separation by means of the Knudsen compressor, European Journal of Mechanics B/Fluids. 26 (2007) 155–181.

[23] Nakaye S., Studies on a thermal method of gas separation with porous membrane, (2016).

[24] H. Sugimoto, A. Shinotou, Gas Separator with the Thermal Transpiration in a Rarefied Gas, in: Pacific Grove, California, (USA), 2011: pp. 784–789.

[25] H. Sugimoto, M. Hibino, Numerical analysis on gas separator with thermal transpiration in micro channels, in: Zaragoza, Spain, 2012: pp. 794–801.

[26] S. Nakaye, H. Sugimoto, Numerical analysis of gas separator with thermal transpiration in micro channels II, in: Xi'an, China, 2014: pp. 792–798.

[27] M. Matsumoto, S. Nakaye, H. Sugimoto, Gas separation by the molecular exchange flow through micropores of the membrane, in: Victoria, BC, Canada, 2016: p. 080011.

[28] V. Kosyanchuk, V. Kovalev, A. Yakunchikov, Multiscale modeling of a gas separation device based on effect of thermal transpiration in the membrane, Separation and Purification Technology. 180 (2017) 58–68.

[29] H. Sugimoto, T. Abe, Experiment on the Gas Separation Effect of the Pump Driven by the Thermal Edge Flow, in: AIP Conference Proceedings, AIP, Kyoto (Japan), 2008: pp. 1123–1128.

[30] T. Baier, S. Hardt, Gas separation in a Knudsen pump inspired by a Crookes radiometer, Microfluid Nanofluid. 24 (2020) 41.

[31] A. Yakunchikov, V. Kosyanchuk, Numerical investigation of gas separation in the system of filaments with different temperatures, International Journal of Heat and Mass Transfer.138 (2019) 144–151.

[32] F. Ochoa, P.D. Ronney, A thermal transpiration-based self-pressurizing mesoscale combustor, (2006) 5.

[33] A. Bhat, C. Bloomquist, J. Ahn, Y. Kim, D. Kim, Thermal Transpiration Based Micro-Scale Pumping and Power Generation Devices, in: 7th International Energy Conversion Engineering Conference, American Institute of Aeronautics and Astronautics, Denver, Colorado, 2009.

[34] K. Wang, P. Zeng, J. Ahn, P.D. Ronney, A self-sustaining thermal transpiration gas pump and SOFC power generation system, Proceedings of the Combustion Institute. 34 (2013) 3327–3334.

[35] P. Zeng, K. Wang, J. Ahn, P.D. Ronney, Thermal Transpiration Based Pumping and Power Generation Devices, JTST. 8 (2013) 370–379.

[36] J. Wongwiwat, P. Bhuripanyo, P. Ronney, Hydrocarbon-Fueled Electrical Power Generator with no Moving Parts, in: AIAA Scitech 2019 Forum, American Institute of Aeronautics and Astronautics, San Diego, California, 2019.

[37] K. Kugimoto, Y. Hirota, Y. Kizaki, Motionless heat pump – A new application of thermal transpiration, in: Victoria, BC, Canada, 2016: p. 080004.

[38] K. Kugimoto, Y. Hirota, T. Yamauchi, H. Yamaguchi, T. Niimi, A novel heat pump system using a multi-stage Knudsen compressor, International Journal of Heat and Mass Transfer. 127 (2018) 84–91.

[39] K. Kugimoto, Y. Hirota, T. Yamauchi, H. Yamaguchi, T. Niimi, Design and demonstration of Knudsen heat pump without moving parts free from electricity, Applied Energy. 250 (2019) 1260–1269.

[40] J. Liu, N.K. Gupta, K.D. Wise, Y.B. Gianchandani, X. Fan, Demonstration of motion-

less Knudsen pump based micro-gas chromatography featuring micro-fabricated columns and on-column detectors, Lab Chip. 11 (2011) 3487.

[41] Y. Qin, Y.B. Gianchandani, A facile, standardized fabrication approach and scalable architecture for a micro gas chromatography system with integrated pump, in: 2013 Transducers & Eurosensors XXVII: The 17th International Conference on Solid-State Sensors, Actuators and Microsystems (TRANSDUCERS & EUROSENSORS XXVII), IEEE, Barcelona, Spain, 2013: pp. 2755–2758.

[42] Yutao Qin, Y.B. Gianchandani, iGC1: An Integrated Fluidic System for Gas Chromatography Including Knudsen Pump, Preconcentrator, Column, and Detector Microfabricated by a Three-Mask Process, J. Microelectromech. Syst. 23 (2014) 980–990.

[43] Y. Qin, Y.B. Gianchandani, A fully electronic microfabricated gas chromatograph with complementary capacitive detectors for indoor pollutants, Microsyst Nanoeng. 2 (2016) 15049.

[44] Q. Cheng, Y. Qin, Y.B. Gianchandani, A bidirectional Knudsen pump with superior thermal management for micro-gas chromatography applications, in: 2017 IEEE 30th International Conference on Micro Electro Mechanical Systems (MEMS), IEEE, Las Vegas, NV, 2017: pp. 167–170.

[45] Y. Sone, Molecular gas dynamics: theory, techniques, and applications, 1st ed, Birkhäuser, Boston, 2007.

[46] Y. Sone, Kinetic Theory and Fluid Dynamics, Birkhäuser Boston, Boston, MA, 2002.

[47] A. Mohammadzadeh, A.S. Rana, H. Struchtrup, Thermal stress vs. thermal transpiration: A competition in thermally driven cavity flows, Phys. Fluids. 27 (2015) 112001.

[48] A. Mohammadzadeh, H. Struchtrup, Velocity dependent Maxwell boundary conditions in DSMC, International Journal of Heat and Mass Transfer. 87 (2015) 151–160.

[49] Y. Sone, Flows Induced by Temperature Fields in a Rarefied Gas and their Ghost Effect on the Behavior of a Gas in the Continuum Limit, Annu. Rev. Fluid Mech. 32 (2000) 779–811.

[50] V.S. Galkin, M.N. Kogan, O.G. Fridlender, Free convection in a gas in the absence of external forces, Fluid Dyn. 6 (1973) 448–457.

[51] M.N. Kogan, V.S. Galkin, O.G. Fridlender, Stresses produced in gasses by temperature and concentration inhomogeneities. New types of free convection, 19 (1976) 10.

[52] K. Aoki, Y. Sone, Y. Waniguchi, A rarefied gas flow induced by a temperature field: Numerical analysis of the flow between two coaxial elliptic cylinders with different uniform temperatures, Computers & Mathematics with Applications. 35 (1998) 15–28.

[53] Y. Sone, M. Yoshimoto, Demonstration of a rarefied gas flow induced near the edge of a uniformly heated plate, Physics of Fluids. 9 (1997) 3530–3534.

[54] S. Taguchi, K. Aoki, Rarefied gas flow around a sharp edge induced by a temperature field, J. Fluid Mech. 694 (2012) 191–224.

[55] S. Taguchi, K. Aoki, Motion of an array of plates in a rarefied gas caused by radiometric force, Phys. Rev. E. 91 (2015) 063007.

[56] W. Crookes, Apparats for Indicating the Intensity of Radiation. No. 182,172. Patented Sept. 12, (1876).

[57] S. Chen, K. Xu, C. Lee, The dynamic mechanism of a moving Crookes radiometer, Physics of Fluids. 24 (2012) 111701.

[58] Y.-L. Han, E.P. Muntz, Experimental investigation of micro-mesoscale Knudsen compressor performance at low pressures, J. Vac. Sci. Technol. B. 25 (2007) 703.

[59] P. Zhang, R.X. Du, L. Guo, D.D. Joseph, Y. Matsumoto, Y. Sommerfeld, Y. Wang, A New Energy Harvesting Method Based on Knudsen Compressor, in: Xi'an (China), 2010: pp. 551–556.

[60] Y.-L. Han, E. Phillip Muntz, A. Alexeenko, M. Young, Experimental and Computational Studies of Temperature Gradient–Driven Molecular Transport in Gas Flows through Nano/Microscale Channels, Nanoscale and Microscale Thermophysical Engineering. 11 (2007) 151–175.

[61] J.-S. Heo, Numerical Analysis of Thermal Transpiration Flows for a Nano-Pore Aerogel Membrane, Jnn. 9 (2009).

[62] G. López Quesada, G. Tatsios, D. Valougeorgis, M. Rojas-Cárdenas, L. Baldas, C. Barrot, S. Colin, Thermally driven pumps and diodes in multistage assemblies consisting of microchannels with converging, diverging and uniform rectangular cross sections, Microfluid Nanofluid. 24 (2020) 54.

[63] Yen-Lin Han, Thermal-Creep-Driven Flows in Knudsen Compressors and Related Nano/Microscale Gas Transport Channels, J. Microelectromech. Syst. 17 (2008) 984–997.

[64] Z. Zhang, X. Wang, L. Zhao, S. Zhang, F. Zhao, Study of Flow Characteristics of Gas Mixtures in a Rectangular Knudsen Pump, Micromachines. 10 (2019) 79.

[65] C. Du, X. Wang, F. Han, X. Ren, Z. Zhang, Numerical Investigation into the Flow Characteristics of Gas Mixtures in Knudsen Pump with Variable Soft Sphere Model, Micromachines. 11 (2020) 784.

[66] J. Shao, J. Ye, Y. Zhang, S. Salem, Z. Zhao, J. Yu, Effect of the microchannel obstacles

on the pressure performance and flow behaviors of the hydrogen Knudsen compressor, International Journal of Hydrogen Energy. 44 (2019) 22691–22703.

[67] J. Ye, J. Shao, J. Xie, Z. Zhao, J. Yu, Y. Zhang, S. Salem, The hydrogen flow characteristics of the multistage hydrogen Knudsen compressor based on the thermal transpiration effect, International Journal of Hydrogen Energy. 44 (2019) 22632–22642.

[68] K. Aoki, P. Degond, L. Mieussens, M. Nishioka, S. Takata, Numerical Simulation of a Knudsen Pump Using the Effect of Curvature of the Channel, RGD symposium, rarefied gas dynamics. In: Ivanov MS, Rebrov AK (eds) Siberian Branch of the Russian Academy of Sciences. Novosibirsk, Russia, (2007) 1079–1084

[69] K. Aoki, P. Degond, L. Mieussens, S. Takata, H. Yoshida, A Diffusion Model for Rarefied Flows in Curved Channels, Multiscale Model. Simul. 6 (2008) 1281–1316.

[70] K. Aoki, P. Degond, L. Mieussens, Numerical Simulations of Rarefied Gases in Curved Channels: Thermal Creep, Circulating Flow, and Pumping Effect, CiCP. 6 (2009) 919–954.

[71] V. Leontidis, J.J. Brandner, L. Baldas, S. Colin, Numerical analysis of thermal creep flow in curved channels for designing a prototype of Knudsen micropump, J. Phys.: Conf. Ser. 362 (2012) 012004.

[72] V. Leontidis, J. Chen, L. Baldas, S. Colin, Numerical design of a Knudsen pump with curved channels operating in the slip flow regime, Heat Mass Transfer. 50 (2014) 1065–1080.

[73] D.M. Bond, V. Wheatley, M. Goldsworthy, Numerical investigation of curved channel Knudsen pump performance, International Journal of Heat and Mass Transfer. 76 (2014) 1–15.

[74] D.M. Bond, V. Wheatley, M. Goldsworthy, Numerical investigation into the performance of alternative Knudsen pump designs, International Journal of Heat and Mass Transfer. 93 (2016) 1038–1058.

[75] J. Chen, L. Baldas, S. Colin, Numerical study of thermal creep flow between two ratchet surfaces, Vacuum. 109 (2014) 294–301.

[76] J. Chen, S.K. Stefanov, L. Baldas, S. Colin, Analysis of flow induced by temperature fields in ratchet-like microchannels by Direct Simulation Monte Carlo, International Journal of Heat and Mass Transfer. 99 (2016) 672–680.

[77] G. Tatsios, G. Lopez Quesada, M. Rojas-Cardenas, L. Baldas, S. Colin, D. Valougeorgis, Computational investigation and parametrization of the pumping effect in temperature-driven flows through long tapered channels, Microfluid Nanofluid. 21

(2017) 99.

[78] M.S. Mozaffari, E. Roohi, On the thermally-driven gas flow through divergent micro/nanochannels, Int. J. Mod. Phys. C. 28 (2017) 1750143.

[79] S. Taguchi, Diffusion model for Knudsen-type compressor composed of periodic arrays of circular cylinders, Physics of Fluids. 22 (2010) 102001.

[80] K. Kugimoto, Y. Hirota, Y. Kizaki, H. Yamaguchi, T. Niimi, Performance prediction method for a multi-stage Knudsen pump, Physics of Fluids. 29 (2017) 122002.

[81] N.K. Gupta, Y.B. Gianchandani, Thermal transpiration in zeolites: A mechanism for motionless gas pumps, Appl. Phys. Lett. 93 (2008) 193511.

[82] K. Pharas, S. McNamara, Knudsen pump driven by a thermoelectric material, J. Micromech. Microeng. 20 (2010) 125032.

[83] Q. Cheng, Y. Qin, Y.B. Gianchandani, A Bidirectional Knudsen Pump with a 3D-Printed Thermal Management Platform, Micromachines. 12 (2021) 58.

[84] T. Byambadorj, Q. Cheng, Y. Qin, Y.B. Gianchandani, A monolithic Si-micromachined four-stage Knudsen pump for μ GC applications, J. Micromech. Microeng. 31 (2021) 034001.

[85] H. Kim, A.A. Astle, K. Najafi, L.P. Bernal, P.D. Washabaugh, An Integrated Electrostatic Peristaltic 18-Stage Gas Micropump With Active Microvalves, J. Microelectromech. Syst. 24 (2015) 192–206.

[86] J.C.Maxwell, On the Dynamical Theory of Gases, Philosophical Transactions of the Royal Society of London, 157 (1867) 49–88.

[87] C. Shen, Rarefied gas dynamics: fundamentals, simulations and micro flows, Springer, Berlin ; New York, NY, 2005.

[88] W. Steckelmacher, Molecular gas dynamics and the direct simulation of gas flows, Vacuum. 47 (1996) 1140.

[89] S. Colin, Single-Phase Gas Flow in Microchannels, in: Heat Transfer and Fluid Flow in Minichannels and Microchannels, Elsevier, 2014: pp. 11–102.

[90] K. Koura, H. Matsumoto, Variable soft sphere molecular model for inverse-power-law or Lennard-Jones potential, Physics of Fluids A: Fluid Dynamics. 3 (1991) 2459–2465.

[91] A. Van Itterbeek, E. De Grande, Measurements on the thermomolecular pressure difference for hydrogen and deuterium gas at low temperatures, Physica. 13 (1947) 289–304.

[92] J.M. Los, R.R. Fergusson, Measurements of thermomolecular pressure differences on argon and nitrogen, Trans. Faraday Soc. 48 (1952) 730.

[93] S.C. Liang, Some Measurements of Thermal Transpiration, Journal of Applied Physics. 22 (1951) 148–153.

[94] S.C. Liang, On the Calculation of Thermal Transpiration, Journal of Physical Chemistry. 57 (1953) 910–911.

[95] M.J. Bennett, F.C. Tompkins, Thermal transpiration: application of Liang's equation, Trans. Faraday Soc. 53 (1957) 185.

[96] T. Takaishi, Y. Sensui, Thermal transpiration effect of hydrogen, rare gases and methane, Trans. Faraday Soc. 59 (1963) 2503.

[97] P.L. Bhatnagar, E.P. Gross, M. Krook, A Model for Collision Processes in Gases. I. Small Amplitude Processes in Charged and Neutral One-Component Systems, Phys. Rev. 94 (1954) 511–525.

[98] F. Sharipov, V. Seleznev, Data on Internal Rarefied Gas Flows, Journal of Physical and Chemical Reference Data. 27 (1998) 657–706.

[99] E.M. Shakhov, Generalization of the Krook kinetic relaxation equation, Fluid Dyn. 3 (1972) 95–96.

[100] J.G. Méolans, I.A. Graur, Continuum analytical modelling of thermal creep, European Journal of Mechanics B/Fluids. 27 (2008) 785–809.

[101] F. Sharipov, Rarefied gas flow through a long tube at any temperature ratio, Journal of Vacuum Science & Technology A: Vacuum, Surfaces, and Films. 14 (1996) 2627–2635.

[102] F. Sharipov, Rarefied gas flow through a long tube at arbitrary pressure and temperature drops, Journal of Vacuum Science & Technology A: Vacuum, Surfaces, and Films. 15 (1997) 2434–2436.

[103] F. Sharipov, G. Bertoldo, Rarefied gas flow through a long tube of variable radius, Journal of Vacuum Science & Technology A: Vacuum, Surfaces, and Films. 23 (2005) 531–533.

[104] F. Sharipov, Non-isothermal gas flow through rectangular microchannels, J. Micromech. Microeng. 9 (1999) 394–401.

[105] F. Sharipov, Rarefied gas flow through a long rectangular channel, Journal of Vacuum Science & Technology A: Vacuum, Surfaces, and Films. 17 (1999) 3062–3066.

[106] I. Graur, M.T. Ho, Rarefied gas flow through a long rectangular channel of variable cross section, Vacuum. 101 (2014) 328–332.

[107] J. Chen, Numerical and experimental analysis of flows generated by temperature fields in rarefied gas: application to the design of Knudsen micropumps, PhD thesis, (Univer-

sity of Toulouse, 2016).

[108] F. Sharipov, ed., Discrete Velocity Method, in: Rarefied Gas Dynamics, Wiley-VCH Verlag GmbH & Co. KGaA, Weinheim, Germany, 2015: pp. 83–96.

[109] L. Mieussens, A survey of deterministic solvers for rarefied flows, AIP Conference Proceedings, 1628 (2014): 943–951.

[110] I. Graur, F. Sharipov, Non-isothermal flow of rarefied gas through a long pipe with elliptic cross section, Microfluid Nanofluid. 6 (2009) 267–275.

[111] F. Sharipov, I. Graur, C. Day, Leak rate of water into vacuum through microtubes, Journal of Vacuum Science & Technology A: Vacuum, Surfaces, and Films. 28 (2010) 443–448.

[112] M. Rojas-Cárdenas, E. Silva, M.-T. Ho, C.J. Deschamps, I. Graur, Time-dependent methodology for non-stationary mass flow rate measurements in a long micro-tube: Experimental and numerical analysis at arbitrary rarefaction conditions, Microfluid Nanofluid. 21 (2017) 86.

[113] I. Graur, T. Veltzke, J.G. Méolans, M.T. Ho, J. Thöming, The gas flow diode effect: theoretical and experimental analysis of moderately rarefied gas flows through a microchannel with varying cross section, Microfluid Nanofluid. 18 (2015) 391–402.

[114] I. Graur, J.G. Méolans, P. Perrier, J. Thöming, T. Veltzke, A physical explanation of the gas flow diode effect, Microfluid Nanofluid. 20 (2016) 145.

[115] PRIME Faraday Partnership, An Introduction to MEMS (Micro-electromechanical Systems). (Loughborough University, 2002)

[116] S. Pandey, D. Bansal, D. Panwar, N. Shukla, A. Kumar, P. Kothari, S. Verma, K.J. Rangra, Low cost lift-off process optimization for MEMS applications, in: Baroda (India), 2016: p. 020105.

[117] M. Rojas-Cárdenas, I. Graur, P. Perrier, J.G. Méolans, Time-dependent experimental analysis of a thermal transpiration rarefied gas flow, Physics of Fluids. 25 (2013) 072001.

[118] E. Silva, C.J. Deschamps, M. Rojas-Cárdenas, C. Barrot-Lattes, L. Baldas, S. Colin, A time-dependent method for the measurement of mass flow rate of gases in microchannels, International Journal of Heat and Mass Transfer. 120 (2018) 422–434.

[119] S. Kawata, H.-B. Sun, T. Tanaka, K. Takada, Finer features for functional microdevices, Nature. 412 (2001) 697–698.

[120] M. Deubel, G. von Freymann, M. Wegener, S. Pereira, K. Busch, C.M. Soukoulis, Direct laser writing of three-dimensional photonic-crystal templates for telecommunica-

tions, Nature Mater. 3 (2004) 444–447.

[121] F. Klein, T. Striebel, J. Fischer, Z. Jiang, C.M. Franz, G. von Freymann, M. Wegener, M. Bastmeyer, Elastic Fully Three-dimensional Microstructure Scaffolds for Cell Force Measurements, Adv. Mater. 22 (2010) 868–871.

[122] S. Hengsbach, A.D. Lantada, Rapid prototyping of multi-scale biomedical microdevices by combining additive manufacturing technologies, Biomed Microdevices. 16 (2014) 617–627.

[123] A.D. Lantada, S. Hengsbach, K. Bade, Lotus-on-chip: computer-aided design and 3D direct laser writing of bioinspired surfaces for controlling the wettability of materials and devices, Bioinspir. Biomim. 12 (2017) 066004.

[124] A. Ostendorf, B.N. Chichkov, Two-Photon Polymerization: A New Approach to Micromachining, Photon, Spectra 8 (2006).

[125] D. Zhang, G. López-Quesada, S. Bergdolt, S. Hengsbach, K. Bade, S. Colin, M. Rojas-Cárdenas, 3D micro-structures for rarefied gas flow applications manufactured via two-photon-polymerization, Vacuum. 211 (2023) 111915.

[126] D. Zhang, F. Schweizer, G.L. Quesada, S. Bergdolt, S. Hengsbach, K. Bade, D. Valougeorgis, B. Tondu, M. Rojas-Cárdenas, S. Colin, Isothermal pressure driven gas microflows in tapered microchannels with circular cross section: numerical and experimental investigations, (2023).

[127] B. Tondu, What Is an Artificial Muscle? A Systemic Approach., Actuators. 4 (2015) 336–352.

[128] J. Wang, D. Gao, P.S. Lee, Recent Progress in Artificial Muscles for Interactive Soft Robotics, Adv. Mater. (2020) 2003088.

[129] C. Zhang, P. Zhu, Y. Lin, W. Tang, Z. Jiao, H. Yang, J. Zou, Fluid-driven artificial muscles: bio-design, manufacturing, sensing, control, and applications, Bio-Des. Manuf. 4 (2021) 123–145.

[130] H.A. Baldwin, Realizable Models of Muscle Function, in: D. Bootzin, H.C. Muffley (Eds.), Biomechanics, Springer US, New York, NY, 1969: pp. 139–147.

[131] C. Tawk, M. in het Panhuis, G.M. Spinks, G. Alici, Bioinspired 3D Printable Soft Vacuum Actuators for Locomotion Robots, Grippers and Artificial Muscles, Soft Robotics. 5 (2018) 685–694.

[132] K. Takashima, J. Rossiter, T. Mukai, McKibben artificial muscle using shape-memory polymer, Sensors and Actuators A: Physical. 164 (2010) 116–124.

[133] P. Polygerinos, Z. Wang, J.T.B. Overvelde, K.C. Galloway, R.J. Wood, K. Bertoldi,

C.J. Walsh, Modeling of Soft Fiber-Reinforced Bending Actuators, IEEE TRANSACTIONS ON ROBOTICS. 31 (2015) 12.

[134] R.F. Shepherd, F. Ilievski, W. Choi, S.A. Morin, A.A. Stokes, A.D. Mazzeo, X. Chen, M. Wang, G.M. Whitesides, Multigait soft robot, Proceedings of the National Academy of Sciences. 108 (2011) 20400–20403.

[135] D. Yang, M.S. Verma, J.-H. So, B. Mosadegh, C. Keplinger, B. Lee, F. Khashai, E. Lossner, Z. Suo, G.M. Whitesides, Buckling Pneumatic Linear Actuators Inspired by Muscle, Adv. Mater. Technol. 1 (2016) 1600055.

[136] S. Li, D.M. Vogt, D. Rus, R.J. Wood, Fluid-driven origami-inspired artificial muscles, Proc. Natl. Acad. Sci. U.S.A. 114 (2017) 13132–13137.

[137] D. Yang, M.S. Verma, E. Lossner, D. Stothers, G.M. Whitesides, Negative-Pressure Soft Linear Actuator with a Mechanical Advantage, Adv. Mater. Technol. 2 (2017) 1600164.

[138] W. Felt, M.A. Robertson, J. Paik, Modeling vacuum bellows soft pneumatic actuators with optimal mechanical performance, in: 2018 IEEE International Conference on Soft Robotics (RoboSoft), IEEE, Livorno, 2018: pp. 534–540.

[139] M.S. Verma, A. Ainla, D. Yang, D. Harburg, G.M. Whitesides, A Soft Tube-Climbing Robot, Soft Robotics. 5 (2018) 133–137.

[140] J.-G. Lee, H. Rodrigue, Efficiency of Origami-Based Vacuum Pneumatic Artificial Muscle for Off-Grid Operation, Int. J. of Precis. Eng. and Manuf.-Green Tech. 6 (2019) 789–797.

[141] J.-G. Lee, H. Rodrigue, Origami-Based Vacuum Pneumatic Artificial Muscles with Large Contraction Ratios, Soft Robotics. 6 (2019) 109–117.

[142] V. Oguntosin, A. Akindele, Design and characterization of artificial muscles from wedge-like pneumatic soft modules, Sensors and Actuators A: Physical. 297 (2019) 111523.

[143] C. Tawk, A. Gillett, M. in het Panhuis, G.M. Spinks, G. Alici, A 3D-Printed Omni-Purpose Soft Gripper, IEEE Trans. Robot. 35 (2019) 1268–1275.

[144] C. Tawk, G.M. Spinks, M. in het Panhuis, G. Alici, 3D Printable Linear Soft Vacuum Actuators: Their Modeling, Performance Quantification and Application in Soft Robotic Systems, IEEE/ASME Trans. Mechatron. 24 (2019) 2118–2129.

[145] N. Lin, H. Zheng, Y. Li, R. Wang, X. Chen, X. Zhang, Self-Sensing Pneumatic Compressing Actuator, Front. Neurorobot. 14 (2020) 572856.

[146] S.D. Gollob, C. Park, B.H.B. Koo, E.T. Roche, A Modular Geometrical Framework for

Modelling the Force-Contraction Profile of Vacuum-Powered Soft Actuators, Front. Robot. AI. 8 (2021) 606938.

[147] S. Joe, M. Totaro, H. Wang, L. Beccai, Development of the Ultralight Hybrid Pneumatic Artificial Muscle: Modelling and optimization, PLoS ONE. 16 (2021).

[148] M.J. Mendoza, S.D. Gollob, D. Lavado, B.H.B. Koo, S. Cruz, E.T. Roche, E.A. Vela, A Vacuum-Powered Artificial Muscle Designed for Infant Rehabilitation, Micromachines. 12 (2021) 971.

[149] Z. Zhang, W. Fan, G. Chen, J. Luo, Q. Lu, H. Wang, A 3D Printable Origami Vacuum Pneumatic Artificial Muscle with Fast and Powerful Motion, in: 2021 IEEE 4th International Conference on Soft Robotics (RoboSoft), IEEE, New Haven, CT, USA, 2021: pp. 551–554.

[150] M.A. Robertson, J. Paik, Low-inertia vacuum-powered soft pneumatic actuator coil characterization and design methodology, in: 2018 IEEE International Conference on Soft Robotics (RoboSoft), IEEE, Livorno, 2018: pp. 431–436.

[151] C. Tawk, M. in het Panhuis, G.M. Spinks, G. Alici, Bioinspired 3D Printable Soft Vacuum Actuators for Locomotion Robots, Grippers and Artificial Muscles, Soft Robotics. 5 (2018) 685–694.

[152] S. Li, J.J. Stampfli, H.J. Xu, E. Malkin, E.V. Diaz, D. Rus, R.J. Wood, A Vacuum-driven Origami "Magic-ball" Soft Gripper, in: 2019 International Conference on Robotics and Automation (ICRA), IEEE, Montreal, QC, Canada, 2019: pp. 7401–7408.

[153] M. Fatahillah, N. Oh, H. Rodrigue, A Novel Soft Bending Actuator Using Combined Positive and Negative Pressures, Front. Bioeng. Biotechnol. 8 (2020) 472.

[154] P. Cheng, Y. Ye, J. Jia, C. Wu, Q. Xie, Design of cylindrical soft vacuum actuator for soft robots, Smart Mater. Struct. 30 (2021) 045020.

[155] N. Fadzri, P. Dinata, H. Basri, Simulation-Based Analysis on Novel Vacuum Actuation Concept for Soft Robotic Finger Development:, in: Palembang, Indonesia, 2021.

[156] Z. Jiao, C. Ji, J. Zou, H. Yang, M. Pan, Vacuum-Powered Soft Pneumatic Twisting Actuators to Empower New Capabilities for Soft Robots, Adv. Mater. Technol. 4 (2019) 1800429.

[157] Z. Jiao, C. Zhang, J. Ruan, W. Tang, Y. Lin, P. Zhu, J. Wang, W. Wang, H. Yang, J. Zou, Re-foldable origami-inspired bidirectional twisting of artificial muscles reproduces biological motion, Cell Reports Physical Science. 2 (2021) 100407.

[158] D. Yang, B. Mosadegh, A. Ainla, B. Lee, F. Khashai, Z. Suo, K. Bertoldi, G.M. Whitesides, Buckling of Elastomeric Beams Enables Actuation of Soft Machines, Adv. Ma-

ter. 27 (2015) 6323–6327.

[159] Y. Lin, G. Yang, Y. Liang, C. Zhang, W. Wang, D. Qian, H. Yang, J. Zou, Controllable Stiffness Origami “Skeletons” for Lightweight and Multifunctional Artificial Muscles, Adv. Funct. Mater. 30 (2020) 2000349.

[160] J. Hughes, S. Li, D. Rus, Sensorization of a Continuum Body Gripper for High Force and Delicate Object Grasping, in: 2020 IEEE International Conference on Robotics and Automation (ICRA), IEEE, Paris, France, 2020: pp. 6913–6919.

[161] C. Tawk, G.M. Spinks, M. in het Panhuis, G. Alici, 3D Printable Vacuum-Powered Soft Linear Actuators, in: 2019 IEEE/ASME International Conference on Advanced Intelligent Mechatronics (AIM), IEEE, Hong Kong, China, 2019: pp. 50–55.

[162] R. W. Ogden: Non-linear Elastic Deformations, Ellis Horwood Limited, Chichester, 1984, 532 pp.

[163] D.C. Kellermann, M.M. Attard, An invariant-free formulation of neo-Hookean hyperelasticity: An invariant-free formulation of neo-Hookean hyperelasticity, Z. Angew. Math. Mech. 96 (2016) 233–252.